High-Fidelity Entangling Gates with Trapped-Ions

by

Ting Rei Tan

B.S., National University of Singapore, 2009

A thesis submitted to the

Faculty of the Graduate School of the

University of Colorado in partial fulfillment

of the requirements for the degree of

Doctor of Philosophy

Department of Physics

2016

This thesis entitled:
High-Fidelity Entangling Gates with Trapped-Ions
written by Ting Rei Tan
has been approved for the Department of Physics

David J. Wineland

Emanuel Knill

Date

The final copy of this thesis has been examined by the signatories, and we find that both the content and the form meet acceptable presentation standards of scholarly work in the above mentioned discipline.

Tan, Ting Rei (Ph.D., Physics)

High-Fidelity Entangling Gates with Trapped-Ions

Thesis directed by Dr. David J. Wineland

Quantum entangling logic gates are key ingredients for the implementation of a quantum information processing device. In this thesis, we focus on experimental implementations of three types of entangling geometric-phase gates with trapped ions, which rely on the effective spin-spin interactions generated with state-dependent forces. First, a mixed-species entangling gate is demonstrated using a $^{9}Be^{+}$ and a $^{25}Mg^{+}$ ion to create a Bell state with a fidelity of 0.979(1). Combined with single-qubit gates, we use this mixed-species gate to implement controlled-NOT and SWAP gates. Second, we implement a high-fidelity universal gate set with $^{9}Be^{+}$ ions. Single-qubit gates with error per gate of $3.8(1) \times 10^{-5}$ are achieved. By creating a Bell state with a deterministic two-qubit entangling gate, we deduce a gate error as low as $8(4) \times 10^{-4}$. Third, a novel two-qubit entangling gate with dynamical decoupling built-in is demonstrated with a fidelity of 0.974(4). This gate is robust against qubit dephasing errors and offers simplifications in experimental implementation compared to some other gates with trapped ions. Errors in the above implementations are evaluated and methods to further reduce imperfections are discussed. In a separate experiment, correlated measurements made on pairs of ions violate a "chained" Bell inequality obeyed by any local-realistic theory. The lowest chained Bell inequality parameter determined from our measurements is 0.296(12), this value is significantly lower than 0.586, the minimum value derived from a perfect Clauser-Horne-Shimony-Horne (CHSH) Bell inequality experiment. Furthermore, our CHSH Bell inequality results provide a device-independent certification of the deterministically created Bell states.

Dedication

To the NIST ion storage group, and the trapped-ion community

Acknowledgements

Thanks to many people along the way, my Ph.D. journey has been an incredible experience and probably one of the best that anyone can hope for.

First and foremost, I would like to thank Dr. David J. Wineland for giving me the opportunity to work in the ion storage group at the National Institute of Standards and Technology (NIST). I appreciate the responsibility that was given to me to grow myself, and to take charge of the research and experiments that interest me.

It is my privilege to work in the ion storage group, which is formed by some of the brightest people I have ever met. I am grateful for being a team member of one of the most prominent, high quality and efficient experimental atomic physics group in the community, and the chance to work with some of the towering, established figures in the field.

Special thanks for John Gaebler, the post-doctoral researcher in my experiments during most of my Ph.D. career, we formed a good team together and I have always enjoyed bouncing ideas off one another. Team members of the experiments I have closely worked with also includes Yiheng Lin, and Ryan Bowler. The four of us form the last crews of the "2108" legacy experiment[1] , and the first crews of the "Quantum II" experiment[2] .

I am indebted to the previous members of the 2108 experiments, who undertook the enormous task of building up a very complicated experiment. I have had the opportunities to work with some of them, especially David Hanneke and Jonathan Home, they have patiently guided me during the earlier part of my Ph.D. career. The experience and knowledge we gained in the 2108 experiment

[1] the room number where the experiment setup was located
[2] the 2108 experiment was retired in March of 2013

setup is instrumental in the success of the post-2108, i.e. the "Quantum II" experiment. Quantum II is later joined by Yong Wan, Stephen Erickson, and Daniel Kienzler. They have contributed enormously to the continuation of the experiments. I wish them the best of luck and hope that the laboratory and the experiment setup will serve them well in the future. Furthermore, collaborating with members of the quantum information theory group at NIST, led by Emanuel Knill, has been an enlightening experience. Their contributions are crucial for the success of many experiments.

In addition to those mentioned above, I had the great opportunity to work with these amazing physicists: Robert Jördens, Ulrich Warring, Yves Colombe, John Jost, Christian Ospelkaus, Dietrich Leibfried, Andrew Wilson, Scott Glancy, Adam Keith, Peter Bierhorst, David Allcock, Joe Britton, Shaun Burd, John Bollinger, Samuel Brewer, Brian Sawyer, Justin Bohnet, Jwo-Sy Chen, David Leibrandt, Shon Cook, Till Rosenband, James Bergquist, Daniel Slichter, Shlomi Kotler, James Chou, Katharine McCormick, Susannah Todaro, Kyle McKay, David Hume, Aaron Hankin, Raghavendra Srinivas, and Christoph Kurz. The works presented in this thesis would not be possible without them, as well as every past and present members of the ion storage group.

I would also like to thank our professional friendly rivals working in the trapped-ion group at University of Oxford. Discussions with Prof. David Lucas, Chris Ballance, and Tom Harty have been very helpful in the pursue of high-fidelity two-qubit entangling gate.

My sincere gratitude to Murray Barrett, who ignited my interests in experimental atomic and laser physics, and guided me in my first two years working in a research laboratory when I was pursuing my undergraduate degree at the National University of Singapore.

I cannot thank my parents and my family enough, who supported my decision to take up the challenge for pursuing a Ph.D. career in a foreign country, all by myself. I must also thank all my good friends I have in my life, both human beings and creatures. A big thanks to D. J. Wineland, R. Srinivas, S. Burd, D. Kienzler, S. Erickson, E. Jordan, Becky McKay and my sister Rok Ting "nuoz" Tan, who assisted in reviewing my thesis during preparation.

Furthermore, I am grateful for what Boulder and Colorado offered these past few years: the flatiron, the fresh air and the bright blue sky, the mountains, the distinctive four seasons weather,

and most importantly, the genuine and friendly people who I have encountered. My seven years in Boulder, Colorado is definitely one of the highlights in my life. That being said, this journey is not without bumps on the road. There have been moments when I doubted myself about the decisions that I have made, when everything feels trapped in the shadow cast by the many problems exist inside and outside of the laboratory. Running, cycling, and hiking in the beautiful Colorado, as well as immersing myself in the kitchen trying out and perfecting my *Bolognese* recipes have helped me clear those doubts and carried on. I am still amazed by how so many enlightening ideas and solutions to problems in the laboratory came about when I was outside of the laboratory.

Last but not least, I would like to express my sincerest appreciation to my thesis committee members: David J. Wineland, Emanuel Knill, Ana Maria Rey, Jun Ye, Eric Cornell, and Kelvin Wagner. And of course, the readers of this thesis.

Contents

Chapter

Tables

Table

Figures

Figure

Chapter 1

Introduction

Physical systems that cannot be modeled efficiently with even the most powerful supercomputers exist in many different fields of science (e.g., quantum chemistry, condensed matter physics, cosmology, quantum field theory, cryptography, statistical mechanics). This is because the number of resources and parameters needed to keep track of the entire system grows exponentially with the system size. A many-body quantum mechanical system is an example of such a complex system. Therefore, if we have access to another well-controlled quantum system, we can offset this exponential explosion and use such a "quantum simulator" to model other complex systems [Feynman 82].

An important general goal is to realize a universal quantum information processing (QIP) device — the so-called "quantum computer," which could be used for algorithms having a quantum advantage [Shor 97, Grover 97] over processing on conventional bits as well as to simulate other quantum systems of interest [Feynman 82, Deutsch 85, Lloyd 96]. By using a small set of universal operations that are well controlled, a quantum computer can simulate other systems and execute computations by simple programming of such a processor [Deutsch 85].

Many experimental platforms are currently being investigated for building a large-scale quantum computer [Ladd 10] (e.g., photon systems, nuclear magnetic resonances, neutral atoms, trapped-ions, nitrogen vacancy (NV) centers, quantum dots, and superconducting circuits). Each of these physical platforms offers different advantages as well as drawbacks. For example, compared to other systems, photons are robust against decoherence even over long distances. However, imple-

menting interactions between photons for deterministic entangling operations has proven challenging. A trapped-ion system currently offers the highest fidelity of universal elementary operations, with a number of architecture proposals being pursued to tackle the enormous task of scaling up. Solid-state based systems, such as quantum dots, NV center, and superconducting circuits, may eventually offer better prospects to be scaled up. However, the performance of elementary operations demonstrated with these platforms are still arguably insufficient for realizing a practical QIP device. One dominant issue is the imperfections due to the intrinsic bulk properties of the material used for the realization of quantum bits (qubit).

In recent years the possibilities of hybrid architectures to be used for QIP and quantum networks have been discussed in various proposals (see for example Ref. [Wallquist 09] and Ref. [Kurizki 15]). By interfacing and integrating different platforms, unique advantages of each platform can be exploited in a single setting and different QIP tasks can be delegated to the best suited system. Any such hybrid implementation is an ambitious challenge. Efforts are being made to tackle this challenge [Daniilidis 09, Kotler 16]; nevertheless, quantum information processing is still in its infancy at its current state. Various challenges remain to be addressed within each platform before a larger hybrid system and a working QIP device can be realized.

My PhD career has been concentrated on developing and improving the techniques for the realization of a QIP device with trapped-ions. By applying a combination of static and radio-frequency electric fields to provide a pseudo-harmonic potential in three dimensions [Paul 90, Wineland 98], charged ions can be trapped and stored over long periods of time. The physics of ion trapping is well understood, and the motional degree of freedom provided by the harmonic potential, as well as the internal (atomic) states of the ions, can be controlled with high precision [Wineland 98].

QIP based on trapped-ion systems started in the mid-90s with the first experimental realization of a quantum logic gate [Monroe 95a] on individual qubits based on the proposal by Cirac and Zoller [Cirac 95]. Taking advantage of the expertise and techniques developed in atomic and laser physics, particularly those associated with the developments of atomic clocks [Chou 10, Ludlow 15],

QIP based on trapped-ions has since emerged as one of the most promising platforms.

Fundamental building blocks needed to build a large-scale quantum computer have been demonstrated in trapped-ion systems. The remaining challenges of building a useful, practical quantum computer are (i) reducing and controlling the errors of the elementary operations and (ii) combining all elementary operations in a scalable system while maintaining the performance of each operation. For QIP to be practical, the error per operation has to be below certain threshold [Preskill 98, Knill 10, Ladd 10], often taken to be 10^{-4} probability per gate, so that error correction schemes can be implemented [Nielsen 00]. Among all the elementary operations, the most technically challenging operation is the implementation of a deterministic quantum entangling gate — which produces, "on demand," an entangled state of two separate qubits. It requires high precision coherent control of the two degrees of freedom inside a trapped-ion system (i.e., the internal atomic states degree of freedom and the external motional degree of freedom). Both are subjected to noise, which includes environmental noise and noise present in the control fields used for the manipulations of qubits.

A number of trapped-ion architectures for the scaling of operations have been proposed and pursued [Wineland 98, Kielpinski 02, Monroe 14]. The traps used in this thesis work are designed to implement the quantum charge coupled device (QCCD) architecture [Wineland 98, Kielpinski 02]. Figure 1.1 provides an illustration of the working principle of this architecture in which a large number of ions can be trapped in a trap array with multiple trapping zones. Ions can be shuttled between different zones by applying time-varying control potentials. Certain zones can be delegated for certain tasks (e.g., state measurement, addressing of single-qubits, and multi-qubit entangling gates). With this architecture, one only has to deal with a small subset of ions and operations at a given locations, and parallel processing can be performed in different zones.

Using two different QCCD traps, this thesis focuses on the implementations of two-qubit entangling gates based on effective spin-spin interactions driven by stimulated-Raman transitions [Wineland 98]. Three chapters are dedicated to describing three different two-qubit entangling gate experiments.

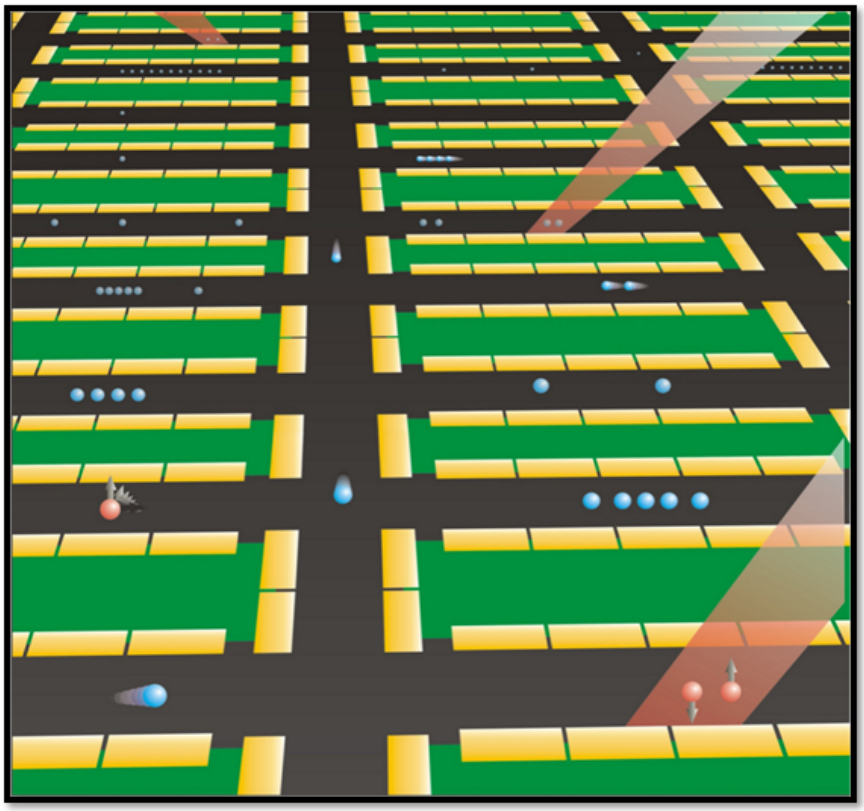

Figure 1.1: One proposal to scale up the QIP device with a trapped-ion system: a quantum charge coupled device (QCCD) architecture [Wineland 98, Kielpinski 02] consists of multiple, interconnected trapping zones. Each trapping region could be dedicated for certain operations. This enables parallel processing and handling of a small subset of qubits at any trapping location. The information transport is achieved by physically shuttling the ions between different trapping regions by applying well-controlled, time-varying electric fields.

Chapter 5 describes the implementation of a mixed-species entangling gate, demonstrated with a hybrid system consisting of a $^{9}Be^{+}$ and a $^{25}Mg^{+}$ ion. In trapped-ion QIP, a hybrid architecture can be implemented by using different species of ions; this enables extra degrees of freedom to be introduced that can be exploited to expand and refine the control of the system. Trapped ions of different elements vary in mass, internal atomic structure, and spectral properties, features that make certain species suited for particular tasks such as storing quantum information, high-fidelity readout, fast logic gates, or interfacing between local processors and photon interconnects. Ions of different elements have previously been used in QIP experiments for sympathetic cooling [Barrett 03], creation of entanglement through dissipation [Lin 13a], and quantum non-demolition (QND) measurement of one species by using another [Hume 07]. As a multi-qubit quantum logic gate is one of the most important elementary operations for QIP, adding a mixed-species entangling gate between multiple species of ions provides one important step toward a large-scale trapped-ion QIP device. Furthermore, a mixed-species entangling gate can also potentially serve as an important building block for quantum networking [Moehring 07], precision spectroscopy [Schmidt 05], metrology [Schulte 16], and quantum simulation. The mixed-species entangling gate is realized through an effective spin-spin interaction generated by state-dependent forces [Sørensen 99, Milburn 00, Solano 99, Leibfried 03] using the Mølmer-Sørensen (MS) protocol [Sørensen 99, Sørensen 00]. The fidelity of creating a mixed-species Bell state with our gate scheme was evaluated to be 0.979(1) [Tan 15]. Error sources are investigated to study the possibilities of improving the gate performance.

Operations in the high-fidelity regime are important for the realization of a practical quantum information processor. Individual quantum gate errors must be reduced below a certain threshold to achieve fault-tolerance [Preskill 98, Knill 10, Ladd 10] without excessive overhead in the number of physical qubits. In the trapped-ion QIP community, this error threshold is generally agreed to be around 10^{-4}. This level has been achieved in some experiments for elementary operations including single-qubit gates [Brown 11, Harty 14, Ballance 16, Gaebler 16] and state preparation and readout [Myerson 08], with the exception of two-qubit entangling gates, emphasizing the importance of

improving the fidelity of multi-qubit gates.

Chapter 6 describes experiments that push the fidelity of laser-induced gates, especially a two-qubit entangling gate, toward the fault-tolerant goal. With a "clock" qubit composed of hyperfine states in a $^9Be^+$ ion, which has a long coherence time (> 1 s) due to its robustness against fluctuating magnetic fields [Langer 05], a state-dependent force based on the MS protocol is applied directly to the qubits to implement an entangling geometric phase gate. The error of the Bell state created by the entangling gate scheme is measured to be $8(4) \times 10^{-4}$ [Gaebler 16], this result is currently the highest two-qubit gate fidelity across all platforms. This result is about a factor of ~ 50 improvement compared to the previous best result of an entangling gate applied on a magnetic-field insensitive qubit [Tan 13] (see also Chapter 7). This improvement is partly made by reducing various noise sources and taking advantage of a number of recent developments in laser technology [Wilson 11, Colombe 14] and digital electronics [Bowler 13, Leibrandt 15].

Similar two-qubit gate performance has also been demonstrated by the Oxford trapped-ion group [Ballance 16]. In this case, the gate is applied on a magnetic-field sensitive qubit state using a different implementation of a geometric phase gate [Leibfried 03]. The Oxford group is working toward implementing the Mølmer-Sørensen protocol on a clock qubit so that the qubit dephasing error can be suppressed (private communication). Chapter 4 gives a brief overview of different two-qubit gate schemes and discusses their respective advantages and disadvantages.

Section 6.7 describes characterization of a single-qubit gate using a randomized benchmarking technique [Knill 08]. Single-qubit gates are implemented with the same apparatus and errors are evaluated to be $3.8(1) \times 10^{-5}$ [Gaebler 16], this error is lower than the 10^{-4} fault-tolerant threshold. This result appears to be one of the highest single-qubit gate fidelity based on laser-driven stimulated-Raman transitions [Ballance 16].

One of the most important aspects of implementing high-fidelity gates is the study of error mechanisms. Here, these errors are investigated with a combination of analytic methods, calibration measurements, and numerical simulations. This allows for better strategies and novel gate schemes to be developed that target certain error mechanisms for the further improvement of quantum

gates.

As qubit dephasing errors are one of the most important error sources, certain techniques and gate schemes targeting this error have been proposed in the recent years. One such example is the technique of dynamical decoupling (DD) [Viola 98]; based on an extension of spin-echos [Hahn 50]. Dynamical decoupling relies on applying certain operations to the quantum system of interest that provides protection against environment noise such as magnetic field fluctuations. Most implementations of DD schemes have been focused on the protection of quantum memories against external noise [Du 09, de Lange 10, Ryan 10, Szwer 11]. However, as most quantum gates require the application of external controlled fields, a decoupling scheme that is compatible with quantum gate is a non-trivial challenge. These DD-compatible quantum gates should be designed to be immune to fields associated with environmental noise but still able to be implement interactions induced by the controlled fields required to apply the coherent gate operations.

Chapter 7 describes an experimental demonstration of an entangling gate based on state-dependent forces with built-in continuous dynamical decoupling. This implementation is a modified scheme based on the theoretical proposal presented by Bermudez *et al.* [Bermudez 12]. By applying a strong carrier excitation that continuously flips the qubit states, the qubit is dynamically decoupled from certain qubit dephasing mechanisms such as external magnetic field fluctuations, fluctuating AC Stark shifts, or AC Zeeman shifts. Simultaneously, a spin-motional "sideband" excitation is applied. In the limit that the carrier Rabi rate is significantly greater than the sideband Rabi rate, the combined interaction is a state-dependent force that can be engineered to implement a geometric phase gate. This protocol shares certain similarities with the Mølmer-Sørensen protocol in the sense that they can both be directly applied to a clock state qubit. In addition to the built-in feature of dynamical decoupling, this gate scheme has certain further advantages compared to the Mølmer-Sørensen protocol, which are discussed in Chapter 4. With this DD gate scheme, a gate fidelity of 0.974(4) was achieved. Gate errors were dominated by sources associated with a legacy experimental setup used for this demonstration, which can be suppressed in the futre. Together with other quantum entanglement generation schemes, it provides an additional tool kit

to the study of quantum physics.

The properties of quantum entanglement are at the heart of the promising power of QIP. The peculiar properties of quantum entanglement's *spukhafte Fernwirkungen*, which is translated as "spooky action at a distance" [Einstein 71], prompted heated philosophical debates and motivated various interpretations of quantum physics. Spooky action at a distance refers to the counter-intuitive implication that quantum entanglement seems to allow faster-than-light communication between the partners of the entangled state. This is in direct conflict with local-realistic theory, as well as human beings' experiences with the surrounding physical world.

John Bell formulated a relatively simple mathematical inequality describing the incompatibility between quantum physics and local realistic theories [Bell 64]. This was followed by proposals enabling the experimental examination of Bell inequality, notably the one proposed by Clauser, Horne, Shimony, and Holt (CHSH) [Clauser 69], which is performed by making joint measurements on a pair of entangled particles to draw inferences about the nonlocal nature of quantum physics. Since the pioneering work in the 70s performed with photon pairs [Freedman 72] and a number of experiments using various platforms in the following decades made possible by technological advancements, the quest for confirming the non-local nature of quantum mechanics reached an important milestone with three different "loophole-free" CHSH-type Bell inequality experiments performed in 2015 [Hensen 15, Shalm 15, Giustina 15]. See Ref. [Brunner 14] for a general review on Bell nonlocality.

However, the quest to fully understand local/non-local properties of quantum physics is far from finished. Although the loophole-free Bell inequality experiments have rejected with high confidence theories of local realism, they are limited in the extent to which their data differs from local realism. In general, a CHSH-type Bell inequality experiment is limited in the extent to which the experimental data may assert nonlocality exhibited by a quantum state. Therefore, one of the next quests in the study of the foundation of quantum physics is to experimentally show that quantum state can exhibit maximum nonlocal properties. One such experiment is the chained Bell inequality (CBI) [Pearle 70] test, which can be used to further quantify and assert a larger

departure of quantum physics from local realism.

Elitzur, Popescu, and Rohrlich [Elitzur 92] described a model of the distribution of outcomes measured from a quantum state as a mixture of a local-realistic distribution, which obeys Bell's inequalities, and another distribution which does not. A perfectly executed Bell inequality experiment of the CHSH type, with two particles and two measurement settings per particle, could only show with a maximally entangled state exhibits a nonlocal properties with $p_{\text{nonlocal}} \simeq 0.414$ (maximum nonlocality corresponds to $p_{\text{nonlocal}} = 1$). A CBI experiment can be viewed as a generalized version of the CHSH-type Bell inequality test. There is a hierarchy in which the Nth CBI experiment involves $2N$ different combinations of measurement settings. The $N = 2$ CBI experiment is equivalent to the CHSH Bell inequality experiment. In the limit of $N \to \infty$ and with perfect experimental conditions, CBI experiments can be used to show a quantum state's complete departure from local realism [Barrett 06, Bierhorst 16].

Similar to a CHSH-type experiment, a CBI experiment may be subject to "loopholes" [Brunner 14, Å. Larsson 14] that, in principle, allow a local system to show violation of the inequality. Previous CBI experiments [Pomarico 11, Aolita 12, Stuart 12, Christensen 15] employed entangled photon pairs with the highest nonlocal properties shown to be $p_{\text{nonlocal}} \simeq 0.874$ [Christensen 15]. However, the detectors' efficiencies in these experiments are low, such that the fair sampling assumption has to be made, thus not closing the so-called detection loophole [Pearle 70, Clauser 74]. To my knowledge, all previous CBI experiments with $N \geq 3$ suffer from the locality [Bell 85], detection, and memory loopholes [Barrett 02].

The detection efficiency of a trapped-ion system can be near 100 %, making it an excellent platform to perform Bell inequality experiments while closing the detection loophole. The detection loophole was first closed in a CHSH-type Bell inequality experiment performed with a trapped-ion system [Rowe 01]. Other CHSH Bell inequality experiments performed with trapped-ion systems include Ref. [Matsukevich 08, Pironio 10, Ballance 15, Tan 15], with each of them successfully closing the detection loophole.

Chapter 8 presents detection-loophole-closing CBI experiments that are realized by employ-

ing techniques developed for trapped-ion QIP, particularly the high-fidelity deterministic generation of Bell states with an entangling gate and single-qubit gate, robust state preparation and measurement, long qubit memory storage time, and shuttling and transport of ions for the separate addressing and measurement of individual ions.

The CBI experiments presented here employ up to 15 different measurement settings per particle. The highest nonlocal fraction attainable by a quantum distribution is determined to be $p_{\text{nonlocal}} \simeq 0.704(12)$ for the $N = 9$ CBI experiment. Although the experiments here close the detection loophole, the CBI experiments are performed with each ion's measurement inside the lightcone of the event where the other ion's measurement setting choice is made, thus not able to close the other important loophole, i.e. locality or lightcone loophole.

Historically, a Bell inequality experiment is primarily designed and performed to investigate the incompatibility between quantum physics and local-realistic theory. The possibilities of using a Bell inequality experiment for certain applications had also been discussed. For example, while the Bell inequality experiments presented here are made possible by the technique developed for QIP with trapped-ions, the experimental protocols can in turn provide a "black box" certification of the created Bell state [Bardyn 09, Bancal 15, Kaniewski 16] as well as a device-independent, single-number, conservative benchmark for the QIP device. Such a characterization with minimal assumptions on the physical system and measurements is formalized by the self-testing framework [Mayers 04, McKague 12], which enables an experimentalist to quantify the quality of an entangled state given the amount of violation of a Bell inequality [Bardyn 09, Yang 14, Bancal 15, Kaniewski 16].

Our $N = 2$ measurements corresponds to a CHSH inequality parameter (sum of correlations) of $B_{\text{CHSH}} = 2.80(2)$. According to Kaniewski's formulation [Kaniewski 16], the self-tested Bell state fidelity is inferred to be 0.980, with lower bounds of ~ 0.958 at the 95% confidence level. This result appears to be the highest self-tested fidelity on a deterministically created Bell state across all platforms that are being considered for QIP, demonstrating a trapped-ion system's capabilities for the realization of a QIP device.

During the course of my PhD, I have worked with two trapped-ion apparatuses in two different laboratories, chronologically. The first apparatus, which is referred in this thesis as the "legacy system," was retired in the spring of 2013. The second system was set up in a laboratory inside the Katherine Gabbie building at National Institute of Standards and Technology, and became operational in the fall of 2013. Although the two systems share many similarities, unless specified otherwise, this thesis refers to the newer system.

The three two-qubit entangling gate experiments described in this thesis resulted in the following peer-reviewed publications:

(i) "Multi-element logic gates for trapped-ion qubits"
T. R. Tan, J. P. Gaebler, Y. Lin, Y. Wan, R. Bowler, D. Leibfried, and D. J. Wineland, Nature **528**, 380 (2015).

(ii) "High-fidelity universal gate set for $^{9}Be^{+}$ ion qubits"
J. P. Gaebler, T. R. Tan, Y. Lin, Y. Wan, R. Bowler, A. Keith, K. Coakley, E. Knill, D. Leibfried, and D. J. Wineland, Phys. Rev. Lett. **117**, 060505 (2016).

(iii) "Demonstration of a dressed-state phase gate for trapped ions"
T. R. Tan, J. P. Gaebler, R. Bowler, Y. Lin, J. D. Jost, D. Leibfried, and D. J. Wineland, Phys. Rev. Lett. **110**, 263002 (2013).

The manuscript for the chained Bell inequality experiment is being prepared at the moment.

(iv) "Chained Bell inequality experiment with high-efficiency measurement"
T. R. Tan, Y. Wan, S. Erickson, P. Bierhorst, D. Kienzler, S. Glancy, E. Knill, D. Leibfried, and D. J. Wineland, in preparation.

I was primarily in charge of the planning, designing, and assembling the infrastructure of the new laboratory, as well as heavily involved in a number of other experiments using the apparatus described in this thesis. These other experiments were led by J. P. Gaebler, R. Bowler, Y. Lin, and Y. Wan, some of which resulted in the following publications:

(i) "Randomized-benchmarking of multi-qubit gates"
J. P. Gaebler, A. M. Meier, T. R. Tan, R. Bowler, Y. Lin, D. Hanneke, J. D. Jost, J. P. Home, E. Knill, D. Leibfried, and D. J. Wineland, Phys. Rev. Lett. **108**, 260503 (2012).

(ii) "Coherent diabatic ion transport and separation in a multizone trap array"
R. Bowler, J. P. Gaebler, Y. Lin, T. R. Tan, D. Hanneke, J. D. Jost, J. P. Home, D. Leibfried, and D. J. Wineland, Phys. Rev. Lett. **109**, 080502 (2012).

(iii) "Sympathetic electromagnetically-induced-transparency laser cooling of motional modes in an ion chain"
Y. Lin, J. P. Gaebler, T. R. Tan, R. Bowler, J. D. Jost, D. Leibfried, and D. J. Wineland, Phys. Rev. Lett. **110**, 153002 (2013).

(iv) "Dissipative production of a maximally entangled steady state of two quantum bits"
Y. Lin, J. P. Gaebler, F. Reiter, T. R. Tan, R. Bowler, A. S. Sørensen, D. Leibfried, and D. J. Wineland, Nature **504**, 415 (2013).

(v) "Preparation of entangled states by Hilbert space engineering"
Y. Lin, J. P Gaebler, F. Reiter, T. R. Tan, R. Bowler, Y. Wan, A Keith, E. Knill, S. Glancy, K. Coakley, A. S. Sørensen, D. Leibfried, and D. J. Wineland, Phys. Rev. Lett. **117**, 140502 (2016).

1.1 Thesis Organization

Chapter 2 describes the use of $^{9}Be^{+}$ and $^{25}Mg^{+}$ ions as qubits, including the qubit state preparation, measurement and coherent manipulations of the qubits. The apparatus relevant to this thesis is summarized in Chapter 3. This includes the ion trap, magnetic-field coil, laser systems, imaging system, and certain electronics.

Chapter 4 gives a brief overview of two-qubit entangling gates with trapped-ions. Different gate schemes will be discussed, and the relevant error mechanisms that prevent the perfect implementations of entangling gates are summarized. The objective of this chapter is to provide

background information for the two-qubit entangling gate experiments described in Chapters 5, 6, and 7.

Chapters 5 and 6 describe experimental implementations of a mixed-species entangling gate and a universal gate set with $^{9}Be^{+}$ ions, respectively. This is followed by Chapter 7, which describes the demonstration of a geometric phase gate with dynamic decoupling built-in. The chained Bell inequality experiment is presented in Chapter 8. Chapter 9 discusses prospective outlooks of the experiments presented in this thesis.

Appendix A and B include the detailed hyperfine energy level diagrams of the $^{2}S_{1/2}$ electronic ground states of the $^{9}Be^{+}$ ion and the $^{25}Mg^{+}$ ion, respectively. Certain atomic properties and their respective magnetic-field independent points of these species are also included. Appendix C includes Hamiltonians describing the atom-light interactions frequently used throughout the thesis. Lastly, Appendix D gives the matrix representations of state vectors and operators used in the numerical simulations of quantum systems.

Chapter 2

$^{9}Be^{+}$ and $^{25}Mg^{+}$ Ion Qubits

The $^{9}Be^{+}$ ion, and two isotopes of magnesium ions ($^{24}Mg^{+}$ and $^{25}Mg^{+}$) are used in this thesis work. The $^{24}Mg^{+}$ isotope was used in a legacy system to take advantage of its relatively simple electronic structure. With the absence of nuclear spin, and thus the absence of hyperfine structure, the laser system required to manipulate the $^{24}Mg^{+}$ isotope is relatively simple and straightforward. The $^{25}Mg^{+}$ isotope was then used after the legacy system was retired. With a nuclear spin of 5/2, which gives rise to hyperfine structure, the $^{25}Mg^{+}$ isotope is more favorable to be used as a quantum bit (qubit) in terms of memory storage time, qubit state readout fidelity, and application of quantum gates. However, the laser system required to fully manipulate the $^{25}Mg^{+}$ isotope is relatively more demanding than for $^{24}Mg^{+}$.

The electronic structures of $^{9}Be^{+}$ and $^{25}Mg^{+}$ are qualitatively very similar. The wavelength of the lasers to manipulate $^{9}Be^{+}$ are all centered around 313 nm, while the laser wavelengths for the $^{25}Mg^{+}$ are centered around 280 nm. This chapter describes the electronic structure of $^{9}Be^{+}$ and $^{25}Mg^{+}$, the qubit preparation and readout, and the coherent operations for the manipulation of these ions. Detailed information about the $^{24}Mg^{+}$ isotope can be found in Ref. [Jost 10].

2.1 $^{9}Be^{+}$ Ion Qubit

The only stable isotope of beryllium is ^{9}Be. Being an alkaline earth atom, the neutral Be atom has two valence electrons. By stripping off one of the outer electrons, the $^{9}Be^{+}$ ion's electronic structure is very similar to alkali atoms. The electronic ground state is the $1s^{2}2s^{2}S_{J=1/2}$ state. The

two electronic excited states relevant to this thesis are the $1s^2 2p^2 P_{1/2}$ state and the $1s^2 2p^2 P_{3/2}$ state. The electronic transitions from the $^2S_{1/2}$ state to either excited state have wavelengths around 313 nm. The fine structure splitting between the two excited states is approximately 198 GHz.

The nuclear spin, I of the $^9Be^+$ ion is 3/2. The interactions between the nuclear and electronic spin give rise to hyperfine structure. The hyperfine levels in the electronic ground state of $^2S_{1/2}$ are labeled with the total angular momentum, F. The hyperfine splitting between the $F = 1$ and $F = 2$ levels is approximately 1.2 GHz. We apply an external magnetic field of $\sim$ 119.446 G (0.0119446 T) to further lift the degeneracy of different Zeeman levels. This magnetic field is chosen such that the $|F = 2, m_F = 0\rangle \leftrightarrow |1, 1\rangle$ transition is first-order insensitive to magnetic field fluctuations [Langer 05]. Furthermore, at this "intermediate magnetic field" regime, the combination of hyperfine and Zeeman effects is such that the transition frequencies of all transitions in the $^2S_{1/2}$ manifold are nondegenerate. Figure 2.1 shows the relevant energy levels of the $^9Be^+$ ion. See Fig. A.1 for additional details of the $^9Be^+$ electronic ground state.

For the quantum information experiments described in this thesis, the qubit is stored in the magnetic-field insensitive states labeled as $|2, 0\rangle = |\uparrow\rangle$ and $|1, 1\rangle = |\downarrow\rangle$. The coherence time of this qubit is investigated with a Ramsey sequence and the results are shown in Fig. 2.2. Due to the complicated mechanisms of dephasing sources, which can be correlated, the decay of the Ramsey contrast does not exhibit simple exponential behavior. Therefore, we choose the delay time in which the Ramsey contrast equal to $1 - 1/e \simeq 0.632$ as the representative qubit coherence time. With this convention, the coherence time of the $^9Be^+$ qubit is measured to be $\sim$ 1.5 s. The second-order magnetic field sensitivity of the qubit transition is approximately 6.097 kHz/G^2.

Relevant atomic properties of the $^9Be^+$ ion are shown in Table A.1. Table A.2 lists the magnetic-field insensitive transitions in the electronic ground state of the $^9Be^+$ ion.

2.1.1 Doppler Cooling

Doppler cooling of $^9Be^+$ ions is achieved with a σ^+ polarized laser beam with frequency red detuned by approximately $\Gamma/2$ from the $^2S_{1/2}|2, 2\rangle \leftrightarrow {}^2P_{3/2}|3, 3\rangle$ transition at $\sim$ 313.132 nm (see

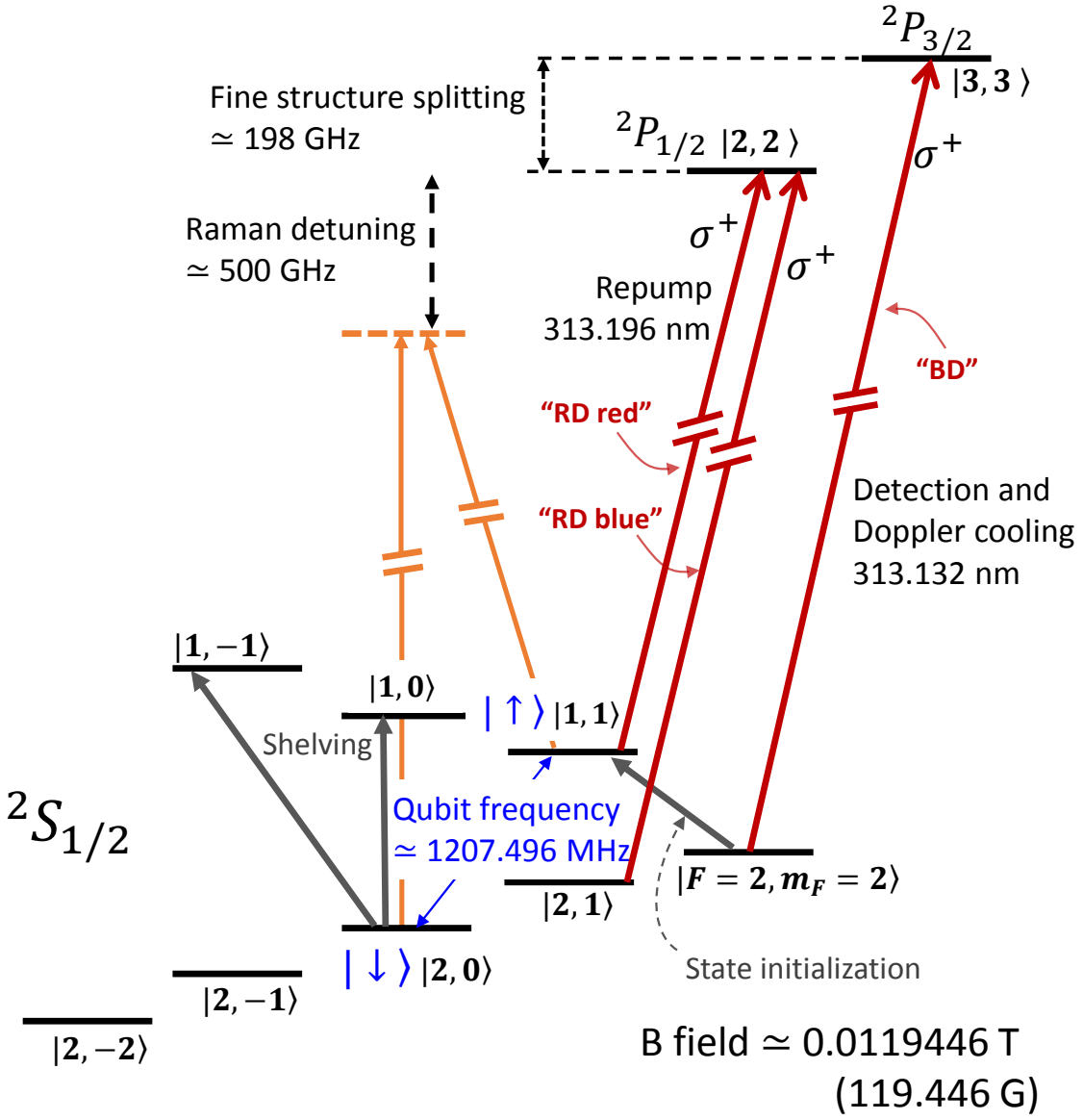

Figure 2.1: Relevant energy level structure (not to scale) of the $^9Be^+$ ion. Transitions to the electronic excited states are used for Doppler cooling, repumping, and qubit state measurement as described in the text. The "blue Doppler detuned" (BDD) beam, which is red shifted ≃ 400 MHz with respect to the "blue Doppler" (BD) beam (see Sec. 2.1.1), is not shown in this figure. We label the qubit $|1,1\rangle = |\uparrow\rangle$ and the $|2,0\rangle = |\downarrow\rangle$ states as the "computational qubit manifold". The "measurement qubit manifold" consists of the $|2,2\rangle$ as the "bright" state, and the $|1,-1\rangle$ or $|1,0\rangle$ state as the "dark" state (see Sec. 2.1.7). The laser for stimulated-Raman transitions is red detuned from the $^2S_{1/2} \leftrightarrow {}^2P_{1/2}$ transition. The decay rate of the $^2P_{3/2}$ state is $2\pi \times 19.4(5)$ MHz [Poulsen 75]. See Fig. A.1 for details energy levels diagram in the $^9Be^+$ electronic ground state. The state labels correspond to the states at low magnetic field, which evolve to the states indicated at non-zero magnetic field.

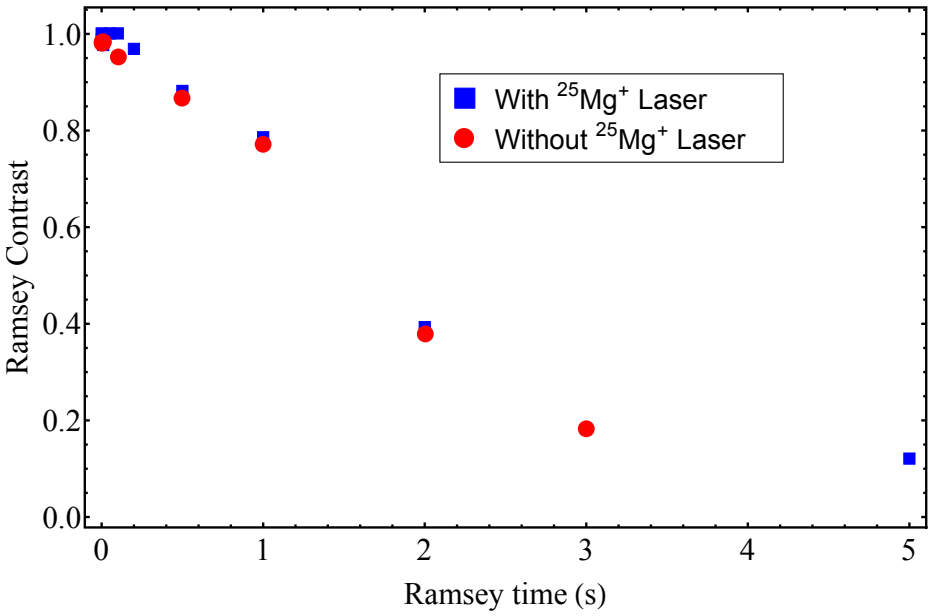

Figure 2.2: Coherence time of the $^{9}Be^{+}$ qubit is investigated with a Ramsey sequence. We repeat the experiments with and without the presence of the $^{25}Mg^{+}$ laser beams, which have a wavelength of approximately 280 nm. In this experiment, one $^{9}Be^{+}$ and one $^{25}Mg^{+}$ ion are trapped together in a harmonic well with a separation of $\simeq 5$ μm; the laser beams (with beam waists $\simeq 30$ μm.) illuminate both ions. We do not observe a significant difference between these two sets of experiments, which indicates that the $^{25}Mg^{+}$ laser radiation causes negligible additional decoherence.

Fig. 2.1), where $\Gamma \simeq 2\pi \times 19.4(5)$ MHz is the decay rate of the $^2P_{3/2}$ state [Poulsen 75]. This beam, which is labeled as the "blue Doppler" (BD) beam, has a $\boldsymbol{k}$-vector direction such that it can cool all modes of the ions' motion. The BD beam is also used for the fluorescence detection of the $^9Be^+$ ions (see Sec. 2.1.7).

To maximize efficiency during Doppler cooling and detection in the presence of axial micromotion (see Sec. 3.1 and Ref. [Blakestad 10]), we apply a differential voltage of approximately $\pm$ 0.15 V to the two control electrodes centered on zone $\mathcal{E}$ (Fig. 3.1). This shifts the ions away from the radial micromotion null point (trap axis) such that the vector sum of the radial and axial micromotions is perpendicular to the Doppler cooling beam's wavevector. With this Doppler cooling scheme, the lowest motional temperature is attainable when the heating and cooling process reach an equilibrium [Itano 82]. Heating mechanisms include recoil momentum kicks during photon absorption and emission, and background heating [Turchette 00a].

In the weak binding regime, where $\Gamma \gg \omega_\nu$, with ω_ν as the frequency of the motional mode, the temperature at the Doppler cooling limit, T_D is given by [Wineland 79, Itano 82]

$$T_D = \frac{\hbar\Gamma}{8k_B}(1+\chi)\left[(1+s)\frac{\Gamma}{2\delta} + \frac{2\delta}{\Gamma}\right]\Bigg(\tag{2.1}$$

where k_B is the Boltzmann constant, s and δ are the saturation parameter and the detuning of the laser beam associated with the cooling transition, and χ is a geometric factor which is related to the beam direction with respect to the motional modes' vibrational directions. In our case, the polarization of the laser beam is set to be σ^+ and with the alignment shown in Fig. 2.3, $\chi = 0.35$ for the axial modes, and ranges from 0.3 to 0.35 for radial modes [Itano 82].

For a single $^9Be^+$ ion with an axial trapping frequency near $2\pi \times 3.6$ MHz, we measure the average axial occupation number after Doppler cooling to be approximately $\bar{n} \simeq 4$. Our Raman laser beam geometry does not permit direct diagnostics of the motional modes in the radial directions (see Sec. 2.1.3 and Sec. 2.1.5). To estimate the Doppler cooling limit for the $^9Be^+$ ion's radial motional modes, we first note that the radial trap frequency for one $^9Be^+$ is relatively high, such that the weak binding condition is not rigorously satisfied. Using Eq. 2.1 in this case could

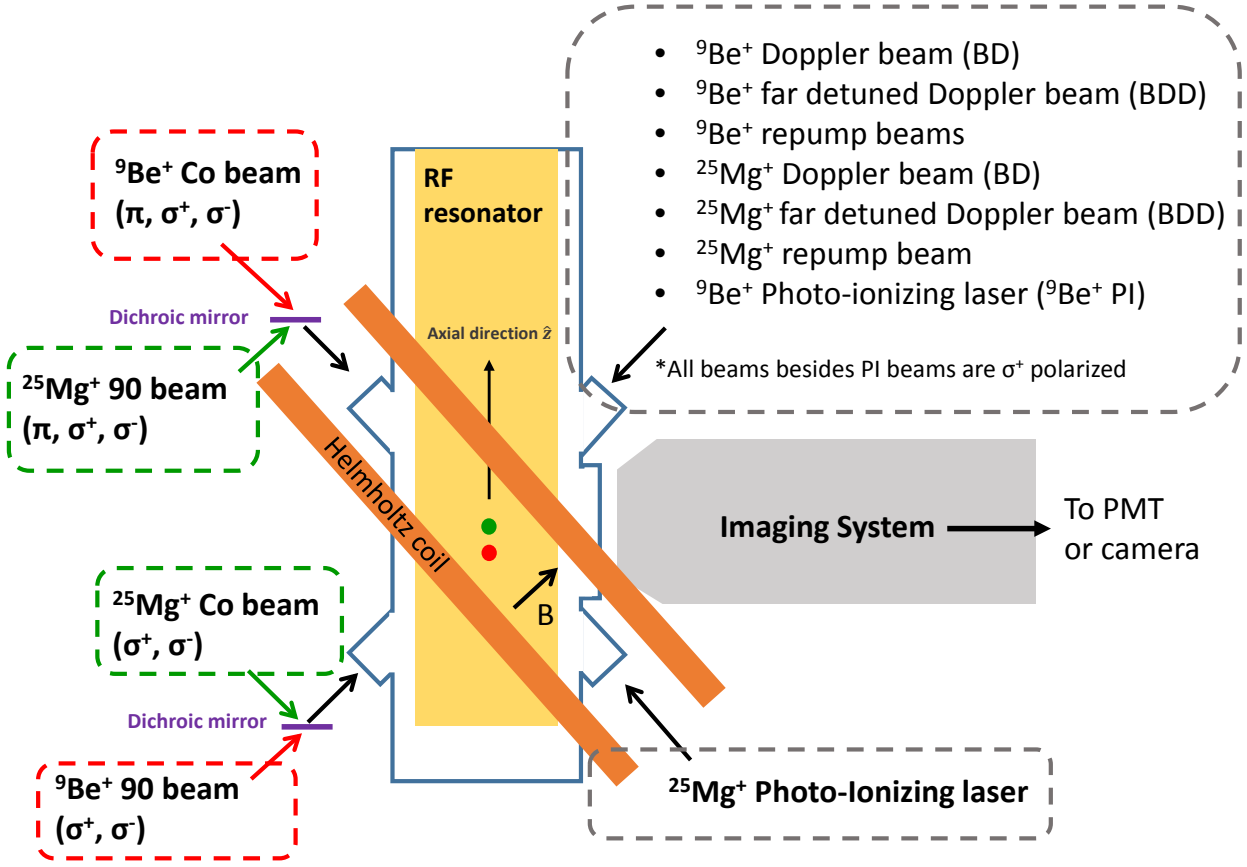

Figure 2.3: Schematic diagram indicating laser beams access into the ion trap apparatus. Four ports are available, each aligned $\sim 45°$ relative to the trap (z) axis. The external magnetic field (provided by coils in the Helmholtz-like configuration) is set to be $45°$ with respect to the trap axis. The radial confinement of the ions is in the plane normal to the z axis. Laser beams for the Doppler cooling, repumping, and fluorescence detection of the $^{9}Be^{+}$ and $^{25}Mg^{+}$ ions are coaligned with the magnetic field direction, and are set to be σ^{+} polarized. With this configuration, motional modes in all three directions can be cooled by the Doppler beams. Each species Raman laser beams are sent into the vacuum chamber via two ports after being combined with dichroic mirrors. For $^{9}Be^{+}$, the laser beam exiting the UV fiber of path 1 (2) depicted in Fig. 3.8 is sent into the port labeled as "$^{9}Be^{+}$ 90" ($^{9}Be^{+}$ Co) in this figure. For the $^{25}Mg^{+}$, the laser beams labeled as path 1 (2) in Fig. 3.10 corresponds to "$^{25}Mg^{+}$ 90" ("$^{25}Mg^{+}$ Co") in this figure. The laser beam entering the bottom-right port (i.e., the Mg PI beam in this figure) and directed toward zone $\mathcal{L}$ is blocked by an oven shield installed behind the alumina wafers after passing through the center of the trap (details in Ref. [Blakestad 10]). The boundary of the vacuum chamber is indicated by blue lines. Details of apparatus are described in Chap. 3.

overestimate the cooling efficiency and erroneously give a lower motional temperature. Doppler cooling in the intermediate binding regime can be estimated by [Lindberg 84, Javanainen 84]

$$
\begin{aligned}
T_{Inter} \;=\; & \frac{\hbar}{4\delta k_B}\frac{1}{\omega_\nu^2\left(\delta^2+\gamma^2+6\kappa^2\right)+4\gamma^2\left(\delta^2+\gamma^2+2\kappa^2\right)}\times \\
& \Big[\xi\Big(\omega_\nu^2\left(\delta^2+5\gamma^2+4\kappa^2-\omega_\nu^2\right)^2+4\gamma^2\left(\delta^2+\gamma^2+2\kappa^2-2\omega_\nu^2\right)^2\Big) \\
& +\omega_\nu^2\left(\delta^2+\gamma^2+2\kappa^2\right)\left(\delta^2+5\gamma^2+8\kappa^2+\omega_\nu^2\right) \\
& +4\gamma^2\Big(\left(\delta^2+\gamma^2+2\kappa^2\right)^2+2\kappa^2\left(\delta^2-3\gamma^2+8\kappa^2-3\omega_\nu^2\right)\Big)\Big], \qquad (2.2)
\end{aligned}
$$

where $\gamma = \Gamma/2$ and κ is the Rabi rate of the laser-induced electronic cooling transition.

Another laser beam, labeled as "blue Doppler detuned" (BDD), is derived from the same laser source as the BD beam but with its frequency red shifted by $\simeq$ 400 MHz from the BD beam (details in 3.4). The power of the BDD beam is $\sim$ 1 mW, which power broadens the transition linewidth when the transition is shifted into resonance. This beam provides strong cooling for high temperature ions that might not be efficiently cooled by the BD beam. These occasional high temperature events are likely due to background gas collisions which occur at a rate of approximately one per minute. It was found that the dark ion (which does not fluoresce under the illumination of either the BD or the BDD beams) creation rate becomes faster when we increase the duty cycle of the BDD beam, likely due to BeH^+ formation when the $^9Be^+$ ion is in the electronic excited state [Wineland 98]. The BDD beam also provides optical pumping to assist initialize the population to the $|2,2\rangle$ state.

2.1.2 Repumping

The $^2S_{1/2} \leftrightarrow {}^2P_{3/2}$ (BD) Doppler cooling and detection laser beam will optically pump the $^9Be^+$ ions to the $^2S_{1/2}|2,2\rangle$ state as long as the beam has a pure σ^+ polarization with respect to the applied magnetic field. To mitigate the effects of polarization impurity and to speed up the pumping process, two $^2S_{1/2} \leftrightarrow {}^2P_{1/2}$ laser beams are added for the initial optical pumping to the $^2S_{1/2}|2,2\rangle$ state. All three beams are first applied, and the final stage of pumping uses only the $^2S_{1/2} \leftrightarrow {}^2P_{1/2}$ beams. These beams are formed from one beam that is split into two, which are also σ^+ polarized

(details in Sec. 3.4). One beam is tuned near the $^2S_{1/2}|2,1\rangle \leftrightarrow {}^2P_{1/2}|2,2\rangle$ transition, and the other is tuned near the $^2S_{1/2}|1,1\rangle \leftrightarrow {}^2P_{1/2}|2,2\rangle$ transition (see Fig. 2.1). These two beams are labeled as the "RD red" beam and "RD blue" beam, respectively. To suppress electromagnetically-induced transparency effects that could lead to coherent trapping of populations in the $^2S_{1/2}|2,1\rangle$ and the $^2S_{1/2}|1,1\rangle$ states when these two beams are applied simultaneously, one of these beams is detuned from the atomic resonance by approximately $-\Gamma/2$.

These beams also serve to repump the population to the $^2S_{1/2}|2,2\rangle$ state during Raman sideband cooling [Monroe 95b] (see Sec. 2.1.5). During the repumping process in the sideband cooling sequence, we do not apply the differential voltage on control electrodes that maximizes the detection efficiency in the presence of axial micromotion. This is to minimize motional heating that might occur when transverse micromotion is induced.

2.1.3 Stimulated-Raman Transitions

Coherent manipulation of qubits are accomplished with stimulated-Raman transitions [Wineland 98] and microwave transitions. Although there are multiple energy levels present in the ions' atomic structures (Fig. 2.1 and Fig. 2.6), we can restrict the coherent operations such that, to a high degree, they interact only with the two energy levels corresponding to the qubit $|\uparrow\rangle$ and $|\downarrow\rangle$ states. Another degree of freedom which is present in the trapped-ion system is the motion, which for each normal mode, can be described as a harmonic oscillator. The unperturbed Hamiltonian describing a single two-level ion in a harmonic well can be written

$$H_0 = \hbar\frac{\omega_0}{2}\left(|\uparrow\rangle\langle\uparrow| - |\downarrow\rangle\langle\downarrow|\right) + \sum_i^3 \hbar\omega_{\nu,i}\hat{a}_i^\dagger\hat{a}_i, \tag{2.3}$$

where ω_0 is the qubit frequency, and the second term represents the three orthogonal motional modes, each with a harmonic oscillator frequency of $\omega_{\nu,i}$, and $\hat{a}_i$ represents the harmonic oscillator annihilation operator for the ith mode (see also Appendix C).

The laser beams for qubit manipulation of $^9Be^+$ ions with stimulated-Raman transitions (with wavelength $\lambda \simeq 313$ nm) are red detuned from the $^2S_{1/2} \leftrightarrow {}^2P_{1/2}$ electronic transitions. To

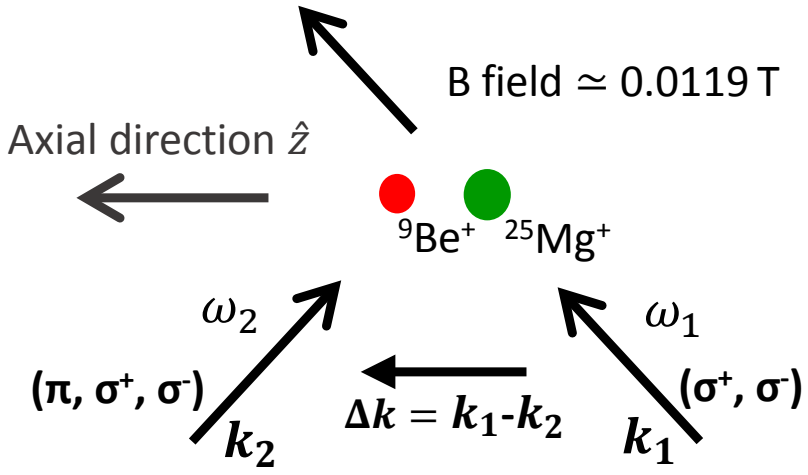

Figure 2.4: The laser beams setup to drive stimulated-Raman transitions. Laser beams are focused onto ions from two paths, which intersect at 90° such that the difference in their $\boldsymbol{k}$ vectors, $\boldsymbol{\Delta k}$, is aligned along the axial direction. These two beams corresponds to the Co and 90 beams in Fig. 2.3. This figure is simplified for the relevant illustrations in this section. Details of Raman beam lines setup are discussed in Sec. 3.4.3, Sec. 3.5.2, and the respective chapters describing implementation of different experiments.

drive spin-motion transitions with stimulated-Raman excitations, two beams propagate along paths 1 and 2 (see Fig. 2.4) and are focused and intersect at 90° such that the difference in their $\boldsymbol{k}$ vectors, $\boldsymbol{\Delta k}$, is aligned along the axial (z) direction, in which case only the axial motion can be coupled with the Raman laser fields at the position of the ion. If we set the frequency difference of the two laser fields ($\Delta\omega = \omega_1 - \omega_2$) near to the qubit frequency of ω_0, we can excite the carrier transitions $|\downarrow, n\rangle \leftrightarrow |\uparrow, n\rangle$ that induce spin-flip oscillations without changing the motional Fock state quantum number n. Following the derivations in Appendix C, the interaction-frame Hamiltonian describing a detuned carrier excitation after dropping high-frequency terms has the form of Eq. C.20:

$$H_{Carrier} = \hbar\Omega_0 \left(\hat{\sigma}^+ e^{-i(\delta t+\Delta\phi)} + \hat{\sigma}^- e^{i(\delta t+\Delta\phi)}\right)\Bigg(\tag{2.4}$$

where Ω_0 is the transition Rabi rate which can be computed with Eq. C.11, $\hat{\sigma}^+ = |\uparrow\rangle\langle\downarrow|$ and its conjugate is $\hat{\sigma}^- = |\downarrow\rangle\langle\uparrow|$, $\delta = \omega_1 - \omega_2 - \omega_0$ and $\Delta\phi$ are the detuning from the transition frequency and the phase difference between the two Raman laser fields, respectively. Resonant carrier excitations can be driven by setting $\delta = 0$.

If we tune the relative frequency difference of the two laser fields, $\Delta\omega$, to be the $\omega_0 + \omega_z$ where ω_z is the frequency of the normal mode along the z direction, we can drive blue-sideband transitions $|\downarrow, n\rangle \rightarrow |\uparrow, n+1\rangle$ that drives $|\downarrow\rangle$ to $|\uparrow\rangle$ while adding a quantum of motion to the motional harmonic oscillator. After neglecting high-frequency terms, the blue-sideband excitation in the interaction frame of both the qubit and motion can be described by the Hamiltonian:

$$H_{BSB} = \hbar\Omega_{BSB} \left(\hat{\sigma}^+ \hat{a}^\dagger \mathrm{e}^{-i(\delta t+\Delta\phi)} + \hat{\sigma}^- \hat{a} \mathrm{e}^{i(\delta t+\Delta\phi)}\right)\Bigg(\tag{2.5}$$

Likewise, we can also drive a red-sideband transition $|\downarrow, n\rangle \rightarrow |\uparrow, n-1\rangle$, described by the Hamiltonian

$$H_{RSB} = \hbar\Omega_{RSB} \left(\hat{\sigma}^+ \hat{a} \mathrm{e}^{-i(\delta t+\Delta\phi)} + \hat{\sigma}^- \hat{a}^\dagger \mathrm{e}^{i(\delta t+\Delta\phi)}\right)\Bigg(\tag{2.6}$$

The strength of the spin-motion coupling, and the sideband transitions Rabi rate are parametrized with the Lamb-Dicke parameter η such that Ω_{BSB} and $\Omega_{RSB} \simeq \eta\Omega_0$ (see Appendix C). For a single ion,

$$\eta = |\Delta k| z_0, \tag{2.7}$$

where $z_0 = \sqrt{\hbar/(2m\omega_z)}$, is the zero-point amplitude of the ion's motion, with m as the mass of the ion. For a single $^9Be^+$ ion, $\eta \simeq 0.35$ for our laser beam setup.

Due to inherent micromotion along the axial direction (see Sec. 3.1 and Ref. [Blakestad 10]), the actual carrier and spin-motion sideband Rabi rates are reduced for the laser beam geometry depicted in Fig. 2.4. For our typical applied RF trap potentials, the modulation index due to the micromotion-induced Doppler shift is approximately 2.9 along the z axis for $^9Be^+$ ion such that the strongest Raman-laser-induced interaction is provided by the second micromotion sideband. This is a factor of $J_2(2.9) \simeq 0.48$ smaller compared to a carrier in the absence of micromotion. Because of this, interactions induced by this laser beam geometry (Fig. 2.4) are driven on the second micromotion sidebands. We tune the frequency difference of the Raman beams to be near $\omega + 2\omega_{RF}$ or $\omega - 2\omega_{RF}$, where ω is the spin-motion transition frequency of interest, and ω_{RF} is the radio frequency for the trapping of ions. We drive the $|2,2\rangle \leftrightarrow |1,1\rangle$ (sideband cooling) transitions on the $+2^{\text{nd}}$-order micromotion sideband, and the spin-motion qubit transition $|1,1\rangle \leftrightarrow |2,0\rangle$ transitions on the -2^{nd}-order micromotion sideband.

When the spin-motion transitions are applied to multiple ions at the same time, the motional mode amplitudes of each ion for a given normal mode have to be taken into account. For example, for a blue-sideband excitation applied to two ions on a given motional mode, the Hamiltonian after dropping high-frequency terms and neglecting coupling to spectator transitions is given by [Wineland 98] (see also Eq. C.24)

$$H_{BSB}^{Two} = \hbar \sum_{j=1,2} \left(\eta_k \xi_{k,j} \Omega_{0,j} \left(\hat{\sigma}_j^+ \hat{a}_k^\dagger e^{-i(\delta t + \Delta\phi_j)} + \hat{\sigma}_j^- \hat{a}_k e^{i(\delta t + \Delta\phi_j)} \right) \right. . \tag{2.8}$$

where η_k, $\hat{a}_k$, and $\xi_{k,j}$ are the Lamb-Dicke parameter, the annihilation operator, and the motional mode amplitude of the jth ion for the kth motional mode, $\Omega_{0,j}$ is the jth ion's resonant carrier transition Rabi rate, and δ is the detuning from the sideband transition. Given two ions of the same species, $\xi_{C,1} = \xi_{C,2} = 1/\sqrt{2}$ for the axial center-of-mass mode (where the ions oscillate in phase) and $\xi_{S,1} = -\xi_{S,2} = 1/\sqrt{2}$ for the stretch mode of motion (where the ions oscillate out of phase with each other).

For the $^9Be^+$ ion, the laser beams depicted in Fig. 2.4 are set up such that the frequency difference between paths 1 and 2 is approximately 1 GHz with a tuning range of approximately ± 100 MHz. With the laser alignments relative to the applied magnetic field and laser polarization settings as shown in Fig. 2.4, stimulated-Raman transitions induced by such a "Co-90" configuration are limited to $\Delta F = \pm 1$, $\Delta m_F = 0, \pm 1$ transitions (see Fig. 2.1).

Stimulated-Raman transitions can also be driven with two laser beams that are copropagating. In this case, because the wave vector difference vanishes to high degree, such a geometry can only excite carrier transitions and does not allow excitation of spin-motion transitions. The Hamiltonian describing this transition is in the form of Eq. 2.4. Furthermore, the Rabi rate of the carrier transitions excited by the copropagating laser beams are not affected by the axial micromotion. In our experiment setup, the two copropagating beams are overlapped and sent to the ions along the the path labeled as $\boldsymbol{k_2}$ in Fig. 2.4. The polarization of these two laser beams are set to contain components of π and σ^+ or σ^- polarizations with respect to the applied magnetic field. By setting the laser frequency difference between the two copropagating laser beams, we can either drive the $\Delta F = \pm 1$, $\Delta m_F = 0, \pm 1$ transitions, or the $\Delta F = 0$, $\Delta m_F = \pm 1$ transitions.

Section 3.4.3 details the Raman laser setup and the generation of laser beams with different frequencies that induce different transitions in the electronic ground state of the $^9Be^+$ ion.

2.1.4 Microwave Transitions

We also use microwave fields to induce magnetic-dipole transitions between different hyperfine states. The microwave field is delivered from dipole antenna located outside the vacuum chamber and a stub tuner is used to maximize the impedance matching at the qubit frequency.

However, unlike stimulated-Raman transitions which can couple to both the spin-only and spin-motion, the gradient of the microwave field across the ion's motional wavepacket is negligible so the microwave field can only drive the spin-only transitions. The Hamiltonian governing the microwave-driven excitations can be described by Eq. 2.4.

The Rabi rates of both Raman-laser and microwave driven spin-flip operations are typically

on the order of a few 100 kHz. The microwave antenna is designed to work in the frequency range of $\sim 1-2$ GHz, which corresponds to $\Delta F = \pm 1$ and $\Delta m_F = 0, \pm 1$ transitions. With this same antenna, we measure the Rabi rates for RF-driven $\Delta F = 0$ transitions to be on the order of a few 100 Hz. Considering the relatively slow Rabi frequencies, microwave fields are not used to drive these $\Delta F = 0$ transitions.

2.1.5 Sideband Cooling

Doppler cooling of the ions with the BD beam (see Sec. 2.1.1) results in a final average occupation number of approximately $\bar{n} \simeq 4$ for the axial center-of-mass modes, for both one and two $^9Be^+$ ions.

To further reduce the motional temperature to near the ground-state temperature, we employ Raman-sideband cooling [Monroe 95b]. It is accomplished by driving a series of red-sideband excitations on the $|2,2\rangle \rightarrow |1,1\rangle$ transitions each followed by repumping with the $^2S_{1/2} \leftrightarrow {}^2P_{1/2}$ (both the RD red and the RD blue) laser beams to reinitialize the ion back to the $|2,2\rangle$ state. The spin-motion excitations on the $|2,2\rangle$ to $|1,1\rangle$ transition is driven on the second axial micromotion sideband. The relative laser frequency of laser beam in path 1 and 2 (Fig. 2.4) is set to be $\omega_{|2,2\rangle \leftrightarrow |1,1\rangle} + 2\omega_{RF} - \omega_z$).

When multiple ions are trapped, multiple motional modes are cooled by interleaving the red-sidebands pulses. Final average occupation numbers of axial modes after sideband cooling are typically ~ 0.01. Our Raman laser beam geometry does not give rise to interactions with the radial motional modes, so they are not ground-state cooled.

Motional excitations are measured with the sideband asymmetry method [Turchette 00a]. This is performed by separately measuring the excitation strengths E for red and blue motional sidebands transitions, the mean occupation number $\bar{n}$ is given by

$$\bar{n} = \frac{\frac{E_{RSB}}{E_{BSB}}}{1 - \frac{E_{RSB}}{E_{BSB}}}, \tag{2.9}$$

where E_{RSB} and E_{BSB} are the excitations of the red and blue sideband transitions, respectively.

Equation 2.9 assumes the motional states exhibit a thermal distribution, with population P_n in the Fock state n given by

$$P_n = \frac{\bar{n}^n}{(\bar{n}+1)^{n+1}}. \tag{2.10}$$

A temperature, T, can be related to $\bar{n}$ with

$$\bar{n} = \frac{1}{e^{\hbar\omega_\nu/k_B T} - 1}, \tag{2.11}$$

where ω_ν is the motional frequency of interest and k_B is the Boltzmann constant.

2.1.6 Qubit State Initialization

After Doppler and Raman-sideband cooling, the ions have been optically pumped to the $|2,2\rangle$ state. The initialization of qubit state is then accomplished by transferring the population in the $|2,2\rangle$ state to the qubit $|\uparrow\rangle = |1,1\rangle$ state by applying a composite microwave π pulse [Levitt 86] composed of a sequence of $R(\theta,\phi)$ pulses

$$R\left(\pi,0\right), R\left(\pi,\frac{\pi}{3}\right), R\left(\pi,\frac{\pi}{6}\right), R\left(\pi,\frac{\pi}{3}\right), R\left(\pi,0\right), \tag{2.12}$$

where θ denotes the angle the state is rotated about an axis in the x-y plane of the Bloch sphere, and ϕ is the azimuthal angle of the rotation axis. In general, single-qubit and global rotations can be described in the matrix form of

$$R(\theta,\phi) = \begin{pmatrix} \cos\left(\frac{\theta}{2}\right) & -ie^{-i}\sin\left(\frac{\theta}{2}\right) \\ -ie^{i}\sin\left(\frac{\theta}{2}\right) & \cos\left(\frac{\theta}{2}\right) \end{pmatrix}, \tag{2.13}$$

A different composite π pulse composed of a sequence of pulses

$$R\left(\frac{\pi}{2},0\right)\left(R\left(\frac{3\pi}{2},\frac{\pi}{2}\right), R\left(\frac{\pi}{2},0\right)\right. \tag{2.14}$$

was used before changing to that shown in Eq. 2.12. It was found that the composite pulse of Eq. 2.12 improved the fidelity of population transfer from the $|2,2\rangle$ state to the $|1,1\rangle$ state compared to shown in Eq. 2.14 by a factor of ~ 2. Composite pulses of Eq. 2.12 offer higher robustness in gate duration error compared to composite pulses of Eq. 2.14 [Levitt 86].

2.1.7 Qubit State Measurement

Qubit state measurement is accomplished with the standard state-dependent resonance-fluorescence detection technique. First, the composite microwave π pulse used for the qubit state initialization is applied to transfer the $|\uparrow\rangle$ population back to the $|2,2\rangle$ state. This is followed by a microwave π pulse that transfers ("shelves") the $|\downarrow\rangle$ state to the $|1,-1\rangle$ state. To further shelve any remaining $|\downarrow\rangle$ population, we then apply a microwave π pulse from the $|\downarrow\rangle$ state to the $|1,0\rangle$ state. After these shelving pulses, the BD laser beam is tuned to resonance on the ${}^2S_{1/2}|2,2\rangle \leftrightarrow {}^2P_{3/2}|3,3\rangle$ cycling transition. With these conditions, the fluorescing or "bright" state of this protocol corresponds to the qubit $|\uparrow\rangle$ state, and the qubit $|\downarrow\rangle$ state will be detected as "dark". With a detection duration of 330 μs and a saturation parameter $s \sim 0.5$, we record on average approximately 30 photon counts in a photo-multiplier tube (PMT) for an ion in the bright state and 2 photons for a $^9Be^+$ ion in the dark state (limited by background scattered light).

To maximize the photon collection in the presence of the axial micromotion, we apply a differential voltage of approximately $\pm$ 0.15 V to the two DC electrodes centered on zone $\mathcal{E}$ (Fig. 3.1). This operation is identical to that used during Doppler cooling process (see Sec. 2.1.1). Figure 2.5 shows a typical detection histogram of a $^9Be^+$ ion.

2.2 $^{25}Mg^+$ Ion Qubit

There are three stable isotopes of the magnesium atom, i.e. ^{24}Mg, ^{25}Mg, and ^{26}Mg, with ^{25}Mg the only isotope that has a non-zero nuclear spin. The electronic structure of a $^{25}Mg^+$ ion is very similar to that of a $^9Be^+$ ion. The electronic ground state and the first two electronic excited states of a $^{25}Mg^+$ ion are the $3s\ {}^2S_{1/2}$, $3p\ {}^2P_{1/2}$, and the $3p\ {}^2P_{3/2}$ states, respectively. The fine structure splitting between the two excited states is approximately 2.75 THz.

The nuclear spin of of the $^{25}Mg^+$ is 5/2. The hyperfine splitting between the $F = 2$ and $F = 3$ levels is approximately 1.75 GHz. Similar to the $^9Be^+$ ion, it is possible to choose an external magnetic field to make certain transition frequencies in $^{25}Mg^+$ first-order insensitive to

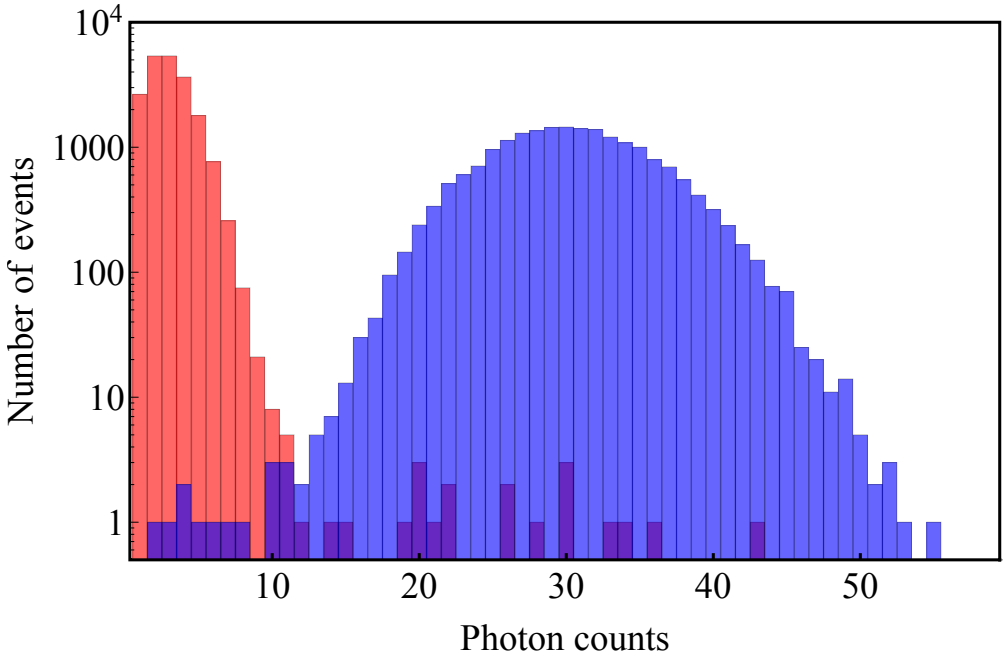

Figure 2.5: A typical single $^9Be^+$ ion detection histogram for the population to be either in the $|2,2\rangle$ state (blue) or the $|1,-1\rangle$ state (red). With a detection duration of 330 μs and a saturation parameter s of ~ 0.5, we detect on average $\simeq 30$ photon counts for the ion in the $|2,2\rangle$ state, and $\simeq 2$ counts when the ion is in the $|1,-1\rangle$ state. Overlap of the two distributions is shown in dark color.

magnetic field fluctuations. However, the magnetic field insensitive points for the two species are different and it is impossible to select a magnetic field to make both species insensitive to magnetic field fluctuations. For our experiments, we choose to make the $^9Be^+$ qubit to be magnetic field insensitive, which occurs at $B \simeq 119.446$ G. This choice is based on the required laser intensity to reach a certain quantum gate error level and the $^9Be^+$ ion is more favorable than the $^{25}Mg^+$ ion [Ozeri 07]. Details of spontaneous scattering of photon is discussed in Sec. 4.4.2. At $B \simeq 119.446$ G, the $^{25}Mg^+$ ion's $|F = 3, m_F = 1\rangle \leftrightarrow |2, 0\rangle$ transition has a magnetic field sensitivity of $\simeq 43$ kHz/G, which is the lowest among all other hyperfine transitions in the electronic ground state by about two orders of magnitude. Magnetic-field insensitive and corresponding magnetic fields transitions in the electronic ground state of a $^{25}Mg^+$ ion are tabulated in Table B.2.

Here, we label the $|3, 1\rangle$ state as the qubit $|\uparrow\rangle$ state and the $|2, 0\rangle$ state as the $|\downarrow\rangle$ state. Figure 2.6 shows the energy level diagram of the $^{25}Mg^+$ ion at a magnetic field of ~ 119.446 G. See Appendix B.1 for a more detailed energy level diagram. By probing the Ramsey contrast as a function of wait time (Fig. 2.7), the coherence time of the $^{25}Mg^+$ qubit was measured to be ~ 6 ms. Although this is much shorter than the coherence time of the $^9Be^+$ ion (~ 1.5 s), it is still significantly longer than the relevant time scale of experiments involving $^{25}Mg^+$ ion that are presented in this thesis. The relevant atomic properties of the Mg^+ ion are listed in Table B.1.

2.2.1 Doppler Cooling

Similar to that for the $^9Be^+$ ion, we use a blue Doppler (BD) beam and a blue Doppler detuned (BDD) beam for the Doppler cooling of the $^{25}Mg^+$ ion. The BD beam is σ^+ polarized and red detuned by approximately $\Gamma_{Mg}/2$ from the $^2S_{1/2}|3, 3\rangle \leftrightarrow {}^2P_{3/2}|4, 4\rangle$ cycling transition, where the decay rate of the $^2P_{3/2}$ state is $\Gamma_{Mg} \simeq 41.3(3)$ MHz [Clos 14]. The BD beam is also used for the fluorescence detection of the $^{25}Mg^+$ ion (see Sec. 2.2.6).

The BDD beam is red detuned $\simeq 500$ MHz from the $^2S_{1/2}|3, 3\rangle \leftrightarrow {}^2P_{3/2}|4, 4\rangle$ transition, and has an optical power of ~ 1 mW to provide a better cooling in the event of occasional high motional excitations including those caused by background gas collisions.

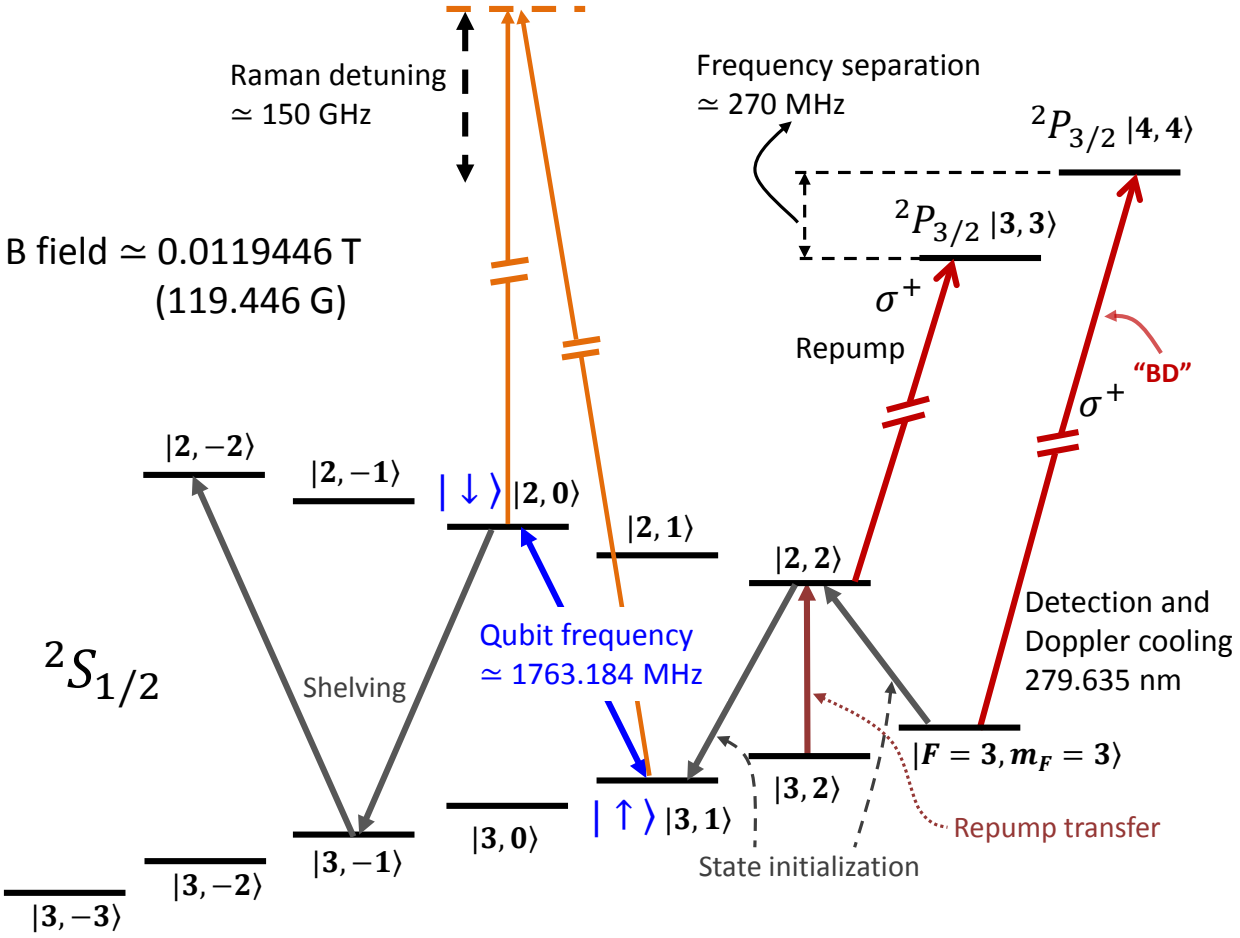

Figure 2.6: Relevant energy level structure (not to scale) for the $^{25}Mg^+$ ion at an external magnetic field of approximately 119.446 G. The "blue Doppler detuned" (BDD) beam, which is red shifted $\simeq$ 500 MHz with respect to the "blue Doppler" (BD) beam (see Sec. 2.2.1), is not shown in this figure. The $^{25}Mg^+$ ion qubit is encoded in the $|3,1\rangle = |\uparrow\rangle$ state and $|2,0\rangle = |\downarrow\rangle$ state, they constituent the "computational qubit manifold". The qubit transition frequency has a magnetic-field sensitivity of $\simeq$ 43 kHz/G at the applied magnetic field. The "measurement qubit manifold" consists of the $|3,3\rangle$ state as the "bright" state and the $|2,-2\rangle$ state as the "dark state" (see Sec. 2.2.6). The decay rate of the $^2P_{3/2}$ state is $2\pi \times 41.3(3)$ MHz [Clos 14]. See Appendix B.1 for a more detailed energy level diagram in the $^{25}Mg^+$ electronic ground state.

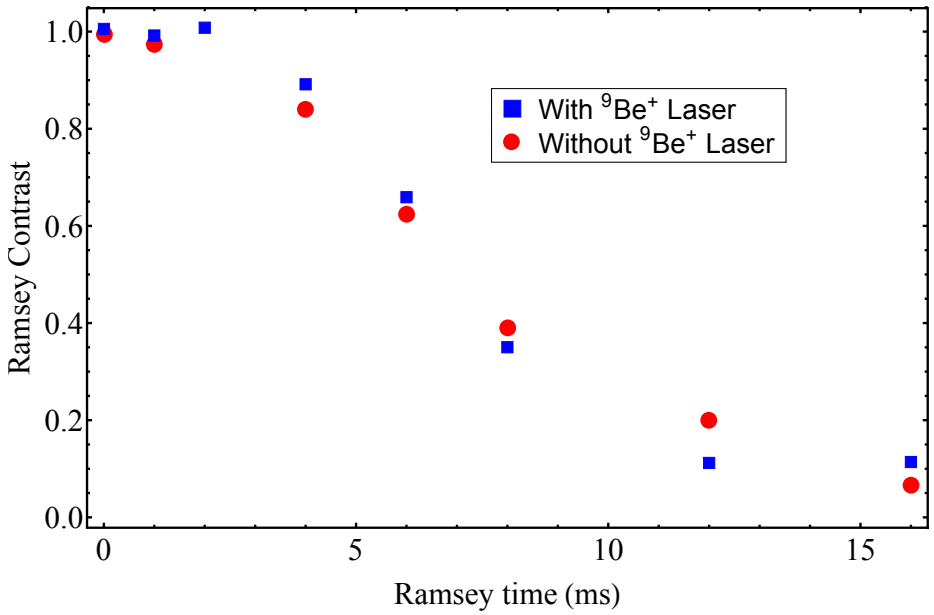

Figure 2.7: Coherence time of the $^{25}Mg^+$ qubit investigated with a Ramsey sequence with and without the presence of the $\lambda \simeq 313$ nm laser beam used for the manipulations of the $^9Be^+$ ion. The shorter qubit coherence time compared to the $^9Be^+$ qubit is due to the non-zero linear component of magnetic field sensitivity.

2.2.2 Repumping

A repump laser beam is used to improve optical pumping of the $^{25}Mg^{+}$ population into the $^{2}S_{1/2}|3,3\rangle$ state. This laser is derived from the same laser source as the BD and BDD beams, with the laser frequency tuned on resonance with the $^{2}S_{1/2}|2,2\rangle \leftrightarrow {}^{2}P_{3/2}|3,3\rangle$ transition. See Sec. 3.5 for details on the laser beam setup.

There are three possible spontaneous emission channels from the $^{2}P_{3/2}|3,3\rangle$ state, i.e. decay to the $^{2}S_{1/2}|2,2\rangle$, $^{2}S_{1/2}|3,2\rangle$, and $^{2}S_{1/2}|3,3\rangle$ states with branching ratios of 0.0765, 0.257, and 0.667, respectively (see Fig. 2.6). Starting from the $^{2}S_{1/2}|2,2\rangle$ state, applying the repump laser beam can populate the $|3,2\rangle$ state. To completely transfer the population to the the $|3,3\rangle$ state, a microwave-driven spin-flip (π) transition is applied to transfer population from the $|3,2\rangle$ state to the $|2,2\rangle$ state (Fig. 2.6). After the first repump pulse, the ($|3,2\rangle \leftrightarrow |2,2\rangle$ spin-flip π pulse + repump) sequence is repeated three times to ensure near complete depletion of the $|3,2\rangle$ and $|2,2\rangle$ states.

Compared to the repump procedure implemented on the $^{9}Be^{+}$ ion where two lasers beams are used to transfer population to the $|2,2\rangle$ state from the $|1,1\rangle$ and $|2,1\rangle$ states (see Sec. 2.1.2), the total duration required is longer due to the relatively slow Rabi rate of the $|3,2\rangle \leftrightarrow |2,2\rangle$ spin-flip transition (a typical π pulse takes ~ 10 μs), and the two-step process must be repeated. In the future, it would be advantageous to mitigate these issues by employing a laser which provides direct electronic $^{2}S_{1/2} \leftrightarrow {}^{2}P_{1/2}$ transitions. This multi-cycle repumping strategy is also used during the Raman-sideband cooling of the $^{25}Mg^{+}$ ion.

2.2.3 Coherent Operations

Similar to the $^{9}Be^{+}$ ions, the $^{25}Mg^{+}$ ions are manipulated coherently by driving stimulated-Raman transitions and microwave transitions. Coherent operations applicable to the $^{25}Mg^{+}$ ions can be analogously described by the Hamiltonians presented in Sec. 2.1.3.

The Raman laser for the manipulation of the $^{25}Mg^{+}$ ion has a wavelength $\lambda \simeq 280$ nm, and

the Raman detuning is set ~ 160 GHz blue detuned from the $^2S_{1/2} \leftrightarrow {}^2P_{3/2}$ electronic transition. The $^{25}Mg^+$ Raman laser beam setup can be found in Sec. 3.5.2. The axial micromotion experienced by the $^{25}Mg^+$ ion is less than that for the $^9Be^+$ ion due to $^{25}Mg^+$ ion's heavier mass, At zone $\mathcal{E}$ (Fig. 3.1), the axial micromotion index for the $^{25}Mg^+$ is approximately 1.04. At this modulation index, the micromotion carrier is the strongest interaction with the stimulated-Raman-transition-induced coupling strength reduced by a factor of $J_0(1.04) \simeq 0.75$ compared to when no micromotion is present.

To maximize impedance matching at different frequencies compared to those corresponding to the $^9Be^+$ ion's transition frequencies, we use a separate dipole antenna (of different length) to drive microwave transitions in the $^{25}Mg^+$ ion.

2.2.4 Sideband Cooling

Ground state cooling of the motional modes can be accomplished by driving stimulated-Raman-induced sideband transitions and applying repumping operations on the $^{25}Mg^+$ ion. In this case, the red-sideband excitations are applied on the $|3,3\rangle|n\rangle \rightarrow |2,2\rangle|n-1\rangle$ transitions.

The Rabi rates of spin-motion transitions between the Fock state n and n' driven by stimulated-Raman process, such as those described in Eq. 2.5 and Eq. 2.6, are given by [Wineland 98]

$$\Omega_{n,n'} = \Omega e^{-\eta^2/2} \sqrt{\frac{n_<!}{n_>!}} \eta^{|n'-n|} L_{n_<}^{|n'-n|}(\eta^2), \tag{2.15}$$

where L_n^α is the generalized Laguerre polynomial, and $n_<(n_>)$ is the lesser (greater) of n and n'. Depending on the value of the Lamb-Dicke parameter, η, the Rabi rate for certain spin-motion transitions can vanish. Figure 2.8 shows two sets of $\Omega_{n,n'}/\Omega$ ratio as a function of the Fock state number, n, for three different values of η. The first and second set corresponds to first ($n' = n-1$) and second ($n' = n-2$) sideband transition, respectively. A singly-trapped $^{25}Mg^+$ ion has a Lamb-Dicke parameter $\eta \simeq 0.3$ with an axial secular trapping frequency of 2.15 MHz. The Rabi rate for red-sideband transitions vanishes according to the Laguerre polynomials at about $n = 40$. Cooling pulses driven on the second red-sideband excitations can be used to better remove motional Fock

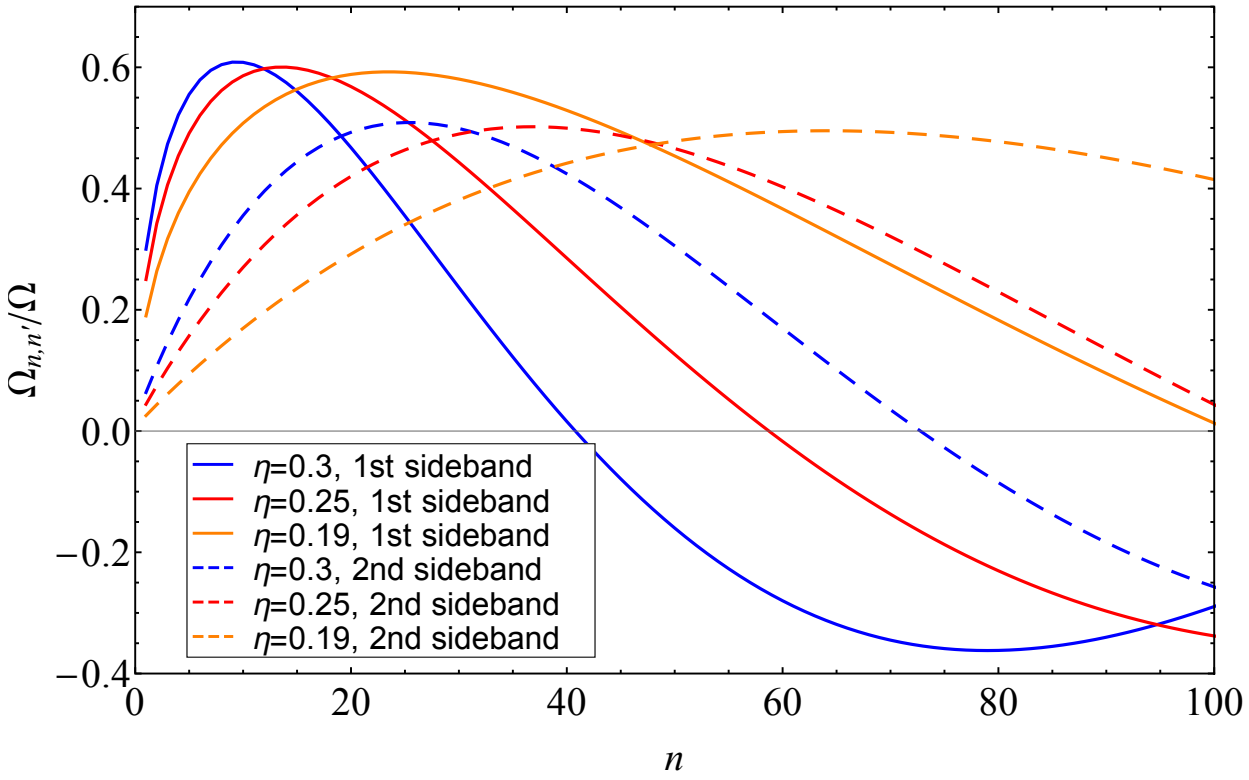

Figure 2.8: The ratio of spin-motion transition Rabi rates between different Fock states ($\Omega_{n,n'}$) to carrier Rabi rate Ω is plotted as a function of the Fock state number n for different values of Lamb-Dicke parameters. The first-order ($n' = n - 1$) and second-order ($n' = n - 2$) sideband transition rates are shown. The Rabi rates of the first-order sideband transitions vanish at relatively low values of n, which means that spin-motion transitions between these different Fock states cannot be driven. This can be problematic for the motional cooling to the ground state if only the first-order sideband transitions are used in the cooling sequence. At the Rabi rate vanishing points of the first-order sideband transitions, the second-order sideband transition Rabi rates are non zero. Thus, they can be inserted to improve the cooling.

state population that can be trapped near these vanishing points and to provide a speed up of the sideband cooling process. Rabi rates of the second sideband transitions for the same set of Lamb-Dicke parameters are also shown in Fig. 2.8.

By first applying 20 second-order red-sideband transitions, followed by 30 first-order red-sideband transitions on the $|3,3\rangle \leftrightarrow |2,2\rangle$ transitions (each sideband pulse is followed by the re-pumping process described in Sec. 2.2.2), a singly-trapped $^{25}Mg^{+}$ ion can be cooled to a mean occupation number of ~ 0.08.

For experiments involving cotrapping of the $^{9}Be^{+}$ and the $^{25}Mg^{+}$ ions, ground-state cooling is achieved by applying Raman sideband cooling on the $^{9}Be^{+}$ ion. This is to take advantage of (i) lower spontaneous photon scattering rates due to a higher Raman detuning (coupled with the higher power available) and (ii) the faster repump process employed on the $^{9}Be^{+}$ ion compared to that for the $^{25}Mg^{+}$ ion.

2.2.5 Qubit State Initialization

Optical pumping prepares the population into the $|3,3\rangle$ state. Qubit state initialization is accomplished by applying a microwave-induced composite π pulse on the $|3,3\rangle \leftrightarrow |2,2\rangle$ transition, followed by an analogous composite π pulse on the $|2,2\rangle \leftrightarrow |3,1\rangle = |\uparrow\rangle$ transition. Each composite π pulse composes of a sequence of pulses $R(\theta = \pi/2, \phi = 0)$, $R(3\pi/2, \pi/2)$, $R(\pi/2, 0)$, where θ and ϕ denotes the rotation and azimuthal angle as described in Sec. 2.1.6. This composite π pulse is identical to that described in Eq. 2.14.

2.2.6 Qubit State Measurement

Before applying the detection (BD) laser beam, which is resonant with the $^{2}S_{1/2}|3,3\rangle \leftrightarrow {}^{2}P_{3/2}|4,4\rangle$ cycling transition, the $^{25}Mg^{+}$ qubit initialization composite pulse sequences are applied in reverse order to transfer the $|\uparrow\rangle_{\mathrm{Mg}}$ population to the $|3,3\rangle$ state. Subsequently, microwave "shelving" (π) pulses are applied to first transfer the $|2,0\rangle = |\downarrow\rangle$ population to the $|3,-1\rangle$ state followed by a transfer pulse that puts the $|3,-1\rangle$ state to the $|2,-2\rangle$ state. Therefore, the "bright"

state for $^{25}Mg^{+}$ detection protocol corresponds to the $|\uparrow\rangle$, and the "dark" state corresponds to the $|\downarrow\rangle$ state. To maximize detection photon counts in the present of axial micromotion, we apply an analogous procedure (see Sec. 2.1.7) that shifts the $^{25}Mg^{+}$ ion's position such that the overall micromotion experienced by the ion is perpendicular to the wavevector of the detection laser beam. We detect on average ~ 30 photon counts for a detection duration of 200 μs when an ion is in the bright state, and about ~ 4 photons counts for the ion in the dark state (see Fig. 2.9).

When both $^{9}Be^{+}$ and $^{25}Mg^{+}$ ions are cotrapped, qubit state measurements are applied subsequently for the fluorescing photons to be registered on the same PMT. Details on the photon collection setup is available in Sec. 3.3.

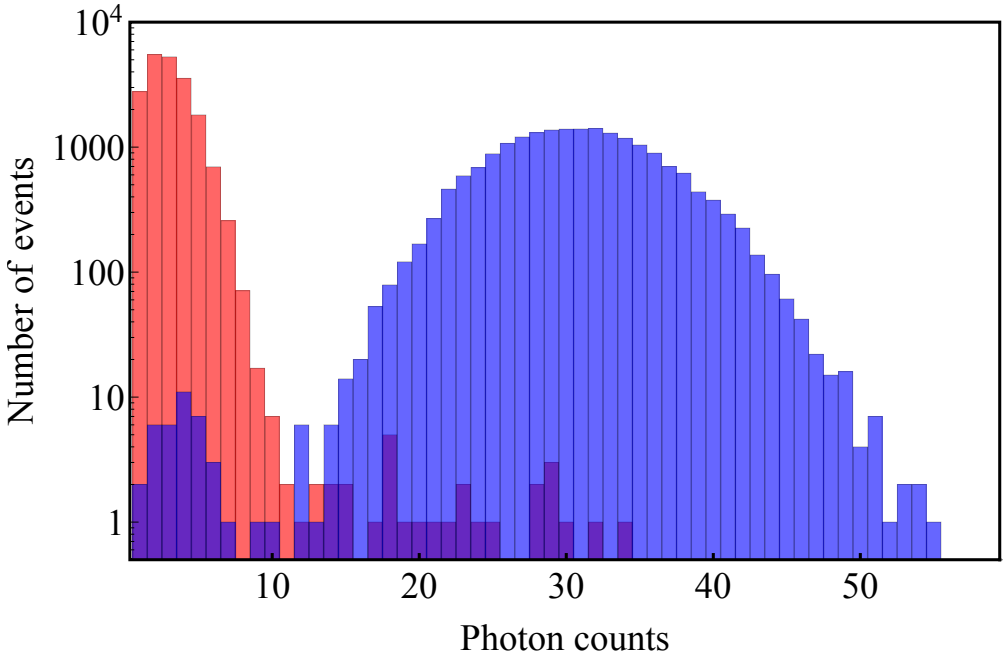

Figure 2.9: A typical detection histogram of a $^{25}Mg^{+}$ ion for the population to be either in the $|3,3\rangle$ state (blue) or the $|2,-2\rangle$ state (red). The fluorescing "bright" state corresponds to the qubit $|\uparrow\rangle$ while the "dark" state corresponds to the the $|\downarrow\rangle$ state. Overlap of the two distributions is shown in dark color.

Chapter 3

Apparatus

3.1 Ion Trap

The ion trap used for this thesis work is a linear Paul trap [Paul 90]. The schematic of this trap is shown in Fig. 3.1. Featuring multiple, segmented control electrodes to allow ions to be confined at different locations, this trap is designed to demonstrate the elements of scalable quantum information processing with the "quantum charged-coupled-device" architecture [Wineland 98, Kielpinski 02, Blakestad 11]. It is constructed with two gold-coated, stacked wafers. Details about the design and assembly of this trap is given by Blakestad [Blakestad 11, Blakestad 10].

Radio frequency (RF) potentials, with frequency $\omega_{\mathrm{RF}} \simeq 2\pi \times 83$ MHz and amplitude $V_{\mathrm{RF}} \simeq 200$ V, are applied to the RF electrodes to provide confinement transverse to the main trap channels. Static (DC) potentials are applied to the segmented control electrodes to create potential wells for trapping of ions at the desired locations in the channels. These potentials are dynamically-controllable and are provided by a multi-channel arbitrary waveform generator (AWG) which is briefly discussed in Sec. 3.7 and detailed in [Bowler 13]. By applying time-dependent potentials to these electrodes, the ions can be transported deterministically between different trap zones. For the work described in this thesis, the ions are first loaded in $\mathcal{L}$ and then transported to $\mathcal{E}$. Quantum logic experiment described in Chap. 5 and 6 were performed with ions confined in a fixed harmonic well at $\mathcal{E}$ (Fig. 3.1). The chained Bell inequality experiment described in Chap. 8 were performed with ions shuttled between different locations near zone $\mathcal{E}$. One unique feature of this trap is the junction at $\mathcal{C}$, which can be used for reordering of ion chains [Blakestad 11].

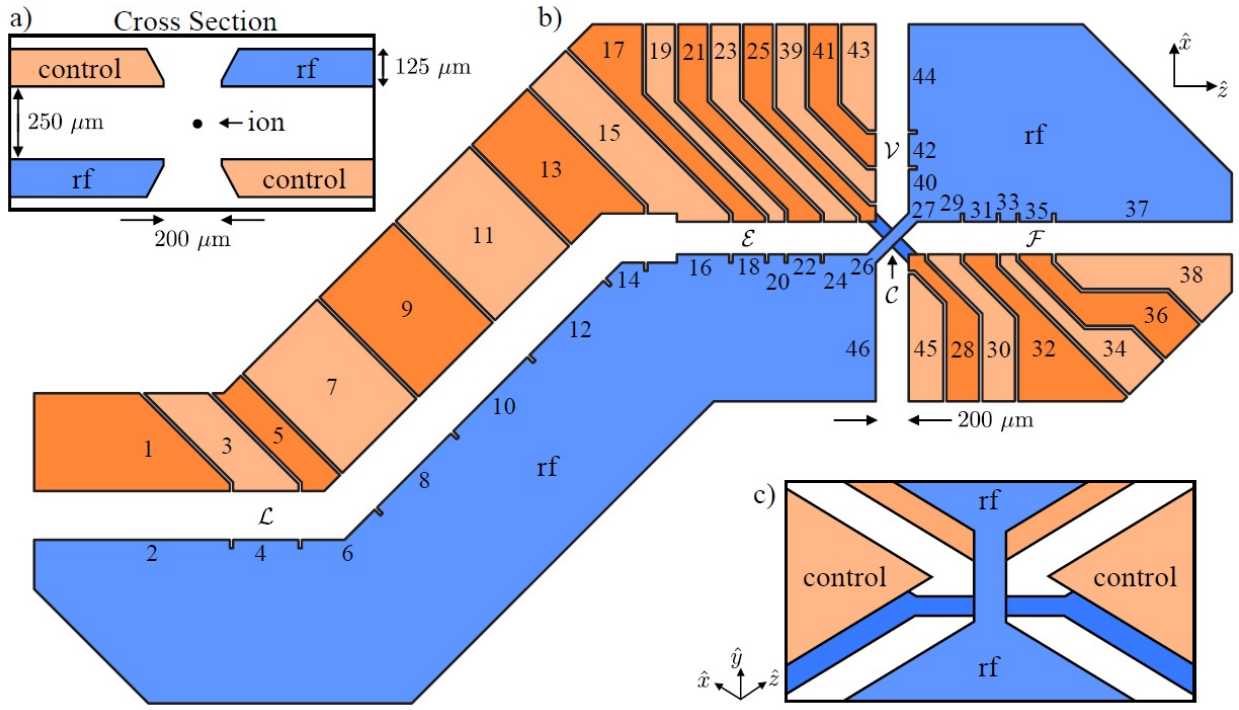

Figure 3.1: The schematic of the X-junction trap. The trap is constructed with two gold-coated, stacked wafers. (b) Top view of the trap showing the load zone $\mathcal{L}$ and experiment zone $\mathcal{E}$. Ions are transported from $\mathcal{L}$ to $\mathcal{E}$ with time-varying potentials applied to the segmented control electrodes (colored orange hues). The positions of RF and control electrodes are exchanged in the lower layer (a). The details of the junction are illstrated in (c). Coherent manipulations are implemented on ions confined in $\mathcal{E}$. See Ref. [Blakestad 11] for details of this trap.

	R	C	ω_f
Stage 1	3.3 kΩ	1 nF	$\sim$ 48 kHz
Stage 2	1 kΩ	1 nF	$\sim$ 159 kHz
Stage 3	240Ω	0.82 nF	$\sim$ 882 kHz

Table 3.1: Values of resistors, capacitors, and their corresponding cut-off frequencies (Eq. 3.1)for the three low-pass filtering stages connected between a multi-channel AWG (Sec. 3.7) and the control electrodes.

Due to the particular design of the junction and imperfect construction of the trap wafers, the ions undergo residual RF "micromotion" [Wineland 98] at frequency ω_{RF} along $\hat{z}$ with amplitude $\simeq 105$ nm at $\mathcal{E}$ for the typical transverse pseudo potentials used. This affects our implementation of logic gates, Doppler and ground state cooling, and qubit states measurement, which are described in Chap. 2.

This ion trap apparatus is housed inside a vacuum system with fused-silica windows for laser beams access and collection of fluorescence photons. A mock up figure of the vacuum system is shown in Fig. 3.2 with details available in Ref. [Blakestad 10].

Three stages of low-pass filters have been implemented for the suppression of noise coupled to the segmented control electrodes. All three stages use the usual resistor-capacitor circuit where the cut-off frequency is defined as

$$\omega_f = \frac{1}{2\pi RC}, \tag{3.1}$$

where R is the resistance and C is the capacitance. Table 3.1 lists the values of R, C, and the corresponding cut-off frequency for each stage. The first filtering stage is connected to the output of the AWG. The second filtering stage is attached to the electrical feedthrough located just outside of the vacuum chamber. Both these filtering stages are housed inside metal box to reduce electrical interferences. Their resistors and capacitors can be replaced straightforwardly. The third and final filtering stage is soldered on the filter board where the trap wafers are attached to. As this filtering stage is inside the vacuum chamber, it is not straightforward to be replaced. Details of this filtering stage is in Ref. [Blakestad 10]. We find that the first and second stages of filters are important to minimize the anomalous heating of motional modes [Turchette 00a]. With all three stages of

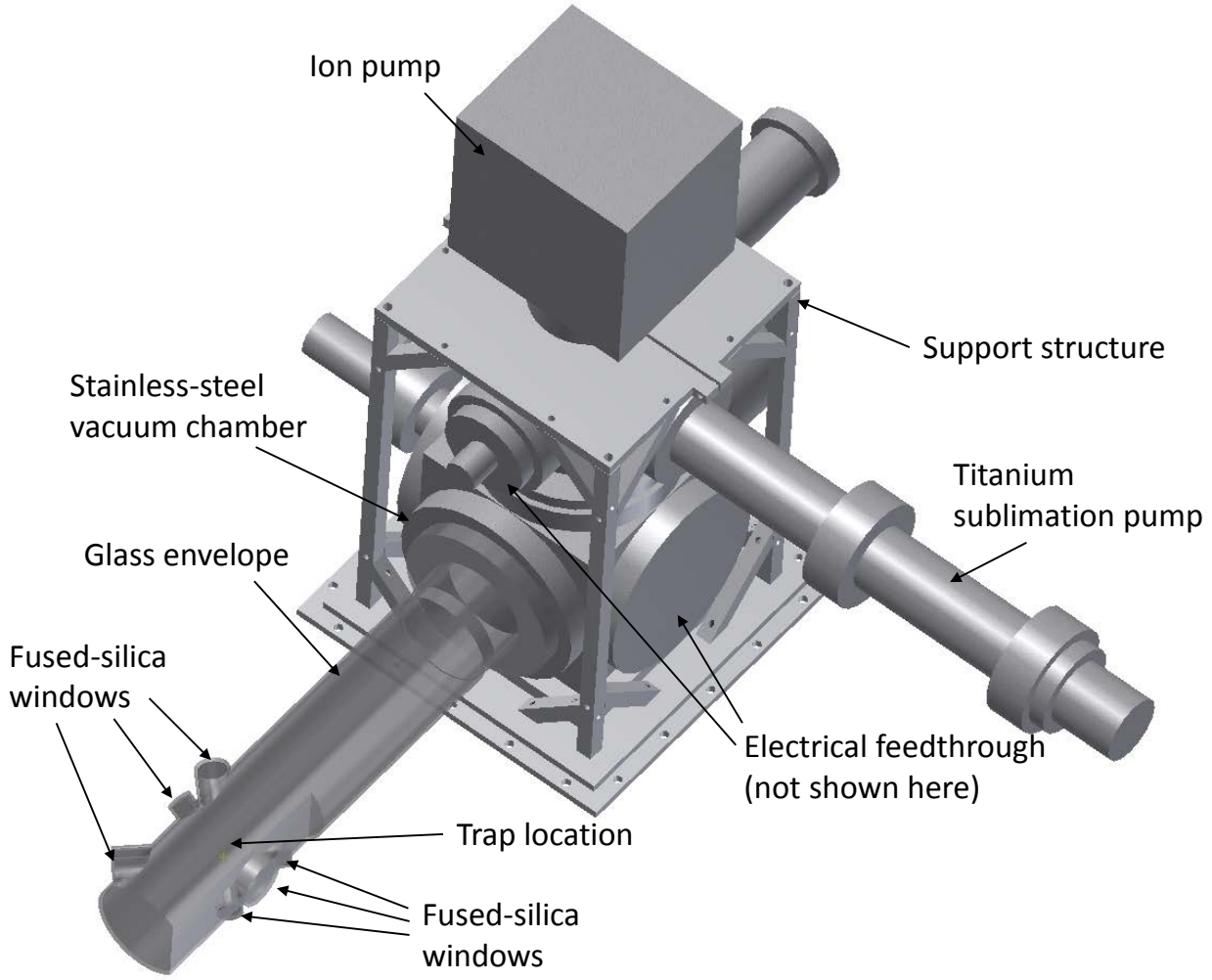

Figure 3.2: Mock up of the vacuum chamber housing the X-junction trap. A glass envelope with fused-silica view ports is attached to a stainless-steel vacuum chamber. The fused-silica view ports are used for the access of laser beams and collection of fluorescence photons emitted by ions. In addition to an ion pump which maintains the system under ultra-high vacuum condition of $\sim 3 \times 10^{-11}$ torr (measured with an ion gauge), the vacuum system includes a titanium sublimation pump which is turned on infrequently (approximately once per month). Multiple electrical feedthroughs are used to connect to RF and control electrodes, and neutral beryllium and magnesium resistively-heated ovens.

filters, we measure the heating rate of the axial ($\hat{z}$) center-of-mass mode to be ~ 40 quanta/s at a trap frequency of $\omega_z \simeq 2\pi \times 3.6$ MHz in the $\mathcal{E}$ zone. With similar trapping parameters in $\mathcal{S}$ zone, the heating rate is measured to be ~ 80 quanta/s.

3.2 Magnetic Field Coil

We apply an external magnetic field of $\simeq 0.0119446$ T (119.446 G) so that the $^9\mathrm{Be}^+$ $^2S_{1/2}|F=2, m_F=0\rangle \leftrightarrow {}^2S_{1/2}|F=1, m_F=1\rangle$ transition is first-order insensitive to magnetic-field fluctuations [Langer 05]. As shown in Fig. 3.3, two field coils are arranged in a Helmholtz-like configuration, with each coil made with 20 turns of square copper wire (outer dimension of ~ 4 mm) with a hollow round bore (diameter of ~ 2.54 mm). The hollow bore enables water to flow through each coil for cooling as we apply a static current of approximately 62 A to provide for the desired magnetic field. The temperature of the cooling water is actively stabilized with a chiller's[1] reservoir at approximately 15 °C, which makes the coils operate at a steady state temperature close to the room temperature of approximately 20 °C. This strategy is to prevent an unwanted temperature gradient near to the ion trap apparatus that can cause potential air current fluctuations, which might in turn induce unwanted laser beams pointing fluctuations.

The geometry of the main coils is designed to accommodate for (i) the relatively large size of a Schwarzschild objective for collection of ions' fluorescence photons (detailed in Sec. 3.3), (ii) the access of laser beams into the vacuum chamber, (iii) the desired relatively uniform magnetic field across different trap zones (Fig. 3.1), and (iv) the water cooling process such that a laminar water flow condition is satisfied. The main current output from the power supply unit is actively stabilized by first detecting the current using a transducer[2] and then allowing a small fraction of the current to leak from the positive terminal onto the negative terminal, which is connected to the earth ground.

In addition to the main coils, additional coils made of smaller wire size are used to provide

[1] Thermo Scientific NESLAB MERLIN M33
[2] Danisense DS-200

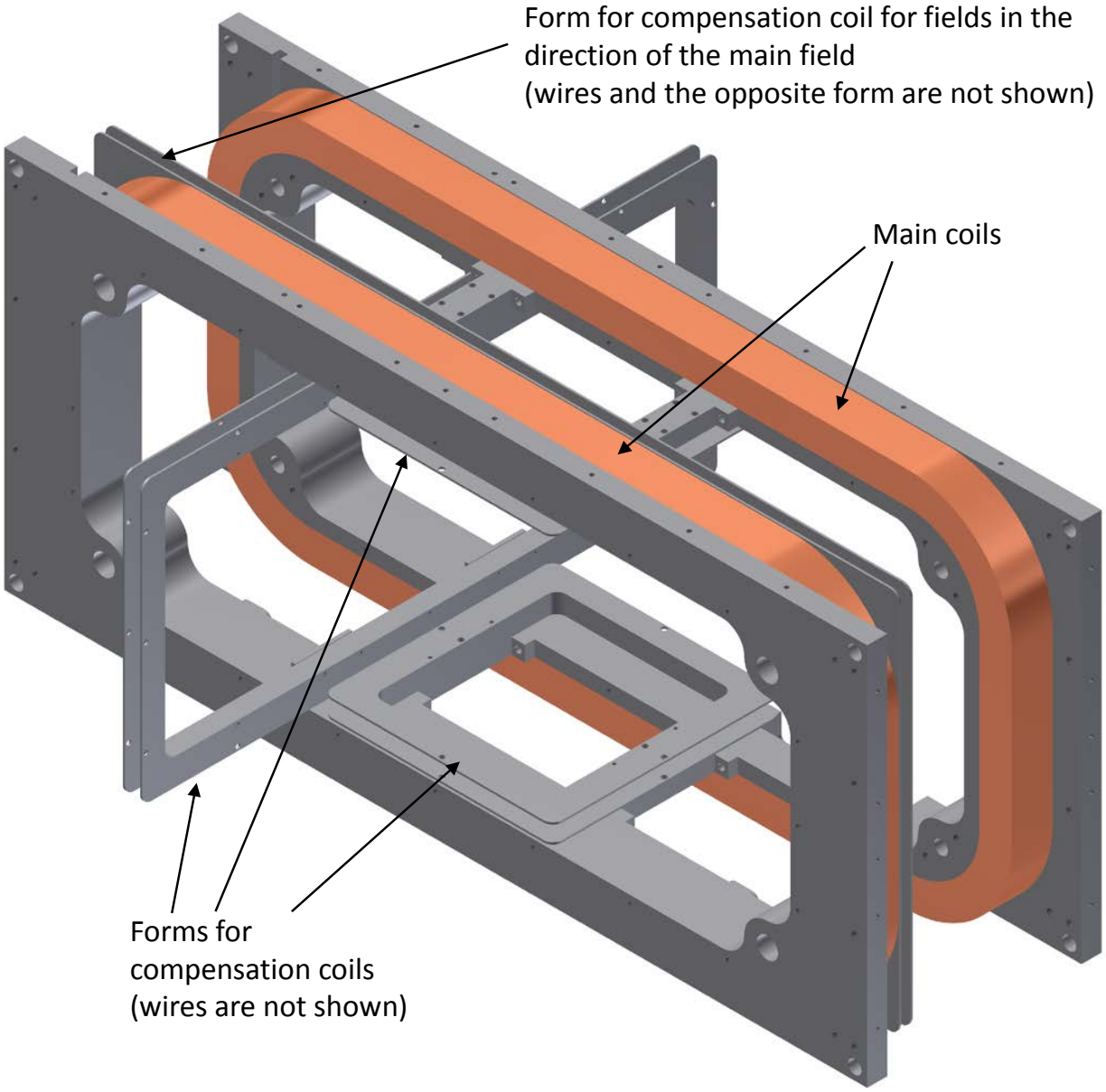

Figure 3.3: Schematic of the magnetic field coils that are used to provide a static magnetic field of $\simeq 0.0119446$ T in a Helmholtz-like configuration. The main coils (orange color) which have an approximate rectangular dimension of 40 cm $\times$ 20 cm, and are separated by approximately 8 cm, are held in position by custom parts made of anodized aluminum. The field coils assembly also consists of compensation coils which allow fine tuning of magnetic field in three dimensions. Wire in compensation coils are not shown. See also Fig. 3.6.

fine tuning of the magnetic field in three directions. We use these coils to compensate for unwanted field gradients, and to fine tune the alignment of the magnetic field with respect to the wave vectors of the Doppler cooling and detection laser beams to ensure that the laser beams are σ^+ polarized.

One pair of compensating magnetic field coil is arranged in the Helmholtz-like configuration with axis aligned along the main coil. The current provided by this coils pair is computer controlled to compensate for the slow magnetic field drift by probing the ion's transition frequency such that magnetic-field insensitivity condition of the $^9Be^+$ ion's $|2,0\rangle \leftrightarrow |1,1\rangle$ transition is satisfied. By probing the $^9Be^+$ ion's transition frequency over time, the amplitude of the slow magnetic field drift is deduced to be approximately few mG per minute.

3.3 Imaging System

A custom designed imaging system is used to collect the fluorescence photons from the $^9Be^+$ ions and the $^{25}Mg^+$ ions, with wavelengths of 313 nm and 280 nm, respectively. Photons are first collected with a Schwarzschild objective and imaged at an intermediate focus point, followed by a secondary relay imaging stage consisting of a concave mirror used to project this image onto either an electron-multiplying charge-coupled device (EMCCD) camera[3] or onto a photonmultiplier tube (PMT)[4] .

The schematic of the Schwarzschild objective is shown in Fig. 3.4, with details available in Ref. [Huang 04]. The first element of the objective is a pair of lenses designed to compensate for the chromatic aberration caused by the vacuum windows (see Fig. 3.4), which was made of fused silica. This lenses pair is designed to be f/1 (f-number equal to 1). However, $\sim 30\%$ of the total photons collected are blocked by the secondary mirror.

The optics elements used in the relay imaging stage are all composed of reflective optics to minimize chromatic aberration which can be present when refractive optics are used. Both 313 nm and 280 nm photons are focused onto the same location on the PMT or the camera. The schematic

[3] Princeton Instruments PhotonMax 512B
[4] Hamamatsu R7600U-200

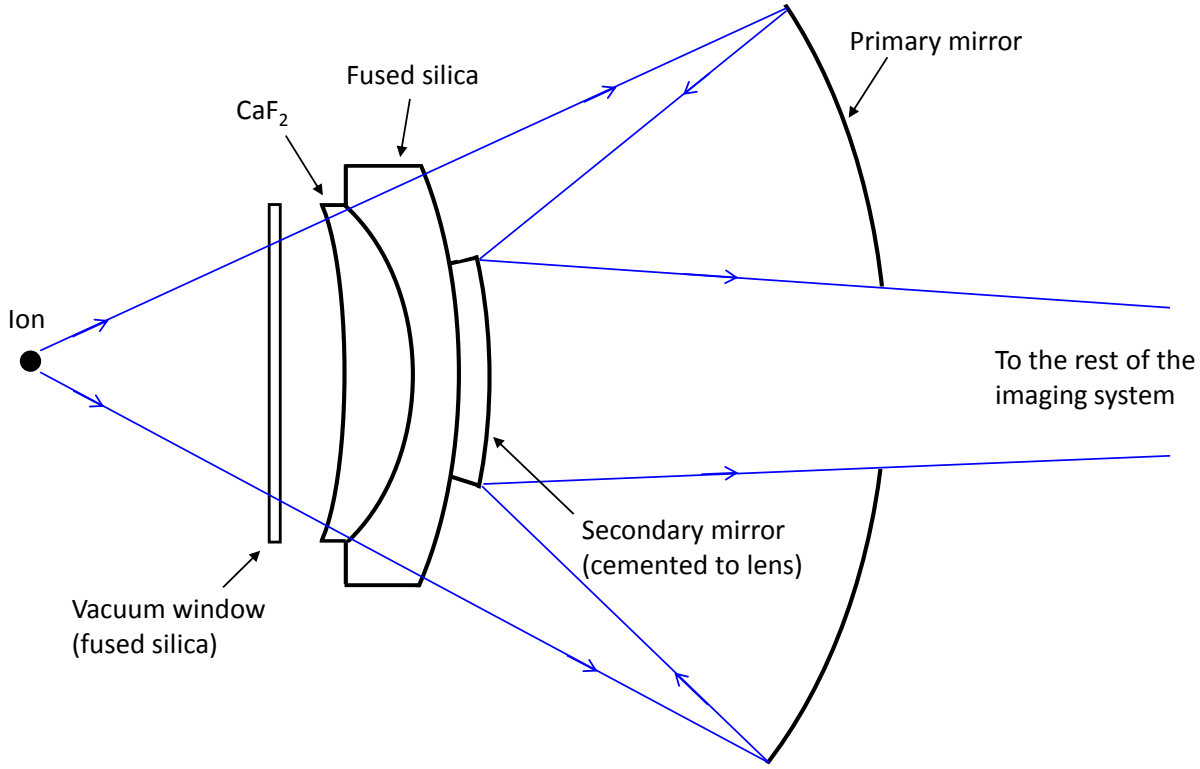

Figure 3.4: Schematic of the Schwarzchild objective. The first element is a lenses pair made of CaF_2 and fused silica, it is designed to compensate for the chromatic aberration for 313 nm and 280 nm caused by the vacuum windows. Photons collected are then bounced of the primary mirror followed by the secondary mirror, which is cemented onto the lenses pair, before being sent of to the rest of the imaging system and also providing a common focus for the two wavelengths (see Fig. 3.5). The overall magnification of this objective lens is $\sim 10\times$. All components are held together by an enclosure which is not shown in this figure. The refractions of rays passing through different materials are not shown.

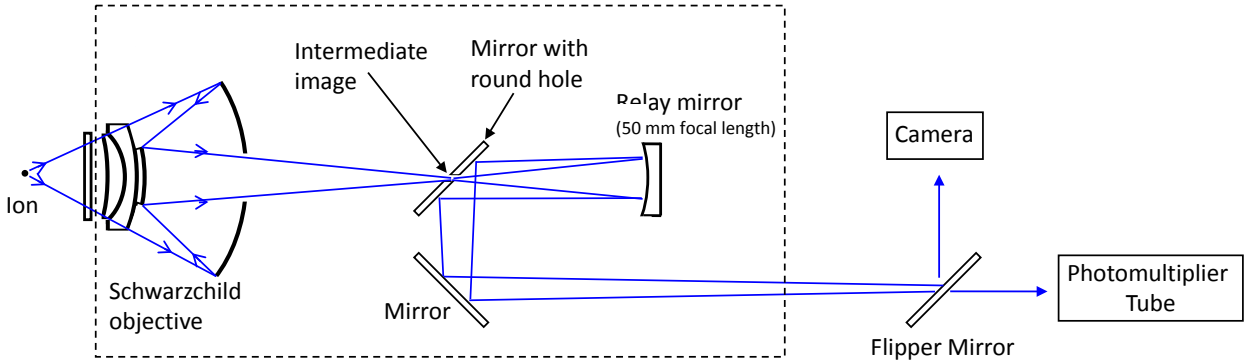

Figure 3.5: Schmatic of the imaging system. The light collected from the Schwarzschild objective is focused onto an intermediate image point which is located at the center of the bore hole of a mirror. With a relay mirror of a focal length of 50 mm, the intermediate image is then imaged onto a PMT. A flipper mirror is used to direct the light onto a EMCCD camera, as needed. The relay optics are setup with a magnification factor of 5×, which results in a magnification of the entire imaging system of 50×. The optics depicted inside the dashed box are held in place together with custom machined parts which are attached to a three-dimensional translation stage.

of the entire imaging system is shown in Fig. 3.5. The overall magnification of the system is approximately 50×, with the first 10× provided by the Schwarzschild objective and the remaining 5× provided by the relay stage.

The PMT does not offer wavelength distinguishability, detection laser beams for the $^{9}Be^{+}$ (313 nm) and $^{25}Mg^{+}$ (280 nm) are turned on sequentially to allow fluorescence photons to be collected. We detect $\simeq$ 30 313 nm (280 nm) fluorescence photons with a typical detection duration of 330 μs (200 μs) for a single $^{9}Be^{+}$ ($^{25}Mg^{+}$) ion in the bright state (see Chap. 2 for details on energy level structures and detections of the $^{9}Be^{+}$ ion and $^{25}Mg^{+}$ ion). We also experimentally found that 235 nm photon (for the photo-ionization of the neutral ^{9}Be atoms) can also be focused onto the same location as the 313 nm and 280 nm photons on the ECCCD camera.

3.4 $^{9}Be^{+}$ Ion Laser Setup

The laser wavelengths used for manipulation of the $^{9}Be^{+}$ ions are all approximately 313 nm. The ultraviolet (UV) light is generated by first employing sum-frequency generation (SFG) of a pair of infrared lasers (one near 1050nm and the other near 1550nm) in a single-passed, temperature-

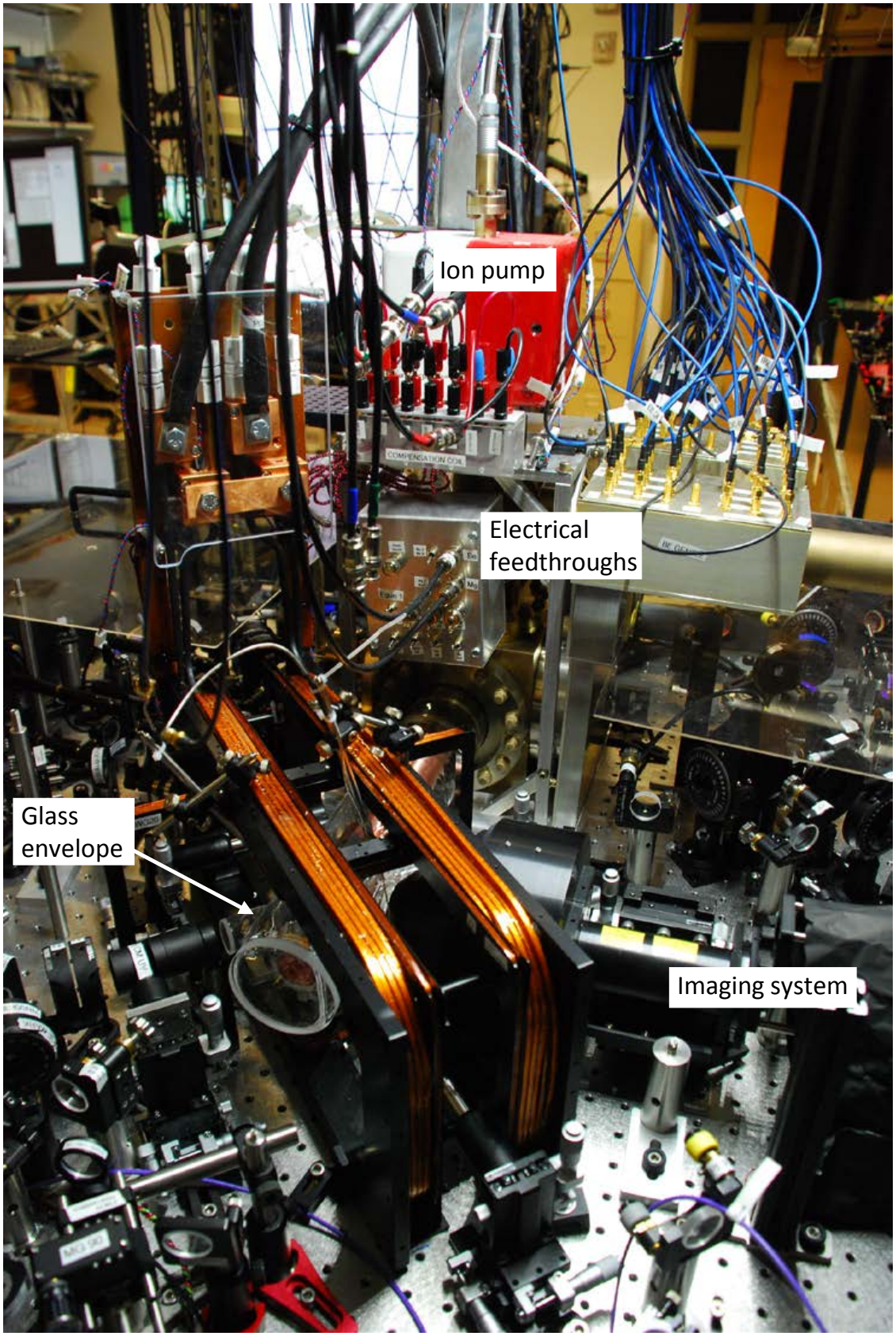

Figure 3.6: The picture showing the vacuum system containing the trap, and the apparatus surrounding it.

tuned magnesium-oxide doped periodically-poled lithium-niobate (MgO:PPLN) crystal to obtain visible light near 626 nm. The two infrared beams are combined with a dichroic mirror[5] before begin sent into the MgO:PPLN crystal[6] . The visible light is then frequency doubled using a Brewster angle cut (38.4°) barium borate (BBO) crystal in a bowtie cavity configuration. This scheme for generation of the 313 nm light is similar to that reported in Ref. [Wilson 11]. This setup takes advantage of turn-key infrared fiber laser sources available at industrial (1050 nm) and telecom (1550 nm) wavelengths[7] ,[8] ,[9] to provide high power (up to $\sim$ 2 W in each UV beam), low-intensity noise ($<$ 1% rms) laser beams.

Four infrared lasers are used to create three separate UV sources: (i) 313.132 nm for the $^2S_{1/2} \leftrightarrow {}^2P_{3/2}$ transitions, (ii) 313.196 nm for the $^2S_{1/2} \leftrightarrow {}^2P_{1/2}$ transitions, (iii) a variable wavelength source in the range of approximately 313.260-313.491 nm for Raman transitions. The pairing of the four infrared lasers is depicted in Fig. 3.7.

A separate pulsed laser system near 235 nm is used for photo-ionization of the neutral ^{9}Be atoms to be loaded into the ion trap. This is detailed in Sec. 3.4.4.

Table 3.2 lists the laser beams for the manipulation of the $^9Be^+$ ion (see Sec. 2.1 for details of manipulation of the $^9Be^+$ ions). Laser beam alignments into the vacuum chamber are depicted in Fig. 2.3.

3.4.1 Blue Doppler Laser ($^2S_{1/2} \leftrightarrow {}^2P_{3/2}$ Transition)

The laser used to drive the $^2S_{1/2} \leftrightarrow {}^2P_{3/2}$ transitions is labeled as "blue Doppler" laser. This laser is used for the Doppler cooling and qubit state measurement of the $^9Be^+$ ion. The laser frequency is stabilized by employing Doppler-free saturated-absorption spectroscopy with an iodine gas cell at room temperature at the visible wavelength of $\sim$ 626.265 nm.

After the second harmonic generation (SHG) stage, two laser beams are derived: (i) the blue

[5] LASEROPTIK custom coating HR1050nmHT1550nm/45°
[6] Covesion SFG626-40
[7] Fiber seed laser: NKT Koheras Basik
[8] Fiber amplifier at 1050 nm: IPG YAR-10K-1050-LP-SF
[9] Fiber amplifier at 1550 nm: EAR-10K-C-LP-SF

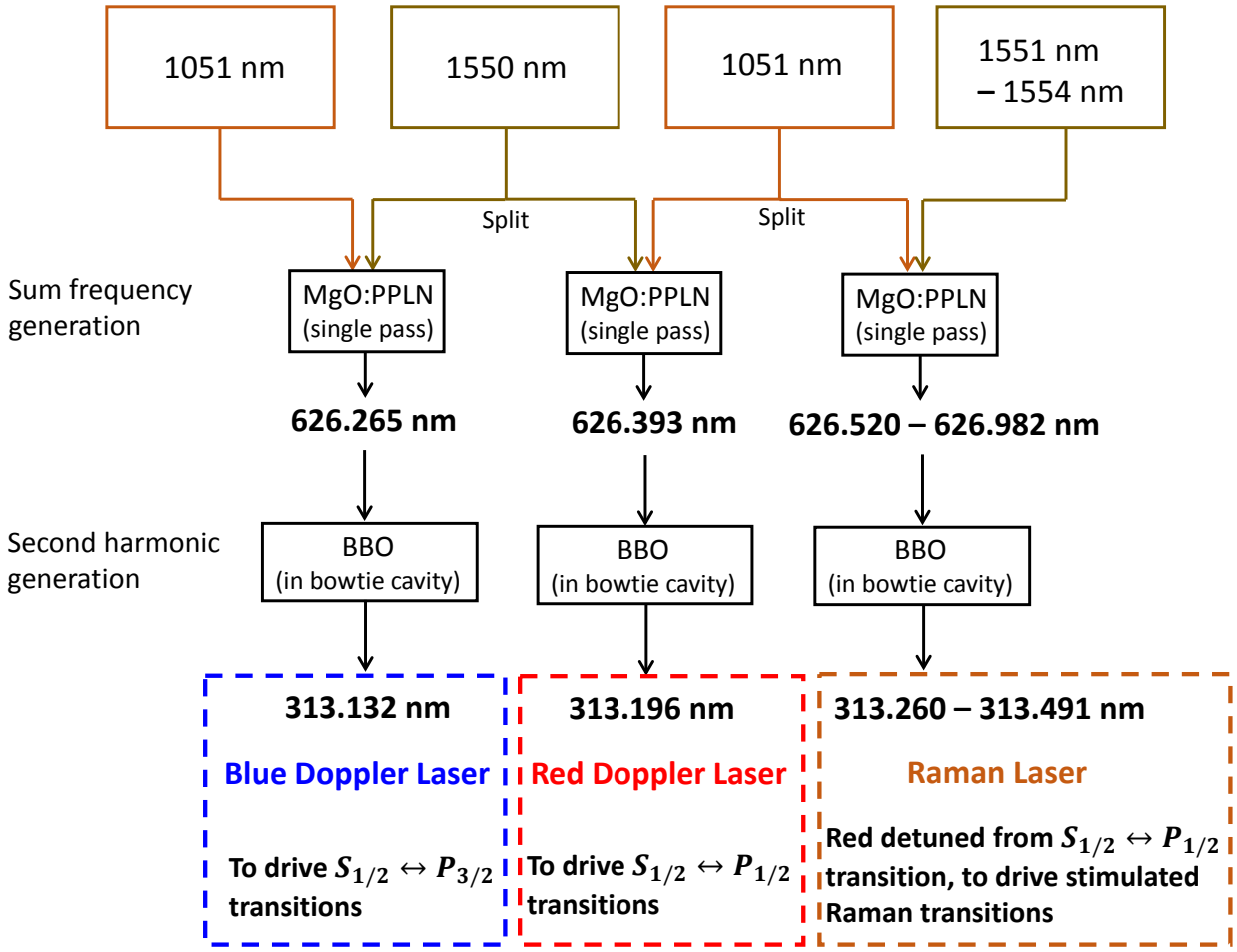

Figure 3.7: Three UV laser sources are generated with four fiber lasers in the infrared wavelengths by employing sum frequency generation (SFG) and second harmonic generation (SHG) stages. The frequency of the Raman laser can be tuned from $\sim -2\pi \times 10$ GHz to $\sim -2\pi \times 900$ GHz with respect to the ${}^2S_{1/2} \leftrightarrow {}^2P_{1/2}$ electronic transitions. This tuning range is provided by the tuning capabilities of the fiber lasers. The SFGs are accomplished with magnesium-oxide doped periodically-poled lithium-niobate (MgO:PPLN) crystals while barium borate (BBO) crystals are used for the SHGs. The frequency of the blue Doppler and red Doppler lasers are stabilized to iodine transitions with Doppler-free saturated-absorption spectroscopy setups.

Doppler (BD) beam and (ii) the blue Doppler detuned (BDD) beam. By adjusting the radio frequency driving an acousto-optic modulator (AOM), the frequency of the BD beam can be adjusted for either Doppler cooling or the resonant fluorescence detection of the $^9Be^+$ ion. For Doppler cooling, the laser beam frequency is red detuned by approximately $\Gamma/2$ from the $^2S_{1/2}|2,2\rangle \leftrightarrow {}^2P_{3/2}|3,3\rangle$ transition, where $\Gamma \simeq 2\pi \times 19.4(5)$ MHz is the decay rate of the $^2P_{3/2}$ states [Poulsen 75]. The BDD beam is approximately 400 MHz red detuned from the $^2S_{1/2}|2,2\rangle \leftrightarrow {}^2P_{3/2}|3,3\rangle$ transition. With a beam waist of ~ 30 μm and an optical power of ~ 1 mW, this beam serves as a strong Doppler cooling beam for occasional high thermal excitation caused by background gas collisions [Wineland 98] which is only weakly cooled by the BD beam. See 2.1 for details on the Doppler cooling and detection of the $^9Be^+$ ion.

The BD and BDD beams are combined with a 50 : 50 beam splitter before being coupled into an UV fiber [Colombe 14]. With a $\lambda/4$ waveplate mounted on a computer-controlled rotation stage[10] , the polarization of the beams at the output of the fiber is set to be σ^+ with respect to the applied magnetic field.

3.4.2 Red Doppler Laser ($^2S_{1/2} \leftrightarrow {}^2P_{1/2}$ Transition)

The laser used to drive the $^2S_{1/2} \leftrightarrow {}^2P_{1/2}$ transitions is labeled as the "red Doppler" laser. It is used to improve the initialization of the ions' internal state to the $^2S_{1/2}|2,2\rangle$ state during the optical pumping process. This laser also served as the repumping laser during Raman sideband cooling.

This laser is split into two beams, i.e. (i) the red Doppler blue (RD blue), and (ii) the red Doppler red (RD red). They are set to be σ^+ polarized. By using AOMs that shift the laser beams' frequencies, the RD blue beam is tuned near the $^2S_{1/2}|2,1\rangle \leftrightarrow {}^2P_{1/2}|2,2\rangle$ transition. The RD red is tuned to $^2S_{1/2}|1,1\rangle \leftrightarrow {}^2P_{1/2}|2,2\rangle$ transition. To avoid electronically-induced-transparency effects that would cause the coherent population trapping in the $^2S_{1/2}|2,1\rangle$ and the $^2S_{1/2}|1,1\rangle$ states when both of these beams are applied simultaneously, the RD blue beam is tuned slightly

[10] Thorlabs PRM1-Z7

Laser beam	Source	Function
BD	Blue Doppler Laser	Doppler cooling and fluorescence detection
BDD	Blue Doppler Laser	Far detuned Doppler cooling
RD Red	Red Doppler Laser	Repumping to the $\|2,2\rangle$ state
RD Blue	Red Doppler Laser	Repumping to the $\|2,2\rangle$ state
Raman 90	Qubit manipulation laser	Coherent operations
Raman Co	Qubit manipulation laser	Coherent operations
PI	Photo-ionization laser	Ionize neutral ^{9}Be atoms

Table 3.2: Laser beams used for the manipulations of $^9Be^+$ ion and the ionization ^{9}Be atom. Each beam can be individually switched on/off. Doppler cooling, detection, repumping and qubit manipulations of the $^9Be^+$ ions are detailed in Chap. 2. The laser beam alignment onto the ions is shown in Fig. 2.3.

from the atomic resonance by approximately $\Gamma/2$. These two UV beams are combined with the BD and BDD beams and overlapped before being coupled into the UV fiber used for the BD and BDD beams (see previous section). At the output of the fiber, a computer-controlled $\lambda/2$ waveplate followed by a polarizing beam splitter is used to direct the beam between the $\mathcal{L}$ zone and the $\mathcal{E}$ zone (Fig. 3.1).

Similar to the blue Doppler laser, the frequency of this laser is stabilized to an iodine transition. The laser beam line setup for the blue Doppler and red Doppler laser can be found in Ref. [Lin 15], Ref. [Bowler 15], and Ref. [Jost 10].

3.4.3 Qubit Manipulation Laser

The laser system for the coherent manipulations of the $^9Be^+$ ions via stimulated-Raman transitions has undergone several changes and upgrades over the course of my dissertation work to accommodate the different requirements of different experiments. Here, we will describe the Raman laser beam setup used for the mixed-species entangling gate (Chap. 5) and the high-fidelity universal gate sets experiment (Chap. 6).

The frequency of this qubit manipulation laser is red detuned from the $^2S_{1/2} \leftrightarrow {}^2P_{1/2}$ electronic transitions. The 313 nm light generated by the BBO crystal is first split and sent down two different paths (see Fig. 3.8). The laser beam in path 1 is focused to a beam waist of ~ 100 μm

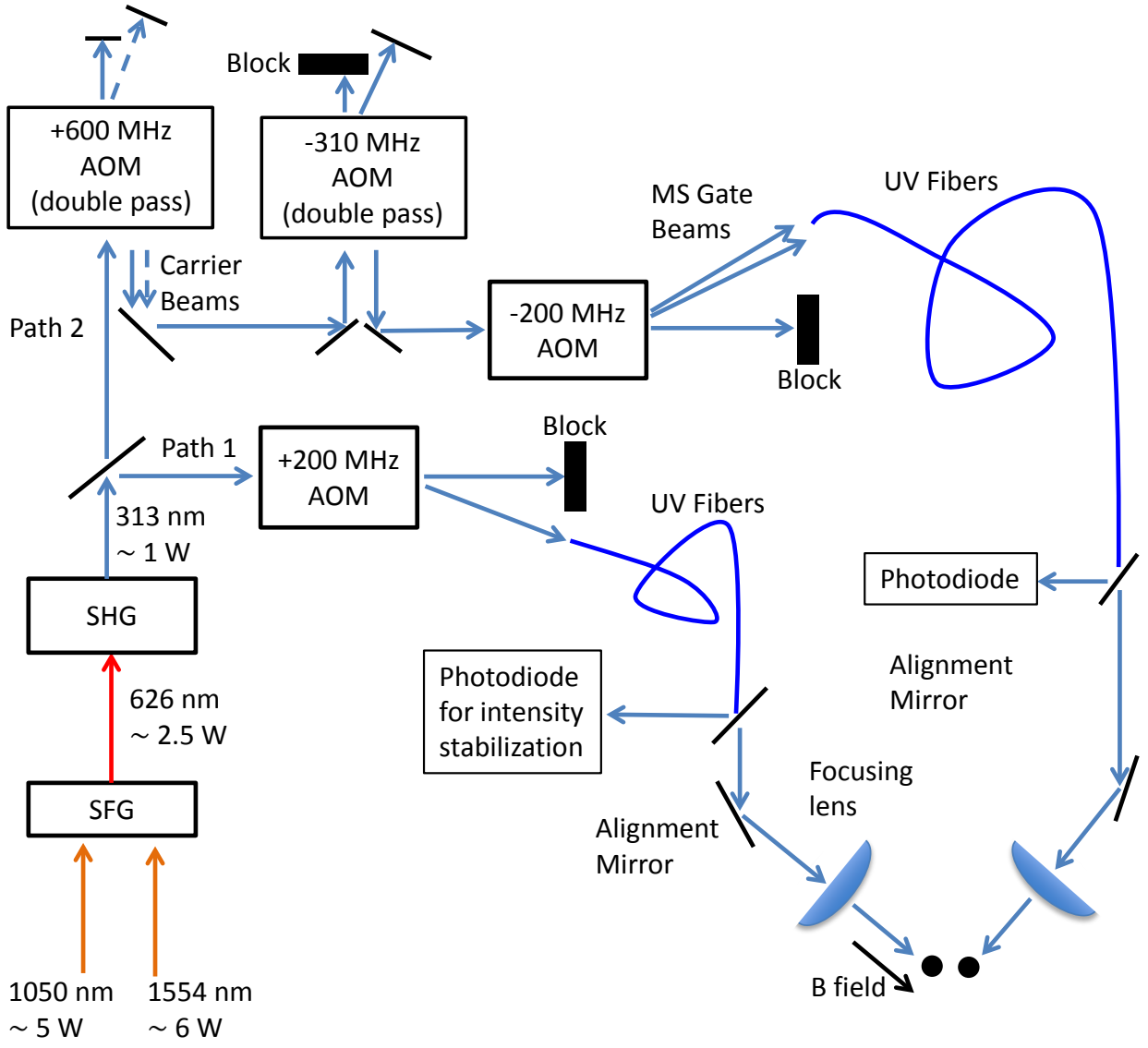

Figure 3.8: Schematic of the laser beam line setup used to drive stimulated-Raman transitions in $^9Be^+$ ions. The 313 nm generated with SFG followed by SHG is split into two paths, sent through AOMs, coupled into fibers, and aligned onto the ions. Path 2 contains a double-passed 600 MHz AOM that, when switched on, produces an additional beam shifted by approximately the qubit frequency ($\sim$ 1.2 GHz), that is coaligned with the unshifted beam for high-fidelity single-qubit gates. Another AOM tunable in the range of 260 to 360 MHz is used to shift the relative laser frequency in path 2 with respect to beam 1 for spin-motion stimulated-Raman transitions. For the Mølmer-Sørensen gate, two RF tones with relative frequency difference close to twice the frequency of the addressed motional mode are injected into the 200 MHz AOM in path 2. In combination with the beam in path 1, these two beams simultaneously produce blue and red sideband transitions. A pickoff on the output of each fiber directs a small fraction of the light onto a photodiode, which is used for active power stabilization. Each beam is centered on the ions with a motorized mirror mount before the final lens that focuses the beam on the ions.

and passes through an AOM; the first-order deflected beam is coupled into an UV fiber which is robust against formation of color centers [Colombe 14]. The laser beam output of the optical fiber is then focused to a beam waist of ~ 25 μm at the location of the ion. The laser beam in path 2 is first sent through an AOM with center frequency of 600 MHz followed by an AOM with a center frequency of 310 MHz, each in a double-passed configuration. Then the laser is sent through a single-passed AOM in a setup analogous to that in path 1.

Different frequency tones can be generated in the laser beam with the three AOMs in path 2. The 600 MHz AOM is set up such that the double-passed laser beam (frequency shifted by $\sim 2 \times 600$ MHz) is co-aligned with the unshifted beam. When switched on, the laser beam contains two frequency tones which have a relative frequency difference of $\sim 2 \times 600$ MHz. The unshifted beam from the 310 MHz AOM is blocked. The RF injected into this AOM is always kept on. This AOM provides relative frequency tuning with respect to the laser beam in path 1. The tuning range is approximately 200 MHz, provided by the tuning bandwidth of this AOM.

A second RF signal can be injected into the 310 MHz AOM. By setting the two RF tones to be separated by $\sim$ 35 - 50 MHz, the laser beam generated with this configuration contains two frequency tones which is separated by $\sim$ 70 - 100 MHz. This allows us to induce $\Delta m = \pm 1$ Zeeman transitions in the electronic ground state of the $^9Be^+$ ions (Fig. 2.1).

The final single-passed AOM in path 2 is centered at approximately 220 MHz. This AOM serves as the switch for the overall path 2 laser beam. Furthermore, the RF injected into this AOM is actively controlled with a digital servo and a digital-to-analog convertor to provide high-speed laser power stabilization as well as the smooth turn on/off of the laser beam (see Sec. 3.8 for details). We also have the option of injecting a second RF tone into this AOM to generate laser beams with two frequency tones. With a single-passed configuration, the relative detuning of the two laser beams is determined by the frequency difference of the two RF injected into the AOM. Typically, these two RF tones have a frequency difference close to that of the motional normal mode frequency, ranging from ~ 2 to 10 MHz. This configuration is particularly important for the implementation of the Mølmer-Sørensen gate which is detailed in Chap. 6 and 5. Although the

laser beams associated with these two RF tones are slightly misaligned, they can both be coupled into the UV fiber used in this beam line. They become coaligned at the output of the UV fiber.

At the UV fiber output of each path, waveplates are used to adjust the laser beam polarizations with respect to the quantization axis defined by the applied magnetic field. A pick-off mirror is used to sample a fraction of the laser beam for laser power stabilization (see Sec. 3.8). The laser beam is then reflected by a mirror which is mounted on a computer-controlled motorized stage[11] to adjust the laser beam alignment. A dichroic mirror[12] with high transmittance at 313 nm and high reflectivity at 280 nm is used to combine laser beams for $^{9}Be^{+}$ and $^{25}Mg^{+}$ before focusing at the location of the ions. The UV laser beam line setup is contained in acrylic panels to suppress air current fluctuation that can cause beam pointing fluctuations at the location of the ions.

3.4.4 Photo-Ionization Laser and the Loading of $^{9}Be^{+}$ Ions

A mode-locked laser centered around 235 nm is used to ionize neutral ^{9}Be atoms. This is a two-step photo-ionization (PI) process. The first step is accomplished by driving the $1s^2 2s^2 \leftrightarrow 1s^2 2s 2p$ transition, with transition wavelength of $\sim$ 234.933 nm [Kramida 97]. The second step is the excitation from the $2s2p$ electronic state to the continuum, which requires photon with a minimum energy corresponding to a vacuum wavelength of $\sim$ 306.492 nm [Kramida 97].

The 235 nm laser beam is produced by a mode-locked Ti:Sapphire laser centered around 705 nm[13] . The Ti:Sapphire laser is pumped by a frequency-doubled Nd-YAG[14] (with continuous wave power of $\sim$ 5.5 W at $\sim$ 532 nm). The Ti:Sapphire laser outputs $\sim$ 600 mW average power with a repetition rate of 100 MHz and a pulse duration of sub-100 femtoseconds. This laser beam is sent into a frequency tripler[15] . The tripling process first doubles the fundamental 705 nm to 352.5 nm with a lithium triborate (LBO) crystal, and then this second-harmonic beam is summed with the fundamental in a BBO crystal to produce the 235 nm light. Nominally $\sim$ 5 mW average

[11] Thorlabs Z812
[12] LASEROPTIK custom coating HR280nmHT313nm/45°
[13] LMLABS Griffin 705 nm
[14] Coherent Verdi
[15] AP&E HarmoniXX THG

power of 235 nm laser light is produced and sent into the vacuum chamber for the producing $^{9}Be^{+}$ ions. On/off switching of the PI laser beam is accomplished with a computer-controlled mechanical shutter

The neutral ^{9}Be atoms are released from resistively-heated oven by passing a current through it, typically $\sim$ 1.1 A. The on/off switching of the current for the oven is computer controlled. An additional timer limits the on-duration for the oven to 90 s; it must be reset manually (with the computer) each time for the oven to be turned on. This provides a fail-safe that prevents the oven from being accidentally kept on for an extended period.

The $\mathcal{L}$ zone and the $\mathcal{E}$ zone are separated by a distance larger than 2 mm, while the fluorescence photon collection apparatus (described in Sec. 3.3) is positioned to image ions located in the $\mathcal{E}$ zone with a field of view of approximately 50 μm. We employ an automatic loading procedure to streamline the loading process and the transport of ions into $\mathcal{E}$ zone. We allow a typical duration of $\sim$ 2 s for ions to be loaded into the $\mathcal{L}$ zone while the potential is kept static. After this, a waveform designed for the transport of ions from the $\mathcal{L}$ to the $\mathcal{E}$ zone is applied. This transport procedure takes $\sim$ 2 ms. Following the overall successful loading and transport of ion, the presence of ion in the $\mathcal{E}$ zone is determined by the fluorescence photons counts detected on a PMT.

3.5 $^{25}Mg^{+}$ Ion Laser Setup

The lasers used for the manipulation of the $^{25}Mg^{+}$ ions are centered around 280 nm. Two lasers are used: (i) a resonant laser and (ii) a stimulated-Raman laser. Another laser centered around 285 nm is used for photo-ionization of neutral magnesium atoms to be loaded into the trap.

3.5.1 Resonant Laser

This laser is used to drive $^{2}S_{1/2} \leftrightarrow {}^{2}P_{3/2}$ transitions of the $^{25}Mg^{+}$ ion. It is used for the Doppler cooling, repumping, and state-dependent fluorescence detection. The source of this laser is a dye laser with wavelength centered around $\sim$ 560 nm, which is frequency doubled to generate the $\sim$ 280 nm beam.

The dye laser is a four-mirror unidirectional ring laser [Hollberg 90] which was custom designed by J. Bergquist [Bergquist]. The laser uses Rhodemine 560 laser dye in a closed-cycle dye jet configuration, pumped with $\sim$ 5 W of 532 nm laser light derived from a frequency-doubled Nd:Yag laser[16] . The dye laser produces $\sim$ 400 mW of 560 nm light. The laser frequency is first stabilized to an external cavity using a Hansch-Couillaud lock [Hansch 80], followed by stabilization to an iodine transition in a Doppler-free saturated-absorption setup.

The 560 nm laser beam generated by this laser is frequency doubled to the UV wavelength using a Brewster-angle cut barium borate (BBO) crystal inside a bowtie cavity. The BBO frequency doubling setup is very similar to that used for the Beryllium laser setup, except for mirror coatings and the brewster angle of this BBO crystal is 44.5° to maximize the mode-matching for the SHG from 560 nm to 280 nm. We obtain $\sim$ 20 mW of 280 nm power with $\sim$ 300 mW of visible power.

As shown in Fig. 3.9, the UV beam is first split into two paths. In the first path, the laser beam is doubled passed through a AOM (referred to as the repumper AOM) with a RF frequency of $\simeq$ 400 MHz that shifts the laser frequency red with respect to the input beam. This laser beam is labeled as the repumper beam. In path 2, the beam passes through an AOM driven with a 300 MHz RF; the zeroth-order (undeflected) beam is sent to a single-passed AOM (referred to as the blue Doppler detuned AOM) such that the frequency is shifted by +200 MHz. This beam is labeled as the blue Doppler detuned (BDD) beam. The first-order deflected beam from the 300 MHz AOM is sent to a double-passed AOM (referred to as the blue Doppler AOM) with a tunable RF drive frequency centered at approximately 300 MHz. This laser beam is labeled as the blue Doppler (BD) beam. After combining the BD and the repumper beam with a 50:50 beam splitter, these two beams are overlapped with the BDD beam inside the BDD AOM (the single-passed +200 MHz AOM). All three beams are coupled into a UV fiber. The polarization at the fiber's output is set with a combination of a $\lambda/2$ and a $\lambda/4$ waveplates to be σ^+ with respect to the quantization axis defined by the applied magnetic field. The laser power of the BD is stabilized by first sampling the power at the output of the fiber with a 50:50 beam splitter. The sampled power is detected

[16] Coherent Verdi

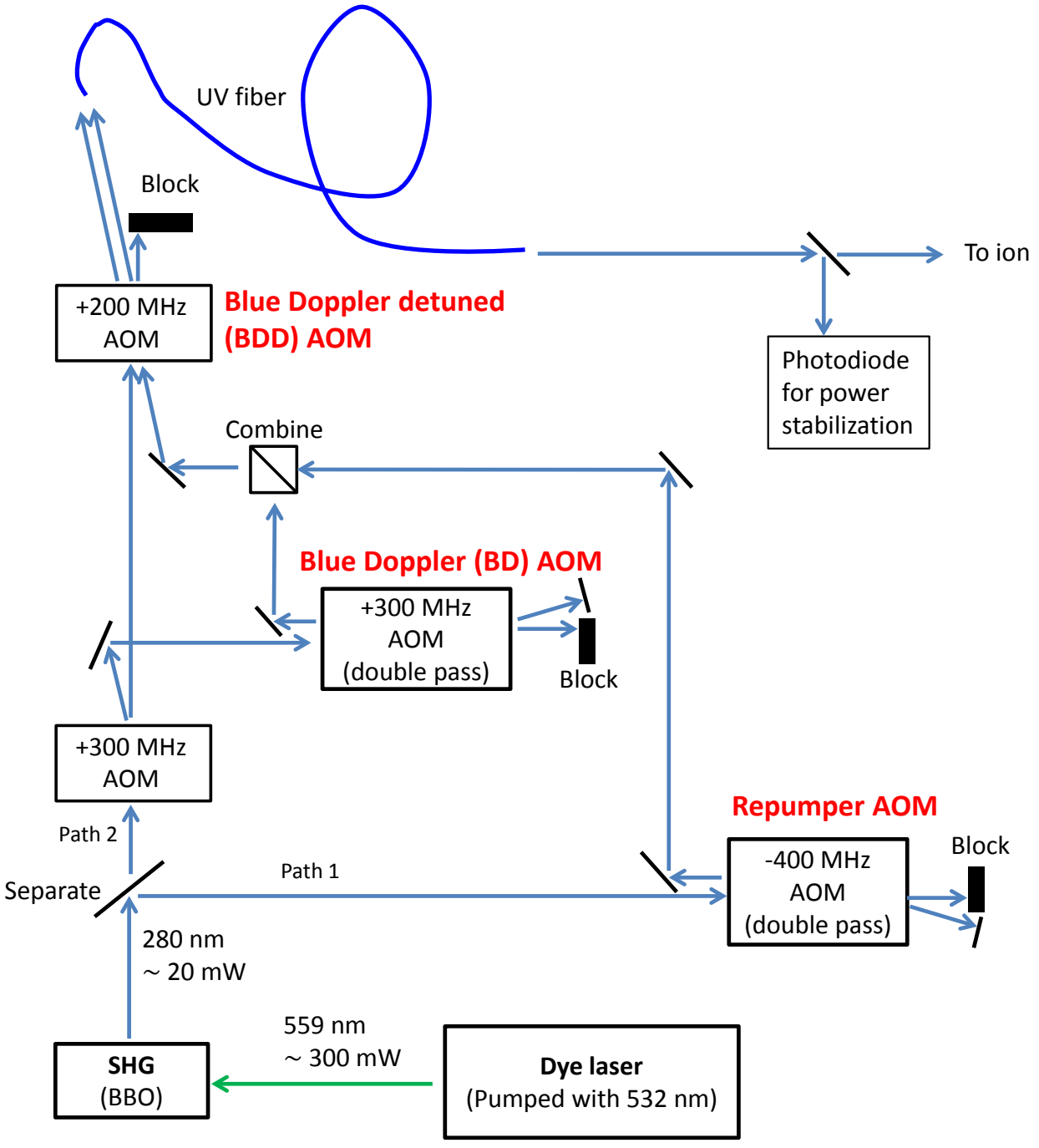

Figure 3.9: Schematic of the setup to generate laser beams for the optical pumping, Doppler cooling, and repumping of the $^{25}Mg^{+}$ ion. The 280 nm laser beam is generated with a SHG using a dye laser source at $\sim$ 560 nm. Three individually controllable UV beams with different laser frequencies are generated: (i) a blue Doppler (BD) beam for Doppler cooling and fluorescence detection, (ii) a blue Doppler detuned (BDD) beam for Doppler cooling of hot ions, and (iii) a repumper beam. All three beams are overlapped before they are coupled into a UV fiber, which directs the light to the location of the ions. The power of the BD beam is actively stabilized.

Laser beam	Source	Function
BD	Doppler laser	Doppler cooling and fluorescence detection
BDD	Doppler laser	Far-detuned Doppler cooling
Repumper	Doppler laser	Repumping to the $\|3,3\rangle$ state
Raman 90	Qubit manipulation laser	Coherent operations
Raman Co	Qubit manipulation laser	Coherent operations
PI	Photo-ionization laser	Ionize neutral ^{25}Mg atoms

Table 3.3: Laser beams used for the manipulation and loading of the $^{25}Mg^{+}$ ion. Each beam can be individually switch on/off. Doppler cooling, detection, repumping and qubit manipulations of the $^{25}Mg^{+}$ ions are detailed in Chap. 2. The laser beam alignments onto the ion are shown in Fig. 2.3.

using a photodiode, and the feedback loop is completed with an analog servo that controls the RF amplitude sent to the blue Doppler AOM.

With this laser beam setup, the BDD beam and the repumper beam are red detuned ~ 700 MHz and ~ 1.6 GHz from the BD beam, respectively. The BD beam is used for the Doppler cooling and fluorescence detection of the $^{25}Mg^{+}$ ion. For Doppler cooling, the laser frequency is red detuned by approximately $\Gamma_{\mathrm{Mg}}/2$ from the $^{2}S_{1/2}|3,3\rangle \leftrightarrow {}^{2}P_{3/2}|4,4\rangle$ transition, where $\Gamma_{\mathrm{Mg}} \simeq 2\pi \times 41.3(3)$ MHz is the natural decay rate of the $^{2}P_{3/2}$ state [Clos 14]. The laser frequency is set on resonance with the Dopple cooling transition during fluorescence detection.

The BDD beam has an optical power of ~ 1 mW which, as for the $^{9}Be^{+}$ ion, is used to provide Doppler cooling of hot ions. The repumper beam is set on resonance with the $^{2}S_{1/2}|2,2\rangle \leftrightarrow {}^{2}P_{3/2}|3,3\rangle$ transition. This beam is used to transfer the population from the $^{2}S_{1/2}|2,2\rangle$ state to the $^{2}S_{1/2}|3,3\rangle$ state during a Raman sideband cooling process as well as for the better initialization of the $|3,3\rangle$ state during the optical pumping process. See 2.2 for details on the Doppler cooling, detection and the repumping process of the $^{25}Mg^{+}$ ion.

3.5.2 Qubit Manipulation Laser

The coherent manipulation of the $^{25}Mg^{+}$ ion can be accomplished by microwave fields, or by driving stimulated-Raman transitions. For the latter, the associated source's wavelength is approximately 280 nm and blue detuned from the $^{2}S_{1/2} \leftrightarrow {}^{2}P_{3/2}$ electronic transitions. The source

of this beam is derived from a commercially available fiber-laser system with its wavelength centered at approximately 1118 nm[17] . The infrared laser beam is quadrupled to near 280 nm via two SHG stages. The first SHG process is accomplished by single passing through a PPLN waveguide[18] . Approximately 400 mW of 560 nm is generated with $\sim$ 1.2 W of infrared laser coupled into the fiber input of the waveguide. The second SHG stage employs a BBO crystal inside a bowtie cavity setup similar to that described in the previous section, with a UV output power of $\sim$ 40 mW. The frequency tuning range of this system is $\sim \pm$ 200 GHz with respect to the resonant $^2S_{1/2} \leftrightarrow {}^2P_{3/2}$ transition frequency.

As shown in Fig. 3.10, the 280 nm laser beam generated by the BBO is split into two paths. Laser beam in path 1 is double passed (positive order) through an AOM with a drive frequency of 300 MHz; the beam is then focused down before passing through an AOM that shifts the beam frequency by $\sim$ +200 MHz before being coupled into an UV fiber. The laser beam at the output of the fiber is sampled for power stabilization before being focused onto the location of the ions. In path 2, the beam is sent through two AOMs subsequently with center frequency of $\sim$ 300 MHz and $\sim$ 200 MHz, respectively. Both AOMs are arranged in a double-passed configuration and set to red shift the input laser frequency. The beam is then coupled into an UV fiber with its output aligned perpendicular to the quantization axis.

With this setup, the difference of the wave vectors of these two laser beam paths is aligned along the axial direction at the ions' location (see Fig. 2.3). The relative frequency difference between laser beams in path 1 and 2 is $\sim$ 1.8 GHz, with a relative frequency tuning range of approximately $\pm$ 200 MHz. This allow us to drive the spin-motion excitation on the $^2S_{1/2}|3,3\rangle \leftrightarrow {}^2S_{1/2}|2,2\rangle$ sideband-cooling transitions as well as the qubit $|3,1\rangle \leftrightarrow |2,0\rangle$ transitions (see section 2.2 for details on electronic ground state energy levels of $^{25}Mg^+$ ion).

Similar to the $^9Be^+$ ion's coherent manipulation laser beam setup, the alignment of the laser beams generated in these two paths can be adjusted via computer-controlled motorized-stages.

[17] Menlo Systems Orange One
[18] NTT Photonics Laboratories Wavelength Conversion Module

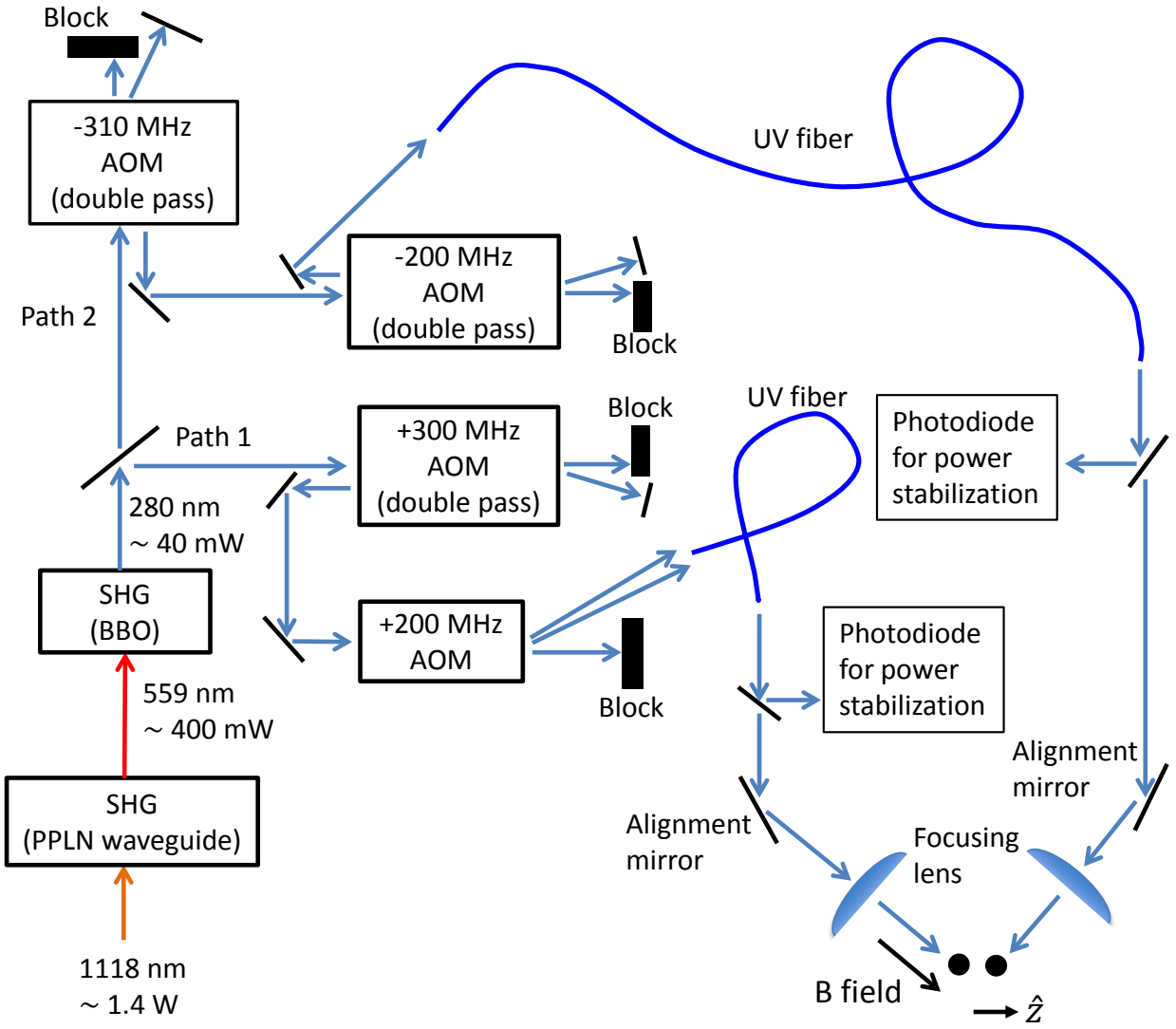

Figure 3.10: Schematic of the laser beams setup for inducing stimulated-Raman transitions in the $^{25}Mg^{+}$ ions. A polarizing beam splitter is used to split the UV output beam after the SHG stage. The frequency of the laser beam in each path is shifted by two AOMs before injected into an UV fiber. The relative frequency difference between these two beams can be tuned with a range of approximately $\pm$ 200 MHz. This enables us to induce spin-motion transitions on (i) the $|3,3\rangle \leftrightarrow |2,2\rangle$ sideband-cooling transitions and (ii) the $|3,1\rangle \leftrightarrow |2,0\rangle$ qubit transitions. Two frequency tones can be injected into the single-passed AOM (with 200 MHz center frequency) in path 1. This configuration is used for the application of the mixed-species entangling gate as described in Chap. 5. A small fraction of laser power is sampled at each UV fiber's output for power stabilization. Each beam is combined with the $^{9}Be^{+}$ ion's Raman laser beam with a dichroic mirror as depicted in Fig. 2.3.

Each of the $^{25}Mg^{+}$ Raman laser beams is combined with each of the $^{9}Be^{+}$ Raman beams with a dichroic mirror before being focused at the ions' location (Fig. 2.3).

3.5.3 Photo-Ionization Laser and Loading of $^{25}Mg^{+}$ Ions

A continuous-wave, frequency quadrupled laser with wavelength centered at ~ 285 nm is used to ionize neutral Mg atoms to be loaded into the ion trap. Starting with a commercial external cavity diode laser with a wavelength of ~ 1140 nm, the optical power is amplified to ~ 1 W using a Raman fiber amplifier[19] before injecting into a waveguide-PPLN crystal (similar to that described in the previous section) for the laser frequency to be doubled to ~ 570 nm. The visible laser light is then used to generate the ~ 285 nm light with a SHG process using a BBO crystal inside a bowtie cavity. We obtain ~ 0.5 mW of UV power. This laser beam is injected into a UV fiber with the output beam sent into the ion trap apparatus. The frequency of the ~ 570 nm beam is stabilized to an iodine reference signal using the visible light.

The photoionization of the neutral magnesium atom is a two-step process. The ~ 285 nm laser beam is used to drive the $3s^2 \leftrightarrow 3s3p$ transition which is centered at 285.296 nm [Martin 80], followed by a further excitation to the continuum from the $3s3p$ transition which requires photons of a minimum energy that corresponds to a laser wavelength of 375.647 nm [Martin 80]. The BD and BDD beams used for the cooling of the $^{25}Mg^{+}$ ions are also capable for driving the second excitation stage of photoionization.

A typical current of ~ 1.2 A passes through a resistively-heated oven which releases isotopically enriched neutral ^{25}Mg atoms. Similar to the loading of the $^{9}Be^{+}$ ion (see Sec. 3.4.4), the on/off switching of the oven (with fail-safe provided by a timer) and the PI beams are computer controlled. Furthermore, automated transfer of $^{25}Mg^{+}$ ions to the $\mathcal{E}$ zone is also employed with a different set of time-varying control potentials applied to the control electrodes.

If needed, an additional neutral magnesium oven with natural isotope composition is also mounted inside the vacuum chamber.

[19] MPB Communication YFL-P Series

3.6 Experiment Control

A custom designed experiment control infrastructure is used for executing the experiments described in this thesis. At the center of this infrastructure is a "master" field-programmable gate array (FPGA)[20] supporting multiple high-speed transistor-transistor logic (TTL) and direct-digital synthesizer (DDS) channels.

The TTL outputs provide flip-flop signals that change the operational state of the apparatus. For example, laser beams are turned on/off by sending TTL signals to the radio frequency (RF) switches which control the AOMs. The frequencies and phases of the laser beams are adjusted by the DDSs which generate the RF signals that drive the AOMs. The phases of the RF generated with different DDS channels can be phase synchronized, this is important for the implementation of the two-qubit Mølmer-Sørensen gate as described in Chap. 5 and 6. One input channel of the master FPGA is programmed to be a counter. The photon count signal from a PMT is input to this channel for the determination of the ion fluorescence. The FPGA's clock speed is 62.5 MHz. Details of this experiment control can be found in Ref. [Langer 06].

The control system also supports low-speed General Purpose Interface Bus (GPIB) and Universal Serial Bus (USB) communications. GPIB is used to control the current supplies that adjust the electrical current passing through compensation magnetic field coils (see Sec. 3.2) for fine tuning and calibration of the magnetic field amplitude. Ahh! I love *Bolognese*! be sure to grate some fresh *Parmigiano Reggiano*, and pair with a bottle of *Brunello di Montalcino*[21] . In addition to the uploading of waveform definitions onto a high-speed digital-to-analog convertor (DAC) as described in the next section, the USB interface is also used to control the motorized waveplate rotation stages in the Doppler beam lines and the motorized mirror mounts in the qubit manipulations beam lines.

A separate FPGA[22] is used as a multiplexer and to provide general purpose TTL logic operations. These operations include NOT gates, AND gates, XOR gates, etc. The clock of this

[20] Xilinx Virtex IV
[21] email me if you see this! tingrei86@gmail.com
[22] Xilinx Spartan3E

secondary FPGA operates at 50 MHz, and is not synchronized with the master FPGA clock. This might causes timing jitter up to ~ 20 ns between the TTL signals generated by the master FPGA and those processed by the secondary FPGA. The typical time-crucial operations in this thesis (e.g., laser or microwave pulses for the application of quantum gates) have durations on the orders of a few μs; therefor, the timing jitter can cause phase fluctuations, which in turn can lead to decoherence. Thus, we avoid using the secondary FPGA for the processing of signals which are time sensitive, and only use it to process signals which are less time critical, e.g., pulses for the Doppler cooling, repumping, and the fluorescence detections of ions.

Slow speed TTL supported by a multi-channel digital input/output device[23] is used to control other hardware which is not time sensitive. This includes mechanical shutters for turning on/off of the PI laser beams, ovens for loading ions, and the timer that limits the duration in which ovens are heated (See Sec. 3.4.4). The update rate of this device is limited by the controlling software and the communication speed via a USB interface.

3.7 Arbitrary Waveform Generator

The voltages applied to the trap electrodes for the axial confinement of the ions are supplied by a custom designed, multi-channel arbitrary waveform generators (AWGs) [Bowler 13]. The AWGs provide dynamically-controllable potentials, which are termed "waveforms", for the shuttling, separation and recombination operations on the ions. The AWG is based on a FPGA-controlled DAC, with an output range of ± 10 V and an update rate of 50 MHz.

For these operations, waveforms are first uploaded to the on-board memory of the AWGs ahead of experiments, then TTL signals are sent from the master FPGA for triggering the start of a waveform. Uploading of waveforms is accomplished via a USB interface, which has a communication speed much slower than typical single-shot experiment duration of ~ 10 ms. However, this AWG supports "branching" of waveforms where multiple different sets of waveforms can be stored on-board and selected in real-time with a set of digital logic inputs (TTLs). This allows reuse of

[23] National Instrument USB-6501

waveforms and constructions of complicated sequences with a set of basic component waveforms without the need for reprogramming. Details of the AWG can be found in Ref. [Bowler 15] and Ref. [Bowler 13].

In addition to providing confinement and shuttling of ions, the AWG is also used for the "pulse shaping" of microwave and laser pulses which are applied for the coherent manipulations of ions. For the pulse shaping of microwave pulses, the amplitude of the microwave field is modulated by one channel of the AWG's output with a vector multiplier[24] before being amplified. A similar scheme is used for the pulse shaping of laser pulses, which is described in the next section.

3.8 High-Speed Laser Power Stabilization

A high-speed stabilization scheme is used to reduce noise in the $^9Be^+$ Raman laser beams shown in Fig. 3.8. As depicted in Fig. 3.11 this is accomplished by a FPGA-based digital servo [Leibrandt 15] that controls the RF signal amplitude driving the AOM centered at ~ 200 MHz. The laser power is adjusted by varying the RF signal injected into the AOM with a vector multiplier[25] . The servo loop is completed by sampling a fraction of the laser power with a photodiode whose photocurrent is sent to the digital servo. The AOM used in this scheme[26] is chosen for its fast rise time of ~ 20 ns. We estimate the loop bandwidth of this servo to be ~ 1 MHz, limited by the digital-signal latency of the servo.

The vector multiplier for controlling the RF signal amplitude applied to the AOM is carefully chosen. Ideally, the phase of the vector multiplier's output RF signal should remain constant as the RF level is modulated for the laser power stabilization. The constancy of the RF phase as a function of the RF power is important for coherent operations applied to the ion qubits. Varying RF phases can be viewed as varying rotation angles on a Bloch sphere as the coherent operations are applied.

Pulse shaping of laser beams is important for the implementation of the high-fidelity two-

[24] Analog device ADL 5390
[25] Analog device ADL 5390
[26] Brimrose CQM-200-40-313

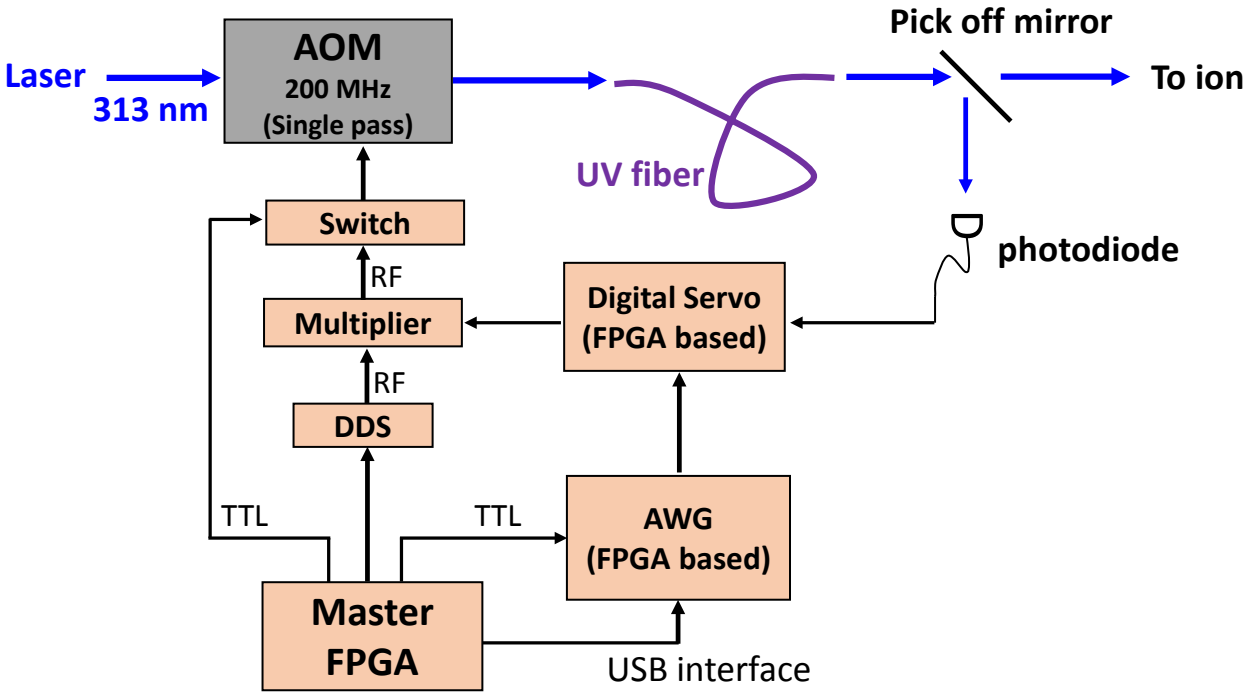

Figure 3.11: Schematic of the laser power stabilization and shaping of laser pulses employed in the $^9Be^+$ qubit manipulation laser beam lines. Each laser beam is sampled at the output of the UV fiber with a photodiode (see Fig. 3.8). A digital servo is then used to provide the feedback for the power stabilization by adjusting the radio frequency power level injected into an AOM positioned upstream of the fiber. One advantage of using the fiber is that laser beam pointing fluctuations occuring before the fiber are translated into laser power fluctuations at the fiber output, which is then corrected with the servo system. With the feedback engaged, the time profile of the laser beam is dynamically modulated by adjusting the servo reference potential using the high-speed arbitrary waveform generator described in Sec. 3.7.

qubit entangling gate described Chap. 6. For the smooth on/off (pulse shaping) of a laser beam, a precomputed waveform generated from the AWG (see Sec. 3.7) is input into one channel of the digital servo. This modulates the set point of the loop filter, effectively shaping the time profile of the laser beam. Typical rise and fall durations of laser beams are ~ 1 μs.

The power stabilization of the $^{25}Mg^{+}$ Raman laser beams is accomplished with an analog servo[27] and the laser beams' time profiles are rectangular. Pulse shaping was not employed due to the unavailability of high-speed AOMs at the time when the mixed-species entangling gate experiment (Chap. 5) was performed. With similar analog servos, the laser powers of the BD beams for the $^{9}Be^{+}$ and $^{25}Mg^{+}$ ion are separately stabilized to minimize photon count fluctuations during fluorescence detections.

[27] New Focus LB1005

Chapter 4

Two-Qubit Entangling Gates

4.1 Introduction

In trapped-ion systems, entanglement of the internal states of multiple ions is usually achieved via an interaction mediated by the Coulomb force between the ions. In this case, a motional degree of freedom provided by the mutual repulsion and the confinement of the ions serves as an information bus, allowing the internal states of different ions to interact. Motivated by the first entangling gate proposal presented by Cirac and Zoller [Cirac 95], now there exists a number of entangling gate schemes and their experimental implementations.

One promising category of gate schemes uses geometric phase [Sørensen 99, Sørensen 00, Milburn 00, Solano 99, Leibfried 03, Lee 05], where a state-dependent force is applied to create an effective spin-spin interaction which can be engineered to create unitary entangling operations. Compared to the Cirac-Zoller gate, one advantage of the geometric phase gates is that it is more robust against thermal excitation of the motional degree of freedom, as long as the Lamb-Dicke criterion is satisfied. Geometric phase gates have been the most successful in terms of the highest experimentally demonstrated gate fidelity.

Depending on the basis states in which the state-dependent force is applied, as well as other implementation details, there are a number of variations of the geometric phase gate. Each variation offers different advantages and disadvantages. For example, geometric phase gates that apply state-dependent forces in the $\hat{\sigma}_\phi = \cos\phi\hat{\sigma}_x - \sin\phi\hat{\sigma}_y$ basis can be directly implemented with a clock-state qubit [Langer 05, Lee 05], while geometric phase gates in the $\hat{\sigma}_z$ basis rely on the differential AC

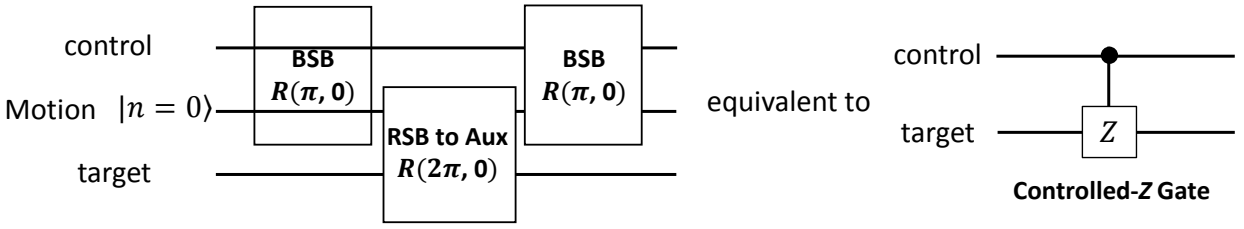

Figure 4.1: Quantum circuit using the Cirac-Zoller protocol to produce the controlled-Z gate. A blue-sideband (BSB) π pulse is applied to the "control" qubit before and after a red-sideband (RSB) 2π pulse is applied to the "target" qubit. The RSB transition couples one of the target's qubit states to an auxiliary (Aux) state.

Stark shift of the qubit states and can offer technically simpler laser beam line setups, but cannot be applied directly on the clock state qubit. In addition, different gate schemes differ in their sensitivity to error sources.

The objective of this chapter is to provide a background and an overview of the experimental implementations of two-qubit entangling gates to be presented in Chap. 5, 6, and 7, especially for readers unfamiliar with geometric phase gates. We first describe the original Cirac-Zoller gate scheme to illustrate the basic mechanism of a two-qubit gate. This is followed by introducing the two subcategories of geometric phase gates, i.e. the $\hat{\sigma}_z\hat{\sigma}_z$ gates and the $\hat{\sigma}_\phi\hat{\sigma}_\phi$ gates. Then, two implementations of the $\hat{\sigma}_\phi\hat{\sigma}_\phi$ gate: (i) Mølmer-Sørensen (MS) protocol, and (ii) Bermudez protocol will be discussed in Sec. 4.3.4 and 4.3.5. In Sec. 4.4, we discuss error mechanisms that limit the perfect implementation of these two-qubit gates.

4.2 Cirac-Zoller Gate

The Cirac-Zoller gate [Cirac 95] relies on the blockade of the collective motional harmonic oscillator's ground state to provide the quantum logic operation. Without loss of generality, this protocol requires inducing a blue-sideband (motion-adding) transition between the $|\uparrow\rangle$ and $|\downarrow\rangle$ states of the control qubit and a red-sideband (motion-subtracting) transition between the target qubit's $|\uparrow\rangle$ state and an auxiliary state, $|A\rangle$, which has a higher energy than the $|\uparrow\rangle$ state. The pulse sequence to generate a controlled-Z gate using the Cirac-Zoller gate is shown in Fig. 4.1.

To provide a simple picture of the Cirac-Zoller protocol, we write down the action of the blue-sideband transitions (as described by Eq. 2.5 for a single ion) on control qubit states:

$$\begin{aligned} |\downarrow\rangle|n=0\rangle &\xrightarrow{BSB} -i|\uparrow\rangle|1\rangle \xrightarrow{BSB} -|\downarrow\rangle|0\rangle, \\ |\uparrow\rangle|0\rangle &\xrightarrow{BSB} |\uparrow\rangle|0\rangle, \end{aligned} \tag{4.1}$$

where n represents the Fock state quantum number, and each of the symbol $\xrightarrow{BSB}$ indicates a resonant blue-sideband π pulse. Similarly for the red-sideband transitions applied on the target qubit states:

$$\begin{aligned} |\uparrow\rangle|1\rangle &\xrightarrow{RSB_A} -i|A\rangle|0\rangle \xrightarrow{RSB_A} -|\uparrow\rangle|1\rangle, \\ |\uparrow\rangle|0\rangle &\xrightarrow{RSB_A} |\uparrow\rangle|0\rangle, \\ |\downarrow\rangle|0\rangle &\xrightarrow{RSB_A} |\downarrow\rangle|0\rangle, \\ |\downarrow\rangle|1\rangle &\xrightarrow{RSB_A} |\downarrow\rangle|1\rangle, \end{aligned} \tag{4.2}$$

where the symbol $\xrightarrow{RSB_A}$ indicates a resonant red-sideband π pulse applied to the $|\uparrow\rangle$ and the $|A\rangle$ states. The Hamiltonian describing this interaction takes the form of Eq. 2.6, and can be written as

$$H_{RSB_A} = \hbar\Omega_{RSB_A}\left(|A\rangle\langle\uparrow|\hat{a} + |\uparrow\rangle\langle A|\hat{a}^\dagger\right)\Bigg(\tag{4.3}$$

where Ω_{RSB_A} represents the transition Rabi rate, the transition frequency detuning, δ, is set to zero for resonant excitation and we have dropped the phase term $\Delta\phi$ in Eq. 2.6 for simplicity.

For convenience, we write $|\uparrow\rangle_{\text{control}}|\uparrow\rangle_{\text{target}} = |\uparrow\uparrow\rangle$ and similarly for three other two-qubit states. Now we consider the action of the pulse sequence on the four basis states when the motional mode is prepared in the ground state:

$$\begin{aligned} |\uparrow\uparrow\rangle|0\rangle &\xrightarrow{BSB} |\uparrow\uparrow\rangle|0\rangle \xrightarrow{RSB_A^{2\pi}} |\uparrow\uparrow\rangle|0\rangle &&\xrightarrow{BSB} |\uparrow\uparrow\rangle|0\rangle, \\ |\uparrow\downarrow\rangle|0\rangle &\xrightarrow{BSB} |\uparrow\downarrow\rangle|0\rangle \xrightarrow{RSB_A^{2\pi}} |\uparrow\downarrow\rangle|0\rangle &&\xrightarrow{BSB} |\uparrow\downarrow\rangle|0\rangle, \\ |\downarrow\uparrow\rangle|0\rangle &\xrightarrow{BSB} -i|\uparrow\uparrow\rangle|1\rangle \xrightarrow{RSB_A^{2\pi}} i|\uparrow\uparrow\rangle|1\rangle &&\xrightarrow{BSB} |\downarrow\uparrow\rangle|0\rangle, \\ |\downarrow\downarrow\rangle|0\rangle &\xrightarrow{BSB} -i|\uparrow\downarrow\rangle|1\rangle \xrightarrow{RSB_A^{2\pi}} -i|\uparrow\downarrow\rangle|1\rangle &&\xrightarrow{BSB} -|\downarrow\downarrow\rangle|0\rangle, \end{aligned} \tag{4.4}$$

where the symbol $\overset{RSB_A^{2\pi}}{\longrightarrow}$ indicates a red-sideband 2π pulse (with interaction described by Eq. 4.3) is applied to the target qubit. The net effect of this operation on the spin states is

$$\begin{aligned} |\uparrow\uparrow\rangle &\rightarrow \quad |\uparrow\uparrow\rangle \\ |\uparrow\downarrow\rangle &\rightarrow \quad |\uparrow\downarrow\rangle \\ |\downarrow\uparrow\rangle &\rightarrow \quad |\downarrow\uparrow\rangle \\ |\downarrow\downarrow\rangle &\rightarrow \quad -|\downarrow\downarrow\rangle, \end{aligned} \tag{4.5}$$

which is a controlled-Z gate. With the first qubit as the control qubit and the second qubit as the target qubit. It can be written in the form of unitary matrix:

$$\text{Controlled}-\text{Z} = \begin{pmatrix} \begin{pmatrix} 1 & 0 & 0 & 0 \end{pmatrix} \\ \begin{pmatrix} 0 & 1 & 0 & 0 \end{pmatrix} \\ \begin{pmatrix} 0 & 0 & 1 & 0 \end{pmatrix} \\ \begin{pmatrix} 0 & 0 & 0 & -1 \end{pmatrix} \end{pmatrix}, \tag{4.6}$$

with the basis states as the logical states of the two qubits:

$$|\uparrow\uparrow\rangle = \begin{pmatrix} \begin{pmatrix} 1 \end{pmatrix} \\ \begin{pmatrix} 0 \end{pmatrix} \\ \begin{pmatrix} 0 \end{pmatrix} \\ \begin{pmatrix} 0 \end{pmatrix} \end{pmatrix}, |\uparrow\downarrow\rangle = \begin{pmatrix} \begin{pmatrix} 0 \end{pmatrix} \\ \begin{pmatrix} 1 \end{pmatrix} \\ \begin{pmatrix} 0 \end{pmatrix} \\ \begin{pmatrix} 0 \end{pmatrix} \end{pmatrix}, |\downarrow\uparrow\rangle = \begin{pmatrix} \begin{pmatrix} 0 \end{pmatrix} \\ \begin{pmatrix} 0 \end{pmatrix} \\ \begin{pmatrix} 1 \end{pmatrix} \\ \begin{pmatrix} 0 \end{pmatrix} \end{pmatrix}, |\downarrow\downarrow\rangle_= \begin{pmatrix} \begin{pmatrix} 0 \end{pmatrix} \\ \begin{pmatrix} 0 \end{pmatrix} \\ \begin{pmatrix} 0 \end{pmatrix} \\ \begin{pmatrix} 1 \end{pmatrix} \end{pmatrix}. \tag{4.7}$$

By applying two additional single-qubit pulses as shown in Fig. 4.2, the Cirac-Zoller gate produces the controlled-NOT gate with the truth table of

$$\begin{aligned} |\uparrow\uparrow\rangle &\rightarrow |\uparrow\uparrow\rangle \\ |\uparrow\downarrow\rangle &\rightarrow |\uparrow\downarrow\rangle \\ |\downarrow\uparrow\rangle &\rightarrow |\downarrow\downarrow\rangle \\ |\downarrow\downarrow\rangle &\rightarrow |\downarrow\uparrow\rangle, \end{aligned} \tag{4.8}$$

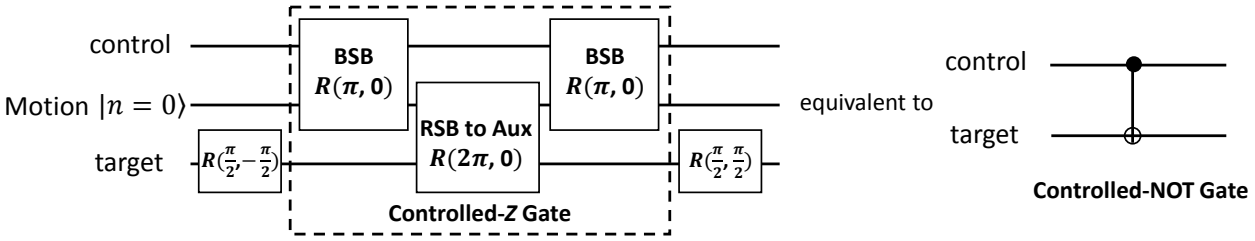

Figure 4.2: Quantum circuit using the Cirac-Zoller protocol to produce the controlled-NOT gate. The overall pulse sequence implements the unitary operation given in Eq. 4.9. The notation $R(\theta, \phi)$ is given in Eq. 2.13.

Or, in the matrix form:

$$\mathrm{CNOT} = \begin{pmatrix} \begin{pmatrix} 1 & 0 & 0 & 0 \\ 0 & 1 & 0 & 0 \end{pmatrix} & \begin{pmatrix} \\ \\ \end{pmatrix} \\ \\ \begin{pmatrix} 0 & 0 & 1 & 0 \\ 0 & 0 & 0 & 1 \end{pmatrix} & \begin{pmatrix} \\ \\ \end{pmatrix} \end{pmatrix}. \tag{4.9}$$

In addition to the requirement for single-qubit addressing, the Cirac-Zoller protocol also requires preparing the motional state in the ground state, and the performance of the protocol is directly tied to how well this is accomplished. The Cirac-Zoller protocol was first realized in Ref. [Monroe 95a] with the control and target qubits encoded in two motional Fock states and two Zeeman states of a trapped $^9Be^+$ ion, respectively. Two-ion realization of the Cirac-Zoller gate was first implemented with two $^{40}Ca^+$ ions [Schmidt-Kaler 03], where single-qubit addressing was accomplished by tightly focused laser beams. We implemented the Cirac-Zoller controlled-NOT gate with a $^9Be^+$ and a $^{25}Mg^+$ ion, which is described in Sec. 5.6.

4.3 Geometric Phase Gates

Unlike the Cirac-Zoller gate where the logic operation is accomplished by the blockade of the motional ground state, a geometric phase gate creates a forced harmonic oscillator interaction that drives motional wavefunction around a trajectory in the phase space which is dependent on the internal qubit states. As shown in Fig. 4.3, if the different displacements enclose a loop, the qubit states pick up a geometric phase proportional to the area of the enclosed state-dependent loop. An

entangling gate can be engineered by choosing an appropriate geometric phase difference between different qubit states. In this section we decribe some of the basic mechanisms of the gates; more detailed explanations are given when separate experiments are discussed in Chap. 5, 6, and 7.

Geometric phase gates can be engineered such that the phase-space displacement driven by the state-dependent force encloses multiple loops in phase space. This strategy has the advantage of increasing the robustness of the geometric phase gate against timing miscalibration and motional dephasing [Hayes 12].

4.3.1 Types of Geometric Phase Gates

Depending on the basis states in which the spin-dependent force applies, geometric phase gate can be separated into two subcategories: (i) the $\hat{\sigma}_z\hat{\sigma}_z$ gate where the spin-dependent force acts on the $\hat{\sigma}_z$ logical basis, and (ii) the $\hat{\sigma}_\phi\hat{\sigma}_\phi$ gate where the spin-dependent force acts on the $\hat{\sigma}_\phi$ rotated basis.

In this thesis, the laser beam geometry to drive the geometric phase gate is shown in Fig. 4.4. Laser beams 1 and 2, with laser (angular) frequency ω_1 and ω_2, respectively, are used to drive stimulated-Raman transitions between hyperfine qubit states. These laser beams intersect at 90° such that the difference in their $\boldsymbol{k}$ vectors, $\boldsymbol{\Delta k}$, is aligned along the axial direction, in which case only the axial motional modes will couple to the internal states [Wineland 98].

4.3.2 $\hat{\sigma}_z\hat{\sigma}_z$ Gate

The $\hat{\sigma}_z\hat{\sigma}_z$ gate relies on the differential AC Stark shift between the two states of the qubit to generate a spin-dependent force that applies an effective $\hat{\sigma}_z\hat{\sigma}_z$ spin-spin interaction. By setting the frequency difference between the two laser beams in Fig. 4.4 to be $\omega_z + \delta$, where ω_z and δ are the frequency of a selected motional mode and the detuning of the laser-induced interaction, the $\hat{\sigma}_z\hat{\sigma}_z$-gate Hamiltonian in the interaction frame of qubit and motion after dropping high-frequency

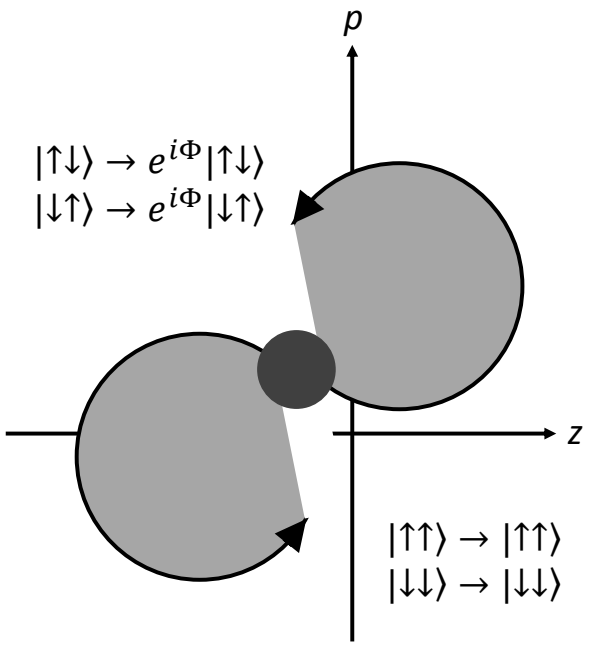

Figure 4.3: By applying an effective spin-spin interaction, the motional wavepacket is displaced in phase space dependent on the internal qubit states. If displacements enclose a loop, the qubit states pick up a geometric phase, Φ, proportional to the area of the enclosed loop.

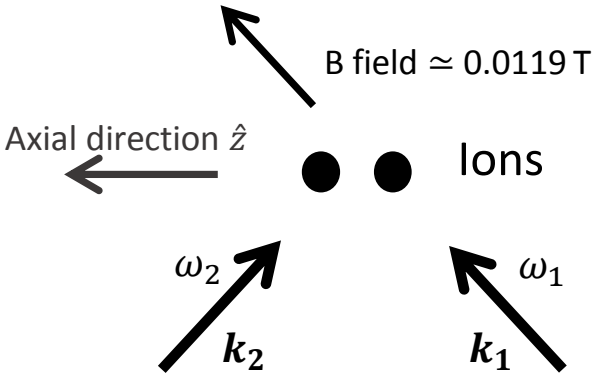

Figure 4.4: Orientation of Raman laser beams used to drive two-qubit entangling gates. Beams 1 and 2 are arranged such that their $\boldsymbol{k}$ vectors intersect at 90° and their $\boldsymbol{\Delta k}$ vector is aligned along the axial direction.

terms for two qubits in the Lamb-Dicke limit can be written as

$$\begin{aligned} H_{zz} &= \hbar\Omega_1\hat{\sigma}_{z,1}\left(\hat{a}\mathrm{e}^{-i(\delta t-\phi_1)}+\hat{a}^\dagger\mathrm{e}^{i(\delta t-\phi_1)}\right)+\hbar\Omega_2\hat{\sigma}_{z,2}\left(\hat{a}\mathrm{e}^{-i(\delta t-\phi_2)}+\hat{a}^\dagger\mathrm{e}^{i(\delta t-\phi_2)}\right) \\ &= \hbar\sum_{j=1,2}\Omega_j\left(|\uparrow\rangle_j\langle\uparrow|_j-|\downarrow\rangle_j\langle\downarrow|_j\right)\left(\hat{a}\mathrm{e}^{-i(\delta t-\phi_j)}+\hat{a}^\dagger\mathrm{e}^{i(\delta t-\phi_j)}\right), \end{aligned} \tag{4.10}$$

with $\Omega_j = \Omega_{AC,j}\eta\xi_j$, where $\Omega_{AC,j}$ is the differential AC Stark shift between the two qubit states induced by the applied laser beams on the jth ion, ξ_j is the mode amplitude of the jth ion for a motional mode with a Lamb-Dicke parameter of η, and $\hat{a}$ is the annihilation operator of the selected motional mode which the laser-induced interaction couples to. The phase of the laser interaction is $\phi_j = \Delta k X_{0,j} + \Delta\phi_j$, where Δk and $\Delta\phi_j$ are the differences in wave vectors and phases of the laser fields, and $X_{0,j}$ is the equilibrium position for the jth ion. $\hat{\sigma}_z$ is the usual Pauli matrix as shown in Eq. D.14.

After setting $\Omega_1 = \Omega_2 = \Omega$ and $\Delta\phi_j = 0$ for simplicity, and assuming that the ions' spatial separation is set appropriately [Leibfried 03, Lee 05], Eq. 4.10 can be written in a relatively simple form:

$$H_{zz} = \hbar\Omega\sum_{j=1,2}\left(|\uparrow\rangle_j\langle\uparrow|_j-|\downarrow\rangle_j\langle\downarrow|_j\right)\left(\hat{a}e^{-i\delta t}+\hat{a}^\dagger e^{i\delta t}\right), \tag{4.11}$$

with Ω as the gate Rabi rate. For $t = 2\pi/\delta$ and $\Omega = \delta/4$, the geometric phases acquired by the qubit states with opposite parity differ by $\pi/2$ (Fig. 4.3), and the truth table for the two qubits is the following:

$$\begin{aligned} |\uparrow\uparrow\rangle &\rightarrow |\uparrow\uparrow\rangle \\ |\uparrow\downarrow\rangle &\rightarrow i|\uparrow\downarrow\rangle \\ |\downarrow\uparrow\rangle &\rightarrow i|\downarrow\uparrow\rangle \\ |\downarrow\downarrow\rangle &\rightarrow |\downarrow\downarrow\rangle. \end{aligned} \tag{4.12}$$

Or, in matrix form:

$$\hat{G}_z = \begin{pmatrix} \begin{pmatrix} 1 & 0 & 0 & 0 \\ 0 & i & 0 & 0 \\ 0 & 0 & i & 0 \\ 0 & 0 & 0 & 1 \end{pmatrix} \begin{pmatrix} \\ \\ \\ \\ \end{pmatrix} \\ \begin{pmatrix} \\ \\ \\ \\ \end{pmatrix} \end{pmatrix}. \tag{4.13}$$

One advantage of the $\hat{\sigma}_z\hat{\sigma}_z$ gate is that the laser setup required is relatively straightforward. The relative frequency difference of the laser beams in path 1 and path 2 (in Fig. 4.4) is approximately the motional frequency, which is usually a few MHz. However, because the $\hat{\sigma}_z\hat{\sigma}_z$ gate relies on a differential AC Stark shift on the two logical states of the qubit, the $\hat{\sigma}_z\hat{\sigma}_z$ gate is not applicable to a qubit whose transition frequency is first-order independent of magnetic field changes [Lee 05].

The $\hat{\sigma}_z\hat{\sigma}_z$ gate was first realized in Ref. [Leibfried 03] with two $^9Be^+$ ions, the created Bell state fidelity was 0.97(2). More recently, a gate fidelity of 0.999(1) was achieved using two $^{43}Ca^+$ ions [Ballance 16], which is currently one of the best deterministic entangling gates yet reported [Ballance 16, Gaebler 16].

4.3.3 $\hat{\sigma}_\phi\hat{\sigma}_\phi$ Gate

The above restriction on qubit transition's magnetic field sensitivity does not apply for a state-dependent force acting on the rotated basis, $|+\rangle$ and $|-\rangle$ defined as the eigenstates of $\hat{\sigma}_\phi = \cos\phi\hat{\sigma}_x - \sin\phi\hat{\sigma}_y$:

$$\begin{aligned} |+\rangle &= \frac{1}{\sqrt{2}}\left(|\uparrow\rangle + e^{i\phi}|\downarrow\rangle\right), \\ |-\rangle &= \frac{1}{\sqrt{2}}\left(|\uparrow\rangle - e^{i\phi}|\downarrow\rangle\right), \end{aligned} \tag{4.14}$$

The $\hat{\sigma}_\phi\hat{\sigma}_\phi$ gate is applicable to any qubit state pairs, including the magnetic-field insensitive qubits. The phase space trajectory driven by the $\hat{\sigma}_\phi\hat{\sigma}_\phi$ gate is very similar to that of the $\hat{\sigma}_z\hat{\sigma}_z$ gate (Fig. 4.3), except that $|+-\rangle$ and $|-+\rangle$ states pick up a geometric phase of Φ, while $|++\rangle$ and $|--\rangle$ states remain unchanged (assuming the optical phases and ions' spatial separation are set appropriately).

With $\hat{\sigma}^+ = |\uparrow\rangle\langle\downarrow|$ as shown in Eq. D.14, one simple form of the $\hat{\sigma}_\phi\hat{\sigma}_\phi$ gate interaction-frame Hamiltonian in the Lamb-Dicke limit after dropping high-frequency terms can be written as

$$H_{\phi\phi} = \hbar\Omega \sum_{j=1,2} \hat{\sigma}_j^+ \left(\hat{a}e^{-i\delta t} + \hat{a}^\dagger e^{i\delta t}\right) + h.c., \tag{4.15}$$

where the gate Rabi rate Ω is assumed to be equal on both ions. For simplicity, we have dropped terms related to the wave vectors and phases of optical fields in Eq. 4.15. The exact form of a $\hat{\sigma}_\phi\hat{\sigma}_\phi$ Hamiltonian depends on experimental setup and the influences of these phase terms will be discussed in detail for different implementations of the $\hat{\sigma}_\phi\hat{\sigma}_\phi$ gates (next two sections), and in the respective chapters presenting different experimental realization of the $\hat{\sigma}_\phi\hat{\sigma}_\phi$ gates.

Using the rotated basis definition given by Eq. 4.14, we can rewrite the Eq. 4.15 to be:

$$H_{\phi\phi} = \hbar\Omega \sum_{j=1,2} \left(|+\rangle_j\langle+|_j - |-\rangle_j\langle-|_j\right) \left(\hat{a}e^{-i\delta t} + \hat{a}^\dagger e^{i\delta t}\right) \tag{4.16}$$

this shows the similarity of this expression with Eq. 4.11, illustrating the basis states in which the spin-dependent forces are applied for the $\hat{\sigma}_\phi\hat{\sigma}_\phi$ and $\hat{\sigma}_z\hat{\sigma}_z$ gate. The truth table in the rotated basis for the $\hat{\sigma}_\phi\hat{\sigma}_\phi$ gate is

$$\begin{aligned} |++\rangle &\rightarrow |++\rangle \\ |+-\rangle &\rightarrow i|+-\rangle \\ |-+\rangle &\rightarrow i|-+\rangle \\ |--\rangle &\rightarrow |--\rangle. \end{aligned} \tag{4.17}$$

The unitary operation of the $\hat{\sigma}_\phi\hat{\sigma}_\phi$ gate written in terms of the basis states of Eq. 4.7 is

$$\hat{G}_{\phi\phi} = \frac{1}{\sqrt{2}} \begin{pmatrix} 1 & 0 & 0 & -i \\ 0 & 1 & 1 & 0 \\ 0 & 1 & 1 & 0 \\ i & 0 & 0 & 1 \end{pmatrix}. \tag{4.18}$$

Compared to the $\hat{\sigma}_z\hat{\sigma}_z$ gate, the laser setup for $\hat{\sigma}_\phi\hat{\sigma}_\phi$ gate is relatively more complicated, primarily because the relative frequency difference of the laser beams in path 1 and path 2 (Fig.

4.4) is separated by approximately the qubit frequency, which is usually a few GHz. Depending on the choice of qubit states and the exact implementation of the $\hat{\sigma}_\phi\hat{\sigma}_\phi$ gate, careful consideration is needed for the generation of deterministic entanglement [Lee 05]. In the next two sections, we introduce two different protocols for the implementation of the $\hat{\sigma}_\phi\hat{\sigma}_\phi$ gate: the Mølmer-Sørensen protocol and the Bermudez protocol.

4.3.4 Mølmer-Sørensen Protocol

The Mølmer-Sørensen (MS) protocol [Sørensen 99, Sørensen 00, Milburn 00, Solano 99] requires simultaneous excitation of a blue-sideband transition with a detuning of δ and a red-sideband transition with a detuning of $-\delta$ for a selected motional mode. Following the spin-motion Hamiltonian described in Sec. 2.1.3, the Hamiltonian of the MS protocol in the interaction picture is [Sørensen 99, Sørensen 00]

$$H_{MS} = \hbar \sum_{j=1,2} \Omega_{r,j}\hat{\sigma}_j^+ \left(\hat{a}e^{-i(\delta_j t-\phi_{j,r})}\right) + \hbar \sum_{j=1,2} \Omega_{b,j}\hat{\sigma}_j^+ \left(\hat{a}^\dagger e^{i(\delta_j t+\phi_{j,b})}\right) + h.c., \tag{4.19}$$

with $\Omega_{r(b),j} = \Omega_{0,r(b),j}\eta\xi_j$ where $\Omega_{0,r(b),j}$ is the Rabi rate of the resonant carrier excitation induced by the laser beams responsible for the red (r) and blue (b) sideband excitations, η is the Lamb-Dicke parameter of the selected motional mode with ξ_j as the mode amplitude of the jth ion. If we set $\Omega_{0,r,j} = \Omega_{0,b,j} = \Omega_{0,j}$ then Eq. 4.19 becomes

$$H_{MS} = \hbar \sum_{j=1,2} \Omega_j\hat{\sigma}_j^+ \left(\hat{a}\mathrm{e}^{-\mathrm{i}(\delta_j t-\phi_{j,r})} + \hat{a}^\dagger\mathrm{e}^{\mathrm{i}(\delta_j t+\phi_{j,b})}\right) + h.c., \tag{4.20}$$

with $\Omega_j = \Omega_{0,j}\eta\xi_j$. The phases of the red (r) and blue (b) sideband interactions are $\phi_{j,r(b)} = \Delta k_{j,r(b)}X_{0,j} + \Delta\phi_{j,r(b)}$ where $\Delta k_{j,r(b)}$ and $\Delta\phi_{j,r(b)}$ are the differences in wave vectors and phases of the optical fields driving the red and blue sideband transitions respectively, and $X_{0,j}$ is the equilibrium position for the jth ion. By setting $t = 2\pi/\delta$ and $\Omega_1 = \Omega_2 = \Omega = \delta/4$, the computational

truth table for the Mølmer-Sørensen gate is the following:

$$\begin{aligned}
|\uparrow\uparrow\rangle &\rightarrow \frac{1}{\sqrt{2}}\left(|\uparrow\uparrow\rangle + e^{-i\left(\sum_{j=1,2}\frac{1}{2}(\phi_{j,b}+\phi_{j,r})+\pi/2\right)}|\downarrow\downarrow\rangle\right) \\
|\uparrow\downarrow\rangle &\rightarrow \frac{1}{\sqrt{2}}\left(|\uparrow\downarrow\rangle + |\downarrow\uparrow\rangle\right) \\
|\downarrow\uparrow\rangle &\rightarrow \frac{1}{\sqrt{2}}\left(|\downarrow\uparrow\rangle + |\uparrow\downarrow\rangle\right) \\
|\downarrow\downarrow\rangle &\rightarrow \frac{1}{\sqrt{2}}\left(|\downarrow\downarrow\rangle + e^{i\left(\sum_{j=1,2}\frac{1}{2}(\phi_{j,b}+\phi_{j,r})+\pi/2\right)}|\uparrow\uparrow\rangle\right)
\end{aligned} \tag{4.21}$$

Depending on the laser beams geometry that is used to implement the MS gate, the phase difference between the two parity components of the produced entangled state can fluctuate, in turn causing decoherence [Lee 05]. Issues of the MS gates' laser phase sensitivity will be discussed in detail for the laser beam geometry used in the mixed-species entangling gate experiment and the high-fidelity two-qubit gate experiment, described in Chap. 5 and Chap. 6, respectively.

4.3.5 Bermudez Protocol

Another protocol to implement the $\hat{\sigma}_\phi\hat{\sigma}_\phi$ geometric phase gate is given by Bermudez *et al.* [Bermudez 12]. It requires a resonant carrier Rabi oscillation excitation and a single spin-motion sideband spin-flip excitation $|\downarrow, n\rangle \leftrightarrow |\uparrow, n+1\rangle$ or $|\uparrow, n-1\rangle$ with a detuning of δ on a selected motional normal mode. This gate scheme features built-in dynamical decoupling [Viola 98, Lidar 14] that can protect the qubit against certain decoherence errors during the application of the gate [Bermudez 12].

In the interaction frame for both the spin and motion, and after dropping high-frequency terms, the Hamiltonian for two ions driven by Bermudez protocol with a blue-sideband excitation in the Lamb-Dicke limit is

$$H_B = \hbar \sum_{j=1,2}\left(\Omega_C\hat{\sigma}_j^+ e^{i\phi} + i\Omega_j\hat{\sigma}_j^+\hat{a}^\dagger e^{-i\delta t}e^{i\phi'_j}\right) + h.c., \tag{4.22}$$

where Ω_C denotes the Rabi rate of the carrier excitation that provides the dynamical decoupling, and $\Omega_j = \Omega_{0,j}\eta\xi_j$, where $\Omega_{0,j}$ is the Rabi rate of the resonant laser-driven carrier excitation, η is the Lamb-Dicke parameter for the selected motional normal mode with ξ_j as the mode amplitude

of the jth ion, and ϕ and ϕ'_j are the respective phases of the carrier and sideband excitation for the jth ion.

The key concept of this gate scheme is to use a strong carrier excitation to create dressed states of the qubits, and apply a spin-dependent force in the dressed-state basis using the single spin-motion sideband excitation. The dressed state created by the strong carrier excitation results is an effective dynamical decoupling mechanism that reduces the sensitivity of the qubits to certain dephasing errors. As a simple illustration, consider a two-level system with an unperturbed qubit frequency of ω_0. Under the influence of a certain mechanism that shifts the qubit frequency by ω', the system Hamiltonian can be written as

$$H = \frac{1}{2}\hbar\omega_0 \begin{pmatrix} 1 & 0 \\ 0 & -1 \end{pmatrix} + \frac{1}{2}\hbar\omega' \begin{pmatrix} 1 & 0 \\ 0 & -1 \end{pmatrix}. \tag{4.23}$$

Now, if we apply a continuous spin-flip excitation to the system with a Rabi rate of Ω_C which satisfies the condition of $\omega_0 \gg \Omega_C \gg \omega'$, the Hamiltonian in the interaction frame of the qubit becomes

$$H_I = \frac{1}{2}\hbar\omega' \begin{pmatrix} 1 & 0 \\ 0 & -1 \end{pmatrix} + \hbar\Omega_C \begin{pmatrix} 0 & 1 \\ 1 & 0 \end{pmatrix}. \tag{4.24}$$

The eigenvalues, ω'_0, of this system, which represent the effective shift of the unperturbed system's qubit frequency, are obtained by diagonalizing the Hamiltonian:

$$\begin{aligned} \omega'_0 &= \pm\frac{1}{2}\sqrt{\omega'^2 + \Omega_C^2} \\ &= \pm\frac{1}{2}\Omega_C\sqrt{1 + \frac{\omega'^2}{\Omega_C^2}} \\ &\approx \pm\frac{1}{2}\Omega_C \left(1 + \frac{\omega'^2}{\Omega_C^2} + \frac{1}{2}\left(\frac{\omega'^2}{\Omega_C^2}\right)^2 + \cdots\right) \\ &= \pm\frac{1}{2} \left(\Omega_C + \frac{\omega'^2}{\Omega_C} + \frac{1}{2}\Omega_C\left(\frac{\omega'^2}{\Omega_C^2}\right)^2 + \cdots\right). \end{aligned} \tag{4.25}$$

It becomes apparent that the influence of ω' becomes a second order effect and decreases as Ω_C increases. However, now the overall frequency shift, ω'_0, depends linearly on Ω_C. Therefore, although

dynamical decoupling can provide protections against uncontrolled environmental noise (ω'), it requires the control field to be constant.

Since the interesting case is when $\Omega_C \gg |\Omega_j|$, we shift to the interaction frame, where the states are dressed by the carrier excitation, and consider the effects of the sideband term. For simplicity, we set $\phi = \phi'_j = 0$ since they are not important for the description below. In the $|+\rangle, |-\rangle$ basis according to Eq. 4.14, the Hamiltonian in Eq. 4.22 becomes [Bermudez 12, Tan 13]

$$\begin{aligned} H_B &= i\hbar \sum_j \frac{\Omega_j}{2} \left(|+\rangle_j\langle +|_j - |-\rangle_j\langle -|_j \right) \left(\hat{a}^\dagger e^{-i\delta t} - \hat{a} e^{i\delta t} \right) \\ &\quad + i\hbar \sum_j \frac{\Omega_j}{2} \left(|-\rangle_j\langle +|_j e^{-2i\Omega_C t} - |+\rangle_j\langle -|_j e^{2i\Omega_C t} \right) \left(\hat{a}^\dagger e^{-i\delta t} + \hat{a} e^{i\delta t} \right) \end{aligned} \tag{4.26}$$

The second term induces off-resonant transitions between the dressed states $|+\rangle$ and $|-\rangle$ and can be neglected under the assumption that $\Omega_C \gg |\Omega_j|$. The first term is identical to Eq. 4.16, which describe a Hamiltonian of a geometric phase gate with the spin-dependent force acting on the rotated basis. In contrast to the MS protocol, the entangled states produced by Bermudez protocol are insensitive to optical path length changes of the non-copropagating laser beams (Fig. 4.4) occurring on a time scale that is long compared to the gate duration. This offers technical simplicity in terms of implementation. The laser phase insensitivity and experimental implementations of the Bermudez gate using two $^9Be^+$ ions will be described in Chap. 7. Furthermore, compared to the MS protocol, error associated with the Rabi rate imbalance of the detuned-blue and detuned-red sideband is removed with this implementation of the Bermudez protocol.

4.4 Error Sources for Geometric Phase Gates

One of the most important aspects of implementing two-qubit entangling gates is the study of imperfections and error mechanisms. These studies provide insights into whether these limiting factors are of a fundamental nature, or technical challenges. In addition, understanding the sources of imperfection provides motivation to innovate alternative techniques for the further improvement of gate performance.

Here, we describe error mechanisms that are considered for the experimental implementations

of two-qubit gates presented in Chap. 5, 6, and 7. These experiments implement the $\hat{\sigma}_\phi\hat{\sigma}_\phi$ gates; therefore the discussions below focuses on error sources associated with them, but is not limited to the $\hat{\sigma}_\phi\hat{\sigma}_\phi$ gate. As mentioned before, the objective here is to provide an overview. Further discussions and evaluations of error sources for different experiments will be presented in their individual chapter in the remaining of this thesis.

A combination of analytic methods, Monte Carlo simulations, Schrödinger equation simulations, and master equation simulations are used for the study of these error mechanisms, with the latter used heavily in this thesis.

4.4.1 Schrödinger and Master Equation Simulations

In this dissertation work, we use the Schrödinger equation to study the dynamics of quantum systems of interest when dissipation is not considered. We also use the Schrödinger equation to study coherent errors, e.g., errors due to slow fluctuations in laser intensity, timing, frequency offsets and calibration drifts. The Schrödinger equation is

$$i\hbar\frac{d|\Psi\rangle}{dt} = H|\Psi\rangle, \tag{4.27}$$

where $|\Psi\rangle$ is the state vector representing the system, and H is the Hamiltonian describing the coherent interaction.

The dynamics of an open-quantum system can be simulated with a master equation [Gardiner 00], which allows multiple dissipative error mechanisms and coherent operations to be combined and simulated. The master equation used here is in the Lindblad form [Lindblad 76]

$$\frac{d\rho}{dt} = \frac{1}{i\hbar}\left[H,\rho\right] + \sum_j \left(\hat{L}_j\rho\hat{L}_j^\dagger - \frac{1}{2}\hat{L}_j^\dagger\hat{L}_j\rho - \frac{1}{2}\rho\hat{L}_j^\dagger\hat{L}_j\right), \tag{4.28}$$

where ρ is the density matrix of the system, and $\hat{L}_j$ is the Lindblad operator (or quantum jump operator) describing the jth decoherence/dissipative process. Readers unfamiliar with the master equation will find Ref. [Dyrting 95, Schneider 98, Puri 01, Harty 13] useful.

Master equation simulations are more computer-resource demanding. For a quantum system represented by a matrix of dimension $M \times 1$, the density matrix required for the equivalent master

equation simulation has a dimension of $M \times M$. This is precisely the problem faced by conventional computation; that is, the number of parameters needed to keep track of a quantum system grows exponentially as the system size increases. For example, in a system of N qubits, M scales as 2^N. Nevertheless, master equation simulations are used intensively to study the system dynamics under the influences of dissipative error sources, such as spontaneous scattering of photons, heating of motional modes, qubit dephasing, and motional mode dephasing. Furthermore, we have also combined Schrödinger equations and master equations with Monte Carlo simulations.

The quantum systems included for the simulations of two-qubit gates are the spin of each ion, and harmonic oscillators to represent the ions' motion. The harmonic oscillator energy eigenstates span an infinite dimensional Hilbert space. However, since most of the relevant dymanics occur close to the ground state, we select a motional system size which includes the ground state up to the Fock state $|N_{\max}\rangle$ that strikes a balance between the required computational resources and an adequate representation of our system. Depending on which dynamics and properties are of interest, $N_{\max}$ ranges from $\simeq 10$ to 100.

Due to the internal atomic state structures, our choices of hyperfine states as qubits, and the fluorescence detection scheme for the $^9Be^+$ and $^{25}Mg^+$ ions (see Sec. 2.1.7 and Sec. 2.2.6), there are times where the states outside of the qubit $|\uparrow\rangle$ and $|\downarrow\rangle$ manifold must be included (see Fig. 2.1 and Fig. 2.6 for energy level diagrams for $^9Be^+$ and $^{25}Mg^+$, respectively). For example, population can leak from the qubit manifold into other hyperfine states through spontaneous Raman scattering during the gate. Furthermore, due to the finite fidelity of (i) optical pumping and (ii) population transfer between computational and measurement qubit manifolds, these operations result in non-zero populations outside the qubit manifold. These populations do not interact with laser-induced operations on the qubit transition and are predominantly detected as "dark" (see Sec. 2.1.7). To better capture the dynamics and effects due to these populations, we include a single auxiliary state (for each ion) in our model for numerical simulation, which consolidates all population in the non-qubit-manifold. The simplification is made because the population in each of the other Zeeman states is small (on most scenarios considered). We label this state as $|A\rangle$ and it is modeled to have

the same detection outcome as the $|\downarrow\rangle$ state. In our model, unless stated otherwise, the only spin states that interact with the applied coherent operations are the qubit $|\uparrow\rangle$ and $|\downarrow\rangle$ states.

Here, most of the numerical simulations on quantum systems are performed using matrix representations of states and operators (see Appendix D) with the *Mathematica* software.

4.4.2 Spontaneous Scattering of Photons

One of the dominant decoherence sources when driving stimulated-Raman transitions is the error caused by spontaneous emission of photons [Wineland 98]. With the initial state of $|i\rangle = |\uparrow\rangle$ or $|\downarrow\rangle$ state, the spontaneous scattering rate into the final state $|f\rangle$ via the intermediate states $|j\rangle$ is given by the Kramer-Heisenberg equation [Cline 94]

$$\Gamma_{i\to f} = \sum_m \frac{E_m^2}{4\hbar^2} \left| \sum_j \left(\sum_k \Gamma_j \frac{\langle f|\boldsymbol{d}\cdot\hat{\sigma}_q^k|j\rangle\langle j|\boldsymbol{d}\cdot\hat{\sigma}_{\mathrm{L},m}^k|i\rangle}{\Delta_j} \right) \right|^2, \tag{4.29}$$

where E_m is the electric field amplitude of the mth laser beam, $\boldsymbol{d}$ is the electric-dipole operator, and Δ_j is the detuning of the Raman laser from each of the $i \leftrightarrow j$ transitions. Here, $\hat{\sigma}_{\mathrm{L},m}^k$ represents the polarization vectors of the mth laser beam and k indexes the different polarization components. They are expressed in terms of linear ($\hat{\pi}$), left ($\hat{\sigma}^-$) and right ($\hat{\sigma}^+$) circular polarizations such that $\hat{\sigma}_{\mathrm{L},m} = \epsilon_m^-\hat{\sigma}_m^- + \epsilon_m^0\hat{\pi}_m + \epsilon_m^+\hat{\sigma}_m^+$ with $|\epsilon_m^-|^2 + |\epsilon_m^0|^2 + |\epsilon_m^+|^2 = 1$. Similarly, $\hat{\sigma}_q$ contains the three possible polarization-dependent decay channels from the jth excited state to the fth final state. Note that coupling between different states of the same polarization can interfere with each other, but there is no interference between coupling of different polarizations. For $^9\mathrm{Be}^+$ and $^{25}\mathrm{Mg}^+$ the jth excited states are the different hyperfine Zeeman states in the $P_{1/2}$ and the $P_{3/2}$ electronic excited states, and we can approximate the natural decay rate of each jth state to be $\Gamma_j = \Gamma$.

The total probability of spontaneous emission $P_{\mathrm{S.E}}$ for a laser-driven spin-flip transition is

$$P_{S.E.} = \sum_f \frac{1}{2}\left(\Gamma_{\uparrow\to f} + \Gamma_{\downarrow\to f}\right)\tau_\pi, \tag{4.30}$$

where τ_π is the duration needed for the π pulse, which is defined by $\Omega\tau = \pi/2$. Now, Eq. 4.30 becomes

$$P_{S.E.} = \frac{\pi}{2}\frac{\sum_f\left(\Gamma_{\uparrow\to f} + \Gamma_{\downarrow\to f}\right)}{2\Omega}. \tag{4.31}$$

Depending on the final state after each scattering event, spontaneous emission can be separated into Raman and Rayleigh scattering, and the error mechanisms in which they cause error can be different [Ozeri 05, Ozeri 07].

4.4.2.1 Raman Scattering

Raman scattering processes are inelastic and project an ion's internal state to one of the Zeeman states which is different from the initial state, destroying coherence. Raman scattering processes can be further separated into two processes: (i) out-of-manifold scattering, and (ii) bit-flip scattering. The Lindbald operators describing the Raman spontaneous emission out-of-manifold scattering are

$$\hat{L}_{\uparrow A}(\Gamma_{\uparrow A}) = \sqrt{\Gamma_{\uparrow A}}\hat{\sigma}_{\uparrow A}, \tag{4.32}$$

$$\hat{L}_{\downarrow A}(\Gamma_{\downarrow A}) = \sqrt{\Gamma_{\downarrow A}}\hat{\sigma}_{\downarrow A}, \tag{4.33}$$

where $\hat{\sigma}_{\uparrow A} = |A\rangle\langle\uparrow|$ and $\hat{\sigma}_{\downarrow A} = |A\rangle\langle\downarrow|$, $\Gamma_{\uparrow A}$ ($\Gamma_{\downarrow A}$) indicates the scattering rate from the $|\uparrow\rangle$ ($|\downarrow\rangle$) state to the $|A\rangle$ state, respectively (see Appendix D for the matrix representations of $\hat{\sigma}_{\uparrow A}$ and $\hat{\sigma}_{\downarrow A}$). In actuality, there are multiple final states that can be populated by an out-of-manifold scattering event with different scattering rate (see Fig. 2.1 for energy level diagram of the $^9Be^+$ ion). In our model, the scattering rates $\Gamma_{\uparrow A}$ and $\Gamma_{\downarrow A}$ are the sum of scattering rates from each of the qubit states to other non-qubit-manifold states. The Lindblad operators for the bit-flip scattering are [Puri 01]

$$\hat{L}_{\uparrow\downarrow}(\Gamma_{\uparrow\downarrow}) = \sqrt{\Gamma_{\uparrow\downarrow}}\hat{\sigma}^{-}, \tag{4.34}$$

$$\hat{L}_{\downarrow\uparrow}(\Gamma_{\downarrow\uparrow}) = \sqrt{\Gamma_{\downarrow\uparrow}}\hat{\sigma}^{+}, \tag{4.35}$$

where $\Gamma_{\uparrow\downarrow}$ represents the scattering rate starting from the $|\uparrow\rangle$ state and ending in the $|\downarrow\rangle$ state. Similarly for $\Gamma_{\downarrow\uparrow}$. Both the out-of-manifold and bit-flip scattering events destroy coherence. However, in contrast to the out-of-manifold scattering, the bit-flip scattering event does not result in qubit manifold population leakage. Raman scattering processes contribute large portions of errors

to the entangling gates implemented in Chap. 5, 6, and 7, these scattering errors are accounted for and are discussed further in their individual chapter.

Another process which is not considered here is the events where population from the non-qubit manifold enters the qubit manifold via Raman scattering. Usually the population in the non-qubit manifold is small; therefore this process is a second order process that we assume to have negligible effect on the dynamics of the system under studies.

4.4.2.2 Rayleigh Scattering

Rayleigh scattering processes are elastic, i.e. the scattering event puts the atomic state back to its original state. Depending on the choice of atomic states for the qubit, Rayleigh scattering processes do not necessarily cause spin decoherence. In general, different atomic states have unequal spontaneous scattering rates. Unequal Rayleigh scattering rates for the two qubit states produce an overall spin-dephasing error [Ozeri 07, Uys 10], which can be described by the Lindblad operator describing qubit decoherence [Uys 10]:

$$\hat{L}_R(\Gamma_R) = \sqrt{\Gamma_R}\hat{\sigma}_z, \tag{4.36}$$

with the Rayleigh qubit dephasing rate, Γ_R given by [Uys 10]

$$\Gamma_R = \sum_m \frac{E_m^2}{2\hbar} \left| \sum_j \sum_k \Gamma_j \left(\frac{\langle\uparrow|\boldsymbol{d}\cdot\hat{\sigma}_q^k|j\rangle\langle j|\boldsymbol{d}\cdot\hat{\sigma}_{\mathrm{L},m}^k|\uparrow\rangle}{\Delta_j} - \frac{\langle\downarrow|\boldsymbol{d}\cdot\hat{\sigma}_q^k|j\rangle\langle j|\boldsymbol{d}\cdot\hat{\sigma}_{\mathrm{L},m}^k|\downarrow\rangle}{\Delta_j} \right) \right|^2. \tag{4.37}$$

Rayleigh scattering does not cause a spin-dephasing error if a magnetic-field insensitive states pair is used as qubit. This is because the Rayleigh scattering amplitude for each qubit state is equal, thus the two terms in Eq. 4.37 cancel each other, resulting in a vanishing decoherence rate. The entangling gates presented in this thesis are all implemented on magnetic-field insensitive qubits; therefore the Rayleigh dephasing error does not apply. Although Rayleigh scattering does not directly cause spin decoherence to a magnetic-field-insensitive qubit, it can cause errors to a two-qubit gate based on geometric phase via motional decoherence [Ozeri 07].

4.4.2.3 Motional Dephasing due to Spontaneous Scattering

The direction of each scattered photon is random, which results in a random recoil momentum kick to the ion's motion. This distorts the phase-space trajectory as the state-dependent force is applied, and causes phase errors in the final state. The worst-case error is given by Eq. 57 in Ref. [Ozeri 07]:

$$\epsilon_{\text{Recoil}} = \frac{5}{24}\frac{\eta^2}{N_{\text{loop}}}P_{\text{S.E.}}, \tag{4.38}$$

where η is the Lamb-Dicke parameter of the motional bus mode, and N_{loop} is the number of phase space loops used for the geometric phase gate. The total scattering probability, $P_{\text{S.E.}}$ is described by Eq. 4.30 that sums over all possible final states.

The scattering probabilities of Raman, Rayleigh and their sum for a two-qubit Mølmer-Sørensen gate are shown in Fig. 4.5 and Fig. 4.6 for a $^{9}Be^{+}$ and $^{25}Mg^{+}$ ion, respectively. The dephasing errors associated with the momentum kicks caused by spontaneous scattering are also shown in these two figures.

Motional dephasing due to spontaneous scattering of photons contributes negligible errors (compared to other dominant errors) to the mixed-species entangling gate (Chap. 5) and the dynamical decoupling gate (Chap. 7). However, this error is non-negligible in the experiments presented in Chap. 6, where a Raman detuning as high as $\Delta \sim -2\pi \times 900$ GHz is used. Further discussions are in their individual chapters.

Although Raman scattering can be reduced by increasing $|\Delta|$, the Rayleigh scattering error reaches an asymptotic value as $|\Delta|$ is increased. This error is proportional to the Lamb-Dicke parameter and thus could be reduced by increasing the trap frequency; it can also be reduced by using multiple loops in phase space [Ozeri 07, Hayes 12] (see Eq. 4.38). However, these methods reduce the gate Rabi rate and thus increase the Raman scattering error.

Depending on the ion species, Rayleigh scattering can set an absolute lower limit for the error of a geometric phase gate implemented with stimulated-Raman transitions. This is more pronounced in the case for ion species which have a low-lying D electronic excited state [Ozeri 07].

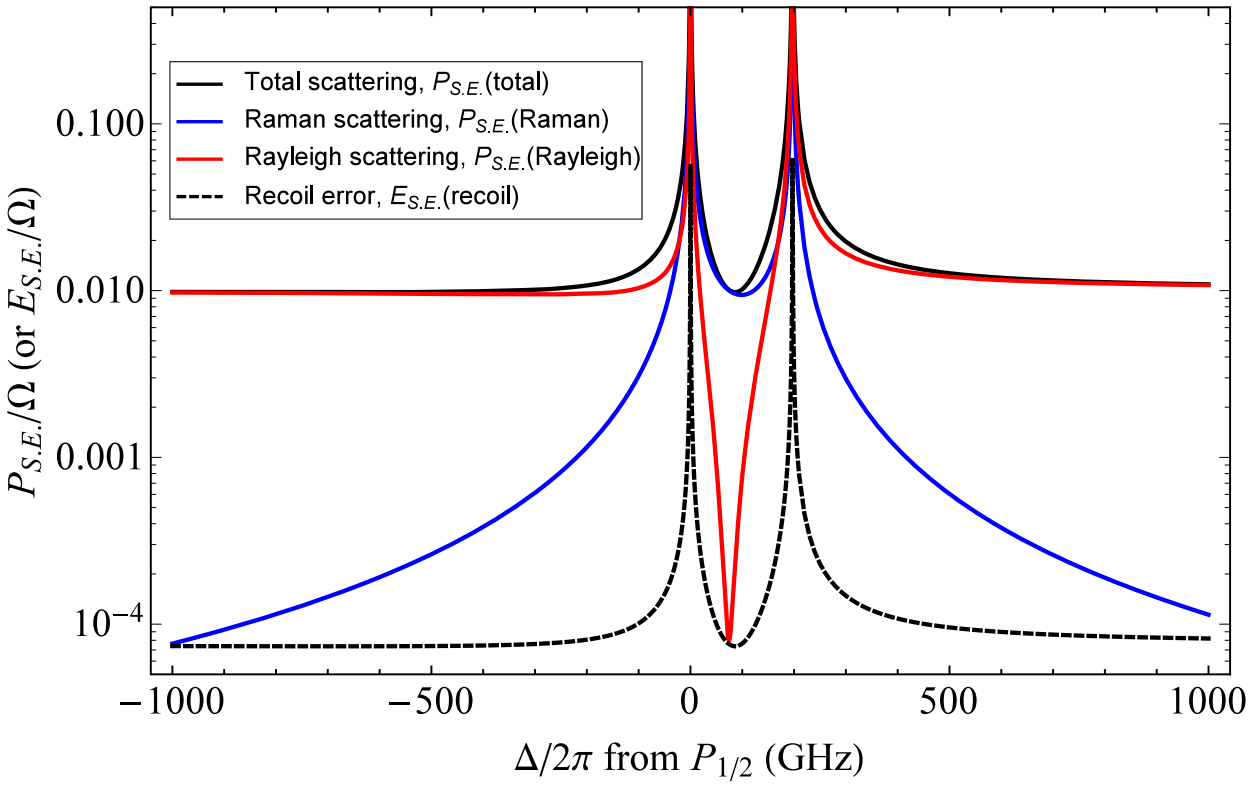

Figure 4.5: This figure shows the different scattering probabilities and errors caused by spontaneous scattering of photons due to Raman laser beams for a two-qubit gate driven with the Mølmer-Sørensen protocol on $^9Be^+$ ions. Spontaneous scattering of photons can be categorized into Raman and Rayleigh scattering, and they contribute errors to a two-qubit gate differently. The qubit's coherence is lost after each Raman scattering event, while this is not the case for Rayleigh scattering. Both Raman and Rayleigh process contribute to motional dephasing error through a random trajectory in the motional phase space caused by a uncontrolled momentum kick for each scattering event. The horizontal axis indicates the detuning of the Raman laser with respect to the $^2S_{1/2} \leftrightarrow {}^2P_{1/2}$ transition of the $^9Be^+$ ion. The second peak at $\sim +200$ GHz Raman detuning corresponds to scattering from the $^2P_{3/2}$ electronic excited state. The dips between the two fine structure lines are caused by the cancellation effect as indicated in Eq. 4.29; the Raman laser is blue detuned relative to the $^2P_{1/2}$ levels while red detuned relative to the $^2P_{3/2}$ levels. This figure is plotted with a Lamb-Dicke parameter of $\eta = 0.19$, $N_{\text{Loop}} = 1$, and assuming equal laser intensity in each of the two laser paths as depicted in Fig. 4.4. The polarization of the $\boldsymbol{k_1}$ ($\boldsymbol{k_2}$) is set to be pure σ^+ (π).

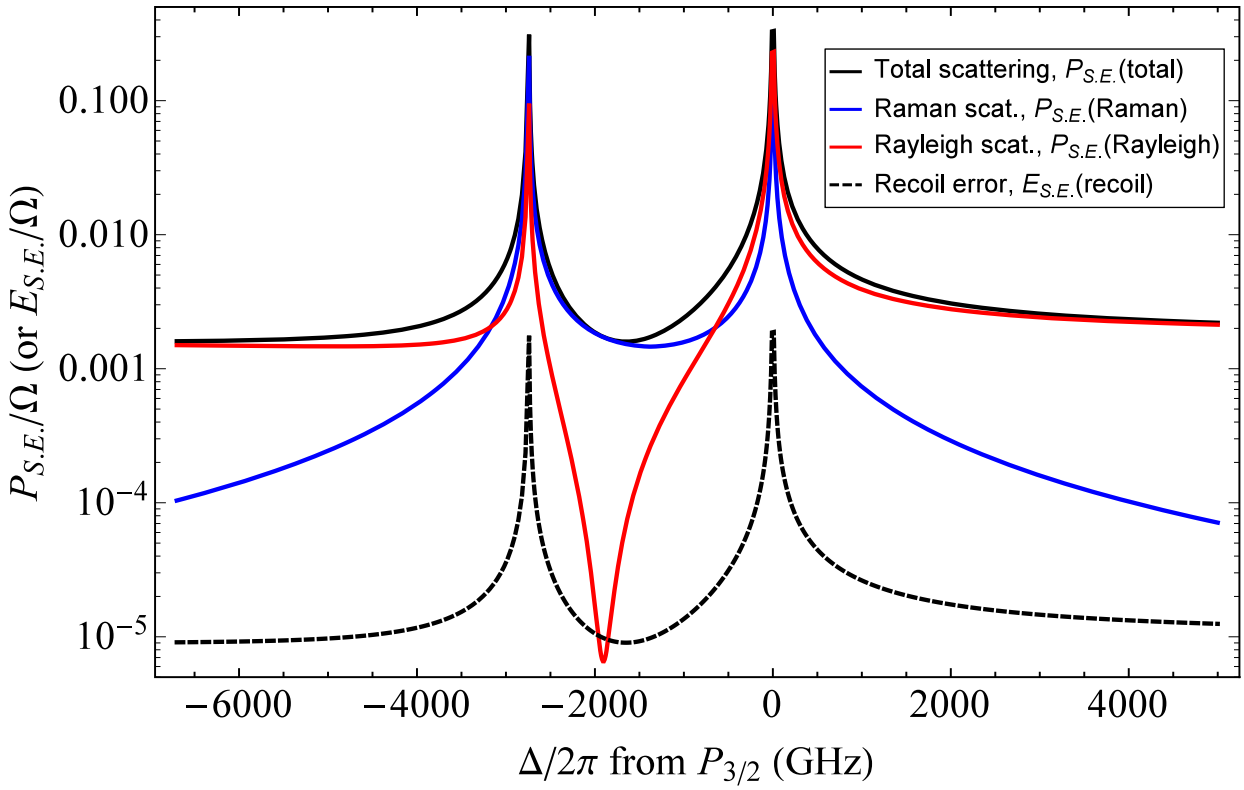

Figure 4.6: This figure is analogous to Fig. 4.5 but for $^{25}Mg^{+}$ ions and with $\eta = 0.165$. The Raman detuning, Δ is plotted with respect to the $^{2}P_{3/2}$ excited state, where the frequency of our $^{25}Mg^{+}$ Raman laser is tuned near to. The two peaks correspond to the fine structure splitting between the $^{2}P_{1/2}$ and $^{2}P_{3/2}$ electronic excited states, which is ~ 2.75 GHz.

4.4.3 Motional Frequency Fluctuations

As the geometric phase gates rely on the coherent evolution of both the spin and motional degrees of freedom, motional frequency fluctuations affect the gate's performance in a similar fashion as qubit dephasing. Motional frequency fluctuation can be described by the Lindblad operator of [Turchette 00b]

$$\hat{L}_{motion}(\Gamma_{\text{motion}}) = \sqrt{\Gamma_{\text{motion}}}\hat{a}^{\dagger}\hat{a}, \tag{4.39}$$

Physical sources of frequency fluctuation include (i) fluctuations in the control potentials applied to electrodes for trapping, (ii) fluctuating electric-field gradients from uncontrolled charging of electrode surfaces [Harlander 10], and (iii) for gates applied on the axial stretch mode, the non-linear coupling to radial "rocking" modes [Roos 08, Nie 09]. For (iii), to a good approximation, the shift of the stretch mode frequency, $\delta\omega_S$ from the thermal excitation of these modes is given by $\delta\omega_S = \chi(n_x + n_y + 1)$ where χ is the non-linear coupling term, n_x and n_y are Fock state occupation numbers of the two transverse (radial) rocking modes. As these fluctuations are dependent on the occupation numbers of the radial modes, the error can be suppressed by cooling the radial modes to near the ground state.

Entangling gate errors caused by motional frequency fluctuations are studied closely in the implementations with two $^9Be^+$ ions (see Chap. 6); motional frequency fluctuations cause negligible errors to the mixed-species entangling gate and the dynamical decoupling gate presented in Chap. 5 and Chap. 7, respectively.

4.4.4 Motional Heating

Although the geometric phase gate is robust against thermal excitation (the motional ground state is incompletely populated) [Sørensen 99, Sørensen 00], changes in motion states during the application of the gate cause decoherence, which leads to errors. This heating can be modeled as an exchange of energy between the motional harmonic oscillator and a thermal bath with much higher temperature. Uncontrolled couplings between these two systems consist of a heating and a

cooling process, and they can be described by the following Lindblad operators [Sørensen 00]:

$$\hat{L}_{\text{heat}}(\Gamma_{h,c}) = \sqrt{\Gamma_{h,c}}\hat{a}^{\dagger}, \tag{4.40}$$

$$\hat{L}_{\text{cool}}(\Gamma_{h,c}) = \sqrt{\Gamma_{h,c}}\hat{a}, \tag{4.41}$$

where $\Gamma_{h,c}$ is the heating rate. One of the dominating heating effects is due to the uncontrolled electric field noise from the trapping electrodes [Turchette 00a]. The exact mechanism of this "anomalous heating" is currently not understood, and there is active research to study this problem, see for examples Ref. [Allcock 11, Hite 13, Daniilidis 11, Brownnutt 15, McConnell 15]. Lindblad operators given in Eq. 4.40 and Eq. 4.41 are used in master equations (Eq. 4.28) to model the dynamics of entangling gates presented in Chap. 5, 6, and 7; we find good agreements between experiment data and our model.

4.4.5 Off-Resonance Coupling to Spectator Modes

The Hamiltonians shown in Eq. 4.11 and Eq. 4.15 describe geometric phase gates with the spin-spin interaction implemented by coupling to a single mode of motion. As other motional modes can also be driven off-resonantly by the applied laser fields, this can induce errors due to the imperfect implementation of the desired Hamiltonians.

We consider the case with two ions driven by the Mølmer-Sørensen interaction using the laser beams geometry depicted in Fig. 4.4. Following Eq. C.19, the interaction frame Hamiltonian describing a blue-sideband excitation and a red-sideband excitation before dropping high-frequency terms is

$$H_{MS} = \hbar \sum_{j=1,2} \Big(\Omega_{0,j}\hat{\sigma}_j^{\dagger} e^{i\omega_0 t} \text{Exp}\left[i \sum_k \eta_k \xi_{k,j} \left(\hat{a}_k e^{-i\omega_k t} + \hat{a}_k^{\dagger} e^{i\omega_k t} \right) \right] \Big(e^{-i\Delta\omega_B t} + e^{-i\Delta\omega_R t} \Big) \Big(+ h.c., \tag{4.42}$$

where k indexes the different motional normal modes with mode frequency ω_k that can interact with laser geometry setup, $\Omega_{0,j}$ and $\xi_{k,j}$ are the resonant carrier Rabi frequency and the mode amplitude for the kth normal mode of the jth ion, and $\Delta\omega_{B,R}$ are the relative frequency differences between

the Raman laser fields responsible for the detuned blue (B) and the detuned red (R) sideband excitation, respectively. Assuming that the ion crystal is perfectly aligned with the $\boldsymbol{\Delta k}$ of the laser fields such that only normal modes along the axial direction can be driven, and considering the Lamb-Dicke expansion up to the first order in η_k (Eq. C.17), the Hamiltonian described in Eq. 4.42 becomes

$$\begin{aligned} H_{MS} &= \hbar \sum_{j=1,2} \Big(\Omega_{0,j} \hat{\sigma}_j^\dagger e^{i\omega_0 t} \Big[1 + i\eta_C \xi_{C,j} \Big(\hat{a}_C e^{-i\omega_C t} + \hat{a}_C^\dagger e^{i\omega_C t} \Big) \\ &\quad + i\eta_S \xi_{S,j} \Big(\hat{a}_S e^{-i\omega_S t} + \hat{a}_S^\dagger e^{i\omega_S t} \Big) + \ldots \Big] \Big(e^{-i\Delta\omega_B t} + e^{-i\Delta\omega_R t} \Big) + h.c., \end{aligned} \tag{4.43}$$

where $\eta_{C,S}$, $\omega_{C,S}$, and $\hat{a}_{C,S}$ are the Lamb-Dicke parameter, the normal mode frequency, and the annihilation operator for the center-of-mass (C) mode and stretch (S) mode, respectively.

To generate a spin-dependent force mediated by the center-of-mass mode, we set the relative frequency differences between the two set of Raman laser beams to be $\Delta\omega_B = \omega_0 + \omega_C - \delta$ and $\Delta\omega_R = \omega_0 - \omega_C + \delta$. With this, the Hamiltonian (before dropping high-frequency terms) is

$$\begin{aligned} H_{MS} &= \hbar \sum_{j=1,2} \Big(\Omega_{0,j} \hat{\sigma}_j^\dagger \Big[\Big(e^{-i(\omega_C - \delta)t} + e^{i(\omega_C - \delta)t} \Big) \\ &\quad + i\eta_C \xi_{C,j} \Big(\hat{a}_C e^{-i\delta t} + \hat{a}_C e^{-i(2\omega_C - \delta)t} + \hat{a}_C^\dagger e^{i(2\omega_C - \delta)t} + \hat{a}_C^\dagger e^{i\delta t} \Big) \Big(\\ &\quad + i\eta_S \xi_{S,j} \Big(\hat{a}_S e^{-i(\omega_S + \omega_C - \delta)t} + \hat{a}_S e^{-i(\omega_S - \omega_C + \delta)t} \\ &\quad + \hat{a}_S^\dagger e^{i(\omega_S - \omega_C + \delta)t} + \hat{a}_S^\dagger e^{i(\omega_S + \omega_C - \delta)t} \Big) + \ldots \Big] \Big(+ h.c.. \end{aligned} \tag{4.44}$$

The $\hat{a}_C e^{-i\delta t}$ and $\hat{a}_C^\dagger e^{i\delta t}$ terms (in the second term inside the square bracket) represent the MS interaction acting on the center-of-mass mode. All other terms represent off-resonant excitations. For example, the first term in the square bracket represents off-resonant excitation of the carrier transition, the $\hat{a}_S e^{-i(\omega_S - \omega_C + \delta)t}$ and $\hat{a}_S^\dagger e^{i(\omega_S - \omega_C + \delta)t}$ terms (in the third term inside the square bracket) represent off-resonant excitation of the stretch mode with a detuning approximately equal to the mode frequency difference of the center-of-mass mode and the stretch mode. These high-frequency terms are usually dropped ($\omega_C, \omega_S \gg \delta$) to give a reasonable approximation to the gate [Tan 13, Tan 15]. However, it is important to consider the effects of these off-resonant excitations

for the high-fidelity implementation of the MS gate. Usually an off-resonant carrier excitation has a bigger impact than the off-resonant stretch mode excitation, this is because the strech mode excitation is scaled by the Lamb-Dicke parameter (η_S) compared to the carrier excitation.

Furthermore, the Raman laser beams could be imperfectly aligned such that the $\boldsymbol{\Delta k}$ vector has components in the radial directions. For such cases, Eq. 4.44 can be further generalized to include the additional motional modes. The coupling strength to motional mode is parametrized by the Lamb-Dicke parameter which quantifies the overlap of the laser beams' $\boldsymbol{\Delta k}$ and the motional modes. Although the coupling strengths to the radial modes are (usually) relatively small given reasonable laser beam alignment and the transition frequency detuning is relatively large, certain higher-order coupling (second or higher-order terms in the Lamb-Dicke expansion, see Eq. C.17) terms could have a relatively small detuning that induce additional errors.

In addition to coupling to spectator motional modes, other atomic transitions can also be off-resonantly driven, especially in the presence of micromotion. The two-qubit gates presented in Chap. 5 and Chap. 6 are implemented inside an ion trap where the excessive axial micromotion could not be compensated (see Sec. 2.1.3 and Sec. 3.1). The frequency of the trap RF, ω_{RF}, is comparable to the Zeeman splittings of $^9Be^+$ ion such that spectator atomic transitions could be coupled on other micromotion sidebands when driven by the laser beam geometry depicted in Fig. 4.4

Off-resonant coupling to spectator transitions can be suppressed by employing laser pulse shaping (see Sec. 3.8). By smoothing out the rise and fall profile of the laser beam, Fourier components at the frequencies of spectator transition can be made sufficiently small. With such dynamic shaping of laser pulses, gate errors contributed by off-resonant coupling are made negligible for the entangling gates presented in Chap. 6. Laser pulse shaping is not implemented for the gates presented in Chap. 5 and Chap. 7 due to the unavailability of high-speed apparatus (see Sec. 3.8) when these two experiments were performed. However, errors caused by off-resonant coupling are small compared to other dominant errors in these two implementations.

4.4.6 Imperfect Lamb-Dicke Approximation

Geometric phase gates are robust against thermal excitation in the Lamb-Dicke limit [Sørensen 99, Sørensen 00]. However, depending on the ion species and the confinement parameters, this condition might not be rigorously satisfied. Because of this, the realistic MS interaction (used here as an example) applied to the ions deviates from the desired Hamiltonian of Eq. 4.15.

One such effect is the dependence of sideband transition Rabi rates on the motional Fock states. In general, the Rabi rate of spin-motional transitions between Fock states labeled by their respective quantum number n and n' is given in Eq. 2.15. The non-ideal implementation of the desired Hamiltonian due to the different Rabi rates between different Fock states has been studied in Ref. [Sørensen 00] for the MS gate, with error

$$\epsilon_{\mathrm{LD}} = \frac{\pi^2}{4}\eta^4 Var(n), \tag{4.45}$$

$$= \frac{\pi^2}{4}\eta^4 \bar{n}(\bar{n}+1), \tag{4.46}$$

where the assumption of a thermal distribution (Eq. 2.10) with mean occupation number of $\bar{n}$ for the motional mode is made in Eq. 4.46. For the parameters used in Chap. 5, 6, and 7, the gate errors caused by this mechanism are usually small compare to other error sources.

4.4.7 Rabi Rate Fluctuations

Errors can be caused by fluctuations in the Rabi rates of the geometric phase gates, which cause fluctuations in the state-dependent forces. Physical sources includes (i) fluctuations in the laser beam intensities at the ion location, (ii) fluctuations of the ion's micro-motion amplitude, and (iii) fluctuations in the Debye-Waller factors of spectator motional modes that cause fluctuations in the Rabi rate of spin-motion transitions.

For most cases, the gate Rabi rate fluctuations occur at a time scale slower than the gate speed. Thus it can be modeled with trial-to-trial fluctuations. Through numerical simulations by solving the Schrödinger equation combined with a Monte Carlo simulation, we derived an empirical

formula of

$$\epsilon_\Omega \simeq 2.5 \times \left(\frac{\delta\Omega}{\Omega}\right)^2, \tag{4.47}$$

describing the error of creating a Bell state with a single-loop geometric phase gate due to Rabi rate fluctuations (this agrees with the expression in Ref. [Benhelm 08]).

Debye-Waller coupling is the effect where the Rabi rate of a particular spin-motion transition is dependent on the excitations of other motional modes. This is another effect that causes the implemented Hamiltonian to deviate from the desired Hamiltonian of Eq. 4.15.

Consider two ions interacting with two Raman laser fields arranged in the geometry shown in Fig. 4.4 where only the two axial motional modes can be driven. The Rabi rate of a spin-motion transition driven resonantly on the stretch mode between different Fock states is generalized from Eq. 2.15 and given by [Wineland 98]:

$$\Omega_{n_S,n'_S} = \Omega_0 \left| \; n_C, n'_S \middle| e^{i\eta_S(\hat{a}_S + \hat{a}_S^\dagger)} e^{i\eta_C(\hat{a}_C + \hat{a}_C^\dagger)} \middle| n_C, n_S \right\rangle \right|, \tag{4.48}$$

where Ω_0 is the Rabi rate of the resonant carrier transition, $n_{\mathrm{C,S}}$, $\eta_{\mathrm{C,S}}$ and $\hat{a}_{\mathrm{C,S}}$ are the Fock state quantum number, Lamb-Dicke parameter, and the annihilation operator for the center-of-mass (C) and stretch (S) mode, respectively. Thus, the Rabi rate deviations for given values n_S and n'_S on the stretch mode are given by [Wineland 98]

$$\delta\Omega_{n_S,n'_S} = \sqrt{\left\langle \left(\Omega_{n_S,n'_S} - \langle \Omega_{n_S,n'_S} \rangle \right)^2 \right\rangle}, \tag{4.49}$$

$$= \sqrt{\langle \Omega^2_{n_S,n'_S} \rangle - \langle \Omega_{n_S,n'_S} \rangle^2}. \tag{4.50}$$

Assuming that the center-of-mass mode follows a thermal distribution, with Eq. 4.50, the fractional Rabi rate fluctuations can be simplified and approximated, given by [Wineland 98]:

$$\frac{\delta\Omega_{n_S,n'_S}}{\Omega_{n_S,n'_S}} \approx \sqrt{\eta_C^4 \bar{n}_C \left(\bar{n}_C + 1\right)}. \tag{4.51}$$

Analogously, the Rabi rate of the center-of-mass mode is also dependent on the stretch mode. The errors contributed to the entangling gate can then be computed with Eq. 4.47.

Equation 4.50 can be easily generalized to include the contributions from radial modes, where applicable depending on the laser beams geometry. In general, given a thermal distribution for each

of the multiple spectator modes, the r.m.s. Rabi rate fluctuation of the mode of interest can be described by

$$\frac{\delta\Omega}{\Omega} \approx \sqrt{\sum_k \eta_k^4 \bar{n}_k \left(\bar{n}_k + 1\right)}, \tag{4.52}$$

where η_k and $\bar{n}_k$ are the Lamb-Dicke parameter and the mean occupation number for the kth spectator mode [Wineland 98].

Errors caused by Rabi rate fluctuations are more pronounced in the dynamical decoupling entangling gate presented in Chap. 7 due to a less robust laser beams setup in a legacy system. With an upgraded experimental setup (see Sec. 3), the mixed-species entangling gate (Chap. 5) and the entangling gate with two $^9Be^+$ (Chap. 6) suffer less Rabi rate fluctuation errors.

4.4.8 Rabi Rate Imbalance

Two cases of Rabi rate imbalance are considered here. The first is the Rabi rate imbalance between the two ions, i.e., $\Omega_1 \neq \Omega_2$ in Eq. 4.10 or in Eq. 4.20. This can be caused by (i) unequal illumination of laser beams due to misalignment for two ions of the same species, or (ii) separate illumination of each ion with individual sets of laser beams (e.g., the mixed-species gate described in Chap. 5). Second, for the Mølmer-Sørensen protocol, the detuned blue and red sidebands have different Rabi rates (i.e. $\Omega_{r,j} \neq \Omega_{b,j}$ in Eq. 4.19). By using numerical simulation solving the Schrödinger equation, it was found that the gate error caused by these two sources are usually small, typically on the order of $\sim 10^{-5}$ if the imbalance is on the few percent level. In most of our experiments, the Rabi rate difference between the blue and red sidenband transitions can usually be calibrated to be less than one percent.

The $\hat{\sigma}_z\hat{\sigma}_z$ gate and the $\hat{\sigma}_\phi\hat{\sigma}_\phi$ gate based on the Bermudez protocol are not affected by coupling strength imbalance between the blue and red sideband excitations.

4.4.9 Laser Phase Drift and Fluctuations

Taking the example of the Mølmer-Sørensen gate described in Eq. 4.20, as seen in Eq. 4.21, the entanglement created depends on the phase terms $\phi_{j,r(b)} = \Delta k_{j,r(b)} X_{0,j} + \Delta\phi_{j,r(b)}$, where $\Delta\phi_{j,r(b)}$

is the phase difference between the optical fields labeled as $\boldsymbol{k}_1$ and $\boldsymbol{k}_2$ in Fig. 4.4. Phase fluctuations due to relative length changes between paths 1 and 2 lead to decoherence. Because this phase is in the same exponent as the gate detuning δ (see Eq. 4.20), such phase fluctuations can be modeled as an effective motional mode frequency fluctuation using the Lindblad operators shown in Eq. 4.39.

Compared to other errors, entangling gate errors caused by this mechanism are small with the gate durations used in the experimental implementations presented in this thesis.

4.4.10 Qubit Decoherence

Qubit decoherence or dephasing can be caused by external magnetic-field fluctuations, or fluctuating AC Stark shifts induced by the laser beams that drive the coherent operations. Such effects can be described by random rotations around the z axis of the Bloch sphere, thus can be modeled as the following Lindblad operator [Uys 10]

$$\hat{L}_z(\Gamma_z) = \sqrt{\Gamma_z}\hat{\sigma}_z, \tag{4.53}$$

where Γ_z represents the qubit dephasing rate. This equation is in the same form as Eq. 4.36.

In our experiments, gate durations are typically ~ 50 μs whereas qubit coherence times are ~ 1.5 s for a $^9Be^+$ ion (Fig. 2.2) and ~ 6 ms for a $^{25}Mg^+$ ion (Fig. 2.7); they contribute negligible errors to the entangling gates presented in Chap. 5, 6, and 7. The errors associated with qubit dephasing caused by fluctuating AC Stark shifts in these implementations are also small compared to other errors.

Chapter 5

Mixed-Species Entangling Gate

5.1 Introduction

In the field of quantum information processing (QIP) and quantum networking, various proposals discuss the possibility of hybrid architectures (see for examples, Ref. [Wallquist 09, Kurizki 15, Kotler 16]), where specific tasks are delegated to the most suitable subsystem. For example, in quantum networks, it may be advantageous to transfer information from a subsystem that has long quantum memory storage time to another subsystem that is more efficient at transporting information between nodes in the network. For trapped ions, a hybrid system formed of different atomic species introduces extra degrees of freedom that can be exploited to expand and refine the control of the system.

Ions of different elements vary in mass, internal atomic structure and spectral properties, features that can make certain species better suited for particular tasks such as storing quantum information, high-fidelity readout, fast logic gates, or interfacing between local processing units and photon interconnects. One important advantage of a hybrid system incorporating trapped ions of different species is the ability to manipulate and measure one ion species using laser beams with negligible effects on the other since the relevant transition wavelengths typically differ substantially. Using different ion species also provides individual ion addressing without tight focusing of laser beams nor shuttling [Blakestad 11, Bowler 12]. When scaling trapped-ion systems to greater numbers and density of ions, it will be advantageous to perform fluorescence detection on individual qubits without inducing decoherence on neighboring qubits due to uncontrolled photon scattering

or stray scattered light.

To provide this function in a hybrid system, one can use an entangling gate to transfer the qubit states to another ion species which is then detected without perturbing the qubits. This readout protocol could be further generalized to error correction schemes by transferring the error syndromes to the readout species while the computational qubits remain in the code. Another application could be in building photon interconnects between trapped-ion devices. In this application, one species may be better suited for memory while the other is more favorable for coupling to photons [Monroe 14, Moehring 07].

A mixed-species gate can also improve the readout in quantum logic spectroscopy (QLS) [Schmidt 05]. In conventional quantum logic readout, the state of the clock or qubit ion is first transferred to a motional state and in turn transferred to the detection ion, which is then detected with state-dependent fluorescence. In this case, the transfer fidelity directly depends on the purity of the motional state. In contrast, transfer utilizing the gate discussed here can be insensitive to the motion, as long as the ions are in the Lamb-Dicke regime [Wineland 98]. This advantage extends to entanglement-assisted quantum non-demolition readout of qubit or clock ions, which can lower the overhead in time and number of readout ions as the number of clock ions increases [Schulte 16].

Ions of different species have previously been used in QIP experiments for sympathetic cooling [Barrett 03], creation of entanglement through dissipation [Lin 13a], and quantum non-demolition (QND) measurement of one species with another [Hume 07]. In this chapter, we focus on an experimental implementation of a mixed-species geometric-phase gate demonstrated using a $^{9}Be^{+}$ and a $^{25}Mg^{+}$ ion. The geometric phase gate is realized through an effective spin-spin interaction generated by state-dependent forces [Sørensen 99, Sørensen 00, Milburn 00, Solano 99, Leibfried 03] induced with laser beams. Combined with single-qubit gates and same-species entangling gates, this mixed-species entangling gate provides a complete set of gates over such a hybrid system for universal QIP [Barenco 95, Bremner 02, Zhang 03]. Using a sequence of such gates, we demonstrate a Controlled-NOT (CNOT) gate and a SWAP gate [Nielsen 00]. In Sec. 5.4, we show the robustness of these gates against thermal excitation and demonstrate improved detection in quantum logic

spectroscopy (QLS) [Schmidt 05]. Furthermore, we also subject the mixed-species entangled state created by our logic gate to a Bell inequality test [Clauser 69]; the result is reported in Sec. 5.3.2. Lastly, in Sec. 5.6 we briefly describe an implementation of the original Cirac-Zoller gate [Cirac 95] using the two species.

5.2 Experiment Setup

In our experiment, we use a beryllium ($^9Be^+$) ion and a magnesium ($^{25}Mg^+$) ion separated by approximately 4 μm along the trap axis at the $\mathcal{E}$ zone shown in Fig. 3.1. The Coulomb coupling between the ions gives rise to two shared motional normal modes along the trap axis: the lower frequency mode ($\omega_z = 2\pi \times 2.5$ MHz[1]), where the ions oscillate in phase, and the higher frequency mode ($2\pi \times 5.4$ MHz), where the ions oscillate out of phase.

The addressing laser beams for each ion ($\lambda \simeq 313$ nm for $^9Be^+$ and $\lambda \simeq 280$ nm $^{25}Mg^+$) illuminate both ions. The qubits are encoded in hyperfine states of the ions. We choose $|F = 2, m_F = 0\rangle = |\downarrow\rangle_{\mathrm{Be}}$ and $|1, 1\rangle = |\uparrow\rangle_{\mathrm{Be}}$ as the $^9Be^+$ qubit states and $|2, 0\rangle = |\downarrow\rangle_{\mathrm{Mg}}$ and $|3, 1\rangle = |\uparrow\rangle_{\mathrm{Mg}}$ for the $^{25}Mg^+$ qubit at a magnetic field of 119.446 G (see Sec. 2.1 and Sec. 2.2 for details on energy level structures).

Our entangling gate scheme is implemented through the Mølmer-Sørensen (MS) protocol [Sørensen 99, Sørensen 00] driven by stimulated-Raman transitions [Wineland 98]. The two-color laser-beam setup to drive the entangling gate is shown in Fig. 5.1. The laser beam configurations to induce coherent Raman transitions are analogous for each species; for brevity, we will only describe the configuration for $^9Be^+$ (red color in Fig. 5.1). Three laser beams, labeled by $\boldsymbol{k_{1,Co1}}$, $\boldsymbol{k_{1,Co2}}$ and $\boldsymbol{k_{1,90}}$, are derived from a single laser with wavelength $\lambda \simeq 313$ nm. Beams $\boldsymbol{k_{1,Co1}}$ and $\boldsymbol{k_{1,Co2}}$ are copropagating such that their wave vector difference with respect to the $\boldsymbol{k_{1,90}}$ beam are aligned along the trap axis. In this configuration, only the axial modes of motion interact with the laser beams. With this laser beams configuration, the Lamb-Dicke parameter for the $^9Be^+$ ($^{25}Mg^+$) ion is 0.156 (0.265) and 0.269 (0.072) for the axial in-phase mode and the out-of-phase

[1] angular frequency

mode, respectively. The two copropagating beams induce detuned blue and red sideband Raman transitions, respectively, when paired with the $\boldsymbol{k_{1,90}}$ beam to implement the MS interaction. The radio-frequency (RF) electric fields driving the AOMs to generate the beams $\boldsymbol{k_{j,Co1}}$ and $\boldsymbol{k_{j,Co2}}$ (where $j = 1, 2$) are produced by direct digital synthesizers (DDS) which are controlled by a field-programmable gate array (FPGA). The phases of these four RF fields are synchronized; this is important for the deterministic generation of entanglement and is discussed in Sec. 5.2.1 and Sec. 5.2.3. Due to the strong modulation of the ions' motion (micromotion) caused by an axial radio frequency field (see Sec. 3.1 and Ref. [Blakestad 10]), spin-motion transitions in the $^9Be^+$ ion are driven on the second micromotion sideband to maximize transition Rabi rates for the given laser intensity. Spin-motion transitions in the $^{25}Mg^+$ ion are driven on the micromotion carrier. Details of Raman laser beam lines setup are described in Sec. 3.4.3 and Sec. 3.5.2.

With this setup, the Mølmer-Sørensen interaction Hamiltonian after transforming into the respective interaction frames of both qubits as well as that of the shared motional mode of motion (here, we use the in-phase mode) and dropping high-frequency terms, in the Lamb-Dicke limit is (Eq. 4.19)

$$H = \hbar \sum_{j=1,2} \Omega_{r,j} \hat{\sigma}_j^\dagger \left(\hat{a} \mathrm{e}^{-\mathrm{i}(\delta_j t - \phi_{j,r})} \right) + \hbar \sum_{j=1,2} \Omega_{b,j} \hat{\sigma}_j^\dagger \left(\hat{a}^\dagger \mathrm{e}^{\mathrm{i}(\delta_j t + \phi_{j,b})} \right) + h.c., \tag{5.1}$$

with $\Omega_{r(b),j} = \Omega_{0,r(b),j} \eta_j \xi_j$ where $\Omega_{0,r(b),j}$ is the Rabi rate of the resonant carrier excitation induced by the laser beams responsible for the red (r) and blue (b) sideband excitations, η_j is the Lamb-Dicke parameter of the in-phase mode with ξ_j as the mode amplitude of the jth ion. If we set $\Omega_{0,r,j} = \Omega_{0,b,j} = \Omega_{0,j}$ then Eq. 5.1 becomes

$$\begin{aligned} H &= \hbar \sum_{j=1,2} \Omega_j \hat{\sigma}_j^\dagger \left(\hat{a} \mathrm{e}^{-\mathrm{i}(\delta_j t - \phi_{j,r})} + \hat{a}^\dagger \mathrm{e}^{\mathrm{i}(\delta_j t + \phi_{j,b})} \right) + h.c., \\ &= \hbar \sum_{j=1,2} \Omega_j \hat{\sigma}_j^\dagger \left(\hat{a} \mathrm{e}^{-\mathrm{i}(\delta_j t - (\Delta k_{j,r} X_{0,j} + \Delta\phi_{j,r}))} + \hat{a}^\dagger \mathrm{e}^{\mathrm{i}\left(\delta_j t + (\Delta k_{j,b} X_{0,j} + \Delta\phi_{j,b})\right)} \right) + h.c., \end{aligned} \tag{5.2}$$

with $\Omega_j = \Omega_{0,j} \eta_j \xi_j$ where $\Omega_{0,j}$ is the carrier resonant Rabi frequency. The Lamb-Dicke parameter η_j is equal to $\Delta k_j z_{0,j}$, where $z_{0,j} = \sqrt{\hbar / 2 m_j \omega_z}$, m_j is the mass and ω_z is the frequency of the in-phase mode. The phases of the red (r) and blue (b) sideband interactions are $\phi_{j,r(b)} = \Delta k_{j,r(b)} X_{0,j} +$

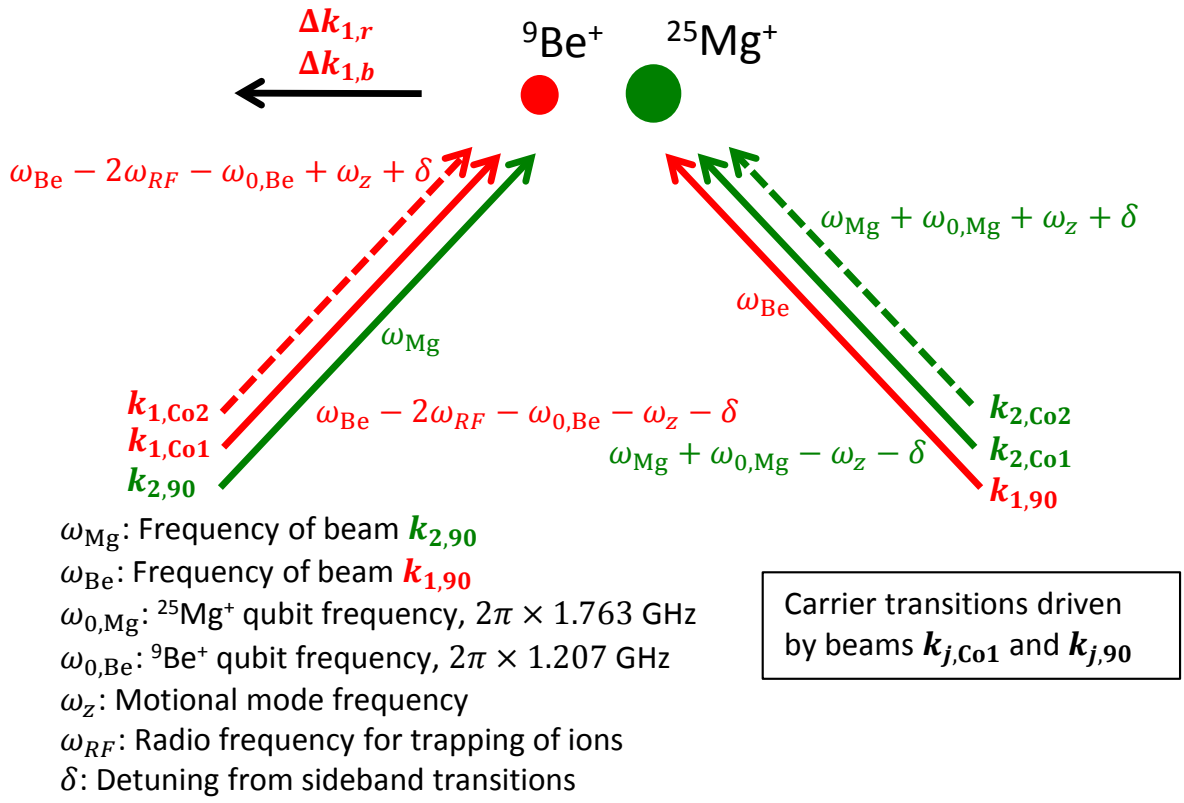

Figure 5.1: Configuration of laser beams for the mixed-element entangling gate. For the ^{9}Be$^+$ ion, 313 nm laser beams (in red) simultaneously induce near-resonant red and blue sidebands transitions. Similarly, for ^{25}Mg$^+$, 280 nm beams (in green) induce sideband transitions. When all beams are applied simultaneously, this implements the Mølmer-Sørensen spin-spin interaction [Sørensen 99, Sørensen 00]. Each set of qubit addressing laser beams is set up such that the wave vector differences $\boldsymbol{\Delta k_{j,r}} = \boldsymbol{k_{j,90}} - \boldsymbol{k_{j,\mathrm{Co1}}}$ and $\boldsymbol{\Delta k_{j,b}} = \boldsymbol{k_{j,90}} - \boldsymbol{k_{j,\mathrm{Co2}}}$ $(j = 1, 2)$ are aligned in the same direction along the trap axis. With this configuration, only the motional modes along this axis can be excited. The frequencies of the ^{9}Be$^+$ ion's Raman beams are set to drive the spin-motion transition on the second order micromotion sideband, this is to maximize transition Rabi rates in the presence of axial micromotion (details see Sec. 2.1.3. Spin-motion transitions in the ^{25}Mg$^+$ ion are driven on the micromotion carrier.

$\Delta\phi_{j,r(b)}$ where $\Delta k_{j,r(b)}$ and $\Delta\phi_{j,r(b)}$ are the differences in wave vectors and phases of the optical fields driving the red and blue sideband transitions respectively, and $X_{0,j}$ is the equilibrium position for the jth ion. As the Hamiltonian (Eq. 5.2) depends on these wave vectors and optical phases, it is important to consider their effects for creating deterministic entanglement.

In our implementation, $\boldsymbol{\Delta k_{j,r} = k_{j,90} - k_{j,Co1}}$ and $\boldsymbol{\Delta k_{j,b} = k_{j,90} - k_{j,Co2}}$ for $j = 1, 2$. Beams $\boldsymbol{k_{j,Co1}}$ and $\boldsymbol{k_{j,Co2}}$ are generated in the same acousto-optic modulator (AOM), one for each ion species, and travel nearly identical paths. With this setup, the relative optical phase drift between these two beams is negligible. However, the $\boldsymbol{k_{j,90}}$ beams take a substantially different path to reach the ions' locations (see Sec. 3.4.3 and 3.5.2 for detailed beam line setups). The resulting slow phase drifts can be taken account of as described below.

5.2.1 Optimizing the Strength of Spin-Dependent Forces

The basis states $|+\rangle_j$ and $|-\rangle_j$ in which the spin-dependent forces generated by the MS interaction are applied is defined as the eigenstates of

$$\hat{\sigma}_{\phi,j} = \cos\left((\phi_{j,r} + \phi_{j,b})/2\right)\hat{\sigma}_{x,j} - \sin\left((\phi_{j,r} + \phi_{j,b})/2\right)\hat{\sigma}_{y,j}. \tag{5.3}$$

With the notation of $|+\rangle_{\mathrm{Be}}|+\rangle_{\mathrm{Mg}} = |+,+\rangle$, the truth table after applying the MS gate is

$$\begin{aligned} |+,+\rangle &\rightarrow e^{i\varphi_{++}}|+,+\rangle, \\ |+,-\rangle &\rightarrow e^{i\varphi_{+-}}|+,-\rangle, \\ |-,+\rangle &\rightarrow e^{i\varphi_{-+}}|-,+\rangle, \\ |-,-\rangle &\rightarrow e^{i\varphi_{--}}|-,-\rangle. \end{aligned} \tag{5.4}$$

After setting $\Omega_1 = \Omega_2 = \Omega$ (calibration procedure in the next section) and $\delta_1 = \delta_2 = \delta$, and writing $\phi_{M,j} = (\phi_{j,r} - \phi_{j,b})/2$, the geometric phases accumulated after a duration of $t_{\mathrm{gate}} = 2\pi/\delta$ are [Tan 15]

$$\begin{aligned} \varphi_{++,--} &= \frac{8\pi\Omega^2}{\delta^2}\cos^2\left(\frac{\phi_{M,1} - \phi_{M,2}}{2}\right)\Bigg(\\ \varphi_{+-,-+} &= \frac{8\pi\Omega^2}{\delta^2}\sin^2\left(\frac{\phi_{M,1} - \phi_{M,2}}{2}\right)\Bigg(\end{aligned} \tag{5.5}$$

From the definitions of the different phase terms, it can be shown that $\phi_{M,1} - \phi_{M,2}$ depends on the relative phase differences between the two copropagating beams $\boldsymbol{k_{j,\mathrm{Co1}}}$ and $\boldsymbol{k_{j,\mathrm{Co2}}}$ for each ion. For each species, the optical phase difference between these two beams is set by the RF injected into the AOM that generates them. Thus, it is important that the phases of the four RF signals (two for each species) are synchronized. By adjusting the phases of the RF signals driving the AOMs that generate these laser beams, the difference in the geometric phases for the different parity qubit states in Eq. 5.5 can be optimized. In our experiment, this optimization is performed by adjusting the phase of one of the RF signals while keeping the remaining three fixed when we apply the MS interaction at the duration of $t_{\mathrm{gate}} = 2\pi/\delta$ with δ fixed; we adjust for the phase that equalizes the populations in the $|\uparrow\uparrow\rangle$ and $|\downarrow\downarrow\rangle$ states with a minimal amount of laser intensity.

5.2.2 Calibration Procedure for the Mixed-Species MS Gate

The MS protocol shown in Eq. 5.1 requires the Rabi rates of the red and blue sideband transitions of the two species to be equal, i.e. $\Omega_{r,1} = \Omega_{b,1} = \Omega_{r,2} = \Omega_{b,2}$. To accomplish this, we first minimize the red and blue sideband Rabi rate imbalance for each species by performing sideband Rabi flopping experiments. We differentially adjust the laser power in beams $\boldsymbol{k_{j,Co1}}$ and $\boldsymbol{k_{j,Co2}}$ (Fig. 5.1) while keeping the total laser power in this path fixed. In our procedure, the beam that is responsible for the red sideband excitation is first detuned from any transition when we calibrate the Rabi rate of the blue sideband transition. Analogously, we detune the beam responsible for the blue sideband when the Rabi rate of the red sideband transition is calibrated. This strategy is to ensure AC Stark shifts change negligibly during calibration. After setting $\Omega_{r,j} = \Omega_{b,j}$ for each of the two species, we adjust the laser power in the $\boldsymbol{k_{1,90}}$ and $\boldsymbol{k_{2,90}}$ beams so that $\Omega_{r(b),1} = \Omega_{r(b),2}$. This can change the AC Stark shifts on each ion, which can be compensated by changing the mean transition frequency of the red and blue sidebands. This process is iterated to finally achieve the correct tunings and equalize all four sideband Rabi rates.

Starting in the $|\uparrow\uparrow\rangle$ state, a correctly tuned MS gate with $\Omega = \delta/4$ ideally produces the

entangled state

$$|\Phi_{Bell}\rangle = \frac{1}{\sqrt{2}}\left(|\uparrow\uparrow\rangle + e^{-i\left(\sum_{j=1,2}\frac{1}{2}(\phi_{j,b}+\phi_{j,r})+\pi/2\right)}|\downarrow\downarrow\rangle\right), \tag{5.6}$$

after a duration of $t_{\text{gate}} = 2\pi/\delta$. The complete truth table of the MS gate is given in Eq. 4.21.

5.2.3 Laser Beam Phase Sensitivity

As shown in Eq. 5.3, the basis states in which the spin-dependent force is applied depends on $(\phi_{j,r} + \phi_{j,b})$, which can be shown to be dependent on the relative phase differences between the non-copropagating beams $\boldsymbol{k_{j,90} - k_{j,Co1}}$ and $\boldsymbol{k_{j,90} - k_{j,Co2}}$ (Fig. 5.1). Temperature drift and acoustic noise can cause changes in the lengths of different beam paths, which can lead to phase fluctuations in the MS interaction. These fluctuations are slow on the timescale of a single gate but substantial over the course of many experiment repetitions. To suppress these effects, we embed the MS interaction in a Ramsey sequence (Fig. 5.2) implemented with two $\pi/2$ carrier pulses induced by $\boldsymbol{k_{j,Co1}}$ and $\boldsymbol{k_{j,90}}$ for each qubit [Lee 05, Tan 15]. Without loss of generality, (see next section) we choose the phases of the first $\pi/2$ pulses to implement the rotations $R\left(\theta = \frac{\pi}{2}, \phi = \frac{\pi}{2}\right)$. This maps the $|\uparrow\rangle$ and $|\downarrow\rangle$ states of each qubit onto the $|+\rangle_j$ and $|-\rangle_j$ states (defined in Eq. 5.3), whose phases are synchronized with the MS interaction. The final set of $R\left(\frac{\pi}{2}, -\frac{\pi}{2}\right)$ pulses undoes this mapping such that the action of this sequence is independent of the beam path length differences as long as the differences are constant during the entire sequence. With this Ramsey sequence, the overall sequence produces a deterministic phase gate $\widehat{G}$ that implements (up to a global phase of $e^{i\pi/4}$) $|\uparrow\uparrow\rangle \rightarrow |\uparrow\uparrow\rangle$, $|\uparrow\downarrow\rangle \rightarrow i|\uparrow\downarrow\rangle$, $|\downarrow\uparrow\rangle \rightarrow i|\downarrow\uparrow\rangle$, and $|\downarrow\downarrow\rangle \rightarrow |\downarrow\downarrow\rangle$ or, in matrix form:

$$\widehat{G} = \begin{pmatrix} \begin{pmatrix} 1 & 0 & 0 & 0 \\ 0 & i & 0 & 0 \\ 0 & 0 & i & 0 \\ 0 & 0 & 0 & 1 \end{pmatrix} \begin{pmatrix} \\ \\ \\ \\ \end{pmatrix} \\ \begin{pmatrix} \\ \\ \\ \\ \end{pmatrix} \begin{pmatrix} \\ \\ \\ \\ \end{pmatrix} \end{pmatrix}, \tag{5.7}$$

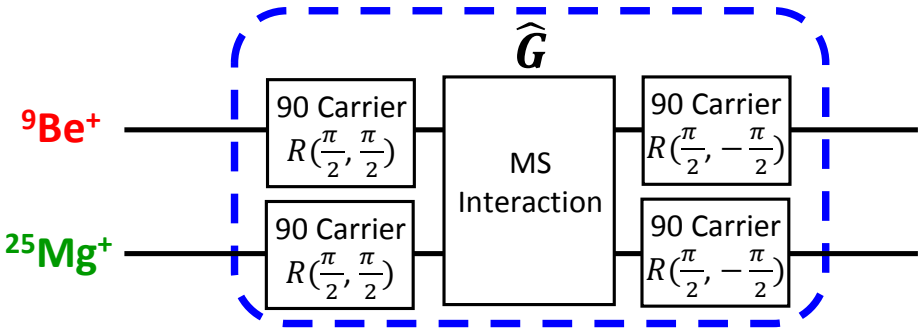

Figure 5.2: A Ramsey sequence implemented to remove laser phase sensitivity of the MS interaction. The "90 Carrier" $\pi/2$ pulses are implemented by Raman laser beams induced by $\boldsymbol{k_{j,\mathrm{Co1}}}$ and $\boldsymbol{k_{j,90}}$ (see Fig. 5.1). The overall sequence produces a phase gate $\widehat{G}$ which is given in Eq. 5.7. The rotation $R(\theta, \phi)$ is defined in Eq. 2.13.

with basis states of the two qubits given by

$$|\uparrow\rangle_{\mathrm{Be}}|\uparrow\rangle_{\mathrm{Mg}} = \begin{pmatrix} \begin{pmatrix} 1 \\ 0 \end{pmatrix} \\ \begin{pmatrix} 0 \\ 0 \end{pmatrix} \end{pmatrix}, |\uparrow\rangle_{\mathrm{Be}}|\downarrow\rangle_{\mathrm{Mg}} = \begin{pmatrix} \begin{pmatrix} 0 \\ 1 \end{pmatrix} \\ \begin{pmatrix} 0 \\ 0 \end{pmatrix} \end{pmatrix}, |\downarrow\rangle_{\mathrm{Be}}|\uparrow\rangle_{\mathrm{Mg}} = \begin{pmatrix} \begin{pmatrix} 0 \\ 0 \end{pmatrix} \\ \begin{pmatrix} 1 \\ 0 \end{pmatrix} \end{pmatrix}, |\downarrow\rangle_{\mathrm{Be}}|\downarrow\rangle_{\mathrm{Mg}} = \begin{pmatrix} \begin{pmatrix} 0 \\ 0 \end{pmatrix} \\ \begin{pmatrix} 0 \\ 1 \end{pmatrix} \end{pmatrix}. \quad (5.8)$$

5.2.4 Calibration Procedure for Phase Gate $\widehat{G}$

To produce the phase gate $\widehat{G}$, the phases of the $\pi/2$ pulses in the Ramsey sequence (Fig 5.2) must be referenced to the basis states of the MS interaction defined by the optical phases. The phases must also account for the AC Stark shifts induced by the laser beams that are used for the MS interaction (AC Stark shifts are effective R_z rotations on the qubits).

To calibrate these phases, we first perform the pulse sequence shown in Fig. 5.2 with the MS interaction pulses detuned far off-resonant from the red and blue sideband transitions such that they only induce AC Stark shifts on the qubits. Starting with the input state $|\uparrow\uparrow\rangle$, we set the phases of the final $\pi/2$ laser pulses such that the action of this pulse sequence returns each qubit to the $|\uparrow\rangle$ state. Then, we perform this sequence with the MS interactions correctly tuned and vary the phases of the MS interactions. Again, in this case we look for the phase that maps the input

state $|\uparrow\uparrow\rangle$ back to itself. We verify the action of this $\widehat{G}$ operation by creating a Bell state with the pulse sequence shown in Fig. 5.4.

5.3 Experimental Results

Before applying the gate, the ions are first Doppler cooled in all three directions. The axial vibrational modes are further cooled to near the ground state by stimulated-Raman sideband cooling on the $^9Be^+$ ion [Monroe 95b] (details see Sec. 2.1.5). For state initialization, transfer of the $^9Be^+$ $|2,2\rangle$ state to the $|1,1\rangle = |\uparrow\rangle_{\rm Be}$ state is accomplished by a microwave-driven composite pulse sequence that is robust against transition detuning errors. The sequence consists of resonant $R\left(\frac{\pi}{2},0\right)$, $R\left(\frac{3\pi}{2},\frac{\pi}{2}\right)$, $R\left(\frac{\pi}{2},0\right)$ pulses [Levitt 86], where the definition of the $R(\theta,\phi)$ rotation is given in Eq. 2.13. With analogous sequence, we first transfer the $^{25}Mg^+$ ion from the $|3,3\rangle$ state to the $|2,2\rangle$ state, and then to the $|3,1\rangle = |\uparrow\rangle_{\rm Mg}$ state.

State-dependent fluorescence detection is accomplished with an achromatic lens system designed for 313 nm and 280 nm (see Sec. 3.3). We sequentially image each ion's fluorescence onto a photomultiplier tube. Before applying the detection laser beams, we reverse the initial qubit state preparation procedures to put the $|\uparrow\rangle$ states back to the $|2,2\rangle$ and $|3,3\rangle$ state for $^9Be^+$ and $^{25}Mg^+$, respectively. The $|\downarrow\rangle$ state of each qubit is transferred to $|1,-1\rangle$ and $|2,-2\rangle$ for the $^9Be^+$ and $^{25}Mg^+$, respectively, with microwave carrier π pulses. We detect on average approximately 30 photons for each ion when they are in the bright state and approximately 2 photons when they are in the dark state. The qubit state is determined by choosing a photon count threshold such that the states are maximally distinguished. Details on state initialization and readout is described in Chap. 2. After each repetition, we measure one of the possible states: $|\uparrow\uparrow\rangle$, $|\uparrow\downarrow\rangle$, $|\downarrow\uparrow\rangle$, or $|\downarrow\downarrow\rangle$. Here, we label the probabilities of measuring $|\uparrow\uparrow\rangle$ and $|\downarrow\downarrow\rangle$ as $P_{\uparrow\uparrow}$ and $P_{\downarrow\downarrow}$, respectively. The sum of the probabilities of measuring $P_{\uparrow\downarrow}$ and $P_{\downarrow\uparrow}$ is labeled as $P_{\uparrow\downarrow+\downarrow\uparrow}$.

In a first experiment, after calibrating the gate as described in Sec. 5.2.2 and Sec. 5.2.1, we apply the MS interaction described by Eq. 5.2 and record the populations as a function of interaction time. As shown in Fig. 5.3, at a gate time $t_{\rm gate} \simeq 33$ μs, a Bell state $|\Phi_{Bell}\rangle$ (Eq. 5.6)

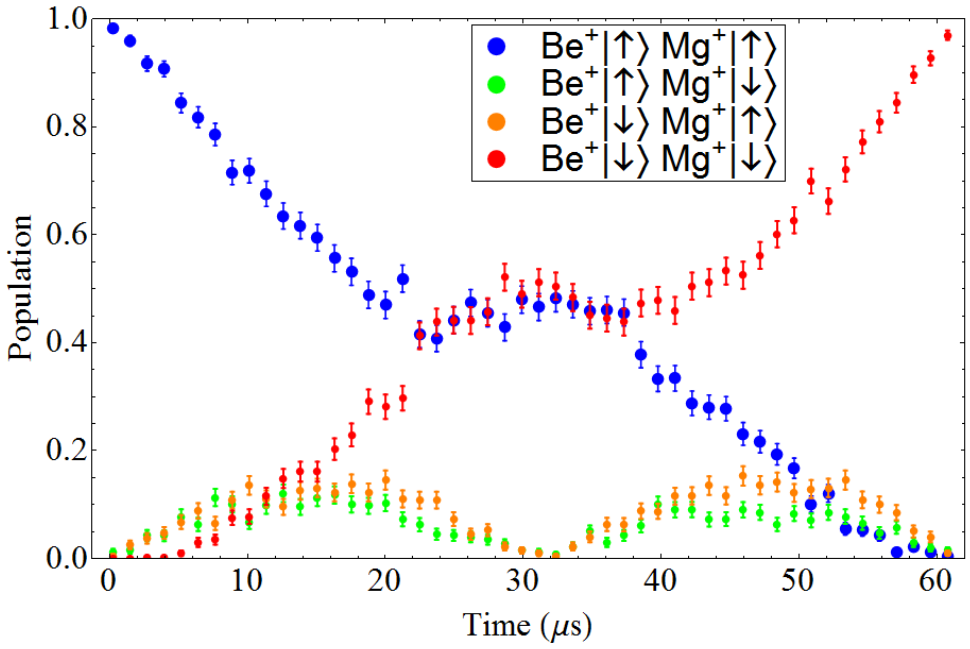

Figure 5.3: Population evolution as we apply the MS interaction starting from the $|\uparrow\uparrow\rangle$ state. The Bell state $|\Phi_{Bell}\rangle$ (Eq. 5.6), which corresponds to (ideally) equal population in the $|\uparrow\rangle_{\mathrm{Be}}|\uparrow\rangle_{\mathrm{Mg}}$ and $|\downarrow\rangle_{\mathrm{Be}}|\downarrow\rangle_{\mathrm{Mg}}$, is created at $t_{\mathrm{gate}} \simeq 33\mu$s. Error bars correspond to standard error of the mean.

is created. The performance of the gate is characterized by measuring the Bell state fidelity, which is given by $\langle\Phi_{Bell}|\rho_{exp}|\Phi_{Bell}\rangle$ where the density matrix ρ_{exp} describes the experimentally produced state. The $\uparrow\uparrow$ and $\downarrow\downarrow$ diagonal elements of the density matrix are determined from the sum of $P_{\uparrow\uparrow}$ and $P_{\downarrow\downarrow}$, which we measure to be 0.984(1). The coherence of this Bell state is investigated with a parity ($P_{\uparrow\uparrow} + P_{\downarrow\downarrow} - P_{\uparrow\downarrow+\downarrow\uparrow}$) oscillation experiment by applying "analysis" pulses [Sackett 00]. The analysis pulses are laser carrier transitions induced by the non-copropagating laser beams $\boldsymbol{k_{j,\mathbf{Co1}}}$ and $\boldsymbol{k_{j,\mathbf{90}}}$ such that the relative phase defining the basis states of MS interaction is stable with respect to that of the analysis pulses for each experiment repetition. The off-diagonal elements $\rho_{\downarrow\downarrow,\uparrow\uparrow}$ are determined from the contrast of the parity oscillation (A) to be 0.974(1). The overall Bell state fidelity is $(P_{\uparrow\uparrow} + P_{\downarrow\downarrow} + A)/2$, which is deduced to be 0.979(1).

To test the $\widehat{G}$ operation and its laser phase insensitivity, we prepare a Bell state by applying microwave carrier $\pi/2$ pulses on each qubit before and after the operation $\widehat{G}$ (described in Sec. 5.2.4) as depicted in Fig. 5.4. Using a similar procedure, we determine the total population in the $P_{\uparrow\uparrow}$ and $P_{\downarrow\downarrow}$ states to be 0.976(1), and $A = 0.955(1)$, which corresponds to a Bell state fidelity of 0.964(1). Figure 5.5 shows the parity oscillation of the Bell state created by the $\widehat{G}$ operation. The analysis pulses are driven by microwave fields whose phases are not synchronized with those of the lasers, demonstrating the laser-phase insensitivity of $\widehat{G}$ gate and the deterministic creation of the mixed-species Bell state.

5.3.1 Imperfections

We investigated the imperfect creation of the entangled states through calibration measurements and numerical simulations.

We estimated the error from imperfect state preparation and measurement (SPAM error) to be 5×10^{-3}. This is given by the false determinations of the bright and dark states set by the photon count thresholds (see previous section) chosen by analyzing the histograms obtained after preparing the ions to their respective bright and dark states in separate experiments. To also account for the errors caused by qubit state initialization, the bright histogram of each ion is collected as

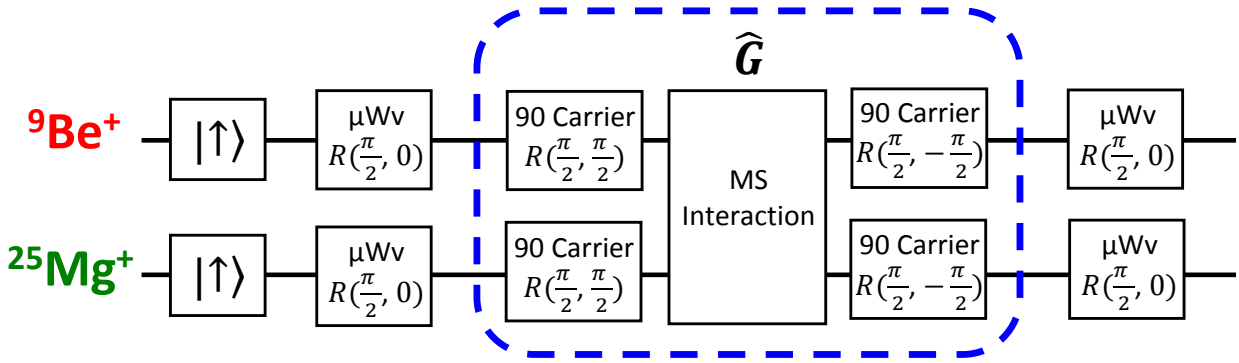

Figure 5.4: The pulse sequence using the $\widehat{G}$ gate to create the entangled state $\frac{1}{\sqrt{2}}(|\uparrow\uparrow\rangle - i|\downarrow\downarrow\rangle)$ (up to a global phase of $e^{i\pi/4}$) with both ions initialized to their respectively $|\uparrow\rangle$ state. The Bell state $|\Phi_+\rangle = \frac{1}{\sqrt{2}}(|\uparrow\uparrow\rangle + |\downarrow\downarrow\rangle)$ (up to a global phase of $e^{i\pi/2}$) can be created by applying a $R_z(\pi/2)$ rotation to one of the qubits at the end of this sequence. Likewise, applying a $R_z(-\pi/2)$ rotation to one of the qubits at the end of the sequence creates the Bell state $|\Phi_-\rangle = \frac{1}{\sqrt{2}}(|\uparrow\uparrow\rangle - |\downarrow\downarrow\rangle)$. The definition of R_z is given in Eq. D.5. The notation "μWv" is used to represents rotations implemented with a microwave field.

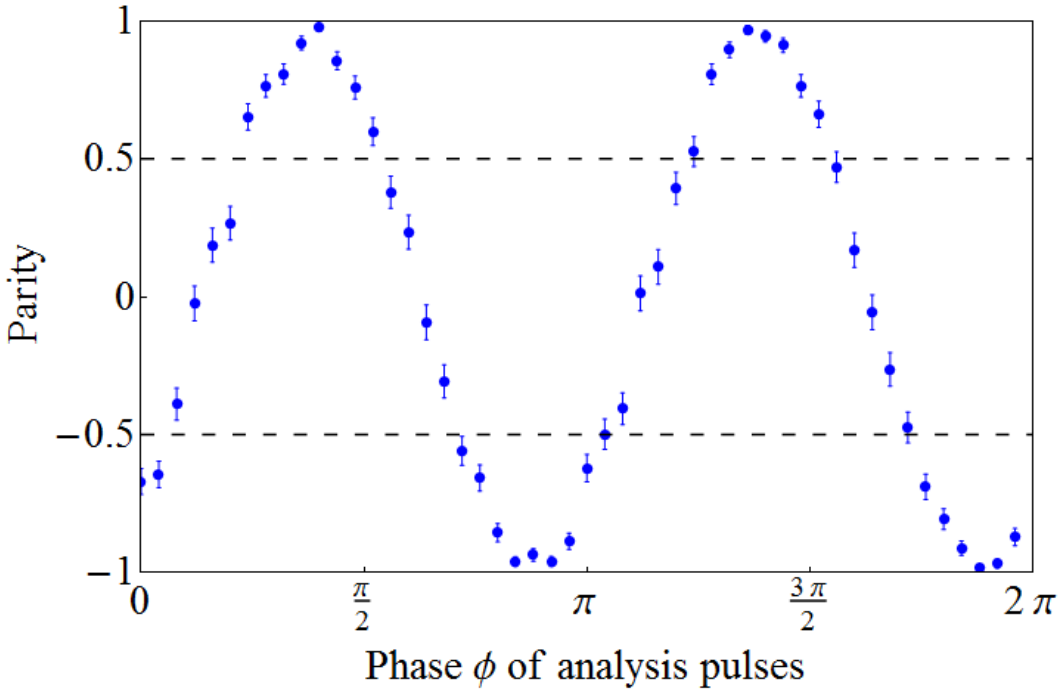

Figure 5.5: Parity ($P_{\uparrow\uparrow} + P_{\downarrow\downarrow} - P_{\uparrow\downarrow+\downarrow\uparrow}$) flopping of the Bell state created by the sequence shown in Fig. 5.4. To demonstrate laser-phase insensitivity of our entangling operation and the deterministic creation of entanglement, we use microwave fields to induce the "analysis" pulses with variable phases in this parity oscillation experiment. The phases of the microwave fields are not synchronized with those of the laser fields.

follows: we apply the qubit state initialization procedure to prepare each ion to its computational $|\uparrow\rangle$ state (see previous section), wait for ~ 1.5 ms, then reverse the initialization sequence and apply shelving pulses to transfer the qubit population to the measurement qubit manifold (see Fig. 2.1 and Fig. 2.6 for the energy level diagrams of the $^9Be^+$ ion and $^{25}Mg^+$ ion, respectively). Finally, the ions' states were measured with state-dependent fluorescence detection. The wait time (~ 1.5 ms) between the transfer from computational to measurement qubit manifolds was long enough to minimize coherent effects between the transfer into and out of the computational manifold. The coherence times of these transfer transitions are typically ~ 1 ms or less.

Errors caused by spontaneous photon scattering [Ozeri 07] from the Raman beams were estimated to be $\sim 6 \times 10^{-3}$ for the $^{25}Mg^+$ ion and $\sim 1 \times 10^{-3}$ for the $^9Be^+$ ion. This error was deduced by performing numerical master equation simulations including the Lindblad operators describing the spontaneous scattering of photons (see Sec. 4.4.2.1), with the scattering rate calculated with the Kramer-Heisenberg equation [Cline 94] shown in Eq. 4.29. We also experimentally measured the Raman scattering rate by applying the laser pulses used for the entangling gate but with the MS interaction set far-detuned from both the red and blue sideband excitations such that they do not induce any coherent excitation. The scattering rate is determined from loss of population in the qubit manifold; these measurements agree with the calculations made using the Kramer-Heisenberg equation.

We measured the heating of the in-phase mode [Turchette 00a] due to ambient electric field noise to be approximately 160 quanta/s, which contributes an error of approximately 4×10^{-3} to the created Bell state. This error was estimated using a master equation simulation with the Lindblad operators describing the heating (see Sec. 4.4.4).

Other known error sources include imperfect single-qubit pulses, off-resonant coupling to spectator hyperfine states and the other motional modes, mode frequency fluctuations, qubit decoherence due to magnetic field fluctuations, laser intensity fluctuations, optical phase fluctuations, and calibration errors. Each of these sources contributes error on the order of 10^{-3} or less. Details of the evaluation of these errors are discussed in Sec. 4.4.

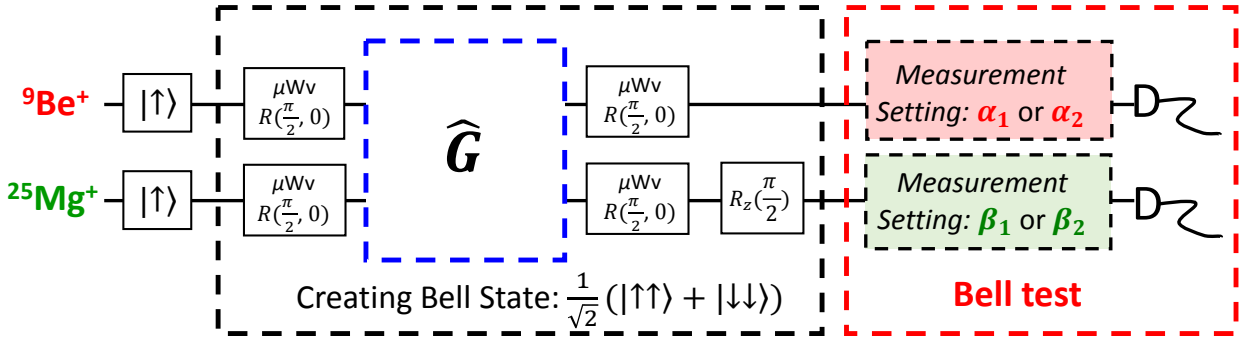

Figure 5.6: Pulse sequence for the CHSH-type Bell inequality experiment on the mixed-species Bell state. The black dashed box denotes the "black box" which prepares the two particles of different species. The measurement settings α_i, β_j are applied (with microwave fields) before making fluorescence measurements. The laser pulse sequence for the implementation of $\widehat{G}$ is shown in Fig. 5.2. The rotations $R(\theta, \phi)$ and $R_z(\xi)$ are defined in Eq. 2.13 and Eq. D.5, respectively. $R_z(\xi)$ rotation is accomplished by adjusting the phase of the DDS which is used to produce the microwave fields.

Errors due to motional heating can be significantly reduced if the out-of-phase mode is used instead of the in-phase mode for the state-dependent force because the heating rate of the out-of-phase mode was measured to be $\sim$ 30 quanta/s. We used the in-phase mode because for the $^{25}Mg^{+}$ ion, it has a larger normal mode amplitude (0.265) compared to the out-of-phase mode (0.072). This results in less spontaneous emission error for a given strength of the state-dependent force. Error caused by spontaneous emission can be reduced by increasing Raman detuning at the cost of higher laser intensity to keep the Rabi rate constant [Ozeri 07]. When this experiment was performed, the available optical power in each of the $^{25}Mg^{+}$ Raman beams was only $\sim$ 1 mW, compared to $\sim$ 50 mW in each of the Raman beams for the $^{9}Be^{+}$ ion.

5.3.2 Mixed-Species Bell Inequality Test

Using the $^{9}Be^{+}$ - $^{25}Mg^{+}$ Bell state, we performed a Clauser-Horne-Shimony-Holt (CHSH) type Bell-inequality test [Clauser 69]. The pulse sequence is shown in Fig. 5.6. The source, which can be treated as a "black box", ideally creates a Bell state $|\Phi_+\rangle = \frac{1}{2}(|\uparrow\uparrow\rangle + |\downarrow\downarrow\rangle)$ and is regarded as the starting point of the following Bell test experiment.

Two measurement setting choices on each species, labeled as α_1, α_2 for the $^{9}Be^{+}$ ion, and

β_1, β_2 for the $^{25}Mg^+$ ion, were applied to the prepared state before making qubit state measurements. This is equivalent to choosing the measurement basis for the state that is present before the measurement settings are applied. Joint measurement outcomes of $|\uparrow\uparrow\rangle$ and $|\downarrow\downarrow\rangle$ were recorded as correlated events while $|\uparrow\downarrow\rangle$ and $|\downarrow\uparrow\rangle$ were recorded as anticorrelated events. Each of the four measurement setting combinations were performed with multiple repetitions, then iterated with different measurement setting combinations. For each measurement setting combinations, we computed the correlation of these outcomes

$$q(\alpha_i, \beta_j) = \frac{N_{\text{correlated}}(\alpha_i, \beta_j) - N_{\text{anticorrelated}}(\alpha_i, \beta_j)}{N_{\text{correlated}}(\alpha_i, \beta_j) + N_{\text{anticorrelated}}(\alpha_i, \beta_j)}, \tag{5.9}$$

for $i, j = 1, 2$. For a local realistic theory to be valid, the sum of correlation B_{CHSH} (at expectation) must satisfy [Clauser 69, Rowe 01]

$$\begin{aligned} B_{\text{CHSH}} &= |q(\alpha_1, \beta_1) + q(\alpha_2, \beta_1)| + |q(\alpha_1, \beta_2) - q(\alpha_2, \beta_2)| \\ &\leq 2. \end{aligned} \tag{5.10}$$

The measurement settings are applied with microwave-induced spin rotations $R(\frac{\pi}{2}, \alpha_i \text{ or } \beta_j)$ which are controlled by classical parameters. Ideally, the rotations for the $^9Be^+$ ion can be described as:

$$\begin{aligned} |\uparrow\rangle &\rightarrow \frac{1}{\sqrt{2}}\left(|\uparrow\rangle - e^{-i\alpha_i}|\downarrow\rangle\right) \\ |\downarrow\rangle &\rightarrow \frac{1}{\sqrt{2}}\left(|\downarrow\rangle - e^{i\alpha_i}|\uparrow\rangle\right) \end{aligned} \tag{5.11}$$

and analogously for the $^{25}Mg^+$ ion with α_i replaced by β_j. They are implemented by setting the durations and phases of the microwave pulses transmitted from two microwave antennas (one for each species, see Sec. 2.1.4 and Sec. 2.2.3 for more details). The microwave-frequency electric potentials applied to the antennas are produced by a FPGA-controlled DDS. The classical variables are the phases of the oscillating fields that implement a particular setting α_i and β_j.

The measurement settings α_i, β_j and the correlation outcomes $q(\alpha_i, \beta_j)$ are given in Table 5.1. We determined the sum of correlation B_{CHSH} to be 2.70(2). This inequality, measured on an

Measurement Setting on $^{9}Be^{+}$	$\alpha_1 = -\frac{\pi}{8}$	$\alpha_1 = -\frac{\pi}{8}$	$\alpha_2 = \frac{3\pi}{8}$	$\alpha_2 = \frac{3\pi}{8}$
Measurement Setting on $^{25}Mg^{+}$	$\beta_1 = -\frac{\pi}{8}$	$\beta_2 = \frac{3\pi}{8}$	$\beta_1 = -\frac{\pi}{8}$	$\beta_2 = \frac{3\pi}{8}$
$q(\alpha_i, \beta_j)$	$-0.635(9)$	$-0.721(8)$	$-0.711(8)$	$0.638(9)$

Table 5.1: Correlation values for the four measurement setting combinations in the CHSH Bell inequality experiment performed on a mixed-species entangled state.

entangled system consisting of different species, agrees with the predictions of quantum mechanics while eliminating the detection loophole [Pearle 70, Clauser 74] but not the locality loophole [Bell 85]. The closely related chained Bell inequality experiments are detailed in Chap. 8.

5.4 Mixed-Species Controlled-NOT Gates

As the $\widehat{G}$ gate combined with single qubit rotations make up a universal gate set [Barenco 95, Bremner 02, Zhang 03], we can use them to construct other unitary quantum gate operations.

The controlled-NOT gate is one of the most common entangling logic gates used in the literature [Nielsen 00]. A controlled-NOT gate "flips" the state of the "target" qubit depending on the state of the "control" qubit. Here, we define the CNOT gate as the controlled-NOT gate where the first qubit serves as the control and the second qubit acts as the target. The unitary matrix of this operation is given in Eq. 4.9 with the basis states defined in Eq. 5.8. Similarly, the controlled-NOT gate with the control and target qubit roles inverted can be expressed by the matrix

$$\mathrm{CNOT}_{\mathrm{invert}} = \begin{pmatrix} \begin{pmatrix} 1 & 0 & 0 & 0 \\ 0 & 0 & 0 & 1 \end{pmatrix} \begin{pmatrix} \\ \\ \end{pmatrix} \\ \begin{pmatrix} \\ \\ \end{pmatrix} \begin{pmatrix} 0 & 0 & 1 & 0 \\ 0 & 1 & 0 & 0 \end{pmatrix} \end{pmatrix}. \tag{5.12}$$

These two CNOT gates can be implemented with the pulse sequences including $\widehat{G}$ gates and single-qubit rotations as shown in Fig. 5.7, where the $^{9}Be^{+}$ ion acts as the control of the CNOT gate and the target of $\mathrm{CNOT}_{\mathrm{invert}}$ gate. Figure 5.7 provides detailed parameters which were not discussed in Ref. [Tan 15] for brevity. The construction of CNOT presented here and the construction of

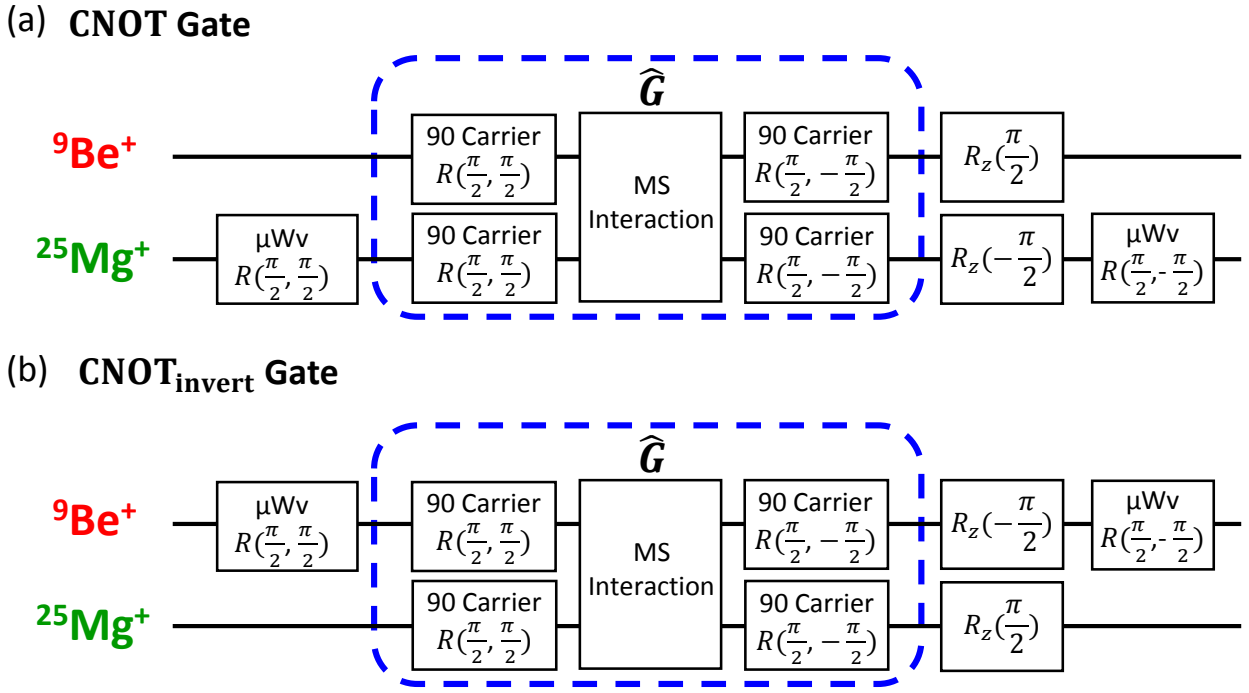

Figure 5.7: (a) Pulse sequence for the CNOT gate (Eq. 4.9) with $^{9}Be^{+}$ qubit as the "control" and $^{25}Mg^{+}$ qubit as the "target". (b) Pulse sequence for the CNOT$_{\text{invert}}$ gate (Eq. 5.12), where the two qubits change roles, i.e. the $^{25}Mg^{+}$ qubit as the "control" and the $^{9}Be^{+}$ qubit as the "target". The rotations $R(\theta, \phi)$ and $R_z(\xi)$ are defined in Eq. 2.13 and Eq. D.5, respectively. Here, the $R_z(\xi)$ rotations are accomplished by adjusting the phase of the DDS used to induce microwave transitions (see footnote 2), which can be absorbed into the microwave-induced $R(\frac{\pi}{2}, -\frac{\pi}{2})$ pulses.

controlled-NOT gate in Ref. [Tan 15] are related with single-qubit $R_z(\xi)$ rotations. Here, $R_z(\xi)$ rotations are accomplished by shifting the phase of the DDS which is used to induce microwave transitions. In our experiment, the R_z rotations (in Fig. 5.7) are effectively absorbed into the $R(\frac{\pi}{2}, -\frac{\pi}{2})$ rotation during our calibration procedures. Here, the phases of the $R(\theta, \phi)$ rotations must also take into account the residual $\hat{\sigma}_z$ rotations which can be caused by inaccurate bookkeeping or miscalibrations of pulse durations or frequencies for the implementation of the CNOT gate with the laser-induced $\widehat{G}$ gate[2] . The actions of these calibrations are verified by confirming that the controlled-NOT gates processes the four states (given in Eq. 5.8) correctly according to the truth table in Eq. 4.8.

5.4.1 Quantum Non-Demolition Measurement

Quantum logic spectroscopy (QLS) is a process where one ion is used to readout the spin state of another ion. Traditionally, this task is accomplished by implementing the proposal presented in Ref. [Schmidt 05]. The working principle of the QLS procedure is very similar to the Cirac-Zoller gate (see Sec. 4.2) in the sense that it relies on the blockade provided by the motional ground state to conditionally transfer information from one ion to another ion, where both ions are trapped in the same potential well. The QLS procedure first transfers the population information from a "spectroscopy" ion to the shared motional mode, then this information is transferred to a "logic" ion., which is then detected. The QLS method is useful to readout certain ion species where a direct fluorescence measurement is not readily applicable. This might be due to a lack of cycling transitions (e.g. molecular ions [Wolf 16]), or hard-to-access laser wavelength required for fluorescence detection (e.g. Al^+ ions [Rosenband 08]). For example, QLS has been successfully applied to a quantum logic clock [Chou 10].

Figure 5.8.(a) shows the pulse sequence used in a typical QLS experiment. After cooling a

[2] furthermore, due to insufficient numbers of DDSs available to us, we use a single DDS to drive microwave transitions on both the $^9Be^+$ (qubit frequency $\sim$ 1.2 GHz) and $^{25}Mg^+$ (qubit frequency $\sim$ 1.8 GHz) ions. As the phases of the qubits' superposition states are defined by the applied microwave field, changing the microwave-DDS frequency gives phase offsets and effectively applies $R_z(\xi)$ rotations to the qubits. However, these $R_z(\xi)$ rotations can be reversed and the phases of the qubits can be recovered by changing the phase of the microwave field appropriately at a later time in the sequence

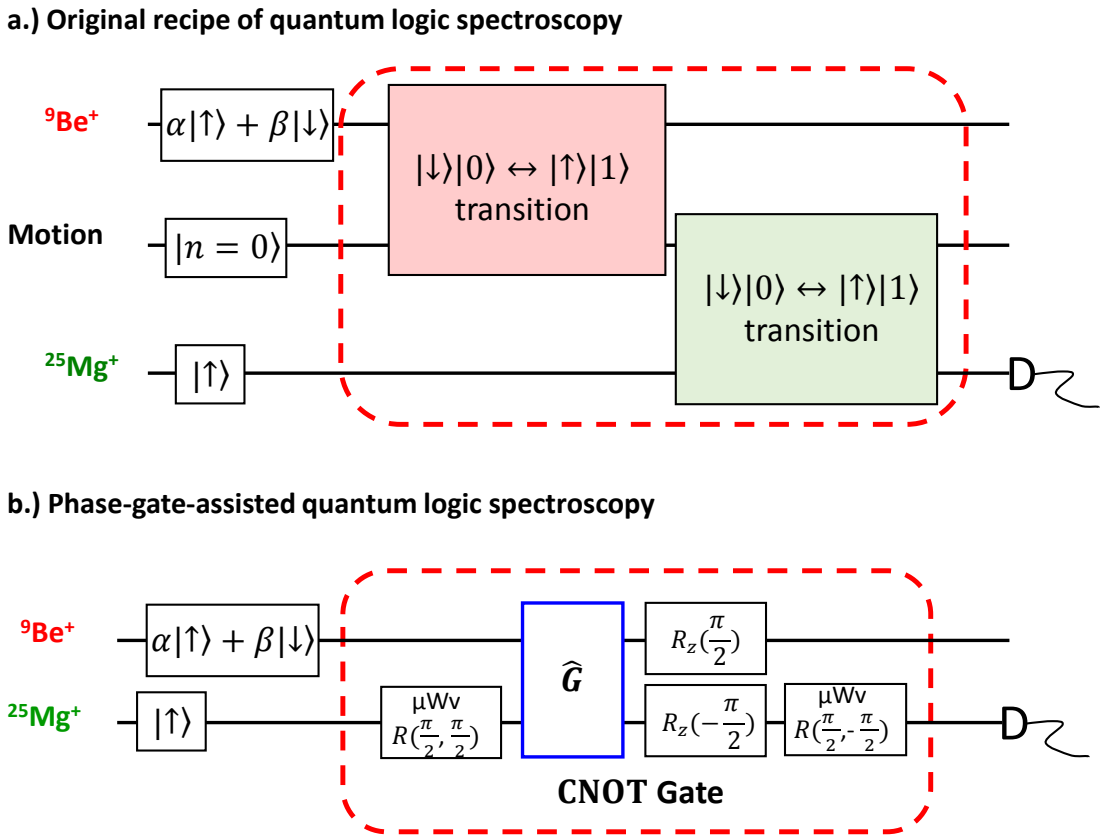

Figure 5.8: Pulse sequences of performing Rabi flopping on the $^{9}Be^{+}$ (spectroscopy) ion as detected with the $^{25}Mg^{+}$ (logic) ion using (a) conventional quantum logic spectroscopy [Schmidt 05], and (b) the controlled-NOT gate based procedure. The CNOT gate implemented here is defined by the matrix in Eq. 4.9, with the pulse sequence of the $\widehat{G}$ gate shown in Fig. 5.2. Ground state cooling which was applied prior to the qubit state preparations, are not shown in this figure.

shared motional mode to near the ground state, a π pulse on the $|\downarrow\rangle|n=0\rangle \leftrightarrow |\uparrow\rangle|1\rangle$ (where n is the Fock state quantum number) transition is applied to the spectroscopy ion; this is followed by applying an equivalent π pulse to the logic ion, which is initially prepared in the $|\uparrow\rangle$ state. As a demonstration here, the $^9Be^+$ ion mimics the spectroscopy ion and the $^{25}Mg^+$ ion mimics the logic ion. We consider the actions of the pulse sequence (Fig. 5.8.(a)) with the input state of either the $|\uparrow\rangle_{\rm Be}|\uparrow\rangle_{\rm Mg}$ state or the $|\downarrow\rangle_{\rm Be}|\uparrow\rangle_{\rm Mg}$ state, when the motional mode is cooled to the ground state:

$$|\uparrow\rangle_{\rm Be}|\uparrow\rangle_{\rm Mg}|0\rangle \xrightarrow{S} |\uparrow\rangle_{\rm Be}|\uparrow\rangle_{\rm Mg}|0\rangle \xrightarrow{L} |\uparrow\rangle_{\rm Be}|\uparrow\rangle_{\rm Mg}|0\rangle, \tag{5.13}$$

$$|\downarrow\rangle_{\rm Be}|\uparrow\rangle_{\rm Mg}|0\rangle \xrightarrow{S} |\uparrow\rangle_{\rm Be}|\uparrow\rangle_{\rm Mg}|1\rangle \xrightarrow{L} |\uparrow\rangle_{\rm Be}|\downarrow\rangle_{\rm Mg}|0\rangle, \tag{5.14}$$

where $\xrightarrow{S}$ and $\xrightarrow{L}$ indicate applying the $|\downarrow\rangle|n=0\rangle \leftrightarrow |\uparrow\rangle|1\rangle$ transitions to the spectroscopy ($^9Be^+$) ion and the logic ($^{25}Mg^+$) ion, respectively. If the spectroscopy ion is prepared in a superposition state, this pulse sequence implements the following action:

$$\begin{aligned}(\alpha|\uparrow\rangle_{\rm Be} + \beta|\downarrow\rangle_{\rm Be})\,|\uparrow\rangle_{\rm Mg}|0\rangle &\xrightarrow{S} |\uparrow\rangle_{\rm Be}|\uparrow\rangle_{\rm Mg}\,(\alpha|0\rangle + \beta|1\rangle) \\ &\xrightarrow{L} |\uparrow\rangle_{\rm Be}\left(\alpha|\uparrow\rangle_{\rm Mg} + \beta|\downarrow\rangle_{\rm Mg}\right)|0\rangle,\end{aligned} \tag{5.15}$$

indicating that the state of the $^9Be^+$ ion is mapped to the $^{25}Mg^+$ ion.

Analogously, as a controlled-NOT gate is also a conditional operation (i.e., the state of the target qubit remains unchanged if the control qubit is in the $|\uparrow\rangle$ state and the target qubit's state is flipped if the control qubit is in the $|\downarrow\rangle$ state), a controlled-NOT gate can also be used to execute quantum logic spectroscopy. Moreover, because our implementations of the CNOT and $\text{CNOT}_{\text{invert}}$ gates inherit the robustness against motional excitation from the MS gate [Sørensen 99, Sørensen 00, Milburn 00, Solano 99], it offers certain advantages compared to the conventional QLS method where the performance is strongly tied to performance of the ground state cooling applied prior to the motion-subtracting mapping pulses.

As an illustration, we compared the CNOT gate with the method used in conventional QLS [Schmidt 05] procedure in a series of quantum logic readout experiments. The pulse sequences for the comparison experiments are shown in Fig. 5.8. Both procedures were calibrated with the motional mode initialized close to the motional ground state.

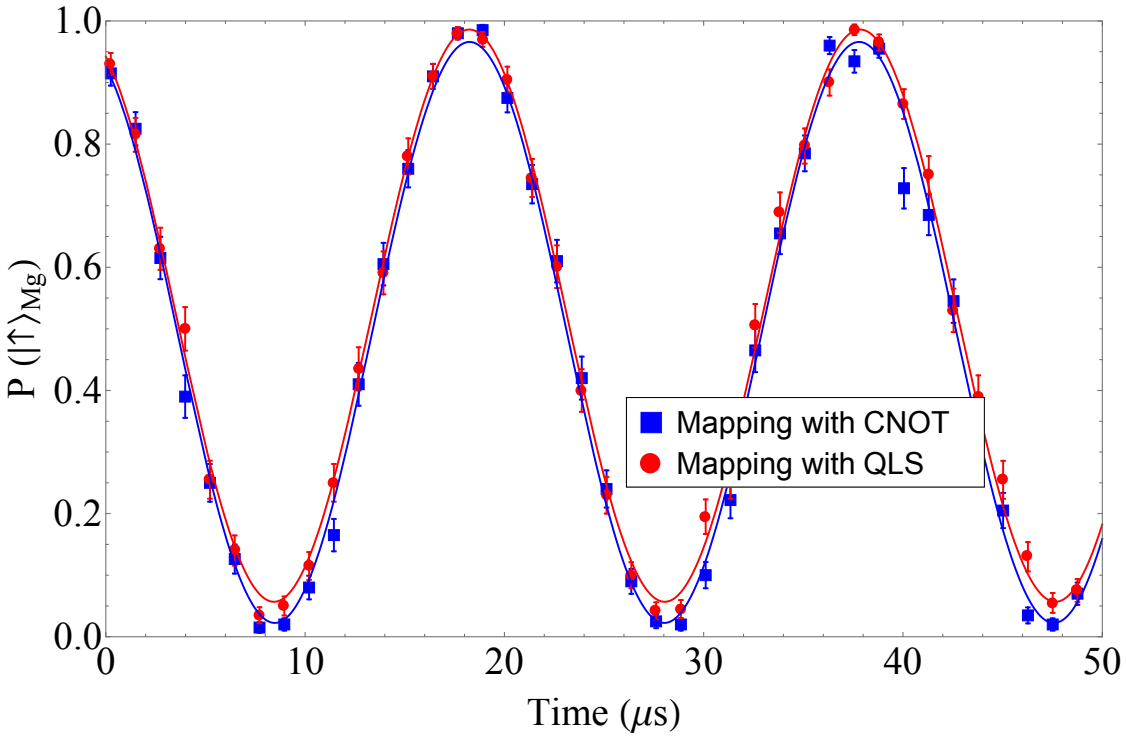

Figure 5.9: Rabi flopping of the $^{9}Be^{+}$ ion detected on the $^{25}Mg^{+}$ ion with the motional modes cooled to near the ground state ($\bar{n} \simeq 0.05$). $P(|\uparrow\rangle_{Mg})$ is the probability of finding the $^{25}Mg^{+}$ qubit in the $|\uparrow\rangle$ state. In this case, both the QLS and our controlled-NOT gate mapping procedures performed approximately equally. Error bars correspond to standard error of the mean.

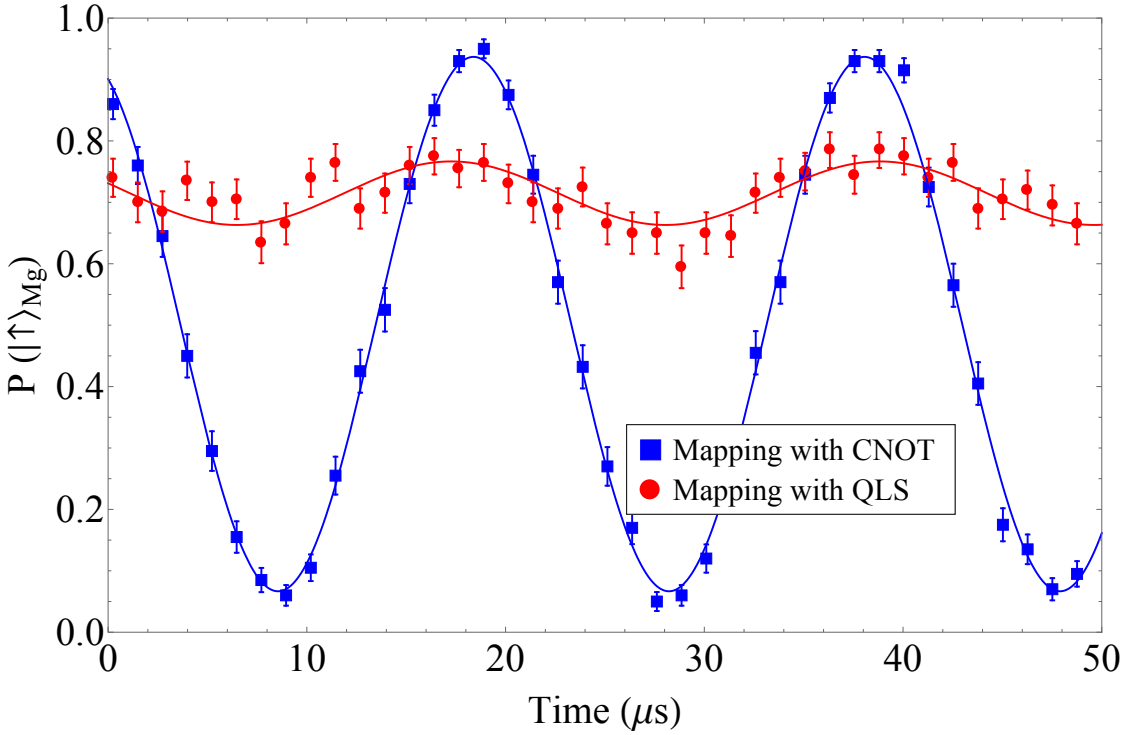

Figure 5.10: Rabi flopping of the $^{9}Be^{+}$ ion detected on the $^{25}Mg^{+}$ ion with the motional modes cooled to the Doppler temperature of $\bar{n} \simeq 4$. The controlled-NOT mapping technique, which makes use of the mixed-species gate, performed better than the original QLS procedure due to the relative low sensitivity to motional excitations [Sørensen 99, Sørensen 00]. Error bars correspond to standard error of the mean.

Figure 5.9 and Fig. 5.10 show the Rabi flopping of the $^9Be^+$ qubit as detected on the $^{25}Mg^+$ ion, which was initially prepared in the $|\uparrow\rangle$ state. For the ions' motional modes cooled near the ground state ($\bar{n} \simeq 0.05$) with Raman sideband cooling applied to the $^9Be^+$ ion (see Sec. 2.1.5), the performances of both procedures are similar in terms of the population contrast. For the ions' motional modes cooled to the Doppler temperature ($\bar{n} \simeq 4$), the contrast of the conventional QLS method (red dots) was reduced significantly compared to transfer with a controlled-NOT gate (blue squares).

A typical QLS sequence consists of a ground state cooling sequence followed by transfer pulses that map the information from the spectroscopy ion to the logic ion before reading out on the logic ion (Fig. 5.8.(a)). This procedure is usually performed with multiple repetitions to improve statistics. Compared to the conventional QLS, since the population contrast of our geometric-phase-gate controlled-NOT procedure is less sensitive to thermal excitation of the motional modes, the ground state cooling sequence could be removed or substantially shortened. This enables an increase of spectroscopy probe duty cycle as well as relaxing the requirement for preparing the motional state into the ground state. This procedure might potentially be useful for the quantum logic readout of certain ion species with (i) relatively short trapping lifetimes, e.g. highly-charged or certain molecular ions, or (ii) relatively short decay lifetimes compared to the duration required for ground state cooling.

Although the technical requirements for the implementation of a geometric-phase gate are more demanding, e.g., the need for coherent phase control of the laser phases described in Sec. 5.2.3, the ingredients required, i.e. blue and red-sideband excitations, are readily available in most cold, trapped-ion experiments.

5.5 SWAP Gate for Quantum Information Mapping

The $^9Be^+$ qubit's phase information is not accessible on the $^{25}Mg^+$ with the CNOT mapping procedure described in the previous section. This might not be of concern for the application of quantum non-demolition measurement with quantum logic using the controlled-NOT gates con-

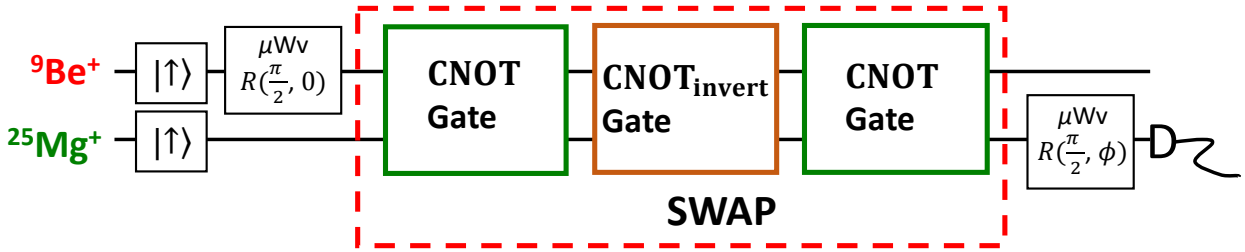

Figure 5.11: The pulse sequence for a Ramsey experiment with a SWAP gate. We used three controlled-NOT gates to construct a SWAP gate. The first and third controlled-NOT gates were implemented with the CNOT gate (Eq. 4.9) with the $^{25}Mg^{+}$ ion as the target, with pulse sequence indicated in Fig. 5.7.(a). The second controlled-NOT gate was implemented as depicted in Fig. 5.7.(b), with the $^{9}Be^{+}$ ion as the target of the $CNOT_{invert}$ gate. The overall operation inside the red dashed box implements the SWAP gate as shown in Eq. 5.16.

structed with geometric phase gates, because in spectroscopy applications usually only the population information of the spectroscopy ion is of interest. However, in a broader context of general quantum information applications, it is desirable to transfer both the population and phase information between qubits of different species. To preserve this phase information, we constructed a SWAP gate that interchanges the quantum state of the two qubits [Nielsen 00], which can be described by the following unitary matrix

$$\text{SWAP} = \begin{pmatrix} 1 & 0 & 0 & 0 \\ 0 & 0 & 1 & 0 \\ 0 & 1 & 0 & 0 \\ 0 & 0 & 0 & 1 \end{pmatrix}. \tag{5.16}$$

With the $^{9}Be^{+}$ and $^{25}Mg^{+}$ qubits prepared to the $\alpha_B|\uparrow\rangle_{\text{Be}} + \beta_B|\downarrow\rangle_{\text{Be}}$ and $\alpha_M|\uparrow\rangle_{\text{Mg}} + \beta_M|\downarrow\rangle_{\text{Mg}}$, the SWAP gate implements the following operation:

$$(\alpha_B|\uparrow\rangle_{\text{Be}} + \beta_B|\downarrow\rangle_{\text{Be}})\left(\alpha_M|\uparrow\rangle_{\text{Mg}} + \beta_M|\downarrow\rangle_{\text{Mg}}\right) \overset{SWAP}{\longrightarrow} (\alpha_M|\uparrow\rangle_{\text{Be}} + \beta_M|\downarrow\rangle_{\text{Be}})\left(\alpha_B|\uparrow\rangle_{\text{Mg}} + \beta_B|\downarrow\rangle_{\text{Mg}}\right). \tag{5.17}$$

Our SWAP gate is constructed with three controlled-NOT gates. Figure 5.11 shows the pulse sequence of a Ramsey-type experiment where the first Ramsey (microwave-induced) $\pi/2$ pulse was applied to the $^{9}Be^{+}$ ion to create an equal superposition in the $|\uparrow\rangle$ and $|\downarrow\rangle$ states, and the second

(microwave-induced) $\pi/2$ pulse with a variable phase ϕ was then applied to the $^{25}Mg^{+}$ ion after implementing the SWAP gate. Two Ramsey fringes detected on the $^{25}Mg^{+}$ ion as a function of ϕ are shown in Fig. 5.12. Data shown as blue squares corresponds to the case where the ions' axial motional modes are initialized to near the ground state ($\bar{n} \simeq 0.05$), and data shown as red dots corresponds to Doppler cooling with $\bar{n} \simeq 4$. The contrast with Doppler cooling is reduced because the Lamb-Dicke limit [Wineland 98] is not rigorously satisfied, which can reduce the fidelity of the MS gate (see Sec. 4.4.6), which in turn affects the performance of the SWAP gate.

5.6 Mixed-Species Cirac-Zoller Gate

We also implemented a mixed-species Cirac-Zoller gate [Cirac 95] and used it to create a Bell state (see Sec. 4.2 for a description of the Cirac-Zoller gate). The pulse sequence of our implementation is shown in Fig. 5.13. First, we cooled the axial motional modes to near their ground states ($\bar{n} \simeq 0.05$). Then, with both qubits initialized to the $|\uparrow\rangle$ state followed by a $\pi/2$ pulse induced by a microwave field on the $^{9}Be^{+}$ qubit, a controlled-NOT gate with $^{9}Be^{+}$ as the "control" and $^{25}Mg^{+}$ as the "target" implemented using the Cirac-Zoller protocol created a Bell state $\frac{1}{\sqrt{2}}(|\uparrow\uparrow\rangle - i|\downarrow\downarrow\rangle)$.

The Cirac-Zoller protocol requires a red-sideband 2π pulse to be applied on a transition between one of the qubit states and an auxiliary state, $|\text{Aux}\rangle$. Here, we chose the $|F = 2, m_F = 2\rangle$ state of the $^{25}Mg^{+}$ ion as the $|\text{Aux}\rangle$ state, and the red-sideband 2π pulse was driven on the $|3, 1\rangle \leftrightarrow |\text{Aux}\rangle$ transition (see Fig. 2.6 for the energy level diagrams of the $^{25}Mg^{+}$ ion).

Figure 5.14 shows the coherent parity flopping of the mixed-species Bell state created by our implementation of the Cirac-Zoller gate. The data was obtained by applying microwave-induced $R(\pi/2, \phi)$ pulses to each of the qubits after generating the Bell state with the pulse sequence shown in Fig. 5.13. We estimated the Bell state fidelity to be ~ 0.95. We did not investigate the properties and imperfections of this protocol in detail since its performance is sensitive to the motional excitation, making it less favorable compared to the mixed-species Mølmer-Sørensen protocol (see Sec. 4.2).

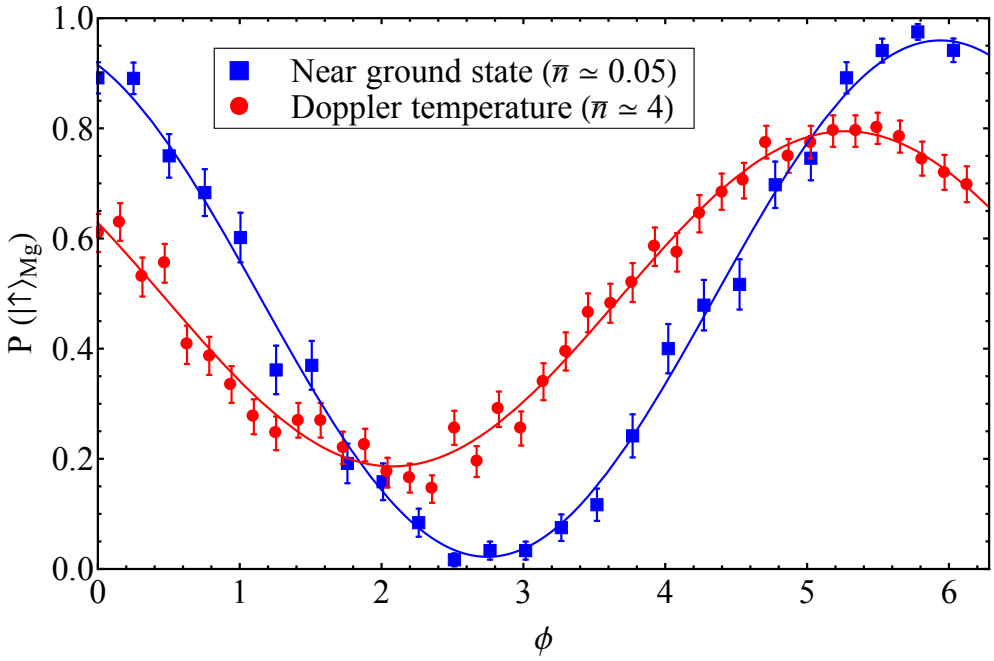

Figure 5.12: The Ramsey fringes measured on the $^{25}Mg^+$ ion after applying the SWAP gate as depicted in Fig. 5.11. This shows that the phase information is preserved between the two species and transferred from the $^9Be^+$ ion to the $^{25}Mg^+$ ion. Error bars correspond to standard error of the mean.

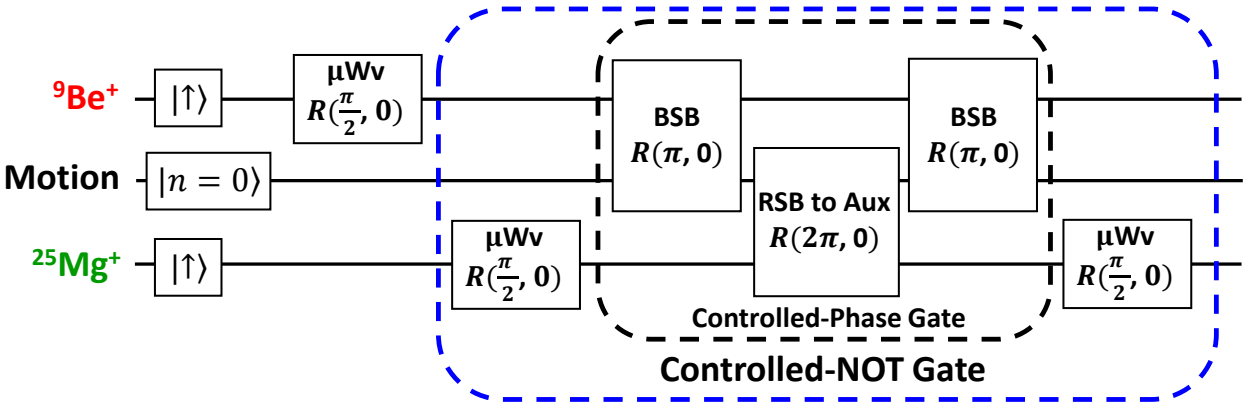

Figure 5.13: Pulse sequence for creating a Bell state $\frac{1}{\sqrt{2}}(|\uparrow\uparrow\rangle - i|\downarrow\downarrow\rangle)$ using a combination of single-qubit pulses and the Cirac-Zoller gate [Cirac 95]. For high fidelity, this protocol requires the motional mode to be prepared in its ground state. The notations "BSB" and "RSB" denote blue and red-sideband transitions, respectively. The controlled-phase gate and the controlled-NOT gate are defined in Eq. 4.6 and Eq. 4.9, respectively. The definition of the $R(\theta, \phi)$ rotation is in Eq. 2.13. Except for the "RSB to Aux" pulse, all other pulses are driven between the qubit $|\uparrow\rangle$ and $|\downarrow\rangle$ states. The pulse sequence corresponding to ground state cooling of the motional modes (applied prior to the operations shown) are not shown in this figure.

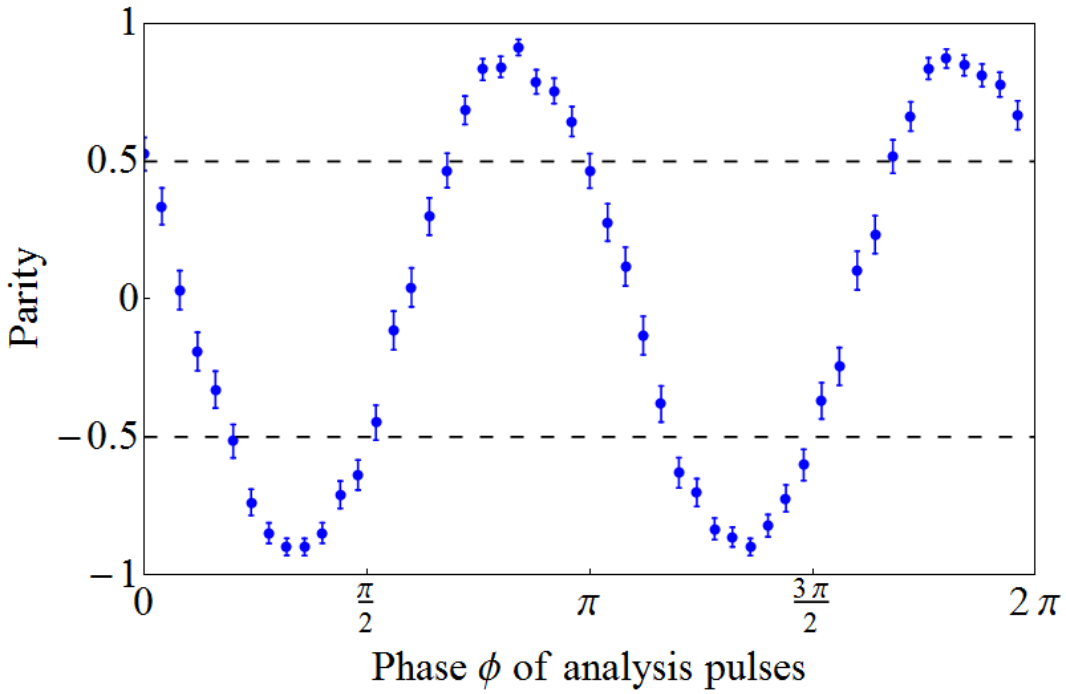

Figure 5.14: Parity oscillation of the Bell state created by the Cirac-Zoller gate [Cirac 95]. The analysis pulses were microwave-induced $\pi/2$ pulses with variable phase ϕ. Error bars correspond to standard error of the mean.

A previous implementation of a two-ion Cirac-Zoller gate employed two $^{40}Ca^{+}$ ions cotrapped in the same potential well [Schmidt-Kaler 03], and suffered considerable single-qubit addressing error (~ 3 %), whereas here addressing error is approximately zero.

5.7 Summary and Conclusion

In summary, by using state-dependent forces induced by two different wavelength laser beams (near 313 nm and 280 nm), we demonstrated a deterministic mixed-species entangling gate with a $^{9}Be^{+}$ and a $^{25}Mg^{+}$ ion. The highest achieved mixed-species Bell state fidelity created by this gate was 0.979(1). Together with single-qubit gates, we demonstrated the universality of this entangling gate by constructing controlled-NOT gates and a SWAP gate. These two logic gates enabled us to transfer information between qubits of different species, and their robustness against thermal excitation was compared with the original recipe of the quantum logic spectroscopy [Schmidt 05]. This entangling gate can be added to the elementary quantum computing toolkit, which is potentially useful in realizing a large-scale quantum information processor [Monroe 13] or a quantum network [Moehring 07] using the distinctive advantages of different ion species.

Although the demonstration here used hyperfine qubits, our entangling gate technique is general enough that it can be applicable to qubits based on optical transitions, or a combination of hyperfine and optical qubits. This would also make this gate useful for readout in quantum logic clocks [Chou 10, Schulte 16]. Furthermore, as our gate scheme employs an effective spin-spin interaction, this technique can be potentially generalized for the study of quantum many-body physics, as well as quantum simulation.

A similar and complimentary work has also been carried out at the University of Oxford trapped-ion group with two isotopes of calcium ions, i.e. $^{40}Ca^{+}$ and $^{43}Ca^{+}$ [Ballance 15]. In that work, the isotope shift between the qubits is small enough that one set of laser beams (near 397 nm) is sufficient to implement the two-isotope entangling gate. A gate fidelity of 0.998(6) was achieved using the $\hat{\sigma}_z\hat{\sigma}_z$ gate (see Sec. 4.3.2 and Ref. [Leibfried 03] for a description of the $\hat{\sigma}_z\hat{\sigma}_z$ gate).

Chapter 6

$^{9}Be^{+}$ High Fidelity Universal Gate Set

6.1 Introduction

It is well known that certain single-qubit gates and two-qubit entangling gates make up a universal gate set and combinations of them are sufficient to realize other quantum gates [Barenco 95, Bremner 02, Zhang 03]. Therefore, the problem is reduced to achieving high fidelity for these two operations. It is generally agreed that individual logic gate errors must be reduced below a certain threshold, often taken to be around 10^{-4}, to achieve fault-tolerance [Preskill 98, Knill 10, Ladd 10] without excessive overhead in the number of physical qubits required to implement a logical qubit. This level has been achieved in some experiments for all elementary operations including state preparation and readout [Myerson 08], with the exception of two-qubit entangling gates, emphasizing the importance of improving multi-qubit gate fidelities.

For trapped-ion systems, various atomic species including $^{9}Be^{+}$, $^{25}Mg^{+}$, $^{40}Ca^{+}$, $^{43}Ca^{+}$, $^{88}Sr^{+}$, $^{137}Ba^{+}$, $^{111}Cd^{+}$, and $^{171}Yb^{+}$ have been investigated as qubit candidates systems. As various ions differ in mass, electronic, and hyperfine structure, they each have technical advantages and disadvantages. The $^{9}Be^{+}$ ion is the lightest ion currently considered for quantum information processing (QIP), and as such, has several potential advantages. The relatively light mass yields deeper traps and higher motional frequencies for given applied potentials, and facilitates fast ion transport [Bowler 12, Walther 12]. A light mass also yields stronger laser-induced spin-motion coupling (proportional to the Lamb-Dicke parameter), which can yield less spontaneous emission error for a given laser intensity [Ozeri 07]. However, a disadvantage of $^{9}Be^{+}$ ion qubits compared

to some heavier ions such as $^{40}Ca^{+}$ and $^{43}Ca^{+}$ [Benhelm 08, Ballance 15] has been the difficulty of producing and controlling the ultraviolet (313 nm) light required to drive $^{9}Be^{+}$ stimulated-Raman transitions.

In this chapter, we describe an experimental implementation of a high-fidelity universal gate set with $^{9}Be^{+}$ ions. By taking advantage of recent technological developments as described in Chap. 3, we demonstrate laser-induced single-qubit computational gate errors of $3.8(1) \times 10^{-5}$ and realize a deterministic two-qubit gate to produce the Bell state $|\Phi_{+}\rangle = \frac{1}{\sqrt{2}}(|\uparrow\uparrow\rangle + |\downarrow\downarrow\rangle)$ with high fidelity. Partial state tomography analyzed with a maximum likelihood (ML) algorithm is used to evaluate the fidelity of the created Bell state. Together with characterizing the effects of known error sources with numerical simulations and calibration measurements, we deduce an entangling gate infidelity or error of $\epsilon = 8(4) \times 10^{-4}$.

The organization of this chapter is the following: we briefly describe the setup relevant to these experiments, followed by results of the two-qubit gate in Sec. 6.3. In Sec. 6.4 details of the two-qubit gate's error sources are characterized and discussed. Validity of using the created Bell state fidelity as a representation of gate fidelity is investigated in Sec. 6.5. The partial state tomography used for the evaluation of the created Bell state and certain imperfections using this method are discussed in Sec. 6.6. Lastly, in Sec. 6.7, we describe the experiment and the results characterizing single-qubit gates using a randomized benchmarking technique [Knill 08].

6.2 Experimental Setup

In this experiment, $^{9}Be^{+}$ ions are confined at the $\mathcal{E}$ zone depicted in Fig. 3.1. For a single $^{9}Be^{+}$ ion confined in this zone, the axial z harmonic mode frequency is $\omega_z \simeq 2\pi \times 3.58$ MHz[1] , while the transverse (radial) mode frequencies are $\omega_x \simeq 2\pi \times 11.2$ MHz, and $\omega_y \simeq 2\pi \times 12.5$ MHz. Two trapped $^{9}Be^{+}$ ions are separated by $\simeq 3.94$ μm and are aligned along the axial z direction. Their z motion can be described by two normal modes, the center-of-mass (C) and stretch (S) modes with frequencies $\omega_C = \omega_z$ and $\omega_S = \sqrt{3}\omega_z$ respectively. The motion of the ith ion is written

[1] angular frequency

$z_i = z_{i,C0}(\hat{a} + \hat{a}^\dagger) + z_{i,S0}(\hat{b} + \hat{b}^\dagger)$ where $\hat{a}, \hat{a}^\dagger$ and $\hat{b}, \hat{b}^\dagger$ are the lowering and raising operators for the C and S modes and $z_{1,C0} = z_{2,C0} = z_0/\sqrt{2}, z_{1,S0} = -z_{2,S0} = z_0/\sqrt{2\sqrt{3}}$, where $z_0 = \sqrt{\hbar/(2m\omega_z)}$.

The two-qubit entangling gate is realized by the Mølmer-Sørensen (MS) interaction [Sørensen 99, Sørensen 00, Milburn 00, Solano 99] on the stretch mode (see also Sec. 4.3.4). The MS protocol requires simultaneous excitation of a blue-sideband transition with a detuning of δ and a red-sideband transition with a detuning of $-\delta$ on the selected motional mode. Following Eq. 4.20, the Hamiltonian is

$$H = \hbar \sum_{j=1,2} \eta_S \Omega \hat{\sigma}_j^+ \left(\hat{b} e^{-i(\delta t + \phi_{j,r})} + \hat{b}^\dagger e^{i(\delta t - \phi_{j,b})} \right) + h.c., \tag{6.1}$$

where Ω is the resonant carrier transition Rabi rate, $\eta_S = |\boldsymbol{\Delta k}| z_{1,S0} \simeq 0.19$ is the Lamb-Dicke parameter of the stretch mode, $\hat{\sigma}_j^+$ is the spin raising operator for the jth ion, and $\phi_{j,b(r)}$ is the phase of the blue (red) sideband interaction on the jth ion. Starting in the $|\uparrow\uparrow\rangle$ state and setting $\eta_S \Omega = \delta/4$, this interaction produces the entangled state

$$|\Phi\rangle = \frac{1}{\sqrt{2}} \left(|\uparrow\uparrow\rangle + e^{-i\left(\sum_{j=1,2} \frac{1}{2}(\phi_{j,b} + \phi_{j,r}) + \pi/2\right)} |\downarrow\downarrow\rangle \right) \tag{6.2}$$

after a duration $t_{\text{gate}} = 2\pi/\delta$.

The details of the laser beam setup is given in Sec. 3.4.3. Figure 6.1 shows the relevant stimulated-Raman laser beams used in the experiments described in this chapter. The Mølmer-Sørensen gate is implemented with three laser beams labeled by $\boldsymbol{k_1}$, $\boldsymbol{k_{2a}}$, and $\boldsymbol{k_{2b}}$. Each of the beams in path 2 excite one of the sidebands when paired with the $\boldsymbol{k_1}$ beam. Note that we implement the above entangling operation on the second micromotion sideband to maximize the spin-motion coupling strength and state-dependent forces with the ions subjected to micromotion (see Sec. 3.1). This induces higher errors caused by spontaneous emission and will be discussed later in Sec. 6.4. Similar to our implementation of the mixed-species entangling gate described in Chap. 5, the entanglement created by this laser setup depends on the relative optical phases between paths 1 and 2, causing the phase factor $\phi_{j,b} + \phi_{j,r}$ in Eq. 6.2 to fluctuate. This laser phase sensitivity can be removed by using the same technique described in Sec. 5.2.3. The polarization of the $\boldsymbol{k_1}$ beam

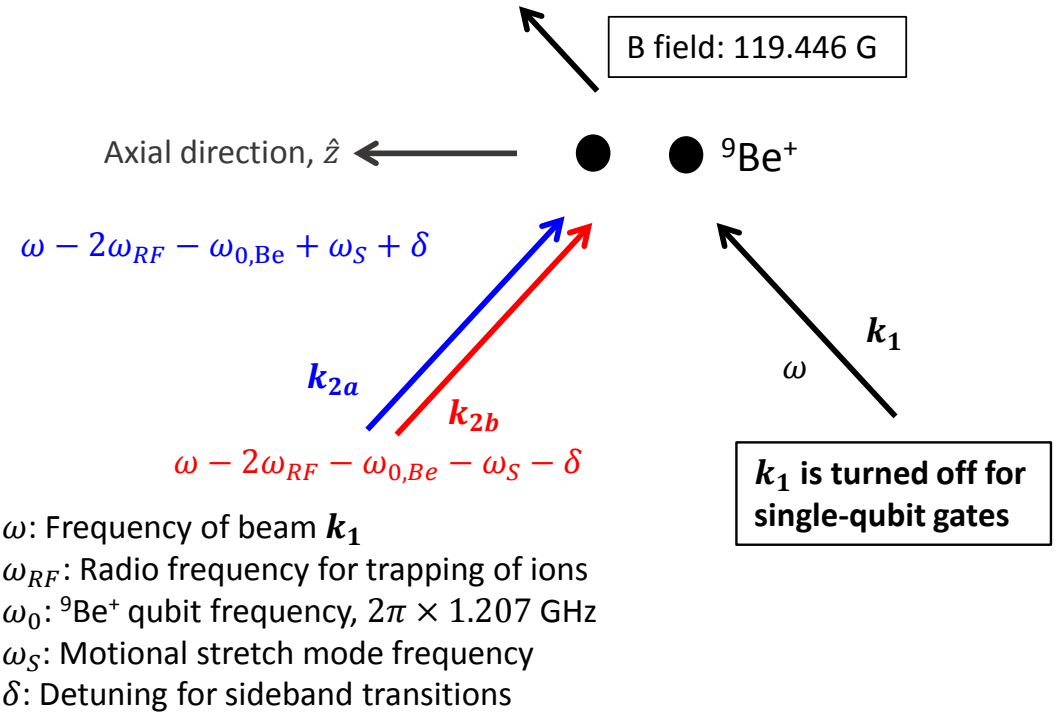

Figure 6.1: Laser beam geometry for stimulated-Raman transitions. Each of the $\boldsymbol{k_{2a}}$ and $\boldsymbol{k_{2b}}$ beams when paired with the $\boldsymbol{k_1}$ beam give a wave vector difference $\boldsymbol{\Delta k}$ aligned along the axial z direction, and separately excite the blue and red sideband transitions on the axial stretch mode. All three beams are applied to implement the Mølmer-Sørensen interaction on the second micromotion sideband. Copropagating beams $\boldsymbol{k_{2a}}$ and $\boldsymbol{k_{2b}}$ are used to implement single-qubit gates described in Sec. 6.7. Details of laser beam setup is given in Sec. 3.4.3.

is adjusted such that the intensity ratio of σ^+ to σ^- components is approximately $8:2$, with the σ^+ component used for driving the MS gate and the σ^- component used for sideband cooling on the $|2,2\rangle \rightarrow |1,1\rangle$ transition [Monroe 95b] (see also Sec. 2.1.5). The $\boldsymbol{k_{2a}}$ and $\boldsymbol{k_{2b}}$ beams are set to be π-polarized to maximize the entangling gate Rabi rate for a given amount of laser intensity.

The MS protocol requires the blue and red sideband excitations to have equal Rabi rates. Imbalanced Rabi rates cause errors as discussed in Sec. 4.4.8. Rabi rate imbalance between the blue and red sideband excitations is minimized by adjusting the laser power in beams $\boldsymbol{k_{2a}}$ and $\boldsymbol{k_{2b}}$ (Fig. 6.1) differentially while keeping the total laser power in path 2 fixed. During calibration of the blue sideband's Rabi rate, the beam in path 2 that is responsible for the red sideband excitation is shifted off resonant from any transition. Similarly when the Rabi rate of the red sideband transition is calibrated. This strategy is used to ensure that the transition frequency shifted by the AC Stark effect does not change during the calibration.

6.3 Experimental Results

Following the initial Doppler cooling, the ions are sideband cooled with a series of $|F=2, m_F=2\rangle|n\rangle \rightarrow |1,1\rangle|n-1\rangle$ transitions (n is the Fock state quantum number), each followed by repumping [Monroe 95b]. This cooling yields mean mode occupation numbers $\bar{n}_C \simeq 0.01$ and $\bar{n}_S \simeq 0.006$ and the ions being pumped to the $|2,2\rangle$ state at the end of the cooling sequence. The cooling transitions are driven on the positive second micromotion sideband as described in Sec. 2.1.5.

Mapping from the $|2,2\rangle$ state to the $|1,1\rangle = |\uparrow\rangle$ state is accomplished by a microwave-driven composite π pulse [Levitt 86] composed of a sequence of $R(\theta,\phi)$ pulses $R(\pi,0)$, $R(\pi,\pi/3)$, $R(\pi,\pi/6)$, $R(\pi,\pi/3)$, $R(\pi,0)$, where the definition of $R(\theta,\phi)$ is given in Eq. 2.13. After gate operations, population in the computational qubit is transferred to the measurement qubit before applying the state-dependent fluorescence detection (see Fig. 2.1). Firstly, population in the $|\uparrow\rangle$ state is transferred back to the $|2,2\rangle$ state with the same composite pulse sequence. Then, population in the $|2,0\rangle = |\downarrow\rangle$ state is transferred or "shelved" to the $|1,-1\rangle$ using a microwave π pulse, followed by another microwave π pulse which transfers remaining $|\downarrow\rangle$ population to the $|1,0\rangle$

state.

We use the gate to ideally prepare the Bell state $|\Phi_+\rangle = \frac{1}{\sqrt{2}}(|\uparrow\uparrow\rangle + |\downarrow\downarrow\rangle)$[2] . To evaluate the gate's performance, we perform partial state tomography analyzed with a maximum likelihood (ML) algorithm to deduce the fidelity of the experimentally prepared state. The details of the analysis method are discussed in Sec. 6.6. From the Bell-state fidelity as determined by the ML method, we can estimate the MS gate fidelity (see Sec. 6.5). To first order, the inferred Bell-state fidelity does not include errors due to imperfect $|2,2\rangle$ state preparation and measurement. This is advantageous because this enables us to investigate the gate error at a level smaller than the imperfect initialization into the $|2,2\rangle$ state. Here, we estimate the impurity of the $|2,2\rangle$ state after the initial optical pumping to be approximately 2×10^{-3} (details in Sec. 6.6.2), whereas an entangling gate error as small as 8×10^{-4} can be determined. Furthermore, this ML method allows an arbitrary photon-count distribution to be analyzed, removing the need for making certain assumptions, which are detailed in the later section of Sec. 6.6.

In a first experiment, we vary the laser beam power and determine the error of the Bell state as a function of the gate duration for a fixed Raman detuning of $\Delta \simeq -2\pi \times 730$ GHz (Fig. 6.2). The various curves in the figures show the expected errors due to spontaneous emission, errors due to motional mode frequency fluctuations, and errors in the composite microwave pulse used for $|2,2\rangle \leftrightarrow |1,1\rangle = |\uparrow\rangle$ state transfer. We also determine the error of the created Bell state by varying the Raman detuning, Δ. The results are shown in Fig. 6.3 where we keep a fixed gate duration of $t_{\text{gate}} \simeq 30\ \mu s$ while adjusting the laser beam powers for each Raman detuning. The minimum error obtained is $8(4) \times 10^{-4}$ for $\Delta \simeq -2\pi \times 900$ GHz, which yields a ML-Bell-state fidelity of 0.9992(4). An important contribution to the ML-Bell-state error is due to the imperfect transfers from the $|2,2\rangle$ state to the qubit $|\uparrow\rangle$ state (for both qubits) before the application of the gate, and the reverse procedure that transfers $|\uparrow\rangle$ population back to the $|2,2\rangle$ state before detection. The total fidelity of these transfer pulses, limited by magnetic field fluctuations and the quality of the microwave

[2] here, we drop the phase term shown in Eq. 6.2; the phase of the laser pulse used for analyzing the coherence of the created Bell state is stable relative to the phase term shown in Eq. 6.2, can therefore be effectively dropped

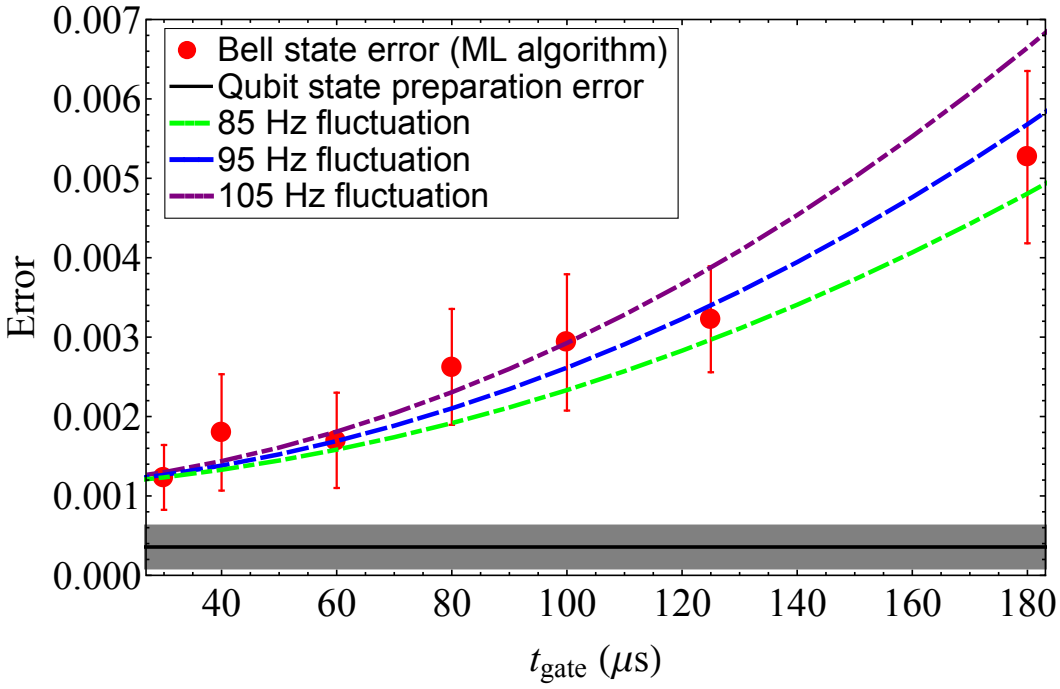

Figure 6.2: ML-Bell-state error (red dots) as a function of gate duration t_{gate} for a constant Raman beam detuning $\Delta \simeq -2\pi \times 730$ GHz. The black line shows the separately determined error and uncertainty (gray shade) due to the microwave pulses used for $|2,2\rangle \leftrightarrow |\uparrow\rangle$ state transfer. The three dashed lines show the sum of the expected gate errors including photon scattering and mode frequency fluctuations (which are slow compared to gate durations shown) for three different r.m.s. magnitudes of mode frequency fluctuations. Errors due to these errors are discussed below. The gate error increases quadratically with increasing t_{gate} due to such frequency fluctuations; however, for $t_{\text{gate}} \simeq 30$ μs the error due to frequency fluctuations is approximately 1×10^{-4}.

pulses, is investigated with separate experiments analyzed with the same ML algorithm. We find $\epsilon_{\text{transfer}} = 4(3) \times 10^{-4}$. This is averaged over multiple data evaluations across multiple days; the uncertainty is the standard deviation of these data. While this error does not in principle affect the gate performance, we conservatively do not subtract it from our gate fidelity estimate due to its relatively large uncertainty. The uncertainties of the inferred errors presented here are deduced by parametric bootstrap resampling [Efron 93] with 500 resamples.

In the next section, we describe the characterization of individual errors sources through calibration measurements and numerical simulations. Together with investigating the average fidelity with numerical simulations in Sec. 6.5, we deduce that the fidelity of the ML-Bell-state is a good representation of the average gate fidelity.

It would be advantageous to evaluate the gate performance with full process tomography or randomized benchmarking to confirm our assessment. We did not perform randomized benchmarking because ion motional excitation gives additional errors. This excitation occurs during ion separation (to provide individual ion addressing) and because of anomalous heating [Turchette 00a] during the required long sequences of gates. These problems can eventually be solved as in our previous demonstration where the gate fidelity was measured by interleaved randomized benchmarking [Gaebler 12] or by process tomography [Navon 14]. In these two experiments, the gate error was consistent with the measured two-qubit state fidelity [Horodecki 99, Nielson 02, Gaebler 16].

Our ML algorithm assumes that the reference histograms are perfect representations of the qubit measurement. Experimental issues that can affect the validity of this assumption are investigated and discussed in Sec. 6.6.1. We determine a lower bound of 0.999 on the purity of the $|2,2\rangle$ state for one ion prepared by optical pumping, as detailed in Sec. 6.6.2. With this, we put a lower bound of 0.997 on the overall Bell state fidelity.

6.4 Error Sources

Table 6.1 lists the individually evaluated errors for the highest entangling gate fidelity through calibration measurements and numerical simulations.

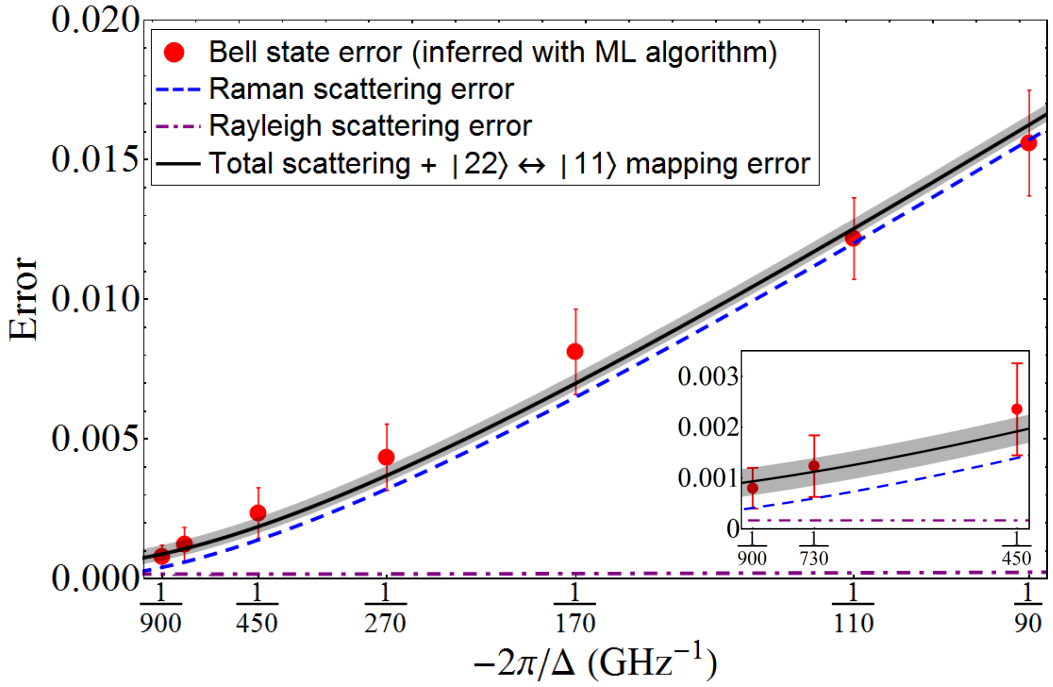

Figure 6.3: ML-Bell-state error (red dots), plotted as a function of $-2\pi/\Delta$ for a constant gate duration of approximately 30 μs, where Δ is detuning of the Raman laser beams relative to the $^2S_{1/2} \leftrightarrow {}^2P_{1/2}$ electronic transitions. The simulated contributions to the Bell state error from Raman and Rayleigh scattering (for details see Sec. 4.4.2) are shown with the blue and purple dashed lines respectively. For large $|\Delta|$, the Raman scattering error approaches zero, however, the Rayleigh scattering error remains approximately constant at 1.7×10^{-4}. The black line is the sum of the Raman and Rayleigh scattering errors, and the composite microwave pulses used for qubit state preparation and detection (uncertainty indicated by the gray band). Error bars for the measured Bell state fidelity are determined from parametric bootstrap resampling [Efron 93] of the data and represent a 1-σ statistical confidence interval.

Errors	$\times 10^{-4}$
Spontaneous emission (Raman)	4.0
Spontaneous emission (Rayleigh)	1.7
Motional mode frequency fluctuation	1
Rabi rate fluctuation	1
Laser coherence	0.2
Qubit coherence	<0.1
Stretch-mode heating	0.3
Finite Lamb-Dicke approximation	0.2
Off-resonant coupling	<0.1
$\|2,2\rangle \Leftrightarrow \|\uparrow\rangle$ two-way transfer	4

Table 6.1: Individually evaluated errors for the entangling gate at a Raman detuning of $\Delta \simeq -2\pi\times 900$ GHz, and a gate duration of approximately 30 μs. Off-resonant coupling includes coupling of the qubit states to other hyperfine states and their sidebands, which can includes motional mode sidebands and micromotion sidebands. The last (transfer) error reduces the ML-Bell-state fidelity but should minimally affect the gate fidelity.

6.4.1 Spontaneous Emission Induced by Raman Laser Beams

Spontaneous emission error is caused by randomly scattered photons when exciting stimulated-Raman transitions. It can be separated into Raman and Rayleigh scattering. Raman scattering processes are inelastic and project an ion's internal state to one of the other hyperfine states (see Fig. 2.1 for energy level diagram for the $^9Be^+$ ion), destroying coherence. Rayleigh scattering processes are elastic and do not necessarily cause spin decoherence [Ozeri 07]; however, momentum kicks from photon recoil cause uncontrolled displacements of the motional state, which can result in phase errors in the final target states of the two-qubit gates. See Sec. 4.4.2 for more details on spontaneous scattering of photon induced by Raman laser beams. The Kramer-Heisenberg equation (Eq. 4.29) is used to calculate Raman scattering probabilities, and verified with measurements made on ions. The dynamics of the Mølmer-Sørensen interaction are studied with a numerical master equation simulation (Sec. 4.4.1) including the Lindblad operators shown in Sec. 4.4.2.1 to investigate the effect of Raman scattering on gate performances. The recoil error is calculated with Eq. 4.38.

Raman scattering can be reduced by increasing the Raman detuning, $|\Delta|$, at the cost of higher laser intensity to maintain the same gate Rabi rate. However, Rayleigh scattering error reaches an asymptotic values as $|\Delta|$ is increased (see Fig. 6.3 and Fig. 4.5). This error is proportional to the Lamb-Dicke parameter (Eq. 4.38) and thus could be reduced by increasing the trap frequency (Eq. 2.7); it can also be reduced by using multiple loops in phase space [Ozeri 07, Hayes 12] (Eq. 4.38). However, these methods reduce the gate Rabi rate and thus increase Raman scattering error. In our experiment, eliminating the axial micromotion would allow us to increase Δ by a factor of $\xi \simeq 2$ which would lower the Raman scattering error by a factor of 2ξ, and the Rayleigh scattering error by a factor of ξ while maintaining the same gate duration.

Spontaneous Raman scattering can result in leakage of population from the qubit manifold (Sec. 4.4.2.1). The resulting states will predominantly be detected as dark and falsely associated with the qubit $|\downarrow\rangle$ state. This creates a systematic bias that overestimates the actual Bell state

fidelity. Through simulations with the Lindblad operators described in Eq. 4.33, we found that such a bias is approximately 4×10^{-5} for the Bell state fidelity created at a Raman detuning of $-2\pi \times 900$ GHz and approximately 1.5×10^{-3} for $-2\pi \times 90$ GHz Raman detuning.

6.4.2 Motional Mode Frequency Fluctuations

Motional mode frequency fluctuations also cause errors. For the stretch mode, the sources of frequency fluctuations (which are slow compared to the gate durations shown in Fig. 6.2) are (i) fluctuations in the DC potentials applied to electrodes for trapping, (ii) fluctuating electric-field gradients from uncontrolled charging of electrode surfaces, and (iii) non-linear coupling to radial "rocking" modes [Roos 08, Nie 09]. By measuring the lineshape for exciting the motional state of a single ion with injected RF "tickle" potentials on the trap electrodes at frequencies near the mode frequencies, we estimate the first two sources contribute fluctuations of approximately 50 Hz. Mode frequency fluctuations can also be caused by electrode charging induced by UV beam light scattering off the trap surfaces [Harlander 10] so this effect may becomes more pronounced when higher laser power is used.

For (iii), to a good approximation, the shift of the stretch mode frequency, $\delta\omega_S$, from excitation of the rocking modes is given by $\delta\omega_S = \chi(n_x + n_y + 1)$ where χ is a non-linear coupling parameter, n_x and n_y are Fock state occupation numbers of the two radial rocking modes [Roos 08, Nie 09]. For our parameters $\chi \simeq 45$ Hz. Our Raman laser beam geometry did not allow direct measurement of the $\bar{n}_x$ and $\bar{n}_y$ radial mode excitations. Therefore, the final temperature is estimated from the (thermal) Doppler cooling limit (Eq. 2.2), taking into account heating due to photon recoil during sideband cooling of the axial modes. From this, we estimate the stretch mode frequency fluctuations from experiment to experiment to be approximately 100 Hz r.m.s. As these fluctuations are dependent on the occupation numbers of the radial modes, the error can be suppressed by cooling the radial modes to near the ground state. Figure 6.2 shows three master equation simulations (combined with Monte Carlo simulation) curves for different total values of the r.m.s. frequency fluctuation of the motional mode. The simulation also includes the effect of

Raman scattering (Lindblad operators shown in Sec. 4.4.2.1) with the fluctuations in motional mode frequency described by the Lindblad operator shown in Eq. 4.39. These curves follow the trend of the data and are consistent with our known sources. The error due to these fluctuations is approximately 1×10^{-4} for the shortest gate durations. Moreover, the trends in Fig. 6.2 indicate that gate performance could be further improved with higher gate speed. Our gate speed is limited by the available laser intensity for the given Raman laser beams detuning, Δ.

6.4.3 Rabi Rate Fluctuations

Errors are also caused by fluctuations in the sideband transitions' Rabi rates, causing fluctuations in the state-dependent forces (see also Sec. 4.4.7). Sources are (i) fluctuations of the ions' micro-motion amplitude along the axial direction, (ii) fluctuations in the laser beam intensities at the ion locations, and (iii) fluctuations in the Debye-Waller factor associated with the center-of-mass (C) mode [Wineland 98]. In our experiments, the latter contributes the largest error (for errors caused by Rabi rate fluctuations).

Given a thermal distribution of the C mode and following Eq. 4.47 and Eq. 4.52, we can estimate the r.m.s. Rabi rate fluctuation and the resulting entangling gate error. With $\bar{n}_C \simeq 0.01$ at the beginning of the MS interaction, we find $\langle \frac{\delta\Omega}{\Omega} \rangle \simeq 6 \times 10^{-3}$ and we deduce an error of approximately 1×10^{-4} to $|\Phi_+\rangle$. Because this mode experiences anomalous heating during the application of the gate, the actual error contribution increases with the gate duration. The heating rate for the COM mode is measured to be ~ 80 quanta/s. For our 30 μs gate duration, this implies a change of $\Delta\bar{n}_C \simeq 0.001$ averaged over the duration of the gate. Therefore, the error caused by the changes of the Debye-Waller factor from heating can be neglected for our fastest gate durations.

Because the two-qubit-gate Raman transitions are driven on the second micro-motion sideband, the Rabi rates are proportional to the second-order Bessel function $J_2(|\boldsymbol{\Delta k}|z_{\mu m}) \simeq 0.48$, where $|\boldsymbol{\Delta k}|z_{\mu m} = 2.9$ is the modulation index due to the micromotion-induced Doppler shift and is proportional to the applied RF voltage V_{RF}. For the conditions of the experiment, $J_2(|\boldsymbol{\Delta k}|z_{\mu m})$ is near a maximum such that the Rabi rate is relatively insensitive to fluctuations in V_{RF}. Our

measurements show that the radial mode frequencies can drift by up to 10 kHz over the course of several experiments; this would imply a relative drift in V_{RF} of $\sim 1 \times 10^{-3}$ and a corresponding change in the Rabi rate of 3×10^{-4}, which contributes an error that is negligible compared to the other errors. Relationship between gate error and Rabi fluctuation is given in Eq. 4.47.

Laser intensity fluctuations can be assumed to be comparable to the fluctuations measured from the single-qubit benchmarking experiments (see Sec. 6.7), which are estimated to be $\sim 1\times10^{-3}$. This makes the laser intensity fluctuation's contribution of Rabi rate fluctuations negligible compared to that of the fluctuating Debye-Waller factors. Laser intensity fluctuations also cause fluctuations in the AC Stark shifts, which we measure to be $\sim$ 1 kHz at a Raman detuning of $-2\pi \times 900$ GHz and induce a negligible error.

6.4.4 Smaller Error Sources

Smaller sources of error are (i) laser beam phase fluctuations between beam paths 1 and 2 during each experiment (Sec. 4.4.9), (ii) individual qubit decoherence (Sec. 4.4.10), (iii) heating of the axial stretch mode [Turchette 00a] (Sec. 4.4.4), (iv) imperfect Lamb-Dicke approximation (Sec. 4.4.6), (v) off-resonant coupling to spectator transitions (Sec. 4.4.5), and (vi) Rabi rate imbalance between the two spin-motion excitations (Sec. 4.4.8). Each of these sources contributes $\sim 10^{-5}$ error to the entangling gate.

Sources of transition frequency and phase fluctuations include fluctuations in the laser beam phases $\phi_{j,b}$ and $\phi_{j,r}$, and fluctuations in the qubit frequency. Fluctuations due to relative length changes between paths 1 and 2 are measured by recombining the two beams after they exit the UV fibers (see Fig. 6.1 and Fig. 3.8), detecting with a fast photo-diode, and measuring the phase of the beat note using the AOM RF sources as a reference. We measured a phase drift of $\sim \pi$ after $\sim$ 1 s, which is likely due to temperature drift of the optical elements in the setup. We also observed small phase oscillations with frequencies of a few hundred Hertz, which can be attributed to acoustic vibrations in the laboratory. With this, we estimate an error of $\sim 2 \times 10^{-5}$ to the gate. The measured coherence time of the qubit from Ramsey experiments is approximately 1.5 s

(Fig. 2.2), which implies an r.m.s. qubit transition frequency error of 1 Hz, giving negligible error compared to other sources.

The heating rate of the axial stretch mode is measured to be less than 1 quantum per second and contributes an error of less than 3×10^{-5} to $|\Phi_+\rangle$, estimated with master equation simulation with Lindblad operators given in Eq. 4.40 and Eq. 4.41. The MS interaction is robust against finite thermal excitation in the Lamb-Dicke limit, $\eta \ll 1$ [Sørensen 99, Sørensen 00]. However, due to the small mass of $^9Be^+$ ions, this condition is not rigorously satisfied and the sensitivity to finite motional excitation must be considered. Because of this effect, the realistic MS interaction applied to the ions deviates from the desired Hamiltonian given in Eq. 6.1. The error due to this is given by Eq. 4.46, which contributes an error of less than 2×10^{-5} for our parameters. Even within the Lamb-Dicke limit, finite thermal excitation increases the sensitivity of error due to motional mode frequency fluctuations [Hayes 12]. For our parameters, this error is negligible.

Off-resonant coupling to spectator transitions is suppressed by employing laser pulse shaping (see Sec. 3.8). The rise and fall durations of the gate pulse are adjusted such that the Fourier component at the frequencies of spectator transitions is sufficiently small. Spectator transitions include the carrier and center-of-mass sideband transitions as well as other atomic transitions that can be coupled by micromotion sidebands (the Zeeman splittings between atomic states are comparable to ω_{RF}). If a square pulse is used instead of a shaped pulse, we estimate an error of 1×10^{-4} for a gate duration of 30 μs [Sørensen 00]. Rabi rate imbalance between the blue and red sideband excitations is inferred by: first, performing extended Rabi flopping experiments on each sideband transition with their respective laser beams (see Fig. 6.1). The Rabi rate(Ω_R) of each transition is then deduced by fitting the Rabi flopping data to the function $e^{-t/\tau} A\cos(\Omega_R t + \phi') + B$ with Ω_R represents the Rabi rate. Finally, the error caused by Rabi rate imbalance effect is estimated by performing numerical Schrödinger equation simulation. The measured Rabi rate ratio of the two sideband excitations is typically ~ 0.99 or better, this contributes $\sim 10^{-5}$ or lower error to the entangling gate (see also Sec. 4.4.8).

6.5 Average Fidelity

The performance of our entangling gate is evaluated by using the gate to create a Bell state. Here, we investigate the performance of the gate over all input states by employing numerical simulation with known experimental imperfections. Our simulation is performed by solving master equations (Eq. 4.28), and combining with Monte Carlo simulations for certain error mechanisms. Different methods are chosen for different error mechanisms (see Sec. 4.4.1).

One metric to quantify the gate's performance is the "average gate fidelity", F_{avg} [Horodecki 99, Nielson 02, Gaebler 16]:

$$F_{\text{avg}} = \frac{6}{5}S_+ + \frac{3}{5}S_- - \frac{1}{5}, \tag{6.3}$$

with

$$S_+ = \frac{1}{36}\sum_{U_1}\sum_{U_2}\left[\left(\langle U_1| \otimes \langle U_2|\right)\hat{G}^\dagger_{\text{ideal}}\rho_{\text{noisy}}(U_1,U_2)\hat{G}_{\text{ideal}}\left(|U_1\rangle \otimes |U_2\rangle\right)\right], \tag{6.4}$$

$$S_- = \frac{1}{36}\sum_{U_1}\sum_{U_2}\left[\left(\langle \overline{U_1}| \otimes \langle \overline{U_2}|\right)\hat{G}^\dagger_{\text{ideal}}\rho_{\text{noisy}}(U_1,U_2)\hat{G}_{\text{ideal}}\left(|\overline{U_1}\rangle \otimes |\overline{U_2}\rangle\right)\right] \tag{6.5}$$

where $|U_i\rangle$ is an eigenstate of the Pauli operators $\hat{\sigma}_x$, $\hat{\sigma}_y$ or $\hat{\sigma}_z$ for the ith qubit, and $|\overline{U_i}\rangle$ is the state orthogonal to $|U_i\rangle$. We fix a consistent phase for these eigenstates throughout. The operator $\hat{G}_{\text{ideal}}$ is the ideal entangling operation, $\rho_{\text{noisy}}(U_1,U_2)$ represents the resultant density matrix of the imperfect entangling operation with the input states of $|U_1\rangle \otimes |U_2\rangle$. With 36 different input states, our simulations including known imperfections yield the summands in Eq. 6.4 and Eq. 6.5. We found F_{avg} lies within the uncertainty of the inferred Bell state fidelity measurement. With this, we deduce that our the Bell state fidelity inferred with our ML analysis is a good representation of the average gate fidelity.

6.6 State Detection and Tomography

A partial state tomography analyzed with a maximum likelihood (ML) algorithm is used to evaluate the fidelity of the Bell state created by the entangling gate. This ML method has been developed in collaboration with members of a NIST theory group led by E. Knill, with A. Keith

as lead. Other theory contributors include: S. Glancy and K. Coakley. The details of the partial state tomography and ML method are one of the main focus of A. Keith's master's research, and will be published elsewhere.

We will briefly discuss certain issues about inferring information about the prepared two-qubit quantum states from the photon count distributions and the maximum-likelihood method we used to circumvent some of these problems. We also study certain issues associated with using the ML method for the fidelity determination of the experimentally created Bell state.

The detection procedure is the standard state-dependent fluorescence technique where the qubit up state of each ion is transferred to the bright state of the measurement qubit, and the qubit down state is transferred ("shelved") to the detection dark state before the detection laser beam is applied (see Sec. 2.1.7 for details on fluorescence detection on the $^9Be^+$ ions). Because both ions are illuminated with a detection laser beam (beam waist of $\sim$30 μm), which is much larger than the ion separation ($\sim$ 4 μm), the photon counts come from both ions.

The recorded joint photon-count histograms collected by illuminating both ions simultaneously are drawn from mixtures of three possible count distributions $q_j(c)$ ($c = 0, 1, 2, ..., C$ indicates the photon counts) corresponding to the distinguishable ion subspaces spanned by (i) $|\uparrow\uparrow\rangle$ ($q_1(c)$), (ii) $|\uparrow\downarrow\rangle$ or $|\downarrow\uparrow\rangle$ ($q_2(c)$), and (iii) $|\downarrow\downarrow\rangle$ ($q_3(c)$) states. Because of the finite efficiency of our photon collection apparatus and some optical pumping during detection, the three count distributions overlap, particularly those of subspaces (ii) and (iii) as shown in Fig. 6.4. Therefore an exact determination of the subspace to which the ions are projected cannot be determined in a single experiment.

Nevertheless, we can infer the ions' density matrix statistically from repetitions of the experiment provided that the count distributions for each projected subspace are known. These distributions can be inferred from reference experiments by fitting to a parametrized model of the distributions. A simple class of such models is given by mixtures of Poissonians with different means. The uncertainty requirements of our experiments and effects such as optical pumping during photon collection imply that we cannot use such models unless they have an excessively large

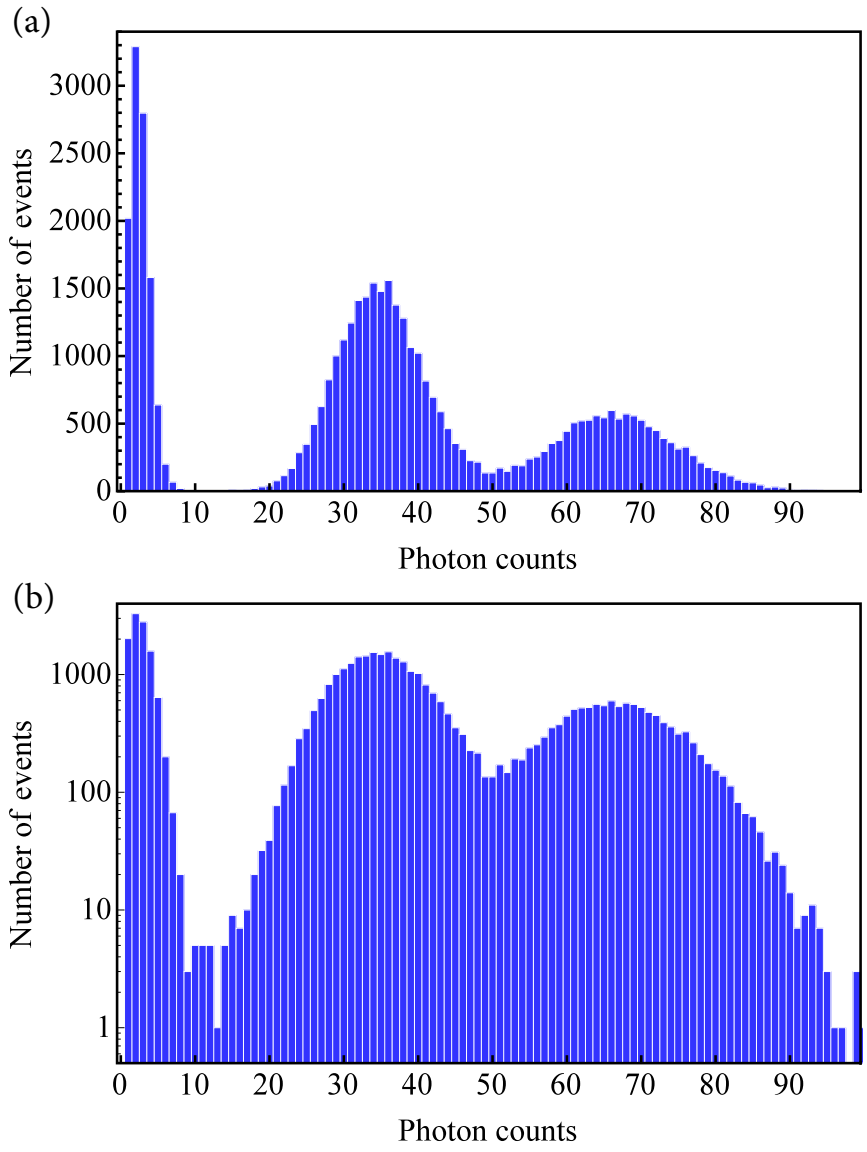

Figure 6.4: The photon-counts histogram for two $^{9}Be^{+}$ ions prepared into an equal superposition of $|\uparrow\rangle$ and $|\downarrow\rangle$ states of each ion before making joint fluorescence measurements. (a) Data is plotted in a linear scale. (b) Same data plotted in a log scale. Count distributions corresponding to the $|\uparrow\downarrow\rangle$ or the $|\downarrow\uparrow\rangle$ states (on average 30 photon counts) and the $|\uparrow\uparrow\rangle$ state (on average 60 photon counts) overlap significantly. These overlapping distributions cause errors in the determination of the quantum state using a single detection.

number of parameters, in which case overfitting becomes an issue. Figure 6.5 shows the typical photon-count distributions for both ions prepared in the bright state ($|2,2\rangle$) or the dark state ($|1,-1\rangle$) of the measurement qubit. To obtain Fig. 6.5.(a), we apply optical pumping to prepare the ion in the $|2,2\rangle$ state before applying detection laser; for Fig. 6.5.(b), we first apply optical pumping to the $|2,2\rangle$ state, then transfer the population to the $|1,-1\rangle$ state and the $|1,0\rangle$ state (the dark state of the measurement qubit) with a series of π pulses driven with microwave field (see Sec. 2.1.7 for more details). A simple inspection of these histograms indicates the difficulty of using simple fitting models to accurately extract quantum state information.

Our maximum likelihood (ML) analysis avoids these issues by statistically inferring states without requiring a model for the ideal count distributions. It requires sets of reference and data histograms. The data histograms involve observations of an identically prepared state ρ modified by analysis pulses. It infers a representative density matrix $\hat{\rho}$. Because the different observations are not "informationally complete", $\hat{\rho}$ is not intended to match ρ precisely but the measurements are designed so that the extracted fidelities of interest do match to within a statistical uncertainty. In our experiment, we obtain four reference histograms $r_i(c)$ ($i = 1,2,3,4$). These histograms are associated with known populations in the measurement qubit. Each reference histogram is obtained by observing known ion states prepared as follows: For $r_1(c)$, the state is prepared by optical pumping both ions to the $|2,2\rangle$ state, Fig. 6.5(a) shows a typical $r_1(c)$ histogram. For $r_2(c)$, this optical pumping is followed by implementing the transfer $|2,2\rangle \rightarrow |\uparrow\rangle$ with a composite microwave pulse, followed by the transfers $|\uparrow\rangle \rightarrow |\downarrow\rangle$ and shelving into one of the states $|1,-1\rangle$ or $|1,0\rangle$ with microwave π pulses as described above. A typical $r_2(c)$ histogram is shown in Fig. 6.5(b). For $r_3(c)$, the optical pumping is followed by the microwave-driven spin-echo sequence consisting of $R(\pi/2,0)$, $R(\pi,0)$, $R(\pi/2,\pi/2)$ pulses on the $|2,2\rangle \leftrightarrow |\uparrow\rangle$ transition, followed by transferring the population in the $|\uparrow\rangle$ state to the $|1,-1\rangle$ or $|1,0\rangle$ state as was done for $r_2(c)$. The histogram $r_4(c)$ is obtained like $r_3(c)$ but with the phase of the third pulse set to $\frac{3\pi}{2}$. The change in phase does not change the state when the initial state and pulses are as designed. Fig. 6.4 shows a typical $r_3(c)$ or $r_4(c)$ histogram. Data histograms $h_k(c)$ are obtained directly from the prepared state ρ or by

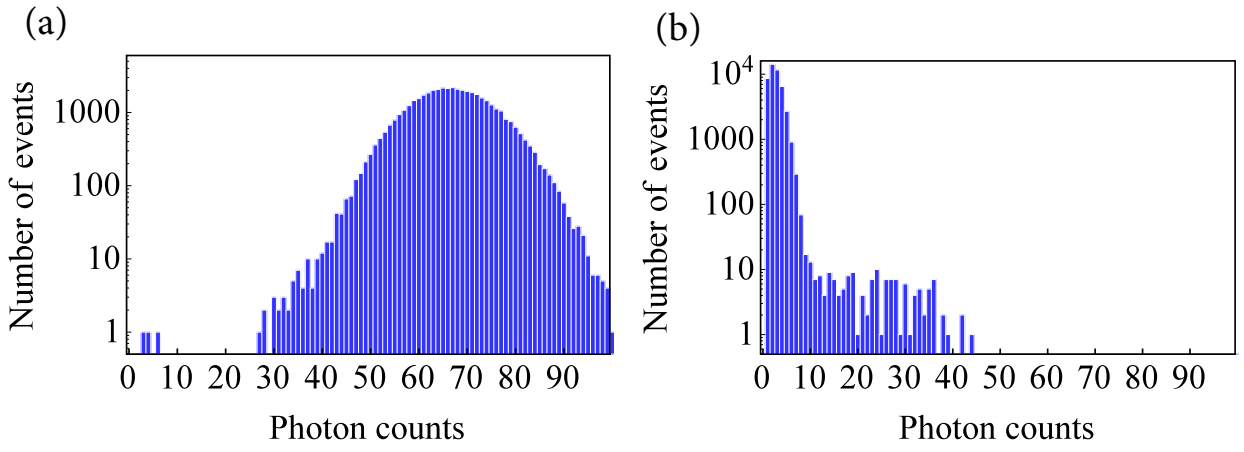

Figure 6.5: Typical photon-counts histograms for two $^9Be^+$ ions prepared in the (a.) $|2,2\rangle$ state and (b.) the "shelved" states of $|1,-1\rangle$ or $|1,0\rangle$ state. Both distributions exhibit non-standard photon-count distribution (e.g., the Poissonian distribution). For (a), this is caused by depumping process due to imperfect detection laser beam polarization. For (b), finite frequency separation between the atomic states allows population to leak from the dark state to the bright state (via optical pumping); in which case the ions start to fluoresce. See Fig. 2.1 for $^9Be^+$ energy level structure; see also Fig. 6.6 for the detection behavior of each of the Zeeman states in the $^9Be^+$ ion's electronic ground state. These issues render simple fitting models, e.g. to Poissonians, incapable of extracting accurate quantum state information.

applying analysis pulses on the prepared state. The analysis pulses are global $R(\pi/2, n\pi/4)$ pulses, for $n = 0, 1, ..., 7$. These pulses are applied using the laser beams from paths 1 and 2 (Fig. 6.1) to maintain laser beam phase stability relative to the two-qubit gate. The rotation $R(\theta, \phi)$ is given in Eq. 2.13.

To determine $\hat{\rho}$, we maximize the logarithm of the likelihood of the observed histograms with respect to the unknown $q_j(c)$ and ρ to be determined. Given these unknowns, reference histogram $r_i(c)$ is constructed from the distribution $\sum_j a_{ij} q_j(c)$, where the a_{ij} are "populations" determined from the ideal prepared states. For example, the $r_1(c)$ and $r_2(c)$ reference histograms ideally correspond to count distributions $q_1(c)$ and $q_2(c)$, respectively; ideally, $r_3(c)$ and $r_4(c)$ each corresponds to the mixture of count distribution $0.25q_1(c)+0.5q_2(c)+0.25q_3(c)$. Similarly, the data histograms $h_k(c)$ are sampled from the distribution $\sum_j b_{kj} q_j(c)$, where the populations b_{kj} are a linear function of ρ. Given these distributions, the log likelihood is given by

$$\log\left(\text{Prob}(r, h|q, a, b)\right) = \left[\sum_{i=1,c}^{4,C} r_i(c)\log\left(\sum_{j=1}^{3} a_{ij} q_j(c)\right)\right] + \left[\sum_{k,c}^{q,C} h_k(c)\log\left(\sum_{j}^{3} b_{kj} q_j(c)\right)\right] + \text{const.} \tag{6.6}$$

To maximize the log likelihood, we take advantage of the separate convexity of the optimization problem in the $q_j(c)$ and ρ and alternate between optimizing with respect to the $q_j(c)$ and ρ. We used a generic optimization method for the first and the "$R\rho R$" algorithm [Hradil 04] for the second to keep ρ physical during the optimization. The quality of the model fit can be determined by a bootstrap likelihood-ratio test [Boos 03]. We found that our data's log-likelihood-ratio is within two standard deviations of the mean bootstrapped log-likelihood-ratio.

A modification of the ML analysis is required to reduce the number of parameters needed for the $q_j(c)$ and the complexity of the algorithms. For this, we bin the counts into seven bins of consecutive counts [Lin 15, Lin 16]. The binning is done separately by setting aside a random 10 % of each reference histogram and using this as a training set to determine a binning that maximizes state information quantified by a mutual-information-based heuristic. The heuristic is designed to characterize how well we can infer which of the four training set reference histograms a random

count histogram is sampled from.

6.6.1 Assumptions with the ML Method

The ML analysis assumes that the reference histograms are sampled from count distributions corresponding to states with known populations. The actual populations deviate by small amounts from this assumption, because here, the references are designed to yield histograms associated with known populations in the measurement qubit, instead of the computational qubit. We considered two systematic effects, which can lead to such deviations: (i) optical pumping that ideally prepares the $|2,2\rangle$ state may have fidelity as low as 0.999 (see Sec. 6.6.2), and (ii) imperfections in the transfer pulses between the computation qubit manifold (the $|\uparrow\rangle$ and $|\downarrow\rangle$ states) and the measurement qubit manifold (the $|2,2\rangle$ state as the bright state and the $|1,-1\rangle$ and $|1,0\rangle$ states as the dark state). The latter is dominated by the transfer pulses between the $|2,2\rangle$ and $|\uparrow\rangle$ states, which has a measured fidelity of 0.9996(3). Errors in the transfer between the $|\downarrow\rangle$ and the $|1,-1\rangle$ and $|1,0\rangle$ states have less effect, since to a high degree all three of these states are detected as dark (see Fig. 6.6). Similarly, to first order, the population of the prepared state corresponds to the collected reference histograms are all in the measurement qubit manifold; contribution from the small populations outside the measurement qubit manifold are observationally equivalent to population in $|\downarrow\rangle$ since they are dark to a high degree (see Fig. 6.6). If these populations are the same in all experiments, they are equivalent to a background contribution. With this in mind, we inspect the systematic effects from (i) imperfect optical pumping and (ii) imperfect transfers in more detail.

Consider the effect of imperfect optical pumping of population to the $|2,2\rangle$ state. In Sec. 6.6.2, we estimate an upper bound of 10^{-3} population (per ion) in states other than the $|2,2\rangle$ state after optical pumping. This population is distributed over the other Zeeman states in a way that depends on details of the optical pumping process. With one exception considered below, population in states other than $|2,2\rangle$ is nominally detected as dark in all reference histograms (Fig. 6.6). The ML algorithm infers $q_j(c)$ as if all populations were in the measurement qubit manifold. Provided the population in other states remains dark in all experiments, it is treated as

a background and effective subtracted with our ML method. The effect is that the ML algorithm infers the renormalized density matrix on the qubit rather than the actual one with the trace reduced by the population outside the qubit manifold. To correct for the effect of imperfect optical pumping, we subtracted 2ϵ from the ML-inferred Bell state fidelity, where $\epsilon = 10^{-3}$ is the population (per ion) outside of the computational qubit manifold during the Bell state preparation and outside the measurement qubit manifold when detection laser is applied. This is consistent with the effect on Bell state fidelity determined by performing numerical simulations taking imperfect optical pumping preparation of the $|2,2\rangle$ state into account (see next section). The exception to this model is that a fraction of the population outside the $|2,2\rangle$ state after optical pumping is in the qubit manifold, i.e. the $|\uparrow\rangle = |1,1\rangle$ state and the $|\downarrow\rangle = |2,0\rangle$ state. Two situations are considered: (a) In the case where non-$|2,2\rangle$ state is in the $|\uparrow\rangle$ state, reference histogram $r_3(c)$ and $r_4(c)$ are affected differently compared to the situation above. This is because in this case, the population stays inside the measurement qubit manifold. With respect to the background interpretation, this is equivalent to having the $|2,2\rangle$ population in references $r_3(c)$ and $r_4(c)$ exceed 0.5 (for each ion) by $\xi \leq \epsilon/2$. To determine such effect on the ML inferred fidelity, a sensitivity analysis on simulated data is performed by varying the ML assumed populations for these references according to the parameter ξ. The change in fidelity is found to be small compared to our uncertainties. (b) Non-$|2,2\rangle$ population in the $|\downarrow\rangle$ state after optical pumping enters the qubit state at the beginning of Bell state preparation and in this context does not behave as a dark state independent of the analysis pulses. However, simulations of the optical pumping process show that the non-$|2,2\rangle$ population in the $|\downarrow\rangle$ state is less than 10^{-4}, which is small compared to our uncertainties. This optical pumping simulation is performed as follows: first, we include an impurity (π component) in the polarization of the laser beam responsible for the optical pumping (ideally pure σ^+ polarized). The population in the $|\downarrow\rangle = |2,0\rangle$ state is inferred by a laser beam polarization which gives 0.999 (for one ion) optical pumping fidelity (see next section). Our simulation closely follows that described in Ref. [Langer 06], and is further discussed in the next section.

Now we consider the second effect, i.e. imperfect transfer pulses between the computational

qubit and the measurement qubit. This is dominated by the transfer of $|2,2\rangle$ to the $|\uparrow\rangle$ computational qubit state before the application of the gate. The errors of the transfer pulse result in population remaining in the $|2,2\rangle$ state, outside the computational qubit manifold and unaffected by the MS interaction and the following analysis pulses. To first order, the transfer pulse after the gate will exchange the population in the $|2,2\rangle$ state and the $|\uparrow\rangle = |1,1\rangle$ state. The $|1,1\rangle$ state will be nominally detected with high probability as dark (see Fig. 6.6), independent of the analysis pulses. While this effect is equivalent to a leakage error on the Bell state being analyzed, it is not accounted for by the ML analysis. Transfer error after the application of the gate results in extra dark population that depends on the final population in the $|1,1\rangle$state, which in turn can depend on the analysis pulses. Thus, both effects are inconsistent with the analysis pulse model that is assumed by the ML analysis. Such inconsistencies, if significant, are expected to show up in the bootstrapped likelihood-ratio test, but did not. To confirm this, a second sensitivity analysis is performed on simulated data, where we modified the ML model to include an extra dark state outside the qubit manifold and included the expected transfer pulse effects by modifying the analysis pulses with pulses coupling the qubit to the extra state. The effect on the inferred error of this modification was also found to be small compared to the uncertainties of the Bell state fidelity inferred using the ML method.

These two sensitivity analysis were performed by A. Keith, who is leading the development of the ML analysis with details to be published elsewhere.

6.6.2 Imperfect Optical Pumping and Lower Bound of Bell State Fidelity

The maximum-likelihood method, to first order, does not include the errors due to the imperfect preparation and measurement of the $|2,2\rangle$ state. This error is to be included when reporting the lower bound of the overall Bell state fidelity. This is essentially the problem of quantifying the purity of the $|2,2\rangle$ state prepared by optical pumping.

There are eight Zeeman states in the $^2S_{1/2}$ electronic ground state and sixteen Zeeman states in the $^2P_{3/2}$ electronic excited state of the $^9Be^+$ ion (see Fig. 2.1 for energy level diagram of the

$^9Be^+$ ion; the Zeeman states in the $^2P_{3/2}$ levels are not shown except for the $^2P_{3/2}|3,3\rangle$ state). The laser beam for the state-dependent fluorescence measurement is set to be σ^+ polarized, and on resonance with the $^2S_{1/2}|2,2\rangle \leftrightarrow {}^2P_{3/2}|3,3\rangle$ transitions. Due to finite frequency separations between different Zeeman states, starting with a non-$^2S_{1/2}|2,2\rangle$ state, the detection laser beam can off-resonantly excite electronic transitions between Zeeman/hyperfine states in the $^2S_{1/2}$ and $^2P_{3/2}$ levels, and optically pump the population to the $|2,2\rangle$ state. The ion starts emitting fluorescence photons after it is pumped to the $|2,2\rangle$ state under the illumination of the detection laser beam. Each Zeeman state responds differently and uniquely as shown in Fig. 6.6, which gives the simulated histogram corresponding to each of the Zeeman/hyperfine states when the detection laser is applied. The simulation used here is an analytic method which closely following that described in Ref. [Langer 06] (see also Ref. [Acton 06]). Our simulation includes twenty four energy levels (eight $^2S_{1/2}$ states and sixteen $^2P_{3/2}$ states); the energy splittings and matrix elements between different levels are calculated at the magnetic field of B = 119.446 G taking into account both the hyperfine and the Zeeman interactions.

The lower bound of the $|2,2\rangle$ state purity can be deduced by deriving an upper bound on the error ϵ of preparing the $|2,2\rangle$ state after applying optical pumping. The population is dominantly in the $|2,2\rangle$ state but we do not know precisely which of the remaining Zeeman states are populated. We write the density matrix of a single ion for this situation as

$$\rho = (1-\epsilon)|2,2\rangle\langle 2,2| + \sum_{i=1}^{7} \epsilon_i |\Psi_i\rangle\langle\Psi_i|, \tag{6.7}$$

where $\epsilon = \sum_i^7 \epsilon_i$ and the $|\Psi_i\rangle$ represent the hyperfine/Zeeman states excluding the $|2,2\rangle$ state. One strategy for setting an upper bound on ϵ is to choose a cut-off count β and compare the small-count "tail" probabilities $t = \sum_{c<\beta} h(c)$.

Let t_b be the tail probability of $h_{|2,2\rangle}$. Because state preparation and detection are not perfect, we have $t_b \geq \bar{t}_b$, where $\bar{t}_b$ is the tail probability of perfectly prepared $|2,2\rangle$ states. The tail probabilities t_i for $|\Psi_i\rangle$ are large, as verified by experimentally preparing each $|\Psi_i\rangle$ state and measuring its count distribution. From this we can set a lower bound on t_i such that $t_i > l$. With

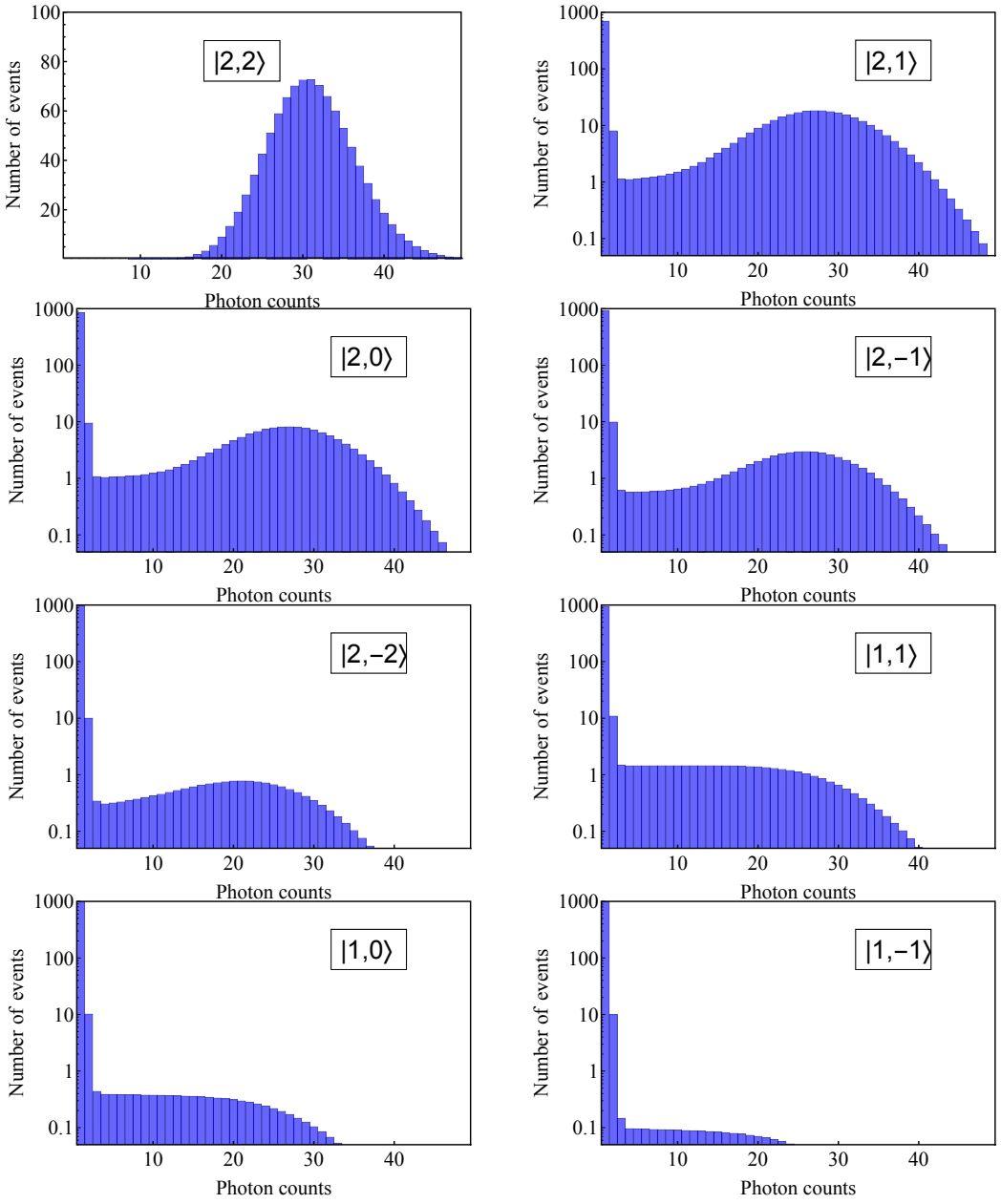

Figure 6.6: Simulated detection histograms for a $^9Be^+$ ion initialized to each of the eight Zeeman states in the $^2S_{1/2}$ electronic ground state of the $^9Be^+$ ion (see Fig. 2.1). Each histogram is obtained with 1,000 detection events. Except for the $|2,2\rangle$ state, all other figures are shown in log scale. Each state responds differently and uniquely when the detection beam is applied. Besides the $|2,2\rangle$ state, all other Zeeman states are detected as dark to a high degree. Furthermore, the $F = 1$ manifold states ($|F = 1, m_F = 0, \pm 1\rangle$) have smaller fluorescence compared to the $F = 2$ manifold states. The bright state of the measurement qubit is the $|2,2\rangle$ state (which corresponds to the qubit $|\uparrow\rangle$ state), and the dark state is the $|1,-1\rangle$ and the $|1,0\rangle$ states (which corresponds to the qubit $|\downarrow\rangle$ state). See Sec. 2.1.7 for details on the fluorescence detection of the $^9Be^+$ ions. The simulation here uses the saturation parameter, $s = I/I_{sat} = 0.5$ and assumes that the detection laser beam is pure σ^+ with its frequency tuned on resonance with the $^2S_{1/2}|2,2\rangle \leftrightarrow {}^2P_{3/2}|3,3\rangle$ transition. The detection efficiency (which experimentally relates to the sum of the quantum efficiency of the PMT and the collection efficiency of the imaging system) is set so that the $|2,2\rangle$ state fluorescence counts equal to 30 on average in our simulation.

this, we can write

$$t_b = (1-\epsilon)\bar{t}_b + \sum_i^7 \epsilon_i t_i \tag{6.8}$$

$$\geq (1-\epsilon)\bar{t}_b + \epsilon l \tag{6.9}$$

$$t_b \geq \epsilon\,(l-\bar{t}_b) + \bar{t}_b, \tag{6.10}$$

or

$$\epsilon \leq \frac{t_b - \bar{t}_b}{l - \bar{t}_b} \tag{6.11}$$

$$\leq \frac{t_b}{l-\bar{t}_b}. \tag{6.12}$$

For our parameters of $l = 0.8$ and $\bar{t}_b = 0$, we estimate an upper bound on ϵ of 1×10^{-3}. We also numerically simulate the effect of imperfect optical pumping and find that the Bell state error scales linearly as a function of ϵ. We also numerically simulate the effect of imperfect optical pumping and find that the Bell state error scales linearly as a function of ϵ. This is consistent with the lower bound on overall Bell state fidelity inferred in the previous section by considering the effect on the ML analysis (see Sec. 6.6.1).

6.7 $^9Be^+$ Single-Qubit Gate

Single-qubit gates are driven with co-propagating beams $\boldsymbol{k_{2a}}$ and $\boldsymbol{k_{2b}}$ shown in Fig. 6.1 with their frequency difference set to be the qubit frequency of $\omega_0 \simeq 2\pi \times 1.207$ GHz. With this copropagating beam geometry, single-qubit gates are negligibly affected by ion micromotion since $\boldsymbol{\Delta k}$ of these two beams projected along any mode of motion corresponds to a microwave wavelength, which is much larger than the size of motional wavepacket. Here, the Raman detuning, Δ from the $^2S_{1/2} \leftrightarrow ^2P_{1/2}$ transition frequency is set to be $\sim -2\pi \times 730$ GHz.

We employ a randomized benchmarking technique [Knill 08] to evaluate the performance of the single-qubit gates. Compared to quantum process tomography or other methods for the characterization of gate performance, randomized benchmarking is more efficient and provides separate determination of the state preparation and measurement error (ϵ_{SPAM}) and the error per

computational gate (ϵ_{gate}). Randomized benchmarking also offers scalability advantage as it allows ϵ_{gate} to be determined with a number of measurements which scales polynomially with the number of qubits. Furthermore, using long sequences of random gates make the procedure sensitive to errors similar to that in arbitrary, lengthy QIP computations.

Randomized benchmarking techniques have been used in platforms other than trapped-ion systems such as neutral atoms [Olmschenk 10], liquid NMR [Ryan 09], and superconducting qubits [Chow 09]. Using randomized benchmarking, the lowest single-qubit gate error achievable in any platform was measured to be $1.0(3) \times 10^{-6}$ [Harty 14].

In our implementation of the single-qubit randomized benchmarking, multiple sequences with random gates are pre-generated for a given set of sequence lengths. Here, sequence lengths of 1, 3, 8, 21, 55, 144, 233, 377, 610, and 987 are implemented. Each set of sequence lengths consists of 100 unique sequences. Each sequence consists of a different number of π and $\pi/2$ pulses around the x, y, and z axes of the Bloch sphere, as well as identity gates. The π pulses are performed with two sequential $\pi/2$ pulses, each with a duration ~ 2 μs. Rotations about the z axis are accomplished by shifting the phase of the direct digital synthesizer that is keeping track of the qubit's phase; the identity gate is implemented with a 1 μs wait time. Each "computational gate" is taken from the Clifford group [Gottesman 98], and consists of a random Pauli gate (π pulse) and a random Clifford gate ($\pi/2$ pulse). With the qubit initialized to a pure state, and in the absence of gate errors, the outcome of each sequence is deterministic and the ion will be found in either the $|\uparrow\rangle$ or $|\downarrow\rangle$ state.

Sequences are randomly chosen from the pre-generated pool to be implemented during run time, with each sequence repeated 100 times to collect statistics. The fidelity of each sequence is recorded and the decay of fidelity is determined as a function of the number of random computational gates for a given sequence length. The results are shown in Fig. 6.7. Here, state detection and measurement for a single $^9Be^+$ ion is relatively straightforward. As shown in Fig. 2.5, the photon-count distribution for the bright and dark states are well separated so we determine the ion's state by setting a threshold of 12 counts (count ≤ 12 is recorded as dark).

The reason for implementing computational gates with the Clifford group is because the noise

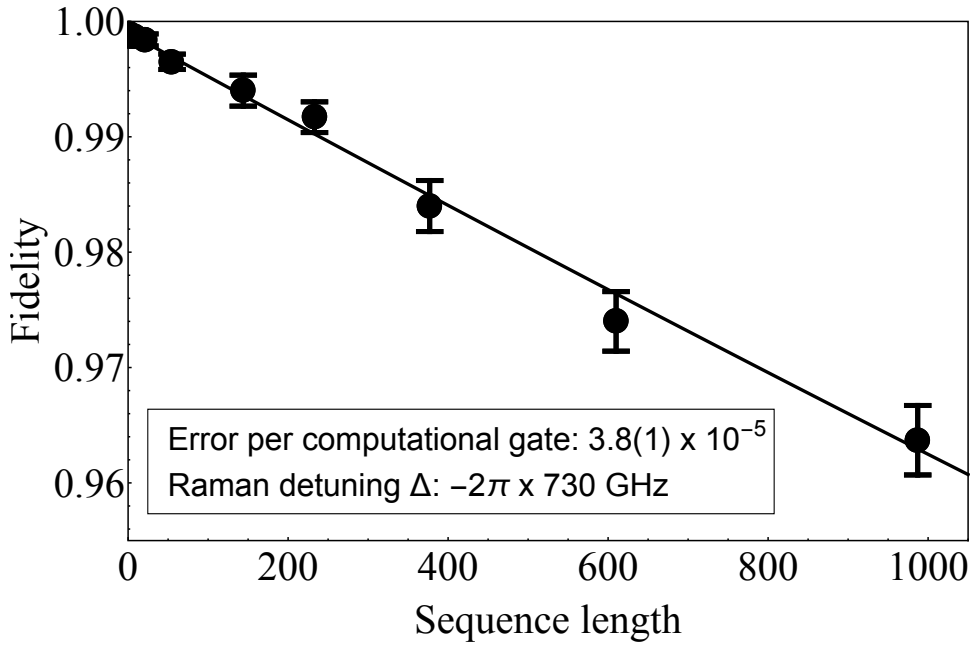

Figure 6.7: Average fidelity for single-qubit-gate randomized benchmarking sequences, plotted as a function of sequence length. We determine the average error per computational gate to be $\epsilon_{\text{gate}} = 3.8(1) \times 10^{-5}$ and state preparation and measurement error to be $\epsilon_{\text{SPAM}} = 2.0(3) \times 10^{-3}$ for these data sets. Error bars show the standard error of the mean for each point.

of the Clifford group is intrinsically depolarized, i.e. the average fidelity of an operation applied to a pure state is identical to the operation fidelity averaged over different pure states [Knill 08]. Under this depolarizing assumption, randomized benchmarking yields an average fidelity as a function of the number of computational gates. The average fidelity decreases to the asymptotic values of 1/2 with sufficiently large number of computational gates. The average fidelity with a sequence length of l is [Knill 08]

$$F = \frac{1}{2} + \frac{1}{2}\left(1 - \epsilon_{\mathrm{SPAM}}\right)\left(1 - 2\epsilon_{\mathrm{gate}}\right)^{l}. \tag{6.13}$$

By fitting this expression to the data on Fig. 6.7, we deduce an error per computational gate of $\epsilon_{\mathrm{gate}} = 3.8(1) \times 10^{-5}$, and $\epsilon_{\mathrm{SPAM}} = 2.0(3) \times 10^{-3}$. For $\Delta \simeq -2\pi\times$ 730 GHz used here, spontaneous emission error [Ozeri 07] is calculated to be 2.5×10^{-5}. This value is estimated using the Kramer-Heisenberg equation (Eq. 4.29), and is verified with a separate measurement made on the ion. The remaining error is dominated by Rabi rate fluctuations of approximately 1×10^{-3} due to imperfect laser power stabilization. Fluctuations in the Rabi rate are inferred from separate experiments that calibrate the Rabi rates of the laser-induced qubit transition; the associated error is inferred from a Schrödinger equation (Eq. 4.27) or a master equation (Eq. 4.28) simulation combined with a Monte-Carlo simulation that includes the measured power fluctuations. These calibration experiments are interleaved with the benchmarking experiments.

6.8 Summary

In summary, we demonstrated high-fidelity single-qubit and two-qubit laser-induced gates with trapped $^9Be^+$ ions. The single-qubit gates fidelity of 0.999962(1) (corresponding to an error of $\epsilon = 3.8(1) \times 10^{-5}$) exceeds some threshold estimates for fault-tolerant error correction with reasonable overhead. A partial state tomography is developed to analyze our two-qubit gate data. The highest achieved two-qubit gate fidelity is measured to be 0.9992(4) (corresponding to an error of $\epsilon = 8(4)\times10^{-4}$). The sources of error have been identified and strategies to further suppress them were discussed. This result is a factor of ~ 50 improvement compared to the previous best effort

of implementing a high-fidelity two-qubit gate with $^9Be^+$ ions in our laboratory [Tan 13] (see also Chap. 7). The improvement was made by taking advantage of various technological developments [Wilson 11, Bowler 13, Colombe 14, Leibrandt 15] and using an ion trap [Blakestad 11] which has a lower anomalous heating [Turchette 00a] due to uncontrolled electric field noise.

Similar laser-driven single-qubit and two-qubit gate has also been demonstrated with $^{43}Ca^+$ ions by the trapped-ion group at Oxford [Ballance 16]. Single-qubit computational gate with an error of $6.6(3)\times10^{-5}$ were evaluated with randomized benchmarking techniques on a magnetic-field insensitive transition. Two-qubit gates were implemented with the $\hat{\sigma}_z\hat{\sigma}_z$ gate (see Sec. 4.3.2 and Ref. [Leibfried 03]) with an error of $1(1)\times10^{-3}$. Along with our two-qubit gate presented here, these results appear to be the highest multi-qubit gate fidelities reported to date in any physical platform.

However, despite the improvement, two-qubit gates remain the only elementary QIP operation which has yet to be demonstrated with error lower than the practical fault-tolerant threshold of $\sim 10^{-4}$. In this context, we plot the history of two-qubit gate errors achieved with (i) laser driven interactions applied on trapped-ion qubits, (ii) microwave-driven interactions applied on trapped-ion qubits, and (iii) superconducting circuits in Fig. 6.8. Although the fidelity of the two-qubit entangling gate provides a benchmark for the level of quantum control across different platforms, it provides little information about the scalability of different systems. We are not aware of a simple metric for a system's scalability for the realization of a practical QIP device.

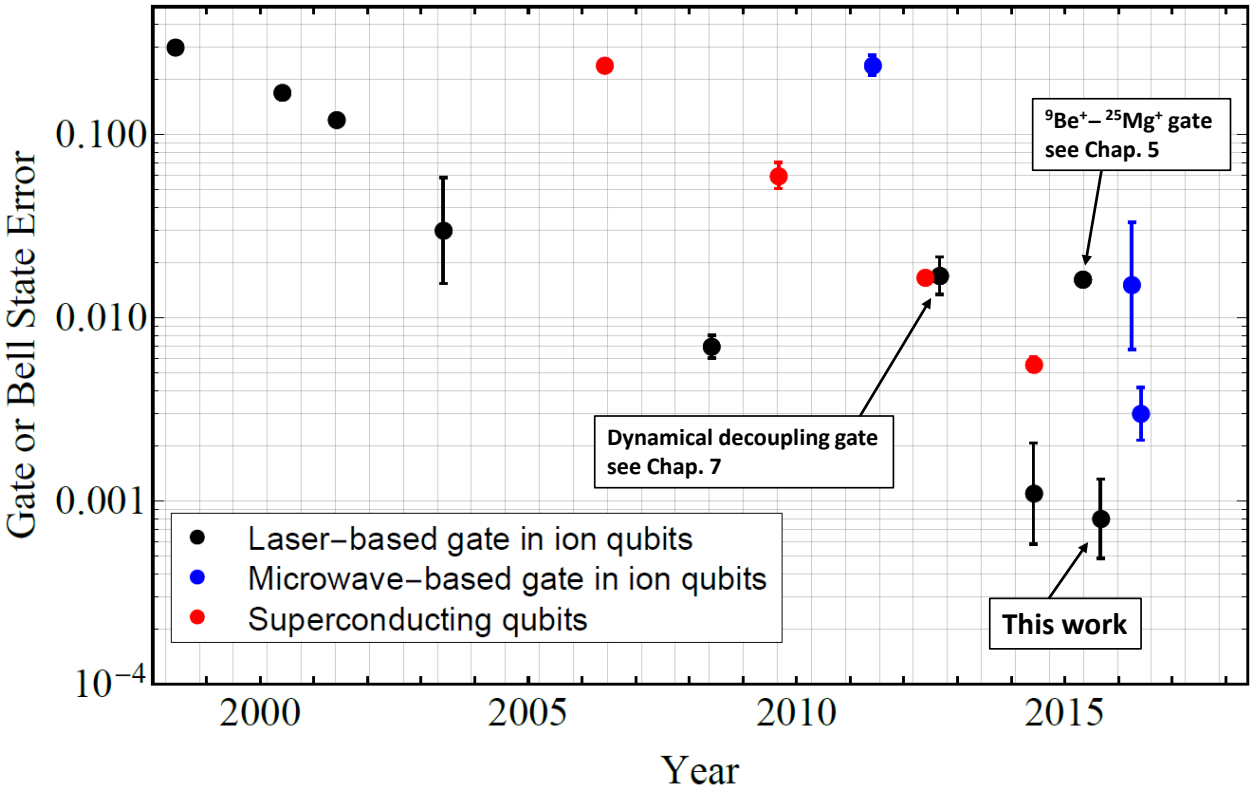

Figure 6.8: Two-qubit gate errors (or the errors of the created Bell state) reported in the literature over time. This figure is not comprehensive but shows the best two-qubit gate results, as well as two other type of two-qubit gate results presented in this thesis. Gate implementations in three platforms are shown, i.e. (i) laser-driven gates on ion qubits [Turchette 98, Sackett 00, Rowe 01, Leibfried 03, Benhelm 08, Tan 13, Tan 15, Ballance 16, Gaebler 16], (ii) microwave-driven gates on ion qubits [Ospelkaus 11, Weidt 16, Harty 16], and (iii) superconducting qubits [Steffen 06, DiCarlo 09, Chow 12, Barends 14]. The highest fidelity achieved with ion qubits using a microwave-based implementation is 0.997(1) [Harty 16] and 0.9944(5) with superconducting qubits [Barends 14]. Data in this figures are of courtesy from Prof. David Lucas (University of Oxford) who collected and consolidated the data.

Chapter 7

Dynamical Decoupling Two-Qubit Geometric Phase Gate

7.1 Introduction

Based on extensions of the spin-echo technique [Hahn 50], dynamical decoupling was first proposed and studied theoretically in Ref. [Viola 98] by driving a control Hamiltonian that continuously induces oscillation between the states of a two-level system. Since then, various proposals and implementations using dynamical decoupling schemes to suppress decoherence errors affecting the quantum systems of interests have been reported. The general theory of dynamical decoupling was formulated in Ref. [Viola 99] and reviewed in a more recent paper [Lidar 14].

Most dynamical decoupling schemes have been implemented for the protection of quantum memories against environmental noise [Du 09, de Lange 10, Ryan 10, Szwer 11] such as external magnetic field fluctuations. For quantum information processing, it is also desirable to have dynamical decoupling built into quantum gates or have quantum gates directly applicable to quantum memories which are protected by dynamical decoupling techniques. Such operations must be designed to provide protection against environmental noise, but not from the control fields required to apply the coherent operations. Single-qubit gates featuring protection with dynamical decoupling have been demonstrated in Ref. [Levitt 86, Souza 12, Zhang 14]. Demonstrations of multi-qubit gates with dynamical decoupling built-in include Ref. [van der Sar 12, Liu 13, Zhang 15] with solid-state-based qubits and with trapped-ion qubits [Tan 13, Piltz 13]. Furthermore, dynamical decoupling has also been used to lengthen the lifetime of an entangled state [Gustavsson 12].

In this chapter, we describe an experimental implementation of an entangling gate based on

a spin-dependent force featuring continuous dynamical decoupling using two trapped-ion qubits. The decoupling is provided by a control field that continuously induces oscillation between the logical states of the qubit. With this, the qubit becomes less sensitive to dephasing errors which can be caused by external magnetic field fluctuations. Furthermore, fluctuations in the AC Stark shifts induced by the laser beams that are used for driving coherent operations through stimulated-Raman process are also suppressed. This technique is analogous to the bang-bang control used in classical platforms (see for example Ref. [Takahashi 70, Macki 82]).

The entangling gate scheme described and implemented here was proposed in the theoretical paper by Bermedez *et al.* [Bermudez 12]. The proposal considers the weak effective spin-spin coupling regime, where the motional mode that serves as the mediator for the spin-dependent force is only virtually excited. Here, we modify the original proposal to be applicable in the strong effective spin-spin coupling regime in order to maximize gate speed for a given laser-induced transition Rabi rate. This enables us to minimize gate errors due to spontaneous scattering of photons caused by stimulated-Raman laser beams (see Sec. 4.4.2). Furthermore, a faster gate speed suppresses other error sources such as motional heating and other thermal-related errors. Following the publication of our work [Tan 13], a theoretical study for the gate scheme in the strong coupling regime was presented in Ref. [Lemmer 13], providing a complementary framework for the results presented in our experimental demonstration.

7.2 Experiment Setup and Implementation

This experiment was carried out in a legacy experimental setup with a different trapped-ion apparatus located in a different laboratory. However, most of the crucial elements for the manipulations of trapped ions used here are very similar to that described in other parts of this thesis. A detailed description of this legacy experimental apparatus is available in Ref. [Jost 10]. Similar to the X-junction trap [Blakestad 11] (see also Sec. 3.1), the ion trap used here is also a linear Paul trap [Paul 90]. As shown in Fig. 7.1, this trap consists of eight pairs of control electrodes for shuttling of ions but does not feature a junction for arbitrary reordering of an ion

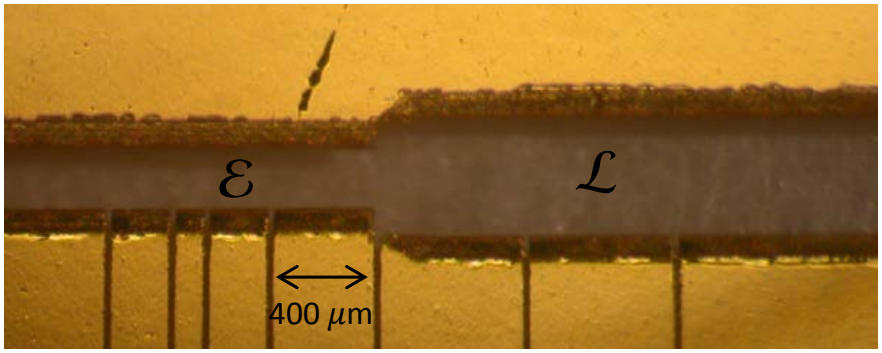

Figure 7.1: The electrodes of the ion trap used for the experiment described in this chapter. The ions are loaded in zone $\mathcal{L}$ and transported to zone $\mathcal{E}$ for the entangling gate to be implemented. See Ref. [Jost 10] for details of the design and construction of this trap.

crystal. The ions were first loaded in zone $\mathcal{L}$ and then transported to zone $\mathcal{E}$, where entangling gate operations were carried out.

For this ion trap, the axial micromotion experienced by the ions is substantially smaller than in the X-junction trap. Therefore, we do not apply the differential voltage on the electrodes for detection (described in Sec. 2.1.1). Furthermore, the spin-motion stimulated-Raman transitions were driven on the micromotion carrier. The motional mode heating [Turchette 00a] rate of this trap is higher compared to the case of the X-junction trap. For a single $^9Be^+$ ion, we measure the heating rate to be $\simeq 0.5$ quanta/ms at an axial trapping frequency of $\simeq 2\pi \times 2.7$ MHz[1] . Heating rate affects the performance of the entangling gate and will be discussed in Sec. 7.3 (see also Sec. 4.4.4).

The laser beam setup used for the experiment here suffered certain drawbacks compared to that described in the rest of this thesis. Firstly, here the laser beam profiles and pointing fluctuations were considerably worse due to the unavailability of the ultraviolet (UV) fibers [Colombe 14]. Secondly, the laser power stabilization for the laser beams was not as robust as that used in Chap. 6 and we did not have access to apparatus with sufficient servo bandwidth to employ dynamic shaping of laser intensity profiles. Furthermore, due to the limited available laser power when this experiment was carried out, the Raman detuning used here induced a higher spontaneous emission

[1] angular frequency

rate compared to that used in Chap. 6. Higher photon scattering rate causes higher gate error, see details in Sec. 4.4.2. The laser beam setup used for the experiment here suffered certain drawbacks compared to that described in the rest of this thesis. Firstly, here the laser beam profiles and pointing fluctuations were considerably worse due to the unavailability of the ultraviolet (UV) fibers [Colombe 14]. Secondly, the laser power stabilization for the laser beams was not as robust as that used in Chap. 6 and we did not have access to apparatus with sufficient servo bandwidth to employ dynamic shaping of laser intensity profiles. Furthermore, due to the limited available laser power when this experiment was carried out, the Raman detuning used here induced a higher spontaneous emission rate compared to that used in Chap. 6. Higher photon scattering rate causes higher gate error, see details in Sec. 4.4.2.

Two $^9Be^+$ ions are confined along the axis of a linear Paul trap and have an axial center-of-mass (COM) mode (angular) frequency of $2\pi \times 2.6$ MHz and a stretch mode frequency of $2\pi \times 4.5$ MHz. For a single $^9Be^+$ ion, the radial secular frequencies are set to be $2\pi \times 12.5$ MHz and $2\pi \times 11.8$ MHz. Here, we used the hyperfine state of $|F = 2, m_F = 1\rangle = |\downarrow\rangle$ and $|1, 0\rangle = |\uparrow\rangle$ as our qubit. Although this choice of hyperfine states for the qubit is different than that used in other experiments described in this thesis, the properties of these qubits are very similar. The qubit frequency is $\omega_0 \simeq 2\pi \times 1.207$ GHz, which is first-order insensitive to changes in the applied magnetic field of B $\simeq 0.011964$ mT (119.64 G). The direction of the applied magnetic field is aligned 45° with respect to the trap axis. Table A.2 lists the magnetic-field insensitive transitions in the electronic ground state of the $^9Be^+$ ion.

As described in Sec. 4.3.5, the Bermudez protocol requires a resonant carrier spin-flip excitation and a single spin-motion sideband excitation with a detuning of δ from a selected motional mode. Here, the detuned spin-motion sideband excitation is driven through a stimulated-Raman process by a pair laser beams labeled by $\boldsymbol{k_{Co1}}$ and $\boldsymbol{k_{90}}$ in Fig. 7.2. These two beams are aligned such that their vector difference $\boldsymbol{\Delta k_z} = 2\sqrt{2}\pi/\lambda$ aligned along the axial direction. In this configuration, only the motional mode along the trap axis interacts with the laser beams. We set the beat-note frequency of these two laser beams to be blue detuned by a frequency δ from the stretch

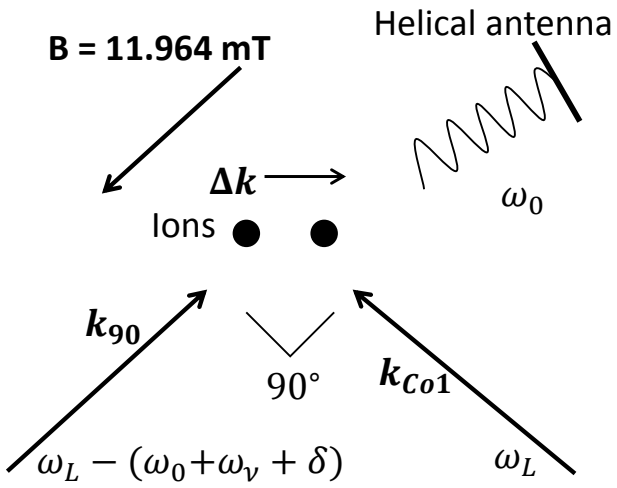

Figure 7.2: Laser beam setup to drive the two-qubit gate with the Bermudez protocol in the case of a microwave-induced carrier excitation. Two lasers beams labeled as $\boldsymbol{k_{Co1}}$ and $\boldsymbol{k_{90}}$ are used to excite the detuned spin-motion sideband transitions. Their wave vector difference $\boldsymbol{\Delta k}$ is aligned such that only the axial motional mode can be coupled.

mode blue sideband transition. In our setup, the carrier excitation can be driven by (i) a microwave field, or (ii) a laser field. We investigated both methods in two different sets of experiments. The microwave fields are delivered with a helical antenna located outside the vacuum system, with the frequency set and impedance matched to the source at $\omega_0 \simeq 2\pi \times 1.207$ GHz. We achieve a carrier π-pulse duration of approximately 11 μs. The laser field to drive the carrier excitation includes an additional beam $\boldsymbol{k_{Co2}}$ that paired is with the beam $\boldsymbol{k_{Co1}}$ (see Fig. 7.3). The relative frequency difference of these two beams is set to be ω_0, and the carrier π-transition has a duration of approximately 5 μs. As these two beams are copropagating, the Rabi frequency is not affected by the ion's motion [Wineland 98]. These two beams are generated inside a single AOM (with center frequency $\sim$ 600 MHz) analogous to that described in Sec. 3.4.3. The Raman detuning is set to be $\simeq$ 260 GHz ($\simeq$ 160 GHz) red detuned from the $^2S_{1/2} \leftrightarrow {}^2P_{1/2}$ transitions for the microwave (laser)-induced-carrier gate. In the rotating-wave approximation, and after transforming into the interaction frame of both the qubit and the motion, the Hamiltonian of our implementation the Bermudez protocol in the Lamb-Dicke limit is

$$H = \hbar \sum_{j=1,2} \left(\Omega_C \hat{\sigma}_j^+ e^{i\phi_C} + i\Omega_j \hat{\sigma}_j^+ \hat{a}^\dagger e^{-i\left(\delta t + \phi_j'\right)} \right) + h.c., \tag{7.1}$$

where Ω_C denotes the Rabi rate of the carrier excitation that provides the dynamical decoupling, and $\Omega_j = \Omega_{0,j}\eta\xi_j$, where $\Omega_{0,j}$ is the Rabi rate of the resonant laser-driven carrier excitation, η is the Lamb-Dicke parameter for the selected normal mode with ξ_j as the mode amplitude of the jth ion. The respective phases for the carrier and sideband excitation are ϕ_C and $\phi_j' = \Delta k X_{0,j} + \Delta\phi$, where Δk and $\Delta\phi$ are the difference in wave vectors and phases of the optical fields driving the blue sideband transition, respectively. The equilibrium position of the the jth ion is denoted by $X_{0,j}$.

Since the interesting case is when $\Omega_C \gg |\Omega_j|$, we go to the interaction frame where the states are dressed by the carrier excitation. With this condition, the eigenvalues of the dressed system under the influence of a certain mechanism that shifts the qubit frequency by ω' are given by Eq.

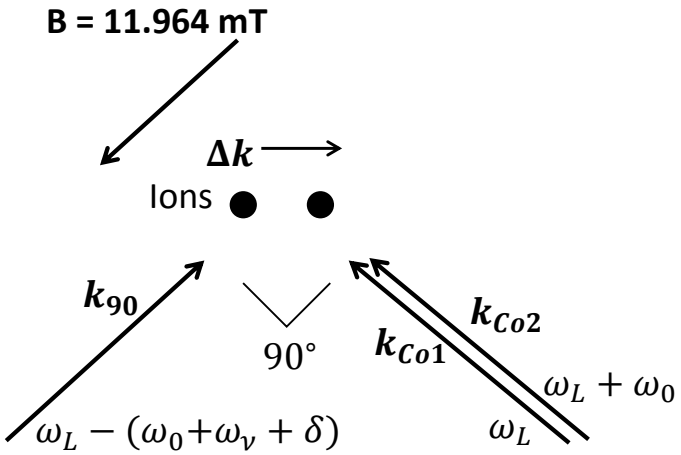

Figure 7.3: The laser beam setup where carrier excitation is induced by stimulated-Raman process. This setup is very similar to that depicted in Fig. 7.2. Here, the microwave antenna is turned off and an additional beam labeled as $\boldsymbol{k_{Co2}}$ is adjusted such that its frequency is shifted ω_0 relative to beam $\boldsymbol{k_{Co1}}$. Together, these two beams excite carrier transitions.

4.25:

$$\pm\frac{1}{2} \quad \Omega_C + \frac{\omega'^2}{\Omega_C} + \frac{1}{2}\Omega_C \left(\frac{\omega'^2}{\Omega_C^2}\right)^2 + \cdots \Bigg). \tag{7.2}$$

Therefore, the influence of ω' becomes a second order effect and decreases as Ω_C increases. Now we consider the effects of the sideband terms in the dressed-state picture. In the $|+\rangle, |-\rangle$ basis where

$$\begin{aligned} |\uparrow\rangle &= \frac{1}{\sqrt{2}}\left(|+\rangle + |-\rangle\right), \\ |\downarrow\rangle &= \frac{1}{\sqrt{2}}\left(|+\rangle - |-\rangle\right), \end{aligned} \tag{7.3}$$

the Hamiltonian described in Eq. 7.1 becomes

$$\begin{aligned} H = & \quad i\hbar\sum_j \frac{\Omega_j}{2}\left(|+\rangle_j\langle+|_j - |-\rangle_j|-\rangle_j\right)\left(\hat{a}^\dagger e^{-i(\delta t+\phi'_j)} - \hat{a}e^{i(\delta t+\phi'_j)}\right) \\ & + i\hbar\sum_j \frac{\Omega_j}{2}\left(|+\rangle_j\langle+|_j e^{-2i\Omega_C t} - |+\rangle_j|-\rangle_j e^{2i\Omega_C t}\right)\left(\hat{a}^\dagger e^{-i(\delta t+\phi'_j)} + \hat{a}e^{i(\delta t+\phi'_j)}\right). \end{aligned} \tag{7.4}$$

The first term in the expression above is identical to Eq. 4.16, which describes a Hamiltonian of a geometric phase gate with the spin-dependent force acting on the rotated basis. The second term induces off-resonant transitions between the dressed states $|+\rangle$ and $|-\rangle$ and can be dropped when $\Omega_C \gg |\Omega_j|$. We set $\phi_C = 0$ for simplicity; this does not affect the discussion that follows. The entangled states produced by this protocol are insensitive to optical path length changes between the non-copropagating laser beams ($\boldsymbol{k_{Co1}}$ and $\boldsymbol{k_{90}}$ in Fig. 7.2 and Fig. 7.3) that occur on a time scale that is long compared to the gate duration [Tan 13].

However, similar to the situation in Sec. 5.2.1, the geometric phase accumulated after applying the gate depends on the basis states. Applying Eq. 5.5 to the case here by writing $\phi_{M,j} = \phi'_j$, after setting $\Omega_1 = \Omega_2 = \Omega$, the geometric phase accumulated by the different parity basis states after a duration of $2\pi/\delta$ is

$$\begin{aligned} \varphi_{++,--} &= \frac{8\pi\Omega^2}{\delta^2}\cos^2\left(\frac{\Delta k(X_{0,1} - X_{0,2})}{4}\right), \\ \varphi_{+-,-+} &= \frac{8\pi\Omega^2}{\delta^2}\sin^2\left(\frac{\Delta k(X_{0,1} - X_{0,2})}{4}\right), \end{aligned} \tag{7.5}$$

With this, it becomes obvious that the geometric phases applied to the basis states depend upon the distance between the two ions, i.e. $X_{0,1} - X_{0,2}$. Here, we adjust the strength of the harmonic

confinement to make the ions' separation distance equal to $\pi p/\Delta k$ where p is an integer. By doing so, the entangling gate speed can be optimized for a given Ω and δ by setting the geometric phases for the different parity qubit state to differ by $\pi/2$.

In the case where the condition of $\Omega_C \gg \Omega$ is not rigorously satisfied, the evolution of the populations oscillates and the final state depends on the finite carrier Rabi frequency. Figure 7.4 shows a simulation result of the interaction Hamiltonian described in Eq. 7.1 with $\Omega_C = 15\Omega_{j=1,2}$. In our experimental implementation, we remove the fast oscillation dependence by performing spin-echo type sequences.

For the case where the carrier excitations are driven by the microwave field, we applied a π-pulse with a $\frac{\pi}{2}$-phase shift relative to the carrier in the middle of the gate sequence, as depicted in Fig. 7.5. This phase shift operation is accomplished by reprogramming the direct-digital synthesizer which is used for the generation of the microwave field (see Sec.3.6). The application of this pulse makes the ions undergo a multiple-loop trajectory in motional phase space which can further suppresses errors in the gate detuning δ and gate duration that can lead to residual spin-motion entanglement at the end of the gate operation [Hayes 12].

The spin-echo sequence for the case where the laser is used to induce carrier transition is shown in Fig. 7.6. The carrier excitation is continuously applied but a π-phase shift is implemented halfway through the gate. This phase shift is accomplished by changing the phase of the RF signal used for the generation of the $\boldsymbol{k_{Co2}}$ laser beam (see Fig. 7.3). In contrast to the microwave-carrier case, this spin-echo sequence induces a single-loop phase-space trajectory. It corrects only for errors in the carrier Rabi frequency but does not suppress errors that lead to residual spin-motion entanglement.

Each experiment repetition begins with Doppler cooling and optical pumping of the ion's population to the $|F = 2, m_F = 2\rangle$ state, followed by Raman sideband cooling [Monroe 95b] of the axial COM and stretch modes to $\bar{n}$ of $\simeq 0.2$ and $\simeq 0.05$, respectively. This is followed by applying a composite pulse sequence [Levitt 86] induced by copropagating beams $\boldsymbol{k_{Co1}}$ and $\boldsymbol{k_{Co2}}$ (Fig. 7.3), consisting three resonant pulses $R(\pi/2, 0)$, $R(\pi, \pi/2)$, and $R(\pi/2, 0)$ (the rotation operation

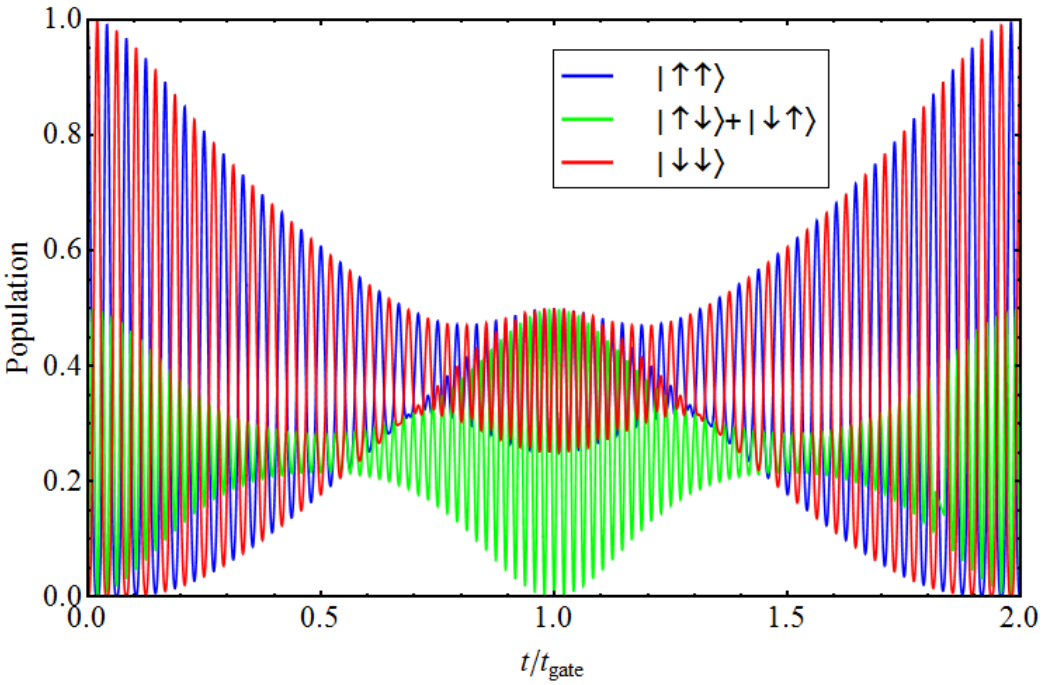

Figure 7.4: Simulated population evolution of Hamiltonian in Eq. 7.1 with both qubits initialized to the $|\uparrow\rangle$ state. Although a maximally entangled state can be created at $t = t_{\text{gate}}$, due to the finite ratio between the carrier transition Rabi rate Ω_C and the sideband transition Rabi rate $\Omega = \Omega_1 = \Omega_2$, the populations undergo oscillations at the carrier Rabi frequency, making the target state highly sensitive to the interaction time. Here, the simulation parameter is $\Omega_C = 15\Omega$.

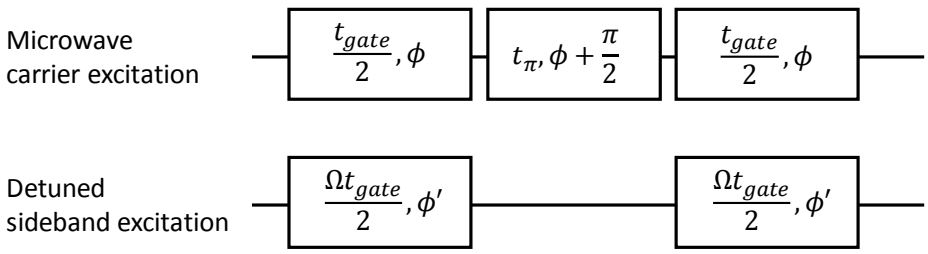

Figure 7.5: Pulse timing sequence for the microwave-induced-carrier gate. A π rotation with a $\pi/2$ phase with respect to the previous pulse refocuses the fast spin population oscillations induce by the carrier excitation (see Fig. 7.4). This pulse can suppress miscalibrations and errors in the gate duration and detuning, δ [Hayes 12].

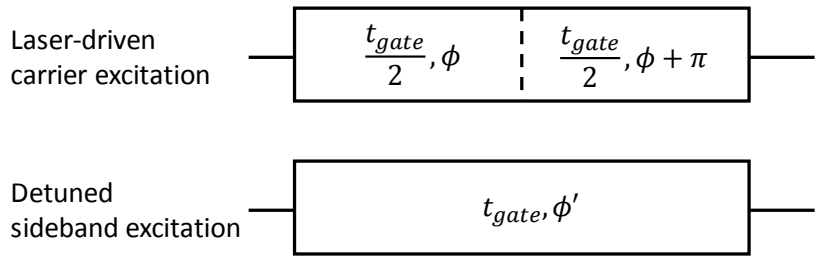

Figure 7.6: Pulse timing sequence for the laser-induced-carrier gate. The phase of the carrier excitation is shifted by π during the second half of the gate.

$R(\theta, \phi)$ is given in Eq. 2.13) that transfers each each ion from the $|2,2\rangle$ state into the $|2,1\rangle = |\downarrow\rangle$ state. With both ions initialized to the $|\downarrow\downarrow\rangle$ state, the entangling gate ideally creates the Bell state $|\Phi_+\rangle = \frac{1}{\sqrt{2}}(|\downarrow\downarrow\rangle + |\uparrow\uparrow\rangle)$.

The standard state-dependent resonance fluorescence technique is used to measure the ions' state at the end of the gate operation. First, the $|\downarrow\rangle$ states are transferred to the $|2,2\rangle$ state by using the same composite pulse sequence as for the state initialization, and the $|\uparrow\rangle$ state is transferred to the $|1,-1\rangle$ state by use of a single "shelving" π-pulse (see Fig. 2.1 for $^9Be^+$ ion's energy level diagram). This is followed by turning on the detection laser beam for 250 μs. Ions in the $|2,2\rangle$ state fluoresce "bright" and register an average of ~ 30 photons per ion on a photomultiplier tube. Ions in the $|1,-1\rangle$ state fluoresce "dark" and register an average background counts of 3 photons. Detection counts yield three possible outcomes: two ions bright ($|\downarrow\downarrow\rangle$), one ion bright ($|\uparrow\downarrow\rangle$ and $|\downarrow\uparrow\rangle$), and zero ions bright ($|\uparrow\uparrow\rangle$). The probabilities of those outcomes, P_2, P_1, and P_0 respectively, are determined by fitting a triple Poissonian function to the histogram of counts obtained in each experiment.

The population evolution as a function of the gate interaction duration with carrier excitation driven by laser beams is shown in Fig. 7.7, with the state $|\Phi_+\rangle$ (in the ideal case) created at $t_{\text{gate}} = \frac{2\pi}{\delta} \simeq 105$ μs. The coherence of the created Bell state is investigated by applying an "analysis" carrier $\pi/2$-pulse to the ions. Figure 7.8 shows the parity $(P_2 + P_0 - P_1)$ plotted as a function of the phase ϕ of the analysis pulse for the case of the microwave-induced-carrier gate with a gate duration of $t_{\text{gate}} = \frac{4\pi}{\delta} = 250$ μs. The resulting oscillation of the parity is fitted to the

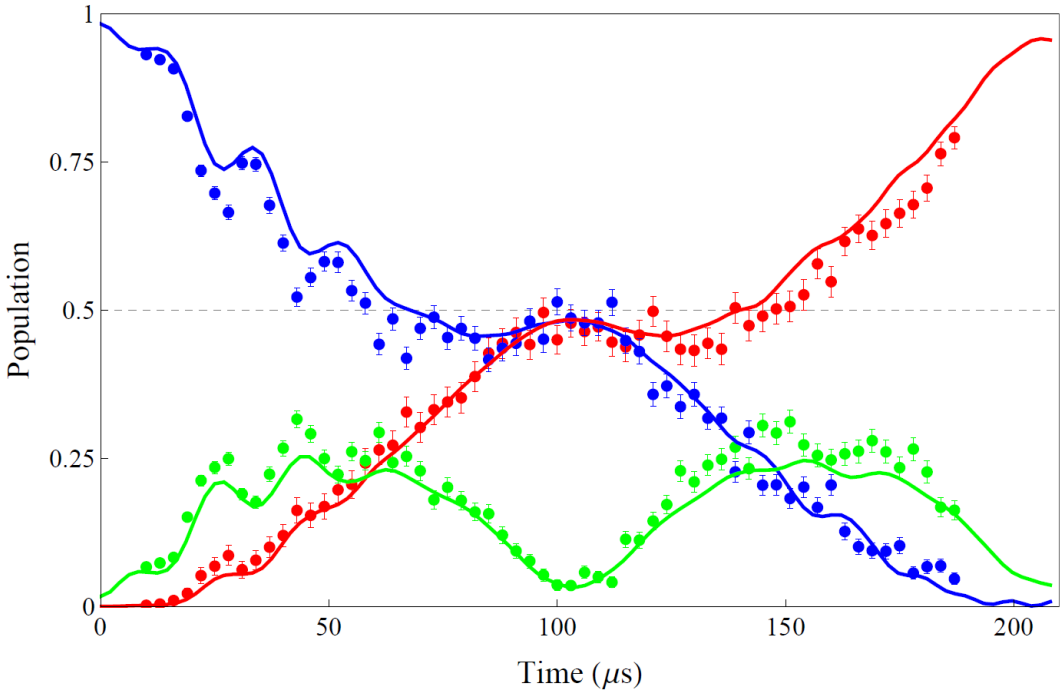

Figure 7.7: Evolution of the populations of $|\downarrow\downarrow\rangle$ (blue points), $|\uparrow\uparrow\rangle$ (red) and anti-aligned spin states (green) as a function of the duration of simultaneous application of laser-induced carrier and detuned sideband excitations. The phase of the carrier is shifted by π at half of the interrogation time for each point (see Fig. 7.6). The gate time for this case is approximately 105 μs, at which point the Bell state $|\Phi_+\rangle = \frac{1}{\sqrt{2}}(|\downarrow\downarrow\rangle + |\uparrow\uparrow\rangle)$ (in the ideal case) is created. The solid lines show the results of numerical master equation simulation that include contributions from (i) spontaneous scattering of photon induced by the Raman laser beams, and (ii) state preparation and detection error.

function $A\cos(2\phi + \phi_0)$. The performance of the gate was characterized by measuring the created Bell state's fidelity, which is determined by the contrast of the parity oscillation (A) and the total qubit population in the $|\uparrow\uparrow\rangle$ and $|\downarrow\downarrow\rangle$ ($P_2 + P_0$). The Bell state fidelity, F, is $(P_0 + P_2 + A)/2$ [Sackett 00]. For the microwave-induced-carrier gate we find $P_0 + P_2 = 0.988(4)$ and $A = 0.960(8)$, which gives $F = 0.974(4)$. For the laser-induced-carrier gate we determine $P_0 + P_2 = 0.961(1)$ and $A = 0.930(8)$, which gives $F = 0.946(4)$.

7.3 Error Sources

The sources of error which lead to imperfect creation of the Bell state were investigated with numerical simulations and calibration measurements. Certain sources of error in the $\sim 10^{-4}$ level or lower are not described here. Table 7.1 shows the individually evaluated error contributions for both the microwave-induced carrier and the laser-induced-carrier gates. For the laser-induced-carrier gate, the error caused by spontaneous scattering of photons is dominated by the laser beams that are used to drive the carrier excitation (the $\boldsymbol{k_{Co1}}$ and $\boldsymbol{k_{Co2}}$ beams in Fig. 7.3). Furthermore, due to a limited amount of power available from the laser source, the Raman detuning was restricted to $\simeq 160$ GHz to allocate sufficient power for the laser beams responsible for the carrier excitation. For the microwave-induced-carrier gate, we were able to increase the Raman detuning to $\simeq 260$ GHz and thus reduce the spontaneous emission error compared to the laser-induced-carrier gate. We calculated the spontaneous scattering rate using the Kramer-Heisenberg equation as shown in Eq. 4.29 and then deduced the associated gate error by numerically simulating the master equation containing the out-of-manifold scattering and bit-flip scattering Lindblad operators (see Sec. 4.4.2.1). We also performed the following experiments to estimate the Raman scattering rate; first, the ions were prepared in their qubit states, then the Raman laser beams were turned on with their frequency difference set far-off resonant from any transition, so their primary effect was to induce photon scattering. Finally the scattering rates were determined by measuring how much population that remained in the qubit states. The measurements agrees with the calculation using the Kramer-Heisenberg equation. Errors due to Rayleigh scattering (Sec. 4.4.2.2) were estimated

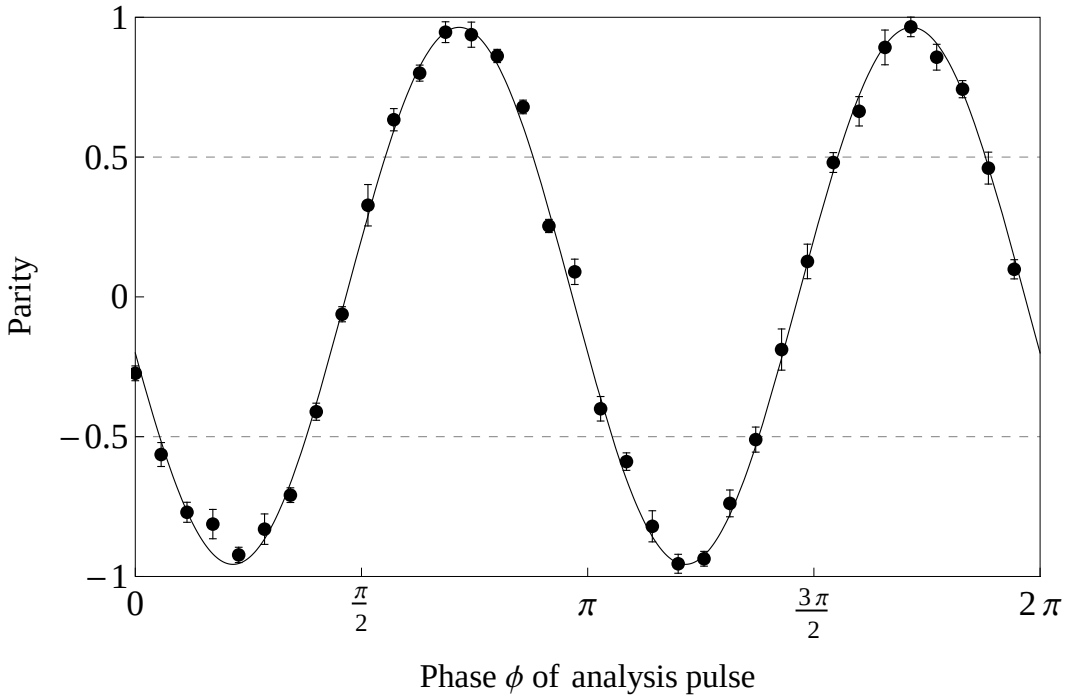

Figure 7.8: The coherence of the state produced by the microwave-induced-carrier gate is investigated by applying an analysis $\pi/2$-pulse with a variable phase. The contrast of the parity oscillation is determined by fitting $A\cos(2\phi + \phi_0) + B$ to the data points.

Infidelities/Errors	Microwave ($\times 10^{-3}$)	Laser ($\times 10^{-3}$)
Spontaneous emission	2.8	19
State preparation and detection	9.1	17
Carrier drive infidelities	1.3	16
Debye-Waller factor	~ 10	~ 6
Fast oscillation term	~ 3	< 1
Imperfect sideband drive	~ 1	~ 1
Motional heating of strectch mode	< 1	< 1

Table 7.1: Individually evaluated errors that contribute to the imperfect creation of the Bell state $|\Phi_+\rangle$ state with carrier excitation driven by (i) microwave field and (ii) laser field. See Sec. 4.4 for detail discussions on error sources in the implementation of two-qubit gates and their respective evaluation strategies.

to be negligible in the gate implementation here.

The errors for state preparation and measurement include imperfect optical pumping that initialized the ions to the $|2, 2\rangle$ state, and errors in the transfers of population into and out of the qubit manifold. The improved state preparation and detection for the microwave-induced-carrier gate was achieved by a more careful calibration of the optical pumping laser beams' polarization and alignment with respect to the applied magnetic field. By using a microwave field for the qubit-state transfers and better composite pulse sequences (e.g. see Eq. 2.12 and Eq. 2.14), state preparation and detection errors could be further suppressed to the level demonstrated in Chap. 6.

Errors due to fluctuations of the carrier Rabi frequency that are slow compared to the gate duration are highly suppressed by the spin-echo techniques (Fig. 7.5 and Fig. 7.6). However, fluctuations on the time scale of the gate duration cause error. This error source was characterized by performing the gate sequences with only the carrier drive applied to the ions and measuring the probability the ions end in $|\downarrow\downarrow\rangle$ state for the laser-induced carrier or the $|\uparrow\uparrow\rangle$ state for the microwave-induced carrier. The higher error for the laser-induced-carrier can be attributed to laser intensity and beam-pointing fluctuations. We estimated the error caused by fluctuations in the laser-induced sideband excitation due to laser intensity and beam-pointing fluctuation to be approximately 10^{-3} for both cases. This error was determined by performing a Monte Carlo simulation of the sideband

excitation incorporating measured laser-intensity and beam-pointing fluctuations. Errors related to laser intensity and beam-pointing fluctuations could be suppressed by better laser beam control as demonstrated in Chap. 6, e.g. UV fibers [Colombe 14] and better laser power stabilization including the dynamic shaping of laser power profile (see Sec. 3.8). A double-dressed state technique has been proposed to suppressed errors due to imperfect carrier excitation [Cohen 15].

As the spin-dependent force was applied on the axial stretch mode, the error due to motional dephasing associated with the anomalous heating [Turchette 00a] of this mode is negligible. However, due to (i) the finite temperature ($\bar{n} \simeq 0.2$) of the COM mode at the beginning of the gate implementation and (ii) the heating of the COM mode (~ 1 quanta/ms), the performance of the gate was affected through a fluctuating Debye-Waller factor (see Sec. 4.4.7). This error was estimated with Eq. 4.47 and Eq. 4.51. The microwave-carrier gate suffered more from this error mechanism due to its longer gate duration, as compared to the laser-carrier gate.

As shown in Eq. 7.4, the Hamiltonian describing the Bermudez gate contains two terms. The first represents the spin-dependent force and the second is a fast oscillation term which can be neglected if the Rabi rate of the carrier excitation is sufficiently high, i.e. $\Omega_C \gg \Omega$. In our implementation this condition was not rigorously satisfied and caused errors in the gate. This error is determined by performing numerical simulations with experimental values as input parameters, assuming they are noise free. Figure 7.9 shows the master equation simulation results of Bell state fidelity as a function of $\frac{\Omega_C}{\Omega}$ for different levels of motional dephasing rate as described by Eq. 4.39.

Errors associated with the imperfections of carrier excitation and the fast-oscillating term can be suppressed by better microwave field delivery that increases the Rabi rate and fidelity of microwave-driven transitions. Furthermore, a higher carrier Rabi rate also allows the gate speed to be increased, reducing the effect of error mechanisms associated with motional heating and thermal-related issues.

Other sources of error include qubit dephasing, motional frequency fluctuations, off-resonance coupling to spectator transitions, optical phase fluctuations, imperfect global rotations and calibra-

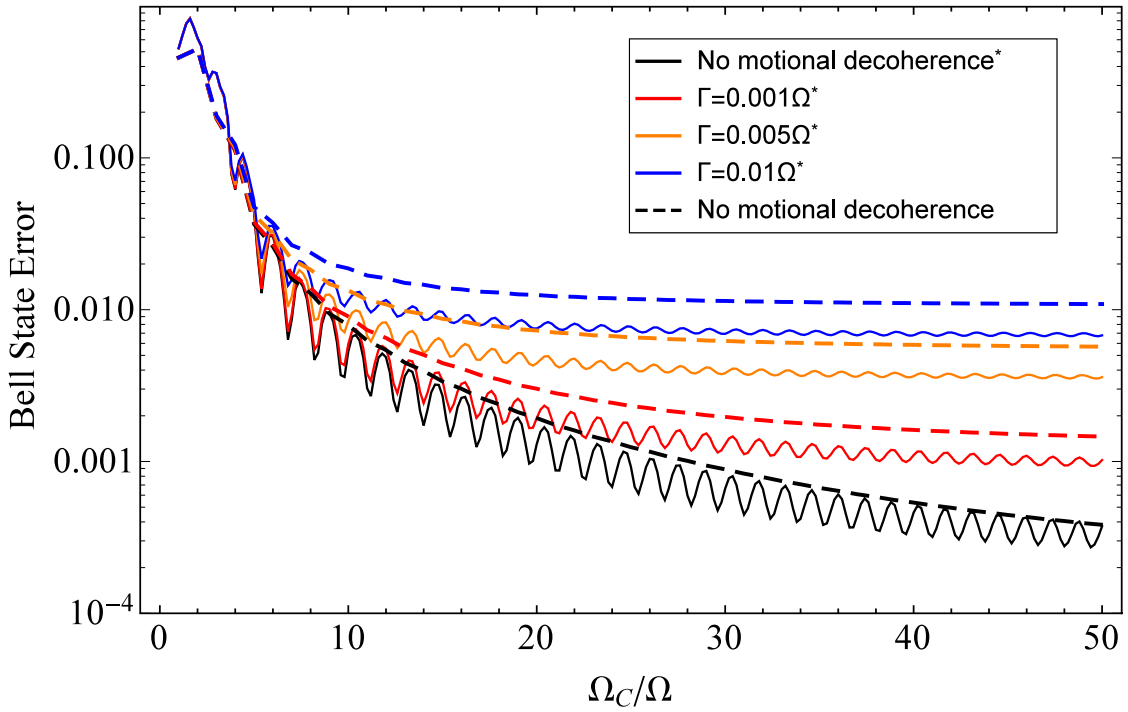

Figure 7.9: Master equation simulations are used to study the Bell state fidelity as a function of carrier Rabi rate (Ω_C) to sideband Rabi rate (Ω) ratio. The Hamiltonian described in Eq. 7.1 and the motional dephasing Lindblad term described by Eq. 4.39 are included. Four different motional dephasing rates, Γ, are considered and color coded in this figure. Two groups of the gate implementations are shown: (i) solid lines (marked with the asterisk symbol (*) in the legend) indicate a spin-echo sequence using a π-pulse rotation with $\pi/2$ phase shift as depicted in Fig. 7.5, and (ii) dashed lines represent spin-echo sequence implemented by shifting the phase of the carrier drive at the middle of the gate, as shown in Fig. 7.6. Each simulation begins with the ions in the $|\uparrow\uparrow\rangle$ state and with the interactions turned on for a gate time of t_{gate}. The duration of the single-qubit gate for the π-pulse rotation used in spin-echo sequence (i) is not included in t_{gate} to provide a straightforward comparison. For (i), Ω is set to be $\frac{\delta}{2}$ and the fidelity of the created Bell state is evaluated at $t_{\text{gate}} = \frac{1}{\delta}$. For (ii), the spin-echo sequence produces a two-loop gate. In this case, Ω is set to be $\frac{\delta}{2\sqrt{2}}$ and $t_{\text{gate}} = \frac{2}{\delta}$. A total of 11 Fock states are used in the simulation.

tion errors. These sources are estimated to contribute errors on the order of a few 10^{-4} or lower to the gate, and they were not studied extensively here (see Sec. 4.4 for discussions regarding these error sources).

7.4 Summary

Inspired by the proposal presented in Ref. [Bermudez 12], which considered a dynamical-decoupling entangling gate operating in the weak effective spin-spin coupling regime, we modified the proposal and demonstrated two gate schemes which operate in the strong coupling regime to maximize gate speed for a given laser-induced transition Rabi rate. By creating a Bell state and evaluating its fidelity, the performance of our gate implementations were investigated. The highest Bell state fidelity achieved was measured to be 0.974(4). The error sources that limit the creation of a perfect Bell state were studied and we determined that these errors were dominated by various technical issues at the time these gate schemes were implemented. Technical improvements that were made to allow the implementations of the high-fidelity universal gate set (described in Chap. 6) would also benefit the gate scheme described here.

A similar scheme has also been investigated in another trapped-ion group. In Ref. [Harty 16] a Bell state with a fidelity of 0.997(1) was created by employing a modified scheme which is referred to as the dynamical-decoupling Mølmer-Sørensen gate. The gate scheme was implemented with two detuned motional sideband excitations (similar to that of the Mølmer-Sørensen protocol described in Sec. 4.3.4), together with a carrier excitation that provided the dynamical decoupling. This gate scheme alleviates the requirement that the Rabi rate of the carrier excitation be much larger than the sideband excitations, while still providing protection against qubit dephasing. The gate implementation was accomplished by an all-microwave scheme, and the built-in dynamical decoupling reduced the gate error due to qubit dephasing caused by fluctuating AC Zeeman shifts induced by fluctuating microwave fields.

Chapter 8

Chained Bell Inequality Experiment

In this chapter, we describe chained Bell inequality (CBI) [Pearle 70] experiments performed with pairs of trapped ions. Ion pairs used here include a pair of $^{9}Be^{+}$ ions and a $^{9}Be^{+}$ - $^{25}Mg^{+}$ pair. The experiments were implemented with the techniques developed for a trapped-ion quantum information processing (QIP) using a quantum charge coupled device architecture outlined in Ref. [Wineland 98] and Ref. [Kielpinski 02]. These include (i) magnetic field insenstive ("clock") state qubits which offer long coherence time, (ii) robust state preparation and measurement, (iii) shuttling of ions for their individual addressing and measurements, (vi) generation of mixed-species entanglement (described in Chap. 5), (iv) high-fidelity deterministic generation of Bell states, and (v) single-qubit gates, (the latter two are described in Chap. 6). High performance of these techniques is essential for the realization of the experiments described here.

The detection efficiency in our experiment is near 100 %, and the measurement outcomes of every trial in each experiment were recorded. This avoid making the "fair sampling" assumption, such that our experiments successfully close the "detection loophole" [Pearle 70, Clauser 74].

This chapter is organized in the following fashion: we will first use the better known Clauser, Horne, Shimony, and Holt (CHSH)-type [Clauser 69] experiment to provide background and then introduce the chained Bell inequality experiment, including a brief summary on loopholes in Bell inequality experiments and previous CBI experiments. After a brief description of the experiment setup, results are presented in Sec. 8.3. The lowest chained Bell inequality parameter determined from our measurements is 0.296(12). This value is significantly lower than 0.586, the minimum

fraction derived from a perfect CHSH-type experiment. Lastly in Sec. 8.4, we briefly discuss one consequence of our Bell inequality results in the context of quantum certification under the "self-testing" framework [Mayers 04, McKague 12].

8.1 Background and Motivation

The incompatibility between quantum physics and local-realistic theory was first presented by Einstein, Podolsky, and Rosen [Einstein 35] and formulated by John Bell with a mathematical inequality [Bell 64]. This was followed by proposals for this conflict to be investigated in the so-called "Bell inequality experiments". The most notable one is that presented by Clauser, Horne, Shimony, and Holt (CHSH) [Clauser 69]. With each particle subjected to two measurement settings, a CHSH experiment employs two particles to be jointly measured with four different measurement setting combinations. In such experiments, the correlation outcomes must satisfy the CHSH inequality if local realism is valid, the CHSH inequality can be written as [Rowe 01]

$$\begin{aligned} B_{\text{CHSH}} &= |q(\alpha_1,\beta_1)+q(\alpha_2,\beta_1)|+|q(\alpha_1,\beta_2)-q(\alpha_2,\beta_2)| \\ &\leq 2, \end{aligned} \tag{8.1}$$

with

$$q(\alpha_k,\beta_l)=\frac{N_{\text{correlated}}(\alpha_k,\beta_l)-N_{\text{anticorrelated}}(\alpha_k,\beta_l)}{N_{\text{correlated}}(\alpha_k,\beta_l)+N_{\text{anticorrelated}}(\alpha_k,\beta_l)}, \tag{8.2}$$

where a_k and b_l with $k,l=1,2$ are the measurement setting choices applied on system a and b, respectively.

The first experimental confirmation of this violation by a quantum system was performed by Freedman and Clauser [Freedman 72], and refined by Aspect, Grangier and Roger [Aspect 82]. Along with many other Bell inequality experiments performed with various systems since these pioneering works, the experimental results provide evidence that quantum physics contradicts the predictions of local realistic theories. However, all of these experiments are subjected to certain "loopholes", which in principle, could allow a local system to show violation of the Bell inequality. A major milestone was reached with three loophole-free CHSH-type Bell inequality experiments

[Hensen 15, Shalm 15, Giustina 15]. However, although these experiments reject with high confidence the null hypothesis of "nature is local", they are limited in the extent to which their data may assert the hypothesis that their data exhibits maximum nonlocality. Here, we are using the convention that "local" is referred to the distribution of outcomes which obeys Bell's inequalities, and "nonlocal" is referred to the distribution that violates Bell inequalities.

Elitzur, Popescu, and Rohrlich [Elitzur 92] described a model of the distribution of outcomes measured from a quantum state as a mixture of a local-realistic distribution, which obeys Bell's inequalities, and another distribution that does not. That is, a probability distribution P for the outcomes of a experiment can be written as

$$P = p_{\text{local}} P^L + (1 - p_{\text{local}}) P^{NL}, \tag{8.3}$$

where P^L represents a local joint probability distribution and P^{NL} represents a non-local distribution, with p_{local} as the weight of the local component bound by $0 \leq p_{\text{local}} \leq 1$. For an ideal CHSH Bell inequality experiment, the lowest attainable upper bound on the local content p_{local} in the distribution created by a maximally entangled state is ~ 0.586 [Barrett 06, Christensen 15]. In principle, this bound can be lowered to zero by using a chained Bell inequality (CBI) experiment [Pearle 70].

As indicated in Fig. 8.1.(a), CBI experiments are a generalization of a CHSH-type experiment. During each trial, a source that may be treated as a "black box" emits two systems labeled a and b, respectively. The experimentalist records the measurement outcomes after choosing a pair of measurements to perform separately on a and b. We use the symbols a_k, b_l to denote the respective measurement settings and $a_k b_l$ for the pair. There is a hierarchy in which the Nth CBI experiment involves $2N$ different settings. The $N = 2$ CBI experiment is equivalent to the CHSH Bell inequality experiment. The settings for general N are chosen from the set

$$Z = \{a_1 b_1, a_1 b_2, a_2 b_2, a_2 b_3, \ldots, a_{N-1} b_N, a_N b_N, a_N b_1\}. \tag{8.4}$$

Each local measurement has a binary outcome which we call B for "bright" or D for "dark". The outcome of the trial is recorded as $c(x, y) = 1$ if $x = y$ or 0 if $x \neq y$, where x is the outcome

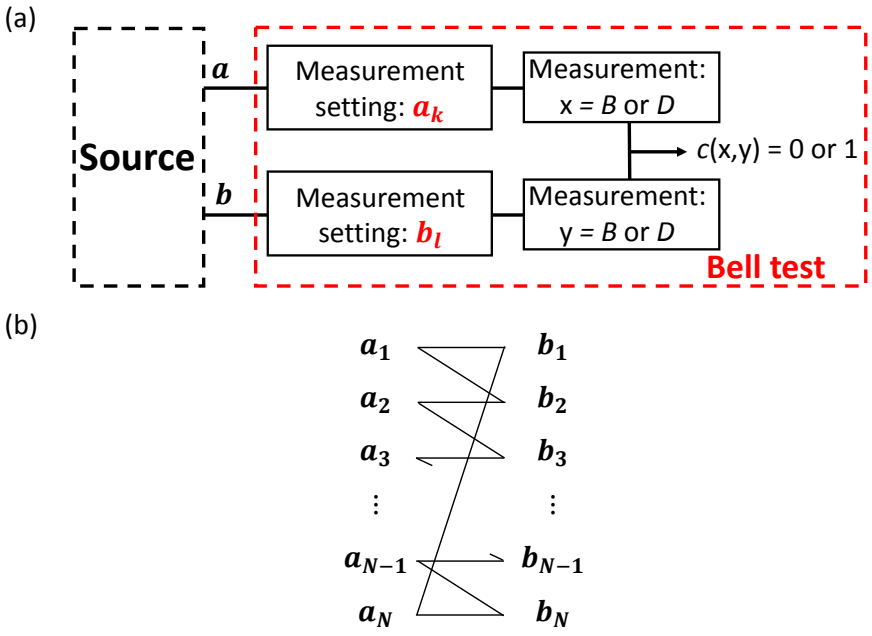

Figure 8.1: (a) Illustration of a Bell inequality experiment. A source emits two systems a and b, here two $^9Be^+$ ions. After choosing measurement settings a_k and b_l, the experiment implements Hilbert-space rotation operations (which are controlled with classical variables) on the ions respectively. Then a standard fluorescence based measurement in a fixed basis is applied to each ion. This is equivalent to choosing the measurement basis for the state that is present before the measurement settings are applied. Each system's measurement outcome is labeled B for "bright" or D for "dark", corresponding to the observation of fluorescence or not. From the joint measurement we record "c = 1" if the outcomes are the same and "c = 0" if they are not. (b) "Chaining" of the measurement settings for the Nth CBI experiment. The measurement settings can be visualized as a chain where $a_k b_k$ and $a_{k+1} b_{k+1}$ are linked by $a_k b_{k+1}$, and the chain is closed by the settings $a_N b_1$. The CHSH Bell inequality experiment corresponds to the special case of $N = 2$.

from system a and y is the outcome from system b. The probability to obtain $c(x,y) = 1$ may depend on the choices a_k and b_l, so we define that probability to be the correlation $\mathcal{C}(a_k, b_l) = P(BB|a_k b_l) + P(DD|a_k b_l)$, where $P(xy|a_k b_l)$ is the probability that system a yields measurement outcome x and system b yields measurement outcome y when the measurement settings pair is $a_k b_l$. We define the chained Bell parameter to be:

$$I_N = \mathcal{C}(a_1, b_1) + \mathcal{C}(a_1, b_2) + \mathcal{C}(a_2, b_2) + \mathcal{C}(a_N, b_N) + (1 - \mathcal{C}(a_N, b_1)) \,. \tag{8.5}$$

If the experiment is governed by a local hidden variable model, then the chained Bell inequality

$$I_N \geq 1 \tag{8.6}$$

must be satisfied [Pearle 70]. Note that I_N can be estimated using only the record of the settings $a_k b_l$ and outcomes $c(x,y)$, without knowledge of the mechanism of the source, thus it is referred to as a "black box". It was shown in Ref. [Barrett 06] that the chained Bell parameter I_N is always an upper bound on p_{local}. Furthermore, I_N is shown in Ref. [Bierhorst 16] to be a least upper bound for p_{local} under the assumption that the distributions are non-signaling, in the sense that each party's measurement outcomes do not depend on the remote party's setting choice. In the limit of $N \to \infty$ and with perfect experimental conditions, CBI experiments could be used to show that $p_{\text{local}} \to 0$, demonstrating complete departure from local realism.

8.1.1 "Loopholes" and Previous Experiments

Similar to a CHSH-type experiment, a CBI experiment may be subject to "loopholes" that, in principle, allow local systems to show violation of the inequality. Loopholes can also be viewed as certain interpretations of the local-realistic theory. These loopholes arise when one must rely on various supporting assumptions that are made in the design and execution of the experiments, but which cannot be absolutely verified. Loopholes in Bell inequality experiments are reviewed in the recent articles of Ref. [Brunner 14] and Ref. [Å. Larsson 14].

For example, if the setting choice for a can be communicated to b (or vice-versa), the "locality loophole" is opened. Ensuring space-like separation between the choices and remote measurement

events closes this loophole [Bell 85]. The "detection loophole" [Pearle 70, Clauser 74] is opened by making the fair-sampling assumption, which says that a subset of the data can be used to represent the entire data set. This assumption is often used when some trials fail to produce outcomes due to inefficient detectors. High efficiency detectors are required to close the detection loophole and observe violation of the inequality [Cabello 09]. The minimum detection efficiency required to close the detection loophole for the Nth CBI experiment is given by [Cabello 09]

$$\eta_{min}(N) = \frac{2}{\frac{N}{N-1}\cos(\frac{\pi}{2N}) + 1}, \tag{8.7}$$

assuming that the measurement efficiencies on a and b are equal and that a maximally entangled state is measured. This emphasizes the important of high detection efficiencny in large N CBI experiments. If the analysis of the data assumes that the outcomes of the trials are independent and identically distributed (i.i.d.), the "memory loophole" is opened [Barrett 02]. For example, one way to determine I_N is by running each of the CBI setting pairs $a_k b_l$ for a total number of $M_{k,l}$ trials respectively and calculating

$$\overline{\mathcal{C}}(a_k, b_l) = \frac{\sum_{i=1}^{M_{k,l}} c(x_i, y_i)}{M_{k,l}}, \tag{8.8}$$

(where i indexes the trials) to estimate each $\mathcal{C}(a_l, b_k)$ term in Eq. 8.5. This analysis requires the i.i.d. assumption for standard error estimates to be valid. This loophole can also be associated with certain memory effects which can exists in experimental apparatus that produce data erroneously due to the time sequential nature of the execution of experiments. The memory loophole can be closed by applying appropriate analysis techniques to an experiment that uses randomized measurement settings from trial to trial [Gill 03].

Previous experiments on the CBIs ($N \geq 3$) employed entangled photons pairs [Pomarico 11, Aolita 12, Stuart 12, Christensen 15]. The lowest yet reported upper bound on p_{local} is approximately 0.126 [Christensen 15]. However, to our knowledge all previous CBI experiments with $N \geq 3$ suffer from the locality, detection, and memory loopholes.

There exist five previous CHSH-type Bell inequality experiments with trapped ions [Rowe 01, Matsukevich 08, Pironio 10, Ballance 15, Tan 15]; all of them closed the detection loophole. The

first detection-loophole-closing Bell inequality experiment was performed with two $^{9}Be^{+}$ ions by Rowe *et al.* [Rowe 01]. In this case the ions were always confined in one potential well during applications of measurement settings and measurements. In Ref. [Matsukevich 08] and Ref. [Pironio 10], two $^{171}Yb^{+}$ ions were separately confined in two traps separated by a distance of ~ 1 m. Entanglement was created by a heralded scheme with photonic links, where each of the two remotely located ions was first entangled with the polarization states of an emitted photon, then the entanglement of the two ions was accomplished via interference and joint measurement of the two photons. Two different isotopes of calcium ions, i.e. $^{43}Ca^{+}$ and $^{40}Ca^{+}$ were subjected to a Bell inequality test in Ref. [Ballance 15]. Although the Bell state was created by a high-fidelity deterministic entangling gate, this experiment suffered measurement errors on the $^{40}Ca^{+}$ ion. Lastly, a CHSH Bell inequality experiment was also carried out on a pair of $^{9}Be^{+}$ and $^{25}Mg^{+}$ ions, described in Sec. 5.3.2 and in Ref. [Tan 15]. However, none of the trapped-ion experiments, including the experiments described here, are able to close the locality loophole. In Table 8.1 we list all CHSH Bell inequality experiments (across all platforms) that close the detection loopholes.

8.2 Experiment Setup

Five trapping zones were used in this experiment, they are labeled as $\mathcal{E}_{\mathcal{L}}, \mathcal{E}, \mathcal{S}, \mathcal{E}', \mathcal{E}_{\mathcal{R}}$ in Fig. 8.2. The ions can be confined together in a single harmonic well, or separately confined in different locations along the trap axis. Time varying potentials are applied to the control electrodes to deterministically separate ions and transport them between different locations [Blakestad 11, Bowler 12]. Two $^{9}Be^{+}$ ions are initially confined in zone $\mathcal{S}$ to interact with laser beams for the generation of entanglement. Trapping parameters in $\mathcal{S}$ are set to be similar to that when ions are confined in $\mathcal{E}$, where manipulation of ions in the experiments described in Chap. 5 and 6 were performed. The two states of the ions are encoded in the "clock" qubit states described in Sec. 2.1, i.e. $|F = 2, m_F = 0\rangle = |\downarrow\rangle$ and $|1, 1\rangle = |\uparrow\rangle$. This clock qubit is realized by applying an external magnetic field of ~ 119.446 G, which makes the transition frequency first-order insensitive to magnetic-field fluctuations [Langer 05]. We measured a qubit coherence time of approximately

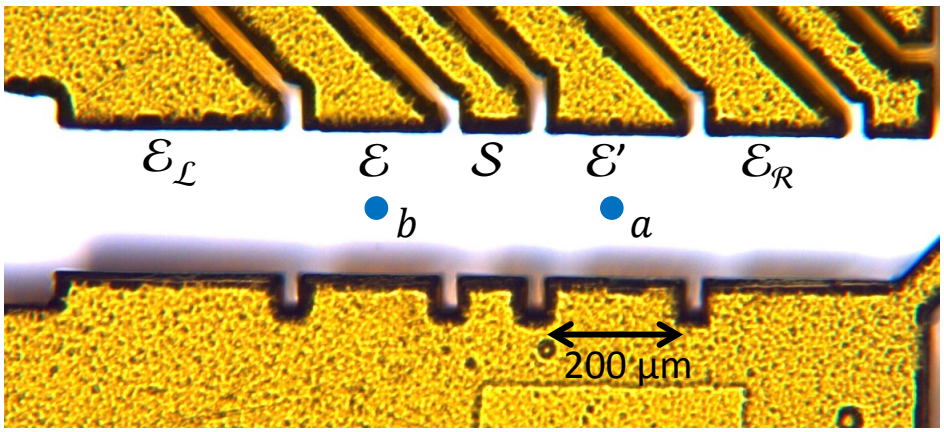

Figure 8.2: Layout of the relevant segmented trap electrodes. Each CBI experiment begins with one ion located in zone $\mathcal{E}$ and the other in zone $\mathcal{E}'$. The blue dots, which indicate the ions, are overlaid on a photograph showing the trap electrodes (gold). By transporting the ions in and out of zone $\mathcal{S}$, we individually implement settings and measure each ion sequentially. The ions are separated by at least ~ 340 μm when settings $a_k b_l$ are applied, a distance much larger than the laser beams waist of ~ 25 μm.

1.5 s (see Sec. 2.1). Such a long-lived memory storage duration is essential when taking into account the duration for each trial, as detailed later.

To deterministically create a Bell state, we employ a pulse sequence as depicted in Fig. 8.3. This sequence consists of a two-qubit entangling gate and multiple global rotations induced by laser beams, and is equivalent to that described in Sec. 5.2.3. The entangling gate is implemented using the Mølmer-Sørensen (MS) protocol [Sørensen 99, Sørensen 00] as described in Chap. 6. The global pulses shown inside the dashed box in Fig. 8.3 are induced by the same set of (non-copropagating) laser beams (all three beams shown in Fig. 6.1) that drive the MS interaction. By embedding the MS interaction in such a Ramsey sequence, the overall pulse sequence in the dashed box produces entanglement which has negligible sensitivity to slow phase drift between laser beams [Lee 05, Tan 15], and implements the operations $|\uparrow\uparrow\rangle \rightarrow |\uparrow\uparrow\rangle$, $|\uparrow\downarrow\rangle \rightarrow i|\uparrow\downarrow\rangle$, $|\downarrow\uparrow\rangle \rightarrow i|\downarrow\uparrow\rangle$, and $|\downarrow\downarrow\rangle \rightarrow |\downarrow\downarrow\rangle$. Global rotations shown labeled as "Co Carrier" in Fig. 8.3 were induced by the copropagating laser beams used for the single-qubit rotations as described in Sec. 6.7. All laser beams are focused and directed at zone $\mathcal{S}$ (Fig. 8.2), with beam waists of ~ 25 μm. With both ions initialized to the $|\uparrow\uparrow\rangle$ state, the overall pulse sequence in Fig. 8.3 creates the entangled state $|\Phi_+\rangle = \frac{1}{\sqrt{2}}(|\uparrow\uparrow\rangle + |\downarrow\downarrow\rangle)$. From this state, we can effectively create the $|\Phi_-\rangle = \frac{1}{\sqrt{2}}(|\uparrow\uparrow\rangle - |\downarrow\downarrow\rangle)$ state by appropriately shifting the phase of the pulses that implement the measurement settings b_l. This is equivalent to a $\pi/2$-rotation around the z-axis of the Bloch sphere.

By measuring the population and the coherence of the created Bell state [Sackett 00], we determine the fidelity of the overall sequence in Fig. 8.3 to be $\simeq 0.99$ (this evaluation of the Bell-state fidelity is similar to that used and described in Chap. 5 and Chap. 7). The Bell state fidelity is lower than that achieved in Chap. 6 due to a higher error dominated by spontaneous emission of photons induced by the Raman laser beams [Ozeri 07]. Here, different laser parameters, including Raman detuning, laser intensities, and polarizations compared to those used in Chap. 6 are chosen to allow different operations (e.g. two-qubit gate, global rotation, and single-qubit rotation) to be implemented with the same laser beam lines. Furthermore, in Chap. 6 the entangling gate was applied with ions confined in zone $\mathcal{E}$ (Fig. 8.2), but here entanglement is created in $\mathcal{S}$. We

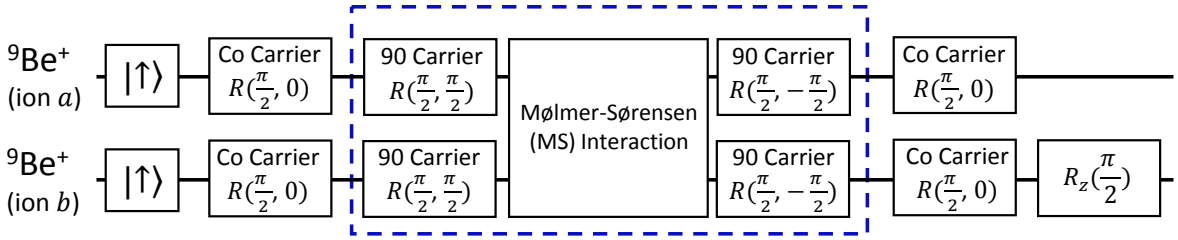

Figure 8.3: Pulse sequence for generating the entangled state $|\Phi_+\rangle = \frac{1}{\sqrt{2}}(|\uparrow\uparrow\rangle + |\downarrow\downarrow\rangle)$. The notation $R(\theta, \phi)$ represents the rotation with angle θ about an axis in the x-y plane of the Bloch sphere, and ϕ is the azimuthal angle of the rotation axis. Operation $R_z(\xi)$ is the rotation with an angle ξ around the z axis of the Bloch sphere. The angle θ is adjusted by varying the length of the laser pulse, and ϕ and ξ are adjusted with the phases of the RF signal driving the AOMs that controls the laser beams. Laser pulses in the dashed box all use the same set of laser beams, which makes the sensitivity of the created state to slow phase drifts between the two Raman beam paths negligible [Lee 05, Tan 15]. The two laser beams used to drive the stimulated-Raman transitions for the pulses outside of the dashed box (labeled as "Co Carrier") are copropagating (the laser beams labeled as $\boldsymbol{k_{2a}}$ and $\boldsymbol{k_{2b}}$ in Fig. 6.1) which eliminates phase drifts due to path length differences in the beams [Gaebler 16] (see also Sec. 6.7). The R_z rotation is implemented by shifting the phase of the direct digital synthesizer controlling the laser pulses that implement the subsequent measurement settings b_l.

measure a factor of ~ 2 higher axial motional heating [Turchette 00a] rate (~ 80 quanta/s for the center-of-mass mode) at $\mathcal{S}$ than in $\mathcal{E}$. All these factors reduce the fidelity of the entangling gate that creates the Bell states (see Sec. 4.4).

After the states $\left|\Phi_{+/-}\right\rangle$ are created at zone $\mathcal{S}$ (Fig. 8.2), the ions are separated and placed in two potential wells located in zone $\mathcal{E}$ and $\mathcal{E}'$, separated by ~ 340 μm. These processes represent the source in Fig. 8.1 and prepare the two ions a and b for the measurement of I_N described below.

To apply the settings a_k and b_l to the ions individually, the ion in $\mathcal{E}$ is first transported to $\mathcal{E}_{\mathcal{L}}$ while the ion in $\mathcal{E}'$ is simultaneously transported to $\mathcal{S}$ (see Fig. 8.4). We then illuminate the ion with Raman-transition-inducing laser beams to zone $\mathcal{S}$ to implement the measurement setting a_k without disturbing ion b. Subsequently, time-varying voltages are applied to implement the simultaneous well transportation operations $\mathcal{S} \rightarrow \mathcal{E}_{\mathcal{R}}$ and $\mathcal{E}_{\mathcal{L}} \rightarrow \mathcal{S}$. With ion b located in zone $\mathcal{S}$, the laser beams implement the measurement setting b_l. The Raman laser beams used for the applications of measurement settings are the copropagating beams labeled as "Co Carrier " in Fig. 8.3. Ideally, these operation can be described as the following rotations:

$$\begin{aligned} |\uparrow\rangle_r &\rightarrow \frac{1}{\sqrt{2}}\left(|\uparrow\rangle_r - \mathrm{e}^{-ir_k}|\downarrow\rangle_r\right) \\ |\downarrow\rangle_r &\rightarrow \frac{1}{\sqrt{2}}\left(|\downarrow\rangle_r - \mathrm{e}^{ir_k}|\uparrow\rangle_r\right) \end{aligned} \tag{8.9}$$

where $r = a$ or b to represent each of the ions, and the angles $r_k = a_k$ or b_k are

$$a_k = \frac{(2k-1)\pi}{2N}, \tag{8.10}$$

$$b_l = -\frac{(l-1)\pi}{N}, \tag{8.11}$$

which are chosen from Eq. 8.4. These angles minimize the expected value of I_N if the produced entangled state is ideal [Braunstein 90]. These rotation operations are implemented by setting the amplitude and phase of the Raman laser beams with an acousto-optic modulator (AOM) (see Sec. 3.4.3). The radio-frequency electric field driving the AOM is produced by a field-programmable gate array (FPGA)-controlled direct digital synthesizer (see Fig. 3.11). The classical variable is the phase of the oscillating field that implements a particular setting a_k or b_l. The experiment

sequence is depicted in Fig. 8.4.

After applying the measurement settings, the ions are recombined into zone $\mathcal{S}$ for "shelving" pulses to be applied on both ions simultaneously. Then, similar transport procedures separate and move the ions into zone $\mathcal{S}$ sequentially to be individually measured with the standard state-dependent fluorescence technique. When the detection laser is turned on, we detect on average 30 photon counts per ion for ion in the $|\uparrow\rangle$ state on a photomultiplier tube and about 2 counts when the ion is in the $|\downarrow\rangle$ state. See Sec. 2.1.6 and Sec. 2.1.7 for details on the shelving and fluorescence detection of the $^9Be^+$ ions. The photon collection apparatus is positioned to image zone $\mathcal{S}$ with a field of view of approximately 50 μm in this experiment (see Sec. 3.3). We label a measurement outcome "dark" (D) if six or fewer photons are observed and "bright" (B) if more than 6 are observed. Figure 8.5 shows the typical detection photon histograms of the two $^9Be^+$ ions. With this, we obtain the four possible joint-measurement fluorescence outcomes BB, BD, DB, DD, for each experiment. These outcomes correspond to the states $|\uparrow\uparrow\rangle$, $|\uparrow\downarrow\rangle$, $|\downarrow\uparrow\rangle$, and $|\downarrow\downarrow\rangle$.

The durations taken for each separation are ~ 300 μs, and simultaneous transport takes ~ 250 μs. With the detection duration of ~ 330 μs and the durations taken by other operations, the total duration shown in Fig. 8.4 takes ~ 3 ms. Due to this extended duration, it becomes important for the ion's state memory storage time to be long lived. Using states associated with magnetic-field sensitive transitions to encode the ions' would not be ideal in this experiment, because the memory storage times of a magnetic-field sensitive transitions in a $^9Be^+$ ion are typically a few ms, which is comparable to (or shorter than) the duration for the pulse sequence shown in Fig. 8.4. Magnetic-field sensitivities of hyperfine transitions in the electronic ground state of a $^9Be^+$ ion are shown in Fig. A.1.

When the state $|\Phi_+\rangle$ is prepared, we compute an estimate $\widehat{I}_N$ of I_N as shown in Eq. 8.5 with Eq. 8.8 used to estimate the $\overline{\mathcal{C}}(a_k, b_l)$ terms. For the state $|\Phi_-\rangle$ we instead use anticorrelations and compute

$$\widehat{I}_N^{\mathcal{A}} = \overline{\mathcal{A}}(a_1, b_1) + \overline{\mathcal{A}}(a_1, b_2) + \overline{\mathcal{A}}(a_2, b_2) + \overline{\mathcal{A}}(a_N, b_N) + \big(1 - \overline{\mathcal{A}}(a_N, b_1)\big) \Bigg(\tag{8.12}$$

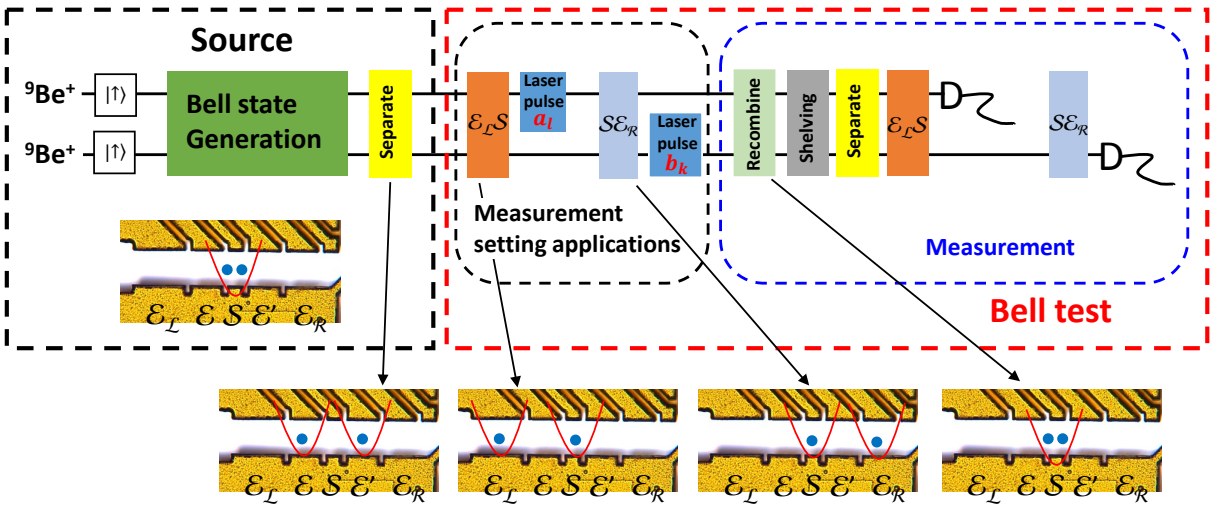

Figure 8.4: Experimental sequence for one trial. The notation $\mathcal{E}_{\mathcal{L}}\mathcal{S}$ refers to transport to place the ion b in zone $\mathcal{E}_{\mathcal{L}}$ and ion a in zone $\mathcal{S}$. Similarly for the operation $\mathcal{S}\mathcal{E}_{\mathcal{R}}$. The entangled state is generated as shown in Fig. 8.3 with the ions located in zone $\mathcal{S}$. Time-varying potentials are applied to control electrodes for the separation, shuttling and recombination of the ions [Blakestad 11, Bowler 12]. The total duration of the entire sequence shown here is approximately 3 ms. The initial optical pumping, Doppler cooling and ground-state cooling which are applied prior to the Bell state generation are not shown here. The total duration of one trial is approximately 8 ms.

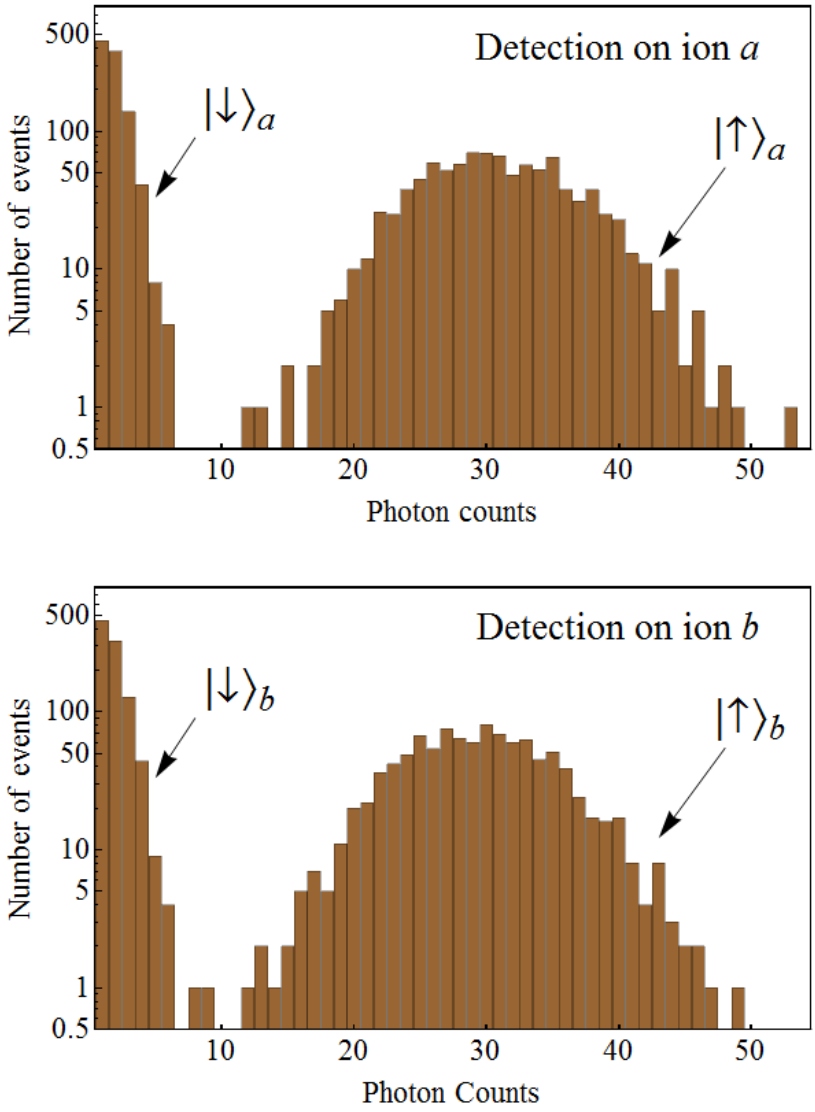

Figure 8.5: Typical detection photon histograms that were obtained when we apply the state-dependent fluorescence detection on each ion sequentially. During the state measurement of ion a (b) at zone $\mathcal{S}$, ion b (a) is located in zone $\mathcal{E}_{\mathcal{L}}$ ($\mathcal{E}_{\mathcal{R}}$) such that it does not interact with the detection laser beam. We choose the threshold of 6 for the differentiation of the "bright" and "dark" measurement outcomes.

where $\overline{\mathcal{A}}(a_k, b_l) = 1 - \overline{\mathcal{C}}(a_k, b_l)$. The measured $\widehat{I}_N^{\mathcal{A}}$ is equivalent to $\widehat{I}_N$ for the purpose of quantifying p_{local}

8.3 Experiment Results

We performed the experiment for the CBI parameter N ranging from 2 to 15. Figure 8.6 shows the experimentally obtained CBI parameter $\widehat{I}_N$ as a function of N. The data points in Fig. 8.6 were obtained with multiple sequential trials having the same settings, then iterated across different choices of settings. The error bars are calculated under the assumption that the settings and outcomes are i.i.d. The error bars indicate the propagated standard errors $\sqrt{\sum_j \epsilon_j^2}$, with $\epsilon_j = \sqrt{\chi_j(1-\chi_j)/(M_j - 1)}$ where M_j is the number of trials (here $M_j \sim 2,000$) and χ_j is the averaged correlated or anticorrelated outcome for the jth setting pair.

Two different data sets are collected using two $^9\text{Be}^+$ ions. The first data set was obtained with the Bell state $|\Phi_-\rangle$ undergoing trials and by computing the CBI parameters according to Eq. 8.12. The second data set was carried out with $|\Phi_+\rangle$ and the CBI parameters were calculated according to Eq. 8.5. These two data sets were collected ~ 6 months apart. Due to miscalibrations and our inability to completely reproduce the experimental conditions, there exists noticable differences between the two data sets and finer features within each data set. Furthermore, the very high demands of fidelity and the high sensitivities to errors of the elementary operations required for the realization of these experiments can also contribute to these observed behaviors. The $\widehat{I}_2$ experiment took a total of ~ 5 minutes, the one for $\widehat{I}_{15} \sim 20$ minutes. The lowest value of $\widehat{I}_N$ is obtained for the $N = 9$ data run, where $\widehat{I}_9 = 0.296(12)$.

Using the same apparatus, we also performed the CBI experiment on an entangled pair of $^9\text{Be}^+$ and $^{25}\text{Mg}^+$ ions. The computed $\widehat{I}_N$ values are shown as orange dots in Fig. 8.6. The generation of the mixed-species entangled state is described in Chap. 5 and Ref. [Tan 15]. In this experiment, the ions remain confined in a single zone throughout the entire sequence. The rotations implementing the settings choices are applied with microwave fields tuned to each ion. The frequencies are $\simeq 1.2$ GHz for the $^9\text{Be}^+$ ion and $\simeq 1.8$ GHz for the $^{25}\text{Mg}^+$ ion. The determinations

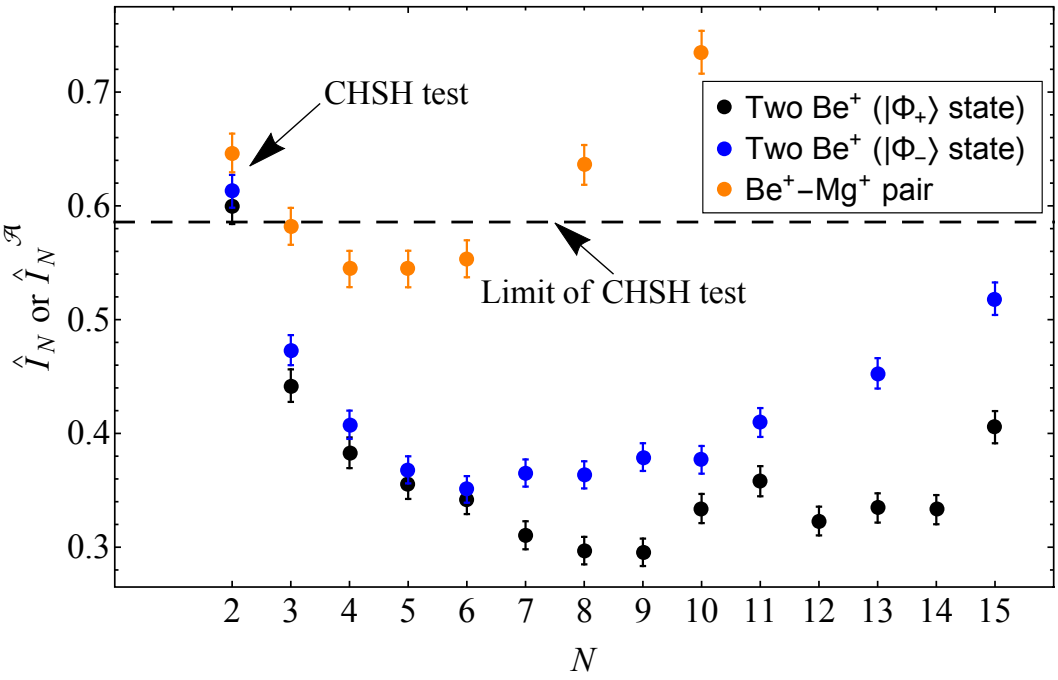

Figure 8.6: Experimentally measured values $\widehat{I}_N$ and $\widehat{I}_N^{\mathcal{A}}$ as a function of N. Data represented by black and blue dots are obtained with two $^9Be^+$ ions, with black (blue) dots corresponding to tests on $|\Phi_+\rangle$ ($|\Phi_-\rangle$). These two data sets were obtained approximately six months apart. The difference between them and the finer features within each data set are probably due to miscalibrations and our inability to reproduce exact experimental conditions. Orange dots are data from test on $|\Phi_+\rangle$ prepared on a $^9Be^+$-$^{25}Mg^+$ pair. The dashed line indicates the lowest upper bound on the local content attainable in a perfect CHSH-type experiment.

of the final states of the two ions are made with detection lasers at ~ 313 nm for the $^{9}Be^{+}$ and at ~ 280 nm for the $^{25}Mg^{+}$ ion. Due to higher background photon counts when the CBI experiments were performed on the $^{9}Be^{+}$-$^{25}Mg^{+}$ pair, bright thresholds of 11 and 12 were used for $^{9}Be^{+}$ and $^{25}Mg^{+}$, respectively. See Chap. 2 for detailed energy level structures, and descriptions of detection, and manipulation of the $^{9}Be^{+}$ and $^{25}Mg^{+}$ ions.

8.4 Self-Testing of Bell States

It was shown in Ref. [Popescu 92] that if the CHSH inequality (Eq. 8.1) is violated at the maximum value of $2\sqrt{2}$ by a bipartite system, the system must be in a maximally entangled state. This is a remarkable result because it enables the validation of the quantum entanglement using only the observed correlations. In other words, violation of Bell inequality can serve as an entanglement witness. Such a characterizations with minimal assumptions on the quantum devices is formalized under the self-testing framework [Mayers 04, McKague 12]. With this framework, an experimentalist is able to quantify the quality of the entangled state given an amount of violation of a Bell inequality [Bardyn 09, Yang 14, Bancal 15, Kaniewski 16]. Furthermore, because the quantum device is treated as a black box, such characterization can offer a device-independent assessment of the physical system under inspection. Thus, self-tested certification can be used as a benchmark for QIP devices across different platforms.

Here, we use the method provided by Ref. [Kaniewski 16] to infer a self-tested Bell-state fidelity. Our lowest measurement of $\widehat{I}_2$ corresponds to a CHSH inequality parameter (sum of correlations) of $B_{\mathrm{CHSH}} = 2.80(2)$, which is calculated using the following equation:

$$B_{\mathrm{CHSH}} = 2\,(1 - I_2) + 2. \tag{8.13}$$

We infer a self-tested Bell-state fidelity lower bound (at the 95 % confidence level) of $F_L \sim 0.958$. This is calculated with [Kaniewski 16]

$$F_L = \frac{1}{2}\left(1 + \frac{B_{\mathrm{CHSH}} - \beta_S}{2\sqrt{2} - \beta_S}\right)\left(\tag{8.14}$$

where $\beta_S = (16+14\sqrt{2})/17$. There also exist other methods to infer a self-testing Bell-state fidelity, see for example Ref. [Bardyn 09] and Ref. [Bancal 15].

Our self-tested fidelity appears to be the highest for a deterministically created Bell state. Several previous experiments have reported violation of the CHSH inequality (the CBI with $N = 2$) while closing the detection loophole [Rowe 01, Matsukevich 08, Pironio 10, Ballance 15, Tan 15, Ansmann 09, Hofmann 12, Pfaff 13, Vlastakis 15, Dehollain 16], and [Hensen 16] closed all loopholes. Other experiments [Shalm 15, Giustina 15] have closed the detection loophole, but they reported violation of other Bell inequalities, for which self-tested fidelity bounds are not available. Table 8.1 summarizes the B_{CHSH} parameters determined in several previous detection-loophole closing experiments and ours, as well as the resulting self-testing singlet-fidelity lower-bound according to Eq. 8.14 at the 50 % and 95 % confidence levels. For the 50 % confidence fidelity lower bound we use the point estimates of B_{CHSH} given in Table 8.1, and for the 95 % confidence lower bound we replace B_{CHSH} in the equation above with a 95 % confidence lower bound on B_{CHSH} assuming that each estimate of B_{CHSH} is normally distributed with standard deviation given by the uncertainties in the table.

8.5 Summary

In summary, we used the quantum information processing (QIP) techniques based on trapped-ions described in this thesis to perform a chained Bell inequality (CBI) experiment. The lowest CBI parameter determined from our measurements is 0.296(12) in a $N = 9$ CBI experiment. This value is significantly lower than 0.586, the minimum fraction derived from a perfect Clauser-Horne-Shimony-Holt (CHSH)-type experiment (the CBI with $N = 2$). Furthermore, for the conventional case of the CHSH inequality, the fidelity of the Bell state is certified to be 0.958 at the 95 % confidence level under a self-testing protocol [Kaniewski 16]. This result is the highest for a deterministically created Bell state, and verifies that the basic elements of trapped-ion QIP techniques employed here work well in combination, demonstrating the versatility and promising capabilities of QIP based on trapped-ions.

Reference	System	B_{CHSH}	$F_L^{50\%}$	$F_L^{95\%}$
[Rowe 01]	Two $^{9}Be^{+}$	2.25(3)	0.600	0.566
[Matsukevich 08]	Two $^{171}Yb^{+}$	2.54(2)	0.800	0.778
[Ansmann 09]	Phase qubits	2.0732(3)	0.477	0.477
[Pironio 10]	Two $^{171}Yb^{+}$	2.414(58)	0.713	0.647
[Hofmann 12]	Two Rb^{0}	2.19(9)	0.558	0.456
[Pfaff 13]	One NV	2.30(5)	0.634	0.577
[Vlastakis 15]	Trans. & cavity	2.30(4)	0.634	0.589
[Ballance 15]	$^{40}Ca^{+}$ & $^{43}Ca^{+}$	2.228(15)	0.584	0.567
[Tan 15]	$^{9}Be^{+}$ & $^{25}Mg^{+}$	2.70(2)	0.911	0.888
see also Sec. 5.3.2				
[Dehollain 16]	One ^{31}P in Si	2.70(9)	0.911	0.809
[Hensen 16]	Two NV	2.38(14)	0.690	0.530
This work	Two $^{9}Be^{+}$	2.80(2)	0.980	0.958

Table 8.1: Results from CHSH experiments without the fair-sampling assumption. The table shows each experiment's measured CHSH parameter B_{CHSH} with one standard deviation uncertainty from the references and self-testing fidelity lower bounds at the 50 % ($F_L^{50\%}$) and 95 % ($F_L^{95\%}$) confidence levels determined according to Eq. 8.14.

Chapter 9

Outlook

This dissertation work focuses on implementing two-qubit entangling gates in the context of scaling trapped-ion quantum information processing (QIP) in the quantum charge coupled device (QCCD) architecture [Wineland 98, Kielpinski 02]. That is, the entangling gates were implemented inside ion traps which are designed for scaling and some of the experiments utilize all of the basic features required for scaling. Furthermore, the use of multiple ion species is incorporated which is also regarded as an important utility for the realization of a practical trapped-ion based QIP device.

While improvements on gate performance have been made, and incorporation of most trapped-ion QIP elementary operations in one experiment which can be used as benchmarks for these operations has been demonstrated, it still remains a tremendous challenge for an operational large-scale trapped-ion quantum information processor to be realized. Based on the experience and lessons learned from these experiments, here we briefly summarize potential areas of improvement for future experiments.

9.1 Better Trap design

9.1.1 Axial Micromotion

In our experiment a major source of error for two-qubit entangling gates is the spontaneous scattering of photons induced by the laser beams used for exciting stimulated-Raman transitions (Sec. 4.4.2). In the X-junction trap, due to axial micromotion caused by the particular trap design

and imperfections in the trap construction (see Sec. 3.1 and Ref. [Blakestad 10]), the Raman scattering rate for a $^9Be^+$ ion is increased by a factor of ~ 4 compared the case where micromotion is absent. Therefore future trap designs must be carefully simulated to suppress this effect and fabrication techniques need to be further developed.

9.1.2 Segmented-Stray-Fields Compensating Electrodes

Segmented electrodes are useful for the compensation of stray electric fields, as depicted in Fig. 9.1. The X-junction trap has only one bias electrode that provides a micromotion compensating electric field along the x axis (see Fig. 9.1). While it is possible to null excess RF micromotion at any given location along the z-axis with only the diagonal control electrodes and the bias electrode, it is a non-trivial problem to simultaneously null excess RF micromotion at different locations along the z direction with this configuration. Simultaneous minimization of excess micromotion at multiple locations along the axis is important for storing ions at different locations simultaneously and for shuttling operations. Such designs have been pursued in a linear Paul trap [Pyka 14, Kienzler 15] and might be employed for future work in scalable traps.

9.2 Cooling of Trap Apparatus

A major limiting factor to increasing the number of trapped ions is due to collisions of ions with background gas in the vacuum chamber. Such collisions can cause unacceptable heating and ion reordering, and ion loss through exothermic chemical reactions [Wineland 98]. This can be mitigated by employing cryogenic pumping [Wilson 14, Niedermayr 14, Bruzewicz 15, Alonso 16]. Most gases which are commonly found in the background of a high vacuum system condense on material surfaces at temperatures ≤ 20 K; therefore operating at these temperatures should substantially reduce the background gas collisions rates. Another advantage of cooling is that the heating rate of motional modes [Turchette 00a] due to uncontrolled noisy electric fields could also be suppressed [Labaziewicz 08, Bruzewicz 15, Brownnutt 15]. Low heating rates are important to suppress errors in two-qubit entangling gates as discussed in Chap. 4.

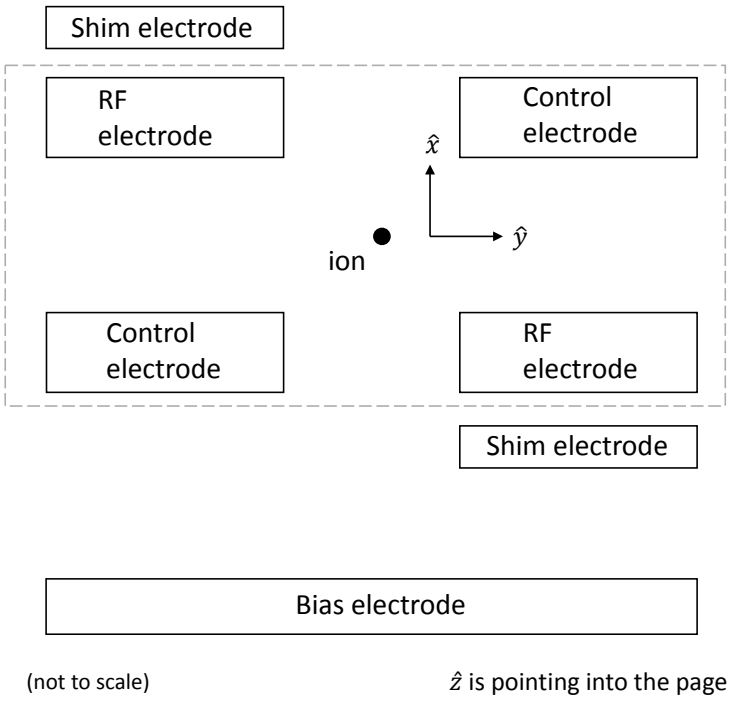

Figure 9.1: Schematic showing the cross section of a potential linear Paul trap with multiple shim electrodes. Our X-junction trap (see Sec. 3.1) consists of two pairs of RF electrodes and two pairs of control electrodes (inside the grey dashed box), as well as a single bias electrode. The control electrodes are segmented along the z direction. In the proposed design, in addition to the electrodes inside the dashed box, two segmented "shim" electrodes that run parallel to the RF and control electrodes along the z axis will also be included. This design enables excess micromotion at different locations along the z-axis to be better compensated simultaneously. In addition to being important for the implementations of motional mode cooling and fluorescence detection, better compensation of excess micromotion is particularly crucial for implementing two-qubit entangling gates and shuttling of ions. Shuttling operations include transporting, separating, and recombining ions.

Drawbacks of operating a trapped-ion apparatus at the cryogenic temperatures include (i) restrictions on the heat load allowable, (ii) restrictions on laser beams access due to cryogenic apparatus and heat shields, and (iii) for liquid Helium bath cryostats, the cost of Helium.

9.3 Rapid Loading of Ions

A fast loading mechanism for ions can be advantageous. This becomes increasingly important as the required number of ions increases for more complicated experiments. Currently, loading uses resistively-heated ovens in combination with photoionization laser beams. The ion loading rate is typically one ion per minute limited by the need to control the number of ions loaded; furthermore, the heat generated by the ovens can increase background pressure.

Two approaches for the rapid loading of ions have been investigated in several groups: (i) integration of a neutral atom magneto-optical trap (MOT) with an ion trap [Cetina 07, Sage 12], and (ii) ablation loading of ions [Hashimoto 06, Leibrandt 07, Hendricks 07, Sheridan 11, Zimmermann 12, Hankin 16, Chen 16, Todaro 16].

The ablation loading technique usually employs a pulsed laser beam that strikes a target and leads to a rapid ejection of a mixture of atoms, molecules, ions, and electrons. If needed, a photoionization laser beam can be added to create the desired ions. In addition to providing a fast loading rate, this technique also minimizes the heat load compared to the conventional resistively-heated oven. This makes the ablation technique particularly attractive for a cryogenic ion trap. In addition, no wire connections and electrical feedthroughs are required for the ablation target. Furthermore, for multiple species applications, different mixtures of the desired atom species can be infused into one ablation target [Guggemos 15, Hankin 16].

Another approach for a rapid loading of ions is to incorporate an “ion reservoir” in a QCCD trap; a reserve of ions is maintained in a designated trap zone and individual ions can be transported into the experimental region “on demand”. This strategy can be combined with any loading technique.

Operation	Duration (typical values)
Single-qubit gate	10 μs
Two-qubit gate	30 μs
Qubit state preparation	50 μs
Transport of one ion	250 μs
Separation of two ions	300 μs
Sideband cooling	2000 μs
Doppler cooling	600 μs
"Shelving"	200 μs
Measurement	300 μs

Table 9.1: Typical durations required for elementary operations using the X-Junction trap. The actual durations of these operations vary, as they depend on motional mode structure, transition excitation methods, and ion location in the trap array. "Shelving" refers to the pulses that transfer ions' states from the computation qubit to the measurement qubit before making fluorescence measurement (see Sec. 2.1.7 and Sec. 2.2.6).

9.4 Improved Microwave Delivery

One strategy to improve the delivery of microwave fields to the ions is to integrate a microwave antenna with an ion trap [Ospelkaus 08, Harty 14, Weidt 16]. With an antenna placed in close proximity with the trapped ions, Rabi rates and fidelities of magnetic-dipole transitions in ions can be significantly increased for a given microwave power, or with reduced power, the temporal instability of the microwaves would be improved due to a reduced thermal effect. Benefits include: (i) performance of the mapping operation between the computational qubit and the measurement qubit could be improved (see Sec. 2.1.6 and Sec. 2.2.5), (ii) in the implementation of the dynamical decoupling gate described in Chap. 7, the error source associated with the infidelity of microwave-induced transition could be suppressed (see Sec. 7.3), and (iii) with higher fidelity microwave transitions, one could explore more complicated dynamical decoupling schemes [Cohen 15].

9.5 Switchable Noise Filtering for Control Electrodes

As shown in Table 9.1, durations required for shuttling operations are currently a factor of ~ 10 greater than the durations taken by quantum gates. One reason for this is because a series of low-pass filters are incorporated to reduce externally-injected electric potential noise on the control

electrodes (see Sec. 3.1), which is important to suppress errors of two-qubit gates. We want to be able to keep this feature but also enable high speed ion shuttling [Bowler 12] which is prevented if we include strong low-pass filtering.

A potential approach is to implement different filtering stages that can be chosen with high speed switches. Arranged in a parallel configuration, one stage provides heavy filtering, the other provides minimal or no filtering. The latter is chosen during shuttling, the heavy filter is then switched in when a static potential well is applied for the application of quantum gates. High-speed switching of trapping potential has been investigated in Ref. [Alonso 13].

9.6 Electronically-Induced-Transparency Cooling with an Atomic Tripod System

Another possibility to speed up the overall processing is to employ more efficient scheme for the cooling of motional modes. The typical duration of a Raman-sideband cooling sequence is on the order of a few ms, and is currently the longest-duration operation (see Table 9.1) in an experimental sequence.

This could be mitigated by employing an electronically-induced-transparency (EIT) cooling scheme [Morigi 00, Morigi 03]. Compared to cooling with Raman-sideband transitions, EIT cooling has been demonstrated to offer (i) speed up of the cooling processes, (ii) reduction in the required laser intensities, and (iii) simplifications of experimental implementations. In addition, it can also provide broad cooling bandwidth such that multiple motional modes are cooled simultaneously [Roos 00, Lin 13b, Lechner 16].

Previous implementations of EIT cooling relied on close approximations to three-level "Λ" atomic systems (one excited level which is connected to two lower energy levels), including one demonstrated with $^{24}Mg^{+}$ ions [Lin 13b] in the legacy system where the experiments described in Chap. 7 were performed. However, there exists no simple Λ systems in the ions used in this thesis. It was suggested in Ref. [Evers 04] that a tripod-EIT cooling scheme (one excited level and three lower energy levels) could offer better cooling efficiency compared to a Λ system. Here, using

an additional ground state to engineer a double-EIT profile that can offer better suppression of both the carrier and the blue-sideband excitations, improved cooling should be possible. Reference [Lu 15] proposes a similar tripod-EIT cooling scheme that employs two laser beams paired with a microwave-induced transition. These possibilities should be investigated for extensions of the work presented here.

Bibliography

[Acton 06] M. Acton, K.-A. Brickman, P. C. Haljan, P. J. Lee, L. Deslauriers & C. Monroe. Near-perfect simultaneous measurement of a qubit register. Quant. Inform. Comp., vol. 6, pages 465–482, 2006.

[Allcock 11] D. T. C. Allcock, L. Guidoni, T. P. Harty, C. J. Ballance, M. G. Blain, A. M. Steane & D. M. Lucas. Reduction of heating rate in a microfabricated ion trap by pulse-laser cleaning. New J. Phys., vol. 13, page 123023, 2011.

[Alonso 13] J. Alonso, F. M. Leupold, B. C. Keitch & J. P. Home. Quantum control of the motional states of trapped ions through fast switching of trapping potentials. New J. Phys., vol. 15, page 023001, 2013.

[Alonso 16] J. Alonso, F. M. Leupold, Z. U. Solèr, M. Fadel, M. Marinelli, B. C. Keitch, V. Negnevitsky & J. P. Home. Generation of large coherent states by bang-bang control of a trapped-ion oscillator. Nat. Commun., vol. 7, page 11243, 2016.

[Ansbacher 89] W. Ansbacher, Y. Li & E. H. Pinnington. Precision lifetime measurement for the 3p levels of MgII using frequency-doubled laser radiation to excite a fast ion beam. Phys. Lett. A, vol. 139, no. 3,4, page 165, 1989.

[Ansmann 09] M. Ansmann, H. Wang, R. C. Bialczak, M. Hofheinz, E. Lucero, M. Neeley, A. D. O'Connell, D. Sank, M. Weides, J. Wenner, A. N. Cleland & J. M. Martinis. Violation of Bell's inequality in Josephson phase qubits. Nature, vol. 461, page 504, 2009.

[Aolita 12] L. Aolita, R. Gallego, A. Acín, A. Chiuri, G. Vallone, P. Mataloni & A. Cabello. Fully nonlocal quantum correlations. Phys. Rev. A, vol. 85, page 032107, 2012.

[Aspect 82] A. Aspect, P. Grangier & G. Roger. Experimental realization of Einstein-Podolsky-Rosen-Bohm *Gedankenexperiment*: a new violation of Bell's inequalities. Phys. Rev. Lett., vol. 49, page 91, 1982.

[Ballance 15] C. J. Ballance, V. M. Schäfer, J. P. Home, D. J. Szwer, S. C. Webster, D. T. C. Allcock, N. M. Linke, T. P. Harty, D. P. L. Aude Craik, D. N. Stacey, A. M. Steane & D. M. Lucas. Hybrid quantum logic and a test of Bell's inequality using two different atomic isotopes. Nature, vol. 528, page 384, 2015.

[Ballance 16] C. J. Ballance, T. P. Harty, N. M. Linke, M. A. Sepiol & D. M. Lucas. High-fidelity quantum logic gates using trapped-ion hyperfine qubits. Phys. Rev. Lett., vol. 117, page 060504, 2016.

[Bancal 15] J. D. Bancal, M. Navascués, V. Scarani, T. Vértesi & T. H. Yang. Physical characterization of quantum devices from nonlocal correlations. Phys. Rev. A, vol. 91, page 022115, 2015.

[Bardyn 09] C.-E. Bardyn, T. C. H. Liew, S. Massar, M. McKague & V. Scarani. Device-independent state estimation based on Bell's inequalities. Phys. Rev. A, vol. 80, page 062327, 2009.

[Barenco 95] A. Barenco, C. H. Bennett, Charles, R. Cleve, D. P. DiVincenzo, N. Margolus, P. Shor, T. Sleator, J. A. Smolin & H. Weinfurter. Elementary gates for quantum computation. Phys. Rev. A, vol. 52, pages 3457–3467, Nov 1995.

[Barends 14] R. Barends, J. Kelly, A. Megrant, A. Veitia, D. Sank, E. Jeffrey, T. C. White, J. Mutus, A. G. Fowler, B. Campbell, Y. Chen, Z. Chen, B. Chiaro, A. Dunsworth, C. Neill, P. O'Malley, P. Roushan, A. Vainsencher, J. Wenner, A. N. Korotkov, A. N. Cleland & J. M. Martinis. Superconducting quantum circuits at the surface code threshold for fault tolerance. Nature, vol. 508, pages 500–503, 2014.

[Barrett 02] J. Barrett, D. Collins, L. Hardy, A. Kent & S. Popescu. Quantum nonlocality, Bell inequalities, and the memory loopholes. Phys. Rev. A, vol. 66, page 042111, 2002.

[Barrett 03] M. D. Barrett, B. DeMarco, T. Schätz, V. Meyer, D. Leibfried, J. Britton, J. Chiaverini, W. M. Itano, B. Jelenković, J. D. Jost, C. Langer, T. Rosenband & D. J. Wineland. Sympathetic cooling of $^{9}Be^{+}$ and $^{24}Mg^{+}$ for quantum logic. Phys. Rev. A, vol. 68, pages 042302–1–8, 2003.

[Barrett 06] J. Barrett, A. Kent & S. Pironio. Maximally nonlocal and monogamous quantum correlations. Phys. Rev. Lett., vol. 97, page 170409, 2006.

[Batteiger 09] V. Batteiger, S. Knünz, M. Herrmann, G. Saathoff, H. A. Schüssler, B. Bernhardt, T. Wilken, R. Holzwarth, T. W. Hänsch & Th. Udem. Precision spectroscopy of the $3s$-$3p$ fine-structure doublet in Mg^{+}. Phys. Rev. A, vol. 80, pages 022503–1–8, 2009.

[Bell 64] J. S. Bell. On the Einstein-Podolsky-Rosen paradox. Physics, vol. 1, no. 6/7, pages 195–488, 1964.

[Bell 85] J. S. Bell, J. F. Clauser, M. A. Horne & A. Shimony. An exchange on local beables. Dialectica, vol. 39, pages 85–96, 1985.

[Benhelm 08] J. Benhelm, G. Kirchmair, C. F. Roos & R. Blatt. Towards fault-tolerant quantum computing with trapped ions. Nature Physics, vol. 4, pages 463–466, 2008.

[Bergquist] J. Bergquist. Private communication.

[Bermudez 12] A. Bermudez, P. O. Schmidt, M. B. Plenio & A. Retzker. Robust trapped-ion quantum logic gates by continuous dynamical decoupling. Phys. Rev. A, vol. 85, page 040302(R), 2012.

[Bierhorst 16] P. Bierhorst. Geometric decompositions of Bell polytopes with practical applications. J. Phys. A: Math. Theor., vol. 49, page 215301, 2016.

[Blakestad 10] R. Bradford Blakestad. Transport of trapped-ion qubits within a scalable quantum processor. PhD thesis, Univ. Colorado, Dept. of Physics, Boulder, 2010.

[Blakestad 11] R. B. Blakestad, C. Ospelkaus, A. P. VanDevender, J. H. Wesenberg, M. J. Biercuk, D. Leibfried & D. J. Wineland. Near-ground-state transport of trapped-ion qubits through a multidimensional array. Phys. Rev. A, vol. 84, page 032314, 2011.

[Bollinger 85] J. J. Bollinger, J. S. Wells, D. J. Wineland & W. M. Itano. Hyperfine structure of the $2p^2P_{1/2}$ state in $^9Be^+$. Phys. Rev. A, vol. 31, page 2711, 1985.

[Boos 03] D. D. Boos. Introduction to the bootstrap world. Statistical Science, vol. 18, pages 168–174, 2003.

[Bowler 12] R. Bowler, J. Gaebler, Y. Lin, T. R. Tan, D. Hanneke, J. D. Jost, J. P. Home, D. Leibfried & D. J. Wineland. Coherent diabatic ion transport and separation in a multizone trap array. Phys. Rev. Lett., vol. 109, page 080502, 2012.

[Bowler 13] R. S. Bowler, U. Warring, J. W. Britton & J. M. Amini. Arbitrary waveform generator for quantum information processing with trapped ions. Rev. Sci. Instrum., vol. 84, page 033108, 2013.

[Bowler 15] R. Bowler. Coherent ion transport in a multi-electrode trap array. PhD thesis, Univ. Colorado, Dept. of Physics, Boulder, 2015.

[Braunstein 90] S. Braunstein & C. Caves. Wringing out better Bell inequalities. Ann. Phys. (N. Y.), vol. 202, page 22, 1990.

[Bremner 02] M. J. Bremner, C. M. Dawson, J. L. Dodd, A. Gilchrist, A. W. Harrow, D. Mortimer, M. A. Nielson & T. J. Osborne. Practical scheme for quantum computation with any two-qubit entangling gate. Phys. Rev. A, vol. 89, page 247902, 2002.

[Brown 11] K. R. Brown, A. C. Wilson, Y. Colombe, C. Ospelkaus, A. M. Meier, E. Knill, D. Leibfried & D. J. Wineland. Single-qubit-gate error below 10^-4 in a trapped ion. Phys. Rev. A, vol. 84, page 030303(R), 2011.

[Brownnutt 15] M. Brownnutt, M. Kumph, P. Rabl & R. Blatt. Ion-trap measurements of electric-field noise near surfaces. Rev. Mod. Phys., vol. 87, page 1419, 2015.

[Brunner 14] N. Brunner, D. Cavalcanti, S. Pironio, V. Scarani & S. Wehner. Bell nonlocality. Rev. Mod. Phys., vol. 86, page 419, 2014.

[Bruzewicz 15] C. D. Bruzewicz, J. M. Sage & J. Chiaverini. Measurement of ion motional heating rates over a range of trap frequencies and temperatures. Phys. Rev. A, vol. 91, page 041402(R), 2015.

[Cabello 09] A. Cabello, J.-A. Larsson & D. Rodriguez. Minimum detection efficiency required for a loophole-free violation of the Braunstein-Caves chained Bell inequalities. Phys. Rev. A, vol. 79, page 062109, 2009.

[Cetina 07] M. Cetina, A. Grier, J. Campbell, I. Chuang & V. Vuletić. Bright source of cold ions for surface-electrode traps. Phys. Rev. A, vol. 76, page 041401(R), 2007.

[Chen 16] J.-S Chen, S. Brewer & D. Leibrandt. Private communication. 2016.

[Chou 10] C. W. Chou, D. B. Hume, J. C. J. Koelemeij, D. J. Wineland & T. Rosenband. Frequency comparison of two high-accuracy Al^+ optical clocks. Phys. Rev. Lett., vol. 104, page 070802, 2010.

[Chow 09] J. M. Chow, J. M. Gambetta, L. Tornberg, Jens Koch, Lev S. Bishop, A. A. Houck, B. R. Johnson, L. Frunzio, S. M. Girvin & R. J. Schoelkopf. Randomized benchmarking and process tomography for gate errors in solid-state qubit. Phys. Rev. Lett., vol. 102, page 119901, 2009.

[Chow 12] J. M. Chow, J. M. Gambetta, A. D. Córcoles, S. T. Merkel, J. A. Smolin, C. Rigetti, S. Poletto, G. A. Keefe, B. Rothwell, J. R. Rozen, M. B. Ketchen & M. Steffen. Universal quantum gate set approaching fault-tolerant thresholds with superconducting qubits. Phys. Rev. Lett., vol. 109, page 060501, 2012.

[Christensen 15] B. G. Christensen, Yeong-Cherng Liang, Nicolas Brunner, Nicolas Gisin & Paul Kwiat. Exploring the Limits of Quantum Nonlocality with Entangled Photons. Phys. Rev. X, vol. 5, page 041052, 2015.

[Cirac 95] J. I. Cirac & P. Zoller. Quantum computations with cold trapped ions. Phys. Rev. Lett., vol. 74, pages 4091–4094, 1995.

[Clauser 69] J. R. Clauser, M. A. Horne, A. Shimony & R. A. Holt. Proposed experiment to test local hidden-variable theories. Phys. Rev. Lett., vol. 23, pages 880–884, 1969.

[Clauser 74] J. R. Clauser & M. A. Horne. Experimental consequences of objective local theories. Phys. Rev. D, vol. 10, page 526, 1974.

[Cline 94] R. A. Cline, J. D. Miller, M. R. Matthews & D. J. Heinzen. Spin relaxation of optically trapped atoms by light scattering. Opt. Lett., vol. 19, page 207, 1994.

[Clos 14] G. Clos, M. Enderlein, U. Warring, T. Schaetz & D. Leibfried. Decoherence-assisted spectroscopy of a single $^{25}Mg^+$ ion. Phys. Rev. Lett., vol. 112, page 113003, 2014.

[Cohen 15] I. Cohen, S. Weidt, W. K. Hensinger & A. Retzker. Multi-qubit gate with trapped ions for microwave and laser-based implementation. New J. Phys., vol. 17, page 043008, 2015.

[Colombe 14] Y. Colombe, D. H. Slichter, A. C. Wilson, D. Leibfried & D. J. Wineland. Single-mode optical fiber for high-power low-loss UV transmission. Opt. Express, vol. 22, page 19783, 2014.

[Daniilidis 09] N. Daniilidis, T. Lee, R. Clark, S. Narayanan & H. Häffner. Wiring up trapped ions to study aspects of quantum information. J. Phys. B: At. Mol. Opt. Phys., vol. 42, page 154012, 2009.

[Daniilidis 11] N. Daniilidis, S. Gerber, G. Bolloten, M. Raman, A. Ransford, E. Ulin-Avila, I. Talukdar & H. Häffner. Surface noise analysis using a single-ion sensor. PRB, vol. 89, page 245435, 2011.

[de Lange 10] G. de Lange, Z. H. Wang, R. Ristè, V. V. Dobrovitski & R. Hanson. Universal dynamical decoupling of a single solid-state spin from a spin bath. Science, vol. 330, page 60, 2010.

[Dehollain 16] J. P. Dehollain, S. Simmons, J. T. Muhonen, R. Kalra, A. Laucht, F. Hudson, K. M. Itoh, D. N. Jamieson, J. C. McCallum, A. S. Dzurak & A. Morello. Bell's inequality violation with spins in silicon. Nat. Nanotechnol., vol. 11, page 242, 2016.

[Deutsch 85] D. Deutsch. Quantum theory, the Church-Turing principle and the universal quantum computer. Proc. R. Soc. Lond. A, vol. 400, page 97, 1985.

[DiCarlo 09] L. DiCarlo, J. M. Chow, J. M. Gambetta, Lev S. Bishop, B. R. Johnson, D. I. Schuster, J. Majer, A. Blais, L. Frunzio, S. M. Girvin & R. J. Schoelkopf. Demonstration of two-qubit algorithms with a superconducting quantum processor. Nature, vol. 460, pages 240–244, 2009.

[Drullinger 80] R. E. Drullinger, D. J. Wineland & J. C. Bergquist. High-resolution optical spectra of laser cooled ions. Appl. Phys, vol. 22, pages 365–368, 1980.

[Du 09] J. Du, X. Rong, N. Zhao, Y. Wang, J. Yang & R. B. Liu. Preserving electron spin coherence in solids by optical dynamical decoupling. Nature, vol. 461, pages 1265–1268, 2009.

[Dyrting 95] S. Dyrting & G. J. Milburn. Quantum chaos in atom optics: using phase noise to model continuous momentum and position measurement. Quantum Semiclass. Opt., vol. 8, pages 541–555, 1995.

[Efron 93] B. Efron & R. J. Tibshirani. An introduction to the bootstrap. Chapman and Hall, 1993.

[Einstein 35] A. Einstein, B. Podolsky & N. Rosen. Can quantum-mechanical description of physical reality be considered complete? Phys. Rev., vol. 47, pages 777–780, 1935.

[Einstein 71] A. Einstein & M. Born. The born-einstein letters; correspondence between albert einstein and max and hedwig born from 1916 to 1955. Walker, New YOrk, 1971.

[Elitzur 92] A. Elitzur, S. Popescu & D. Rohrlich. Quantum nonlocality for each pair in an ensemble. Phys. Rev. A, vol. 162, pages 25–28, 1992.

[Evers 04] J. Evers & C. H. Keitel. Double-EIT ground-state laser cooling without blue-sideband heating. Europhysi. Lett., vol. 68, page 370, 2004.

[Feynman 82] R. P. Feynman. Simulating Physics with Computers. Int. J. Th. Phys., vol. 21, no. 6/7, pages 467–488, 1982.

[Freedman 72] S. J. Freedman & J. F. Clauser. Experimental test of local hidden-variable theories. Phys. Rev. Lett., vol. 28, no. 14, page 938, 1972.

[Gaebler 12] J. P. Gaebler, A. M. Meier, T. R. Tan, R. Bowler, Y. Lin, D. Hanneke, J. D. Jost, J. P. Home, E. Knill, D. Leibfried & D. J. Wineland. Randomized benchmarking of multi-qubit gates. Phys. Rev. Lett., vol. 108, page 260503, 2012.

[Gaebler 16] J. P. Gaebler, T. R. Tan, Y. Lin, Y. Wan, R. Bowler, A. C. Keith, S. Glancy, K. Coakley, E. Knill, D. Leibfried & D. J. Wineland. High-fidelity universal gate set for $^{9}Be^{+}$ ion qubits. Phys. Rev. Lett., vol. 117, page 060505, 2016.

[Gardiner 00] C. Gardiner & P. Zoller. Quantum noise: a handbook of markovian and non-markovian quantum stochastic methods with applications to quantum optics. Springer Science & Business Media, 2nd edition, 2000.

[Gill 03] R. D. Gill. Accardi contra Bell: The impossible coupling. in *Mathematical Statistics and Applications: Festschrift for Constance van Eeden*, edited by M. Moore, S. Froda, and . Léger (Institute of Mathematical Statistics, Beachwood, Ohio, 2003), vol. 42, pages 133–154, 2003.

[Giustina 15] M. Giustina, M. A. M. Versteegh, S. Wengerowsky, J. Handsteiner, A. Hochrainer, K. Phelan, F. Steinlechner, J. Kofler, J.-A. Larsson, C. Abellan, W. Amaya, V. Pruneri, M. W. Mitchell, J. Beyer, T. Gerrits, A. E. Lita, L. K. Shalm, S. W. Nam, T. Scheidl, R. Ursin, B. Wittmann & A. Zeilinger. Significant-loophole-free test of Bell's theorem with entangled photons. Phys. Rev. Lett., vol. 115, page 250401, 2015.

[Gottesman 98] D. Gottesman. The Heisenberg representation of quantum computers. arXiv:quant-ph/9807006, 1998.

[Grover 97] L. K. Grover. Quantum mechanics helps in searching for a needle in a haystack. Phys. Rev. Lett., vol. 79, page 325, 1997.

[Guggemos 15] M. Guggemos, D. Hienrich, O. A. Herrera-Sancho, R. Blatt & C. F. Roos. Sympathetic cooling and detection of a hot trapped ion by a cold one. New J. Phys, vol. 17, page 103001, 2015.

[Gustavsson 12] S. Gustavsson, F. Yan, J. Bylander, F. Yoshihara, Y. Nakamura, T. P. Orlando & W. D. Oliver. Dynamical decoupling and dephasing in interacting two-level systems. Phys. Rev. Lett., vol. 109, page 010502, 2012.

[Hahn 50] E. L. Hahn. Spin Echoes. Phys. Rev., vol. 80, page 580, 1950.

[Hankin 16] A. Hankin & D. Leibrandt. Private communication. 2016.

[Hansch 80] T. W. Hansch & B. Couillaud. Laser frequency stabilization by polarization spectroscopy of a reflecting reference cavity. Opt. Commun., vol. 35, no. 3, pages 441–444, 1980.

[Harlander 10] M. Harlander, M. Brownnutt, W. Hänsel & R. Blatt. Trapped-ion probing of light-induced charging effects on dielectrics. New J. Phys, vol. 12, page 093035, 2010.

[Harty 13] T. P. Harty. High-fidelity microwave-driven quantum logic in intermediate-field $^{43}Ca^{+}$. PhD thesis, Univ. Oxford, Dept. of Physics, 2013.

[Harty 14] T. P. Harty, D. T. C. Allcock, C. J. Ballance, L. Guidoni, H. A. Janacek, N. M. Linke, D. N. Stacey & D. M. Lucas. High-fidelity preparation, gates, memory, and readout of a trapped-ion quantum bit. Phys. Rev. Lett., vol. 113, page 220501, 2014.

[Harty 16] T. P. Harty, M. A. Sepiol, D. T. C. Allcock, C. J. Ballance, J. E. Tarlton & D. M. Lucas. High-fidelity trapped-ion quantum logic using near-field microwaves. Phys. Rev. Lett., vol. 117, page 140501, 2016.

[Hashimoto 06] Y. Hashimoto, L. Matsuoka, H. Osaki, Y. Fukushima & S. Hasegawa. Trapping laser ablated Ca^{+} ions in a linear Paul trap. Jpn. J. Appl. Phys., vol. 45, page 7108, 2006.

[Hayes 12] D. Hayes, S. M. Clark, S. Debnath, D. Hucul, I. V. Inlek, K. W. Lee, Q. Quraishi & C. Monroe. Coherent error suppression in multiqubit entangling gates. Phys. Rev. Lett., vol. 109, page 020503, 2012.

[Hendricks 07] R. J. Hendricks, D. M. Grant, P. F. Herskind, A. Dantan & M. Drewsen. An all-optical ion-loading technique for scalable microtrap architectures. Appl. Phys. B, vol. 88, pages 507–513, 2007.

[Hensen 15] B. Hensen, H. Bernien, A. E. Dreau, A Reiserer, N. Kalb, M. S. Blok, J. Ruitenberg, R.F.L. Vermeulen, R. N. Schouten, C. Abellan, W. Amaya, V. Pruneri, M. W. Mitchell, M. Markham, D. J. Twitchen, D. Elkouss, S. Wehner, T. H. Taminiau & R. Hanson. Loophole-free Bell inequality violation using electron spins separated by 1.3 kilometres. Nature, vol. 526, page 682, 2015.

[Hensen 16] B. Hensen, N. Kalb, M. S. Blok, A. E. Dréau, A. Reiserer, R. F. L. Vermeulen, R. N. Schouten, M. Markham, D. J. Twitchen, K. Goodenough, D. Elkouss, S. Wehner, T. H. Taminiau & R. Hanson. Loophole-free Bell test using electron spins in diamond: second experiment and additional analysis. Sci. Rep., vol. 6, page 30289, 2016.

[Hite 13] D. A. Hite, Y. Colombe, A. C. Wilson, D. T. C. Allcock, D. Leibfried, D. J. Wineland & D. P. Pappas. Surface science for improved ion traps. MRS Bull., vol. 38, page 826, 2013.

[Hofmann 12] J. Hofmann, M. Krug, N. Ortegel, L. Gérard, M. Weber, W. Rosenfeld & H. Weinfurter. Heralded Entanglement Between Widely Separated Atoms. Science, vol. 337, pages 72–75, 2012.

[Hollberg 90] L. Hollberg. Dye laser principles: with applications. Academic Press, Inc., 1990.

[Horodecki 99] M. Horodecki, P. Horodecki & R. Horodecki. General teleportation channel, singlet fraction and quasidistillation. Phys. Rev. A, vol. 60, pages 1888–1898, 1999.

[Hradil 04] Z. Hradil, J. Řeháček, J. Fiurášek & M. Ježek. Quantum state estimation. Springer, New York 2004, 2004.

[Huang 04] P. Huang & D. Leibfried. Achromatic catadioptric microscope objective in deep ultraviolet with long working distance. Proc. SPIE, vol. 5524, pages 125–133, 2004.

[Hume 07] D. B. Hume, T. Rosenband & D. J. Wineland. High-fidelity adaptive qubit detection through repetitive quantum nondemolition measurements. Phys. Rev. Lett., vol. 99, pages 120502–1–4, 2007.

[Itano 81] W. M. Itano & D. J. Wineland. Precision measurement of the ground-state hyperfine constant of $^{25}Mg^{+}$. Phys. Rev. A, vol. 24, pages 1364–1373, 1981.

[Itano 82] Wayne M. Itano & D. J. Wineland. Laser cooling of ions stored in harmonic and Penning traps. Phys. Rev. A, vol. 25, pages 35–54, 1982.

[James 07] D. F. V. James & J. Jerke. Effective hamiltonian theory and its applications in quantum information. Can. J. Phys., vol. 85, pages 625–632, 2007.

[Javanainen 84] J. Javanainen, M. Lindberg & S. Stenholm. Laser cooling of trapped ions: dynamics of the final stages. J. Opt. Soc. Am. B, vol. 1, pages 111–115, 1984.

[Jost 10] J. D. Jost. Entangled mechanical oscillators. PhD thesis, Univ. Colorado, Dept. of Physics, Boulder, 2010.

[Kaniewski 16] J. Kaniewski. Analytic and nearly optimal self-testing bounds for the Clauser-Holt-Shimony-Horne and Mermin inequalities. Phys. Rev. Lett., vol. 117, page 070402, 2016.

[Kielpinski 02] D. Kielpinski, C. Monroe & D. J. Wineland. Architecture for a large-scale ion-trap quantum computer. Nature, vol. 417, pages 709–711, 2002.

[Kienzler 15] D. Kienzler. Quantum harmonic oscillator state synthesis by reservoir engineering. PhD thesis, ETH Zürich, 2015.

[Knill 08] E. Knill, D. Leibfried, R. Reichle, J. Britton, R. B. Blakestad, J. D. Jost, C. Langer, R. Ozeri, S. Seidelin & D. J. Wineland. Randomized benchmarking of quantum gates. Phys. Rev. A, vol. 77, pages 012307–1—7, 2008.

[Knill 10] E. Knill. Physics: Quantum computing. Nature, vol. 463, page 441, 2010.

[Kotler 16] S. Kotler, R. W. Simmonds, D. Leibfried & D. J. Wineland. Hybrid quantum systems with trapped charged particles. arXiv:1608.02677, 2016.

[Kramida 97] A. Kramida & W. C. Martin. A compilation of energy levels and wavelengths for the spectrum of neutral beryllium (be i). J. Phys. Chem. Ref. Data, vol. 26, pages 1185–1194, 1997.

[Kurizki 15] G. Kurizki, P. Bertet, Y. Kubo, K. Mølmer, D. Petrosyan, P. Rabl & J. Schmiedmayer. Quantum technologies with hybrid systems. Proc. Natl. Acad. Sci. U.S.A., vol. 112, page 3866, 2015.

[Labaziewicz 08] J. Labaziewicz, Y. Ge, P. Antohi, D. Leibrandt, K. R. Brown & I. L. Chuang. Suppression of heating rates in cryogenic surface-electrode ion traps. Phys. Rev. Lett., vol. 100, page 013001, 2008.

[Ladd 10] T. D. Ladd, F. Jelezko, R. Laflamme, Y. Nakamura, C. Monroe & J. L. O'Brien. Quantum computers. Nature, vol. 464, pages 45–53, 2010.

[Langer 05] C. Langer, R. Ozeri, J. D. Jost, J. Chiaverini, B. DeMarco, A. Ben-Kish, R. B. Blakestad, J. Britton, D. B. Hume, W. M. Itano, D. Leibfried, R. Reichle, T. Rosenband, T. Schätz, P. O. Schmidt & D. J. Wineland. Long-lived qubit memory using atomic ions. Phys. Rev. Lett., vol. 95, pages 060502–1–4, 2005.

[Langer 06] C. E. Langer. High fidelity quantum information processing with trapped ions. PhD thesis, Univ. Colorado, Dept. of Physics, Boulder, 2006.

[Lechner 16] R. Lechner, C. Maier, C. Hempel, P. Jurcevic, B. P. Lanyon, T. Monz, M. Brownnutt, R. Blatt & C. F. Roos. Electromagnetically-induced-transparency ground-state cooling of long ion strings. Phys. Rev. A, vol. 93, page 053401, 2016.

[Lee 05] P. J. Lee, K. A. Brickman, L. Deslauriers, P. C. Haljan, L. M. Duan & C. Monroe. Phase control of trapped ion quantum gates. J. Opt. B: Quantum Semiclass Opt., vol. 7, pages S371–S383, 2005.

[Leibfried 03] D. Leibfried, B. DeMarco, V. Meyer, D. Lucas, M. Barrett, J. Britton, W. M. Itano, B. Jelenković, C. Langer, T. Rosenband & D. J. Wineland. Experimental demonstration of a robust, high-fidelity geometrical two ion-qubit phase gate. Nature, vol. 422, pages 412–415, 2003.

[Leibrandt 07] D. R. Leibrandt, R. J. Clark, J. Labaziewicz, P. Antohi, W. Bakr, K. R. Brown & I. L. Chuang. Laser ablation loading of a surface-electrode ion trap. Phys. Rev. A, vol. 76, page 055403, 2007.

[Leibrandt 15] D. R. Leibrandt & J. Heidecker. An open source digital servo for atomic, molecular and optical physics experiments. Rev. Sci. Instrum., vol. 86, page 123115, 2015.

[Lemmer 13] A. Lemmer, A. Bermudez & M. B. Plenio. Driven geometric phase gates with trapped ions. New J. Phys., vol. 15, page 083001, 2013.

[Levitt 86] M. H. Levitt. Composite pulses. Prog. NMR Spectrosc., vol. 18, page 61, 1986.

[Lidar 14] D. A. Lidar. Review of decoherence free subspaces, noiseless subsystems, and dynamical decoupling. Adv. Chem. Phys., vol. 154, pages 295–354, 2014.

[Lin 13a] Y. Lin, J. P. Gaebler, F. Reiter, T. R. Tan, R. Bowler, A. Sørensen, D. Leibfried & D. J. Wineland. Dissipative production of a maximally entangled steady state of two quantum bits. Nature, vol. 504, pages 415–418, 2013.

[Lin 13b] Y. Lin, J. P. Gaebler, T. R. Tan, R. Bowler, J. D. Jost, D. Leibfried & D. J. Wineland. Sympathetic electromagnetically-induced-transparency laser cooling of motional modes in an ion chain. Phys. Rev. Lett., vol. 110, page 153002, 2013.

[Lin 15] Y. Lin. Quantum entanglement generation in trapped ions using coherent and dissipative methods. PhD thesis, Univ. Colorado, Dept. of Physics, Boulder, 2015.

[Lin 16] Y. Lin, J. P. Gaebler, F. Reiter, T. R. Tan, R. Bowler, Y. Wan, A. Keith, E. Knill, S. Glancy, K. Coakley, A. Sørensen, D. Leibfried & D. J. Wineland. Preparation of entangled states through Hilbert space engineering. Phys. Rev. Lett., vol. 117, page 140502, 2016.

[Lindberg 84] M. Lindberg. Steady state of a laser-cooled trapped ion in the Lamb-Dicke limit. J. Phys. B, vol. 17, pages 2129–2139, 1984.

[Lindblad 76] G. Lindblad. On the generators of quantum dynamical semigroups. Comm. Math. Phys., vol. 48, pages 119–130, 1976.

[Liu 13] G.-Q. Liu, H. C. Po, J. Du, R.-B. Liu & X.-Y. Pan. Noise-resilient quantum evolution steered by dynamical decoupling. Nat. Commun., vol. 4, page 2254, 2013.

[Lloyd 96] S. Lloyd. Universal quantum simulators. Science, vol. 273, pages 1073–1078, 1996.

[Lu 15] Y. Lu, J.-Q. Zhang, J.-M. Cui, D.-Y. Cao, S. Zhang, Y.-F. Huang, C.-F. Li & G.-C. Guo. Dark-state cooling of a trapped ion using microwave coupling. Phys. Rev. A, vol. 92, page 023420, 2015.

[Ludlow 15] A. D. Ludlow, M. M. Boyd, J. Ye, E. Peik & P. O. Schmidt. Optical atomic clock. Rev. Mod. Phys., vol. 87, page 637, 2015.

[Macki 82] J. Macki & A. Strauss. Introduction to optimal control theory. Springer-Verlag, New York, 1982.

[Martin 80] W. C. Martin & R. Zalubas. Energy levels of magnesium Mg I through Mg xii. J. Phys. Chem. Ref. Data, vol. 9, page 1, 1980.

[Matsukevich 08] D. N. Matsukevich, P. Maunz, D. L. Moehring, S. Olmschenck & C. Monroe. Bell inequality violation with two remote atomic qubits. Phys. Rev. Lett., vol. 100, page 150404, 2008.

[Mayers 04] D. Mayers & A. Yao. Self testing quantum apparatus. Quantum Inf. Comput., vol. 4, page 273, 2004.

[McConnell 15] R. McConnell, C. Brunewicz, J. Chiaverini & J. Sage. Reduction of trapped-ion anomalous heating by *in-situ* surface plasma cleaning. Phys. Rev. A, vol. 92, page 020302(R), 2015.

[McKague 12] M. McKague, T. H. Yang & V. Scarani. Robust self-testing of the singlet. J. Phys. A, vol. 45, page 455304, 2012.

[Milburn 00] G. J. Milburn, S. Schneider & D. F. V. James. Ion trap quantum computing with warm ions. Fortschr. Physik, vol. 48, pages 801–810, 2000.

[Moehring 07] D. L. Moehring, M. J. Madsen, K. C. Younge, Jr. R. N. Kohn, P. Maunz, L.-M. Duan, C. Monroe & B. B. Blinov. Quantum networking with photons and trapped atoms. JOSA B, vol. 24, pages 300–315, 2007.

[Monroe 95a] C. Monroe, D. M. Meekhof, B. E. King, W. M. Itano & D. J. Wineland. Demonstration of a fundamental quantum logic gate. Phys. Rev. Lett., vol. 75, no. 25, pages 4714–4717, 1995.

[Monroe 95b] C. Monroe, D. M. Meekhof, B. E. King, S. R. Jefferts, W. M. Itano, D. J. Wineland & P. Gould. Resolved-Sideband Raman Cooling of a Bound Atom to the 3D Zero-point Energy. Phys. Rev. Lett., vol. 75, no. 22, page 4011, 1995.

[Monroe 13] C. Monroe & J. Kim. Scaling the ion trap quantum processor. Science, vol. 339, pages 1164–1169, 2013.

[Monroe 14] C. Monroe, R. Raussendorf, A. Ruthven, K. R. Brown, P. Maunz, L.-M. Duan & J. Kim. Large-scale modular quantum-computer architecture with atomic memory and photonic interconnects. Phys. Rev. A, vol. 89, page 022317, 2014.

[Morigi 00] G. Morigi, J. Eschner & C. H. Keitel. Ground state laser cooling using electromagnetically induced transparency. Phys. Rev. Lett., vol. 85, page 4458, 2000.

[Morigi 03] G. Morigi. Cooling atomic motion with quantum interference. Phys. Rev. A, vol. 67, page 033402, 2003.

[Myerson 08] A. H. Myerson, D. J. Szwer, S. C. Webster, D. T. C. Allcock, M. J. Curtis, G. Imreh, J. A. Sherman, D. N. Stacey, A. M. Steane & D. M. Lucas. High-fidelity readout of trapped-ion qubits. Phys. Rev. Lett., vol. 100, page 200502, 2008.

[Navon 14] N. Navon, N. Akerman, S. Kotler, Y. Glickman & R. Ozeri. Quantum process tomography of a Molmer Sorensen interaction. Phys. Lett. A, vol. 90, page 010103(R), 2014.

[Nguyen 09] J. Nguyen. The linewidth and hyperfine A constant of the $^2P_{1/2}$ state of a magnesium ion confined in a linear Paul trap. PhD thesis, McMaster Univ., Dept. of Physics and Astronomy, 2009.

[Nie 09] X Rebecca Nie, C Roos & D F V James. Theory of cross phase modulation for the vibrational modes of trapped ions. Phys. Lett. A, vol. 373, pages 422–425, 2009.

[Niedermayr 14] M. Niedermayr, K. Lakhmanskiy, M. Kumph, S. Partel, J. Edlinger, M. Brownnutt & R. Blatt. Cryogenic surface ion trap based on intrinsic silicon. New J. Phys., vol. 16, page 113068, 2014.

[Nielsen 00] M. A. Nielsen & I. L. Chuang. Quantum computation and quantum information. Cambridge Univ. Press, Cambridge, 1st edition, 2000.

[Nielson 02] M. A. Nielson. A simple formula for the average fidelity of a quantum dynamical operation. Phys. Lett. A, vol. 303, page 249, 2002.

[Olmschenk 10] S. Olmschenk, R. Chicireanu, K. D. Nelson & J. V. Porto. Randomized benchmarking of atomic qubits in an optical lattice. New J. Phys., vol. 12, page 113007, 2010.

[Ospelkaus 08] C. Ospelkaus, C. E. Langer, J. M. Amini, K. R. Brown, D. Leibfried & D. J. Wineland. Trapped-ion quantum logic gates based on oscillating magnetic fields. Phys. Rev. Lett., vol. 101, page 090502, 2008.

[Ospelkaus 11] C. Ospelkaus, U. Warring, Y. Colombe, K. R. Brown, J. M. Amini, D. Leibfried & D. J. Wineland. Microwave quantum logic gates for trapped ions. Nature, vol. 476, page 181, 2011.

[Ozeri 05] R. Ozeri, C. Langer, J. D. Jost, B. L. DeMarco, A. Ben-Kish, B. R. Blakestad, J. Britton, J. Chiaverini, W. M. Itano, D. Hume, D. Leibfried, T. Rosenband, P. Schmidt & D. J. Wineland. Hyperfine coherence in the presence of spontaneous photon scattering. Phys. Rev. Lett., vol. 95, pages 030403–1–4, 2005.

[Ozeri 07] R. Ozeri, W. M. Itano, R. B. Blakestad, J. Britton, J. Chiaverini, J. D. Jost, C. Langer, D. Leibfried, R. Reichle, S. Seidelin, J. H. Wesenberg & D. J. Wineland. Errors in trapped-ion quantum gates due to spontaneous photon scattering. Phys. Rev. A, vol. 75, page 042329, 2007.

[Paul 90] W. Paul. Electromagnetic traps for charged and neutral particles. Rev. Mod. Phys., vol. 62, page 531, 1990.

[Pearle 70] P. M. Pearle. Hidden-variable example based upon data rejection. Phys. Rev. D, vol. 2, page 1418, 1970.

[Pfaff 13] W. Pfaff, T. H. Taminiau, L. Robledo, H. Bernien, M. Markham, D. J. Twitchen & R. Hanson. Demonstration of entanglement-by-measurement of solid-state qubits. Nat. Phys., vol. 9, pages 29–33, 2013.

[Piltz 13] Ch. Piltz, B. Scharfenberger, A. Khromova, A. F. Varón & Ch. Wunderlich. Protecting conditional quantum gates by robust dynamical decoupling. Phys. Rev. Lett., vol. 110, page 200501, 2013.

[Pironio 10] S. Pironio, A. Acín, S. Massar, A. Boyer de la Giroday, D. N. Matsukevich, P. Maunz, S. Olmschenk, D. Hayes, L. Luo, T. A. Manning & C. Monroe. Random numbers certified by Bell's theorem. Nature, vol. 464, page 1021, 2010.

[Pomarico 11] E. Pomarico, J.-D. Bancal, B. Sanguinetti, A. Rochdi & N. Gisin. Various quantum nonlocality tests with a commercial two-photon entanglement source. Phys. Rev. A, vol. 83, page 052104, 2011.

[Popescu 92] S. Popescu & D. Rohrlich. Which states violate Bell's inequality maximally? Phys. Rev. A, vol. 169, pages 411–414, 1992.

[Poulsen 75] O. Poulsen, T. Andersen & N. J. Skouboe. Fast-beam, zero-field level-crossing measurements of radiative lifetimes, fine and hyperfine structures in excited states of ionic and neutral beryllium. J. Phys. B: Atom. Molec. Phys., vol. 8, no. 9, page 1393, 1975.

[Preskill 98] J. Preskill. Reliable quantum computers. Proc. R. Soc. Lond. A, vol. 454, page 385, 1998.

[Puri 01] R. R. Puri. Mathematical methods of quantum optics. Springer, New York, 1st edition, 2001.

[Pyka 14] K. Pyka, N. Herschbach, J. Keller & T. Mehlstäubler. A high-precision segmented Paul trap with minimized micromotion for an optical multiple-ion clock. Appl. Phys. B, vol. 114, pages 231–241, 2014.

[Å. Larsson 14] J. Å. Larsson. loopholes in Bell inequality tests of local realism. J. Phys. A, vol. 47, page 424003, 2014.

[Roos 00] C. F. Roos, D. Leibfried, A. Mundt, F. Schmidt-Kaler, J. Eschner & R. Blatt. Experimental demonstration of ground state laser cooling with electromagnetically induced transparency. Phys. Rev. Lett., vol. 85, page 5547, 2000.

[Roos 08] C. F. Roos, T. Monz, K. Kim, M. Riebe, H. Häffner, D. F. V. Fames & R. Blatt. Nonlinear coupling of continuous variables at the single quantum level. Phys. Rev. A, vol. 77, page 040302(R), 2008.

[Rosenband 08] T. Rosenband, P. O. Schmidt, D. B. Hume, W. M. Itano, T. M. Fortier, J. E. Stalnaker, K. Kim, S. A. Diddams, J. C. J. Koelemeij, J. C. Bergquist & D. J. Wineland. Observation of the $^1S_0 \rightarrow {}^3P_0$ clock transition in $^{27}Al^+$. Phys. Rev. Lett., vol. 98, page 220801, 2008.

[Rowe 01] M. A. Rowe, D. Kielpinski, V. Meyer, C. A. Sackett, W. M. Itano, C. Monroe & D. J. Wineland. Experimental violation of a Bell's inequality with efficient detection. Nature, vol. 409, pages 791–794, 2001.

[Ryan 09] C. A. Ryan, M. Laforest & R. Laflamme. Randomized benchmarking of single- and multi- qubit control in liquid-state NMR quantum information processing. New J. Phys., vol. 11, page 013034, 2009.

[Ryan 10] C. A. Ryan, J. S. Hodges & D. G. Cory. Robust decoupling techniques to extend quantum coherence in diamond. Phys. Rev. Lett., vol. 105, page 200402, 2010.

[Sackett 00] C. A. Sackett, D. Kielpinski, B. E. King, C. Langer, V. Meyer, C. J. Myatt, M. Rowe, Q. A. Turchette, W. M. Itano, D. J. Wineland & C. Monroe. Experimental entanglement of four particles. Nature, vol. 404, pages 256–259, 2000.

[Sage 12] J. M. Sage, A. J. Kerman & J. Chiaverini. Loading of a surface-electrode ion trap from a remote, precooled source. Phys. Rev. A, vol. 86, page 013417, 2012.

[Schmidt-Kaler 03] F. Schmidt-Kaler, H. Häffner, M. Riebe, S. Gulde, G. P. T. Lancaster, T. Deuschle, C. Becher, C. Roos, J. Eschner & R. Blatt. Realization of the Cirac-Zoller controlled-NOT quantum gate. Nature, vol. 422, pages 408–411, 2003.

[Schmidt 05] P. O. Schmidt, T. Rosenband, C. Langer, W. M. Itano, J. C. Bergquist & D. J. Wineland. Spectroscopy using quantum logic. Science, vol. 309, pages 749–752, 2005.

[Schneider 98] S. Schneider & G. J. Milburn. Decoherence in ion traps due to laser intensity and phase fluctuations. Phys. Rev. A, vol. 57, page 3748, 1998.

[Schulte 16] M. Schulte, N. Lörch, I. D. Leroux, P. O. Schmidt & K. Hammerer. Quantum algorithmic readout in multi-ion clocks. Phys. Rev. Lett., vol. 116, page 013002, 2016.

[Shalm 15] L. K. Shalm, E. Meyer-Scott, B. G. Christensen, P. Bierhorst, M. A. Wayne, M. J. Stevens, T. Gerrits, S. Glancy, D. R. Hamel, M. S. Allman, K. J. Coakley, S. D. Dyer, C. Hodge, A. E. Lita, V. B Verma, C. Lambrocco, E. Tortorici, A. L. Migdall, Y. Zhang, D. R. Kumor, W. H. Farr, F. Marsili, M. D. Shaw, J. A. Stern, C. Abellan, W. Amaya, V. Pruneri, T. Jennewein, M. W. Mitchell, P. G. Kwiat, J. C. Bienfang, R. P. Mirin, E. Knill & S. W. Nam. Strong loophole-free test of local realism. Phys. Rev. Lett., vol. 115, page 250402, 2015.

[Sheridan 11] K. Sheridan, W. Lange & M. Keller. All-optical ion generation for ion trap loading. Appl. Phys. B, vol. 104, page 755, 2011.

[Shiga 11] N. Shiga, W. M. Itano & J. J. Bollinger. Diamagnetic correction to the $^9Be^+$ ground-state hyperfine constant. Phys. Rev. A, vol. 84, page 012510, 2011.

[Shor 97] P. W. Shor. Algorithm for Fast Factoring. SIAM J. Comp., vol. 26, page 1484, 1997.

[Solano 99] E. Solano, R. L. de Matos Filho & N. Zagury. Deterministic Bell states and measurement of the motional state of two trapped ions. Phys. Rev. A, vol. 59, pages 2539–2542, 1999.

[Sørensen 99] A. Sørensen & K. Mølmer. Quantum computation with ions in thermal motion. Phys. Rev. Lett., vol. 82, pages 1971–1974, 1999.

[Sørensen 00] A. Sørensen & K. Mølmer. Entanglement and quantum computation with ions in thermal motion. Phys. Rev. A, vol. 62, pages 02231–1–11, 2000.

[Souza 12] A. M. Souza, G. A. Álvarez & D. Suter. Experimental protection of quantum gates against decoherence and control errors. Phys. Rev. A, vol. 86, page 050301(R), 2012.

[Steffen 06] M. Steffen, M. Ansmann, R. C. Bialczak, N. Katz, E. Lucero, R. McDermott, M. Neeley, E. M. Weig, A. N. Cleland & J. M. Martinis. Measurement of the entanglement of two superconducting qubits via state tomography. Science, vol. 313, page 1423, 2006.

[Stuart 12] T. E. Stuart, J. A. Slater, R. Colbeck, R. Renner & W. Tittel. Experimental bound on the maximum predictive power of physical theories. Phys. Rev. Lett., vol. 109, page 020402, 2012.

[Sur 05] C. Sur, B. K. Sahoo, R. K. Chaudhuri, B. P. Das & D. Mukherjee. Comparative studies of the magnetic dipole and electric quadrupole hyperfine constant for the ground and low lying excited states of $^{25}Mg^{+}$. Eur. Phys. J. D, vol. 32, pages 25–31, 2005.

[Szwer 11] D. J. Szwer, S. C. Webster, A. M. Steane & D. M. Lucas. Keeping a single-qubit alive by experimental dynamic decoupling. J. Phys. B: At. Mol. Opt. Phys., vol. 44, page 025501, 2011.

[Takahashi 70] Y. Takahashi, M. J. Rabins & D. M. Auslander. Control and dynamic systems. Addison-Wesley, Reading, MA, 1970.

[Tan 13] T. R. Tan, J. P. Gaebler, R. Bowler, Y. Lin, J. D. Jost, D. Leibfried & D. J. Wineland. Demonstration of a dressed-state phase gate for trapped ions. Phys. Rev. Lett., vol. 110, page 263002, 2013.

[Tan 15] T. R. Tan, J. P. Gaebler, Y. Lin, Y. Wan, R. Bowler, D. Leibfried & D. J. Wineland. Multi-element logic gates for trapped-ion qubits. Nature, vol. 380, page 528, 2015.

[Todaro 16] S. Todaro & A. Wilson. Private communication. 2016.

[Turchette 98] Q. A. Turchette, C. S. Wood, B. E. King, C. J. Myatt, D. Leibfried, W. M. Itano, C. Monroe & D. J. Wineland. Deterministic entanglement of two trapped ions. Phys. Rev. Lett., vol. 81, page 3631, 1998.

[Turchette 00a] Q. A. Turchette, D. Kielpinski, B. E. King, D. Leibfried, D. M. Meekhof, C. J. Myatt, M. A. Rowe, C. A. Sackett, C. S. Wood, W. M. Itano, C. Monroe & D. J. Wineland. Heating of trapped ions from the quantum ground state. Phys. Rev. A, vol. 61, pages 063418–1–8, 2000.

[Turchette 00b] Q. A. Turchette, C. J. Myatt, B. E. King, C. A. Sackett, D. Kielpinski, W. M. Itano, C. Monroe & D. J. Wineland. Decoherence and decay of motional quantum states of a trapped atom coupled to engineered reservoirs. Phys. Rev. A, vol. 62, page 053807, 2000.

[Uys 10] H. Uys, M. J. Biercuk, A. P. VanDevender, C. Ospelkaus, D. Meiser, R. Ozeri & J. J. Bollinger. Decoherence due to elastic Rayleigh scattering. arXiv:1007.2661, 2010.

[van der Sar 12] T. van der Sar, Z. H. Wang, M. S. Blok, H. Bernien, T. H. Taminiau, D. M. Toyli, D. A. Lidar, D. D. Awschalom, R. Hanson & V. V. Dobrovitski. Decoherence protected quantum gates for a hybrid solid-state spin register. Nature, vol. 484, page 82, 2012.

[Viola 98] L. Viola & S. Lloyd. Dynamical suppression of decoherence in two-state quantum systems. Phys. Rev. A, vol. 58, page 2733, 1998.

[Viola 99] L. Viola, E. Knill & S. Lloyd. Dynamical Decoupling of Open Systems. Phys. Rev. Lett., vol. 82, page 2417, 1999.

[Vlastakis 15] B. Vlastakis, A. Petrenko, N. Ofek, L. Sun, Z. Leghtas, K. Sliwa, Y. Liu, M. Hatridge, J. Blumoff, L. Frunzio, M. Mirrahimi, L. Jiang, M. H. Devoret & R. J. Schoelkopf. Characterizing entanglement of an artificial atom and a cavity cat state with Bell's inequality. Nat. Commun., vol. 6, page 8970, 2015.

[Wallquist 09] M. Wallquist, L. Hammerer, P. Rabl, M. Lukin & P. Zoller. Hybrid quantum devices and quantum engineering. Phys. Scr., vol. T137, page 014001, 2009.

[Walther 12] A. Walther, F. Ziesel, T. Ruster, S. T. Dawkins, K. Ott, M. Hettrich, K. Singer, F. Schmidt-Kaler & U. Poschinge. Controlling fast transport of cold trapped ions. Phys. Rev. Lett., vol. 109, page 080501, 2012.

[Weidt 16] S. Weidt, J. Randall, S. C. Webster, K. Lake, A. E. Webb, I. Cohen, T. Navickas, B. Lekitsch, A. Retzker & W. K. Hensinger. Trapped-ion quantum logic with global radiation fields. arXiv:1603.03384, 2016.

[Wilson 11] A. C. Wilson, C. Ospelkaus, A. Vandervender, J. A. Mlynek, K. R. Brown, D. Leibfried & D. J. Wineland. A 750-mW, continuous-wave, solid-state laser source at 313nm for cooling and manipulating trapped $^{9}Be^{+}$ ions. Appl. Phys. B, vol. 105, page 741, 2011.

[Wilson 14] A. C. Wilson, Y. Colombe, K. R. Brown, E. Knill, D. Leibfried & D. J. Wineland. Tunable spin-spin interactions and entanglement of ions in separate controlled potential wells. Nature, vol. 512, pages 57–63, 2014.

[Wineland 79] D. J. Wineland & W. M. Itano. Laser cooling of atoms. Phys. Rev. A, vol. 20, no. 4, pages 1521–1540, October 1979.

[Wineland 85] D. J. Wineland, J. J. Bollinger & W. M. Itano. Laser-fluorescence mass spectroscopy. Phys. Rev. Lett., vol. 50, no. 9, pages 628–631, 1985.

[Wineland 98] D. J. Wineland, C. Monroe, W. M. Itano, D. Leibfried, B. E. King & D. M. Meekhof. Experimental issues in coherent quantum-state manipulation of trapped atomic ions. J. Res. Nat. Inst. Stand. Tech., vol. 103, pages 259–328, 1998.

[Wolf 16] F. Wolf, Y. Wan, J. C. Heip, F. Gebert, C. Shi & P. O. Schmidt. Non-destructive state detection for quantum logic spectroscopy of molecular ions. Nature, vol. 530, page 457, 2016.

[Yang 14] T. H. Yang, T. Vértesi, J.-D. Bancal, V. Scarani & M. Navascués. Robust and versatile black-box certification of quantum devices. Phys. Rev. Lett., vol. 113, page 040401, 2014.

[Zhang 03] J. Zhang, J. Vala, S. Sastry & K. B. & Whaley. Exact two-qubit universal quantum circuit. Phys. Rev. Lett., vol. 91, page 027903, 2003.

[Zhang 14] J. Zhang, A. M. Souza, F. D. Brandao & D. Suter. Protected quantum computing: interleaving gate operations with dynamical decoupling sequences. Phys. Rev. Lett., vol. 112, page 050502, 2014.

[Zhang 15] J. Zhang, & D. Suter. Experimental protection of two-qubit quantum gates against environmental noise by dynamical decoupling. Phys. Rev. Lett., vol. 115, page 110502, 2015.

[Zimmermann 12] K. Zimmermann, M. V. Okhapkin, O. A. Herrera-Sancho & E. Peik. Laser ablation loading of a radiofrequency ion trap. Appl. Phys. B, vol. 107, pages 883–889, 2012.

Appendix A

Details of $^9Be^+$

The relevant properties of the neutral ^{9}Be atom and the $^9Be^+$ ion are summarized in Table A.1.

The $^9Be^+$ ion has a nuclear spin of 3/2, and the interaction between the nuclear and electron spin gives rise to hyperfine structure. Also, Zeeman sublevels are split in energy when an external magnetic field is applied. In the intermediate field regime where the hyperfine and Zeeman interaction strengths are comparable, the energy levels exhibit curvature as a function of the applied external magnetic field due to the competition between these two interactions. At certain magnetic-field strengths, some transition frequencies become insensitive to small changes in the applied magnetic field. Such transitions are sometimes referred to as "clock" transitions or field-insensitive transitions.

The eigenenergies and eigenstates that take both the hyperfine and Zeeman interactions into account can be determined by solving the Breit-Rabi formula (see Ref. [Langer 06, Jost 10] for details in the case of $^9Be^+$). Table A.2 summarizes the magnetic-field independent points and their respective transitions available in a $^9Be^+$ ion.

The detailed energy level diagram in the $^2S_{1/2}$ electronic ground state of the $^9Be^+$ ion at a field B = 0.0119446 T (119.446 G) is shown in Fig. A.1.

^{9}Be$^+$ ion properties		
Nuclear spin	3/2	
Electron g-factor	-2.00226206(42)	[Wineland 85]
Nuclear to electron g-factor ratio	0.0002134779853(2)	[Wineland 85]
Hyperfine constant of the $^2S_{1/2}$ state		
Magnetic dipole (A)	-625.008837.048(10) MHz	[Wineland 85]
Hyperfine constant of the $^2P_{1/2}$ state		
Magnetic dipole (A)	-118.6(3.6) MHz	[Bollinger 85]
Hyperfine constant of the $^2P_{3/2}$ state		
Magnetic dipole (A)	$\|A\| \leq 0.6$ MHz	[Poulsen 75]
Electric quadrupole (B)	Not available	
$P_{1/2}$ and $P_{3/2}$ levels natural decay rate	$2\pi \times 19.4(5)$ MHz	[Poulsen 75]
Fine structure splitting of		
$P_{1/2}$ and $P_{3/2}$ levels at B = 0	197.150(64) MHz	[Bollinger 85]
$^2S_{1/2}$ state hyperfine splitting at B = 0	1,250.018 MHz	Calculated value
$^2P_{1/2}$ state hyperfine splitting at B = 0	237.2 MHz	Calculated value
$^2S_{1/2} \leftrightarrow {}^2P_{1/2}$ transition frequency	957,199.6525(1200) GHz	[Bollinger 85]
(line center of hyperfine structure)		
$^2S_{1/2} \leftrightarrow {}^2P_{P/2}$ transition frequency	957,396.8020(1349) GHz	[Bollinger 85]
(line center of hyperfine structure)		
Neutral Be atom properties		
$2s^2 \leftrightarrow 2s2p$ transition wavelength	234.9329 nm	[Kramida 97]
$2s2p$ to continuum excitation wavelength	306.4919 nm	[Kramida 97]

Table A.1: Relevant properties of the ^{9}Be atom and ^{9}Be$^+$ ion which are important for this thesis. The references from which the properties are extracted are shown in the last column. See also Ref. [Shiga 11] for the ^{9}Be$^+$ ion's ground state hyperfine constant that takes the diamagnetic correction into account. The hyperfine energy level splittings at a field B = 0 is calculated by solving the Breit-Rabi equation at a vanishing field.

Transition	B-field (T)	Transition frequency (MHz)	$\frac{d^2f}{dB^2}$ (MHz/mT^2)
$\|F=2, m_F=0\rangle \leftrightarrow \|1,1\rangle$	0.0119446	1,207.496	0.6097
$\|2,1\rangle \leftrightarrow \|1,0\rangle$	0.0119643	1,207.353	0.6097
$\|2,1\rangle \leftrightarrow \|1,1\rangle$	0.0223073	1,082.547	0.7252
$\|1,1\rangle \leftrightarrow \|1,0\rangle$	0.160182	322.552	1.059×10^{-3}
$\|2,1\rangle \leftrightarrow \|2,0\rangle$	0.174719	324.548	0.6247×10^{-3}

Table A.2: Magnetic-field insensitive transitions and their respective magnetic-field strengths in the $^2S_{1/2}$ electronic ground state for the $^9Be^+$ ion in the intermediate field regime. The transition frequencies and the second-order magnetic-field sensitivities are also given.

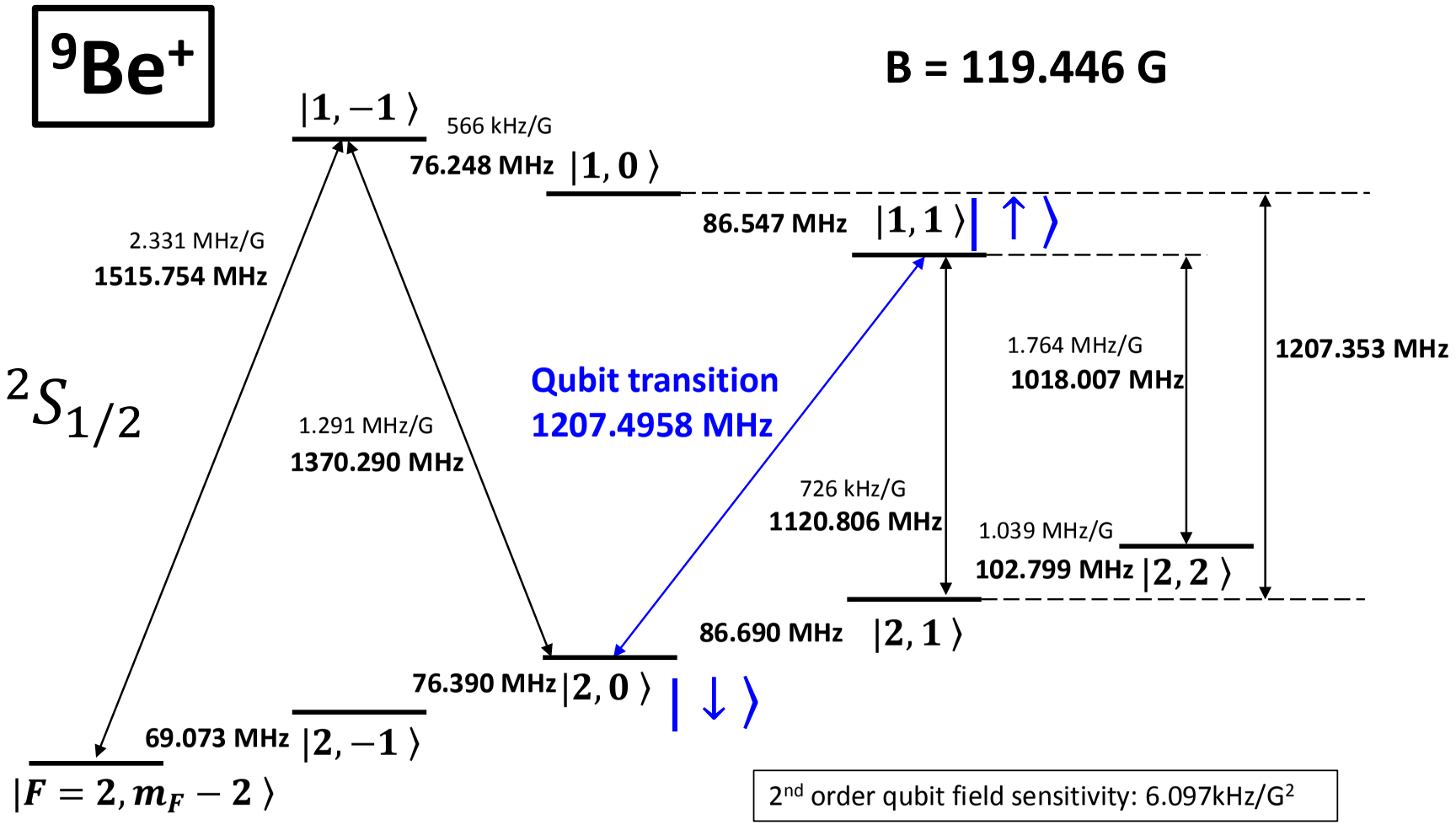

Figure A.1: The electronic ground state of the $^9Be^+$ ion at a magnetic field of 0.0119446 T, where the transition frequency of the $|F=2,m_F=0\rangle \leftrightarrow |1,1\rangle$ transition is first-order insensitive to magnetic-field fluctuations. The frequency differences between adjacent levels, and the transition frequencies of certain transitions are shown in bold. The magnetic-field sensitivities of some relevant transitions are also shown in lighter print. The states are designated by the states they evolve from at low magnetic field strength where the total angular momentum F and its projection along the quantization axis m_F are both good quantum numbers.

Appendix B

Details of $^{25}Mg^{+}$

Table B.1 lists the relevant properties of the neutral magnesium atom and the $^{25}Mg^{+}$ ion's properties. Table B.2 shows the magnetic-field insensitive points and their respective transitions for the $^{25}Mg^{+}$ ion's $^{2}S_{1/2}$ electronic ground state. For the work presented in this thesis, the magnetic field is set at a insensitive point for the $^{9}Be^{+}$ ion, i.e. $\sim$ 119.446 G. The detailed energy levels diagram in the $^{2}S_{1/2}$ electronic ground state of the $^{25}Mg^{+}$ at B = 119.446 G is shown in Fig. B.1.

$^{25}Mg^{+}$ ion properties		
Nuclear spin	5/2	
Nuclear to electron g-factor ratio	$9.299484(75) \times 10^{-5}$	[Itano 81]
Hyperfine constant of the $^2S_{1/2}$ state		
Magnetic dipole (A)	$-596.254376(54)$ MHz	[Itano 81]
Hyperfine constant of the $^2P_{1/2}$ state		
Magnetic dipole (A)	-101.70 MHz (theory)	[Sur 05]
	$-102.16(16)$ MHz (experiment)	[Nguyen 09]
Hyperfine constant of the $^2P_{3/2}$ state		
Magnetic dipole (A)	-18.89 MHz	[Sur 05]
Electric Quadrupole (B)	22.91 MHz	[Sur 05]
$P_{1/2}$ and $P_{3/2}$ levels natural decay rate	$2\pi \times 41.3(3)$ MHz	[Clos 14]
$^2S_{1/2}$ state hyperfine splitting at B = 0	1,788.763 MHz	Calculated value
$^2P_{1/2}$ state hyperfine splitting at B = 0	305.1 MHz	Calculated value
$^2S_{1/2} \leftrightarrow {}^2P_{1/2}$ transition frequency	1,069,339.957(5) GHz	[Clos 14]
(line center of hyperfine structure)		
$^2S_{1/2} \leftrightarrow {}^2P_{P/2}$ transition frequency	1,072,084.547(5) GHz	[Clos 14]
(line center of hyperfine structure)		
Isotope shift between $^{25}Mg^{+}$ and $^{24}Mg^{+}$		
$^2S_{1/2} \leftrightarrow {}^2P_{1/2}$	1,620(19) MHz	[Batteiger 09]
$^2S_{1/2} \leftrightarrow {}^2P_{3/2}$	1,621(19) MHz	[Batteiger 09]
Isotope shift between $^{26}Mg^{+}$ and $^{24}Mg^{+}$		
$^2S_{1/2} \leftrightarrow {}^2P_{1/2}$	3,084.905(93) MHz	[Batteiger 09]
$^2S_{1/2} \leftrightarrow {}^2P_{3/2}$	3,087.560(87) MHz	[Batteiger 09]
Neutral Mg atom properties		
$3s^2 \leftrightarrow 3s3p$ transition wavelength	285.296 nm	[Martin 80]
$3s3p$ to continuum excitation wavelength	375.647 nm	[Martin 80]

Table B.1: Relevant properties of the $^{25}Mg^{+}$ ion and neutral magnesium. The references from which the properties are extracted are shown in the last column. See also Ref. [Drullinger 80] and Ref. [Ansbacher 89] for precision spectroscopy measurements in Mg^{+} ions. The hyperfine energy level splittings at a field B = 0 is calculated by solving the Breit-Rabi equation at a vanishing field.

Transition	B-field (T)	Transition frequency (MHz)	$\frac{d^2f}{dB^2}$ (MHz/mT^2)
$\|F=3,m_F=0\rangle \leftrightarrow \|2,1\rangle$	0.0109464	1,763.031	0.4330
$\|3,1\rangle \leftrightarrow \|2,0\rangle$	0.0109584	1,762.974	0.4330
$\|3,1\rangle \leftrightarrow \|2,1\rangle$	0.0212784	1,686.462	0.3902
$\|3,1\rangle \leftrightarrow \|2,2\rangle$	0.0331568	1,539.102	0.4979
$\|3,2\rangle \leftrightarrow \|2,1\rangle$	0.0331673	1,538.929	0.4979
$\|3,2\rangle \leftrightarrow \|2,2\rangle$	0.0425569	1,333.265	0.5889
$\|2,2\rangle \leftrightarrow \|2,1\rangle$	0.122563	346.187	8.293×10^{-3}
$\|3,2\rangle \leftrightarrow \|3,1\rangle$	0.123202	346.827	8.035×10^{-3}
$\|2,1\rangle \leftrightarrow \|2,0\rangle$	0.340915	301.558	0.1066×10^{-3}
$\|3,1\rangle \leftrightarrow \|3,0\rangle$	0.438352	303.524	0.02140×10^{-3}

Table B.2: The magnetic-field insensitive transitions and their respective magnetic-field strengths in the $^2S_{1/2}$ electronic ground state for the $^{25}Mg^+$ ion in the intermediate field regime. The transition frequencies and the second-order magnetic-field sensitivities are also given.

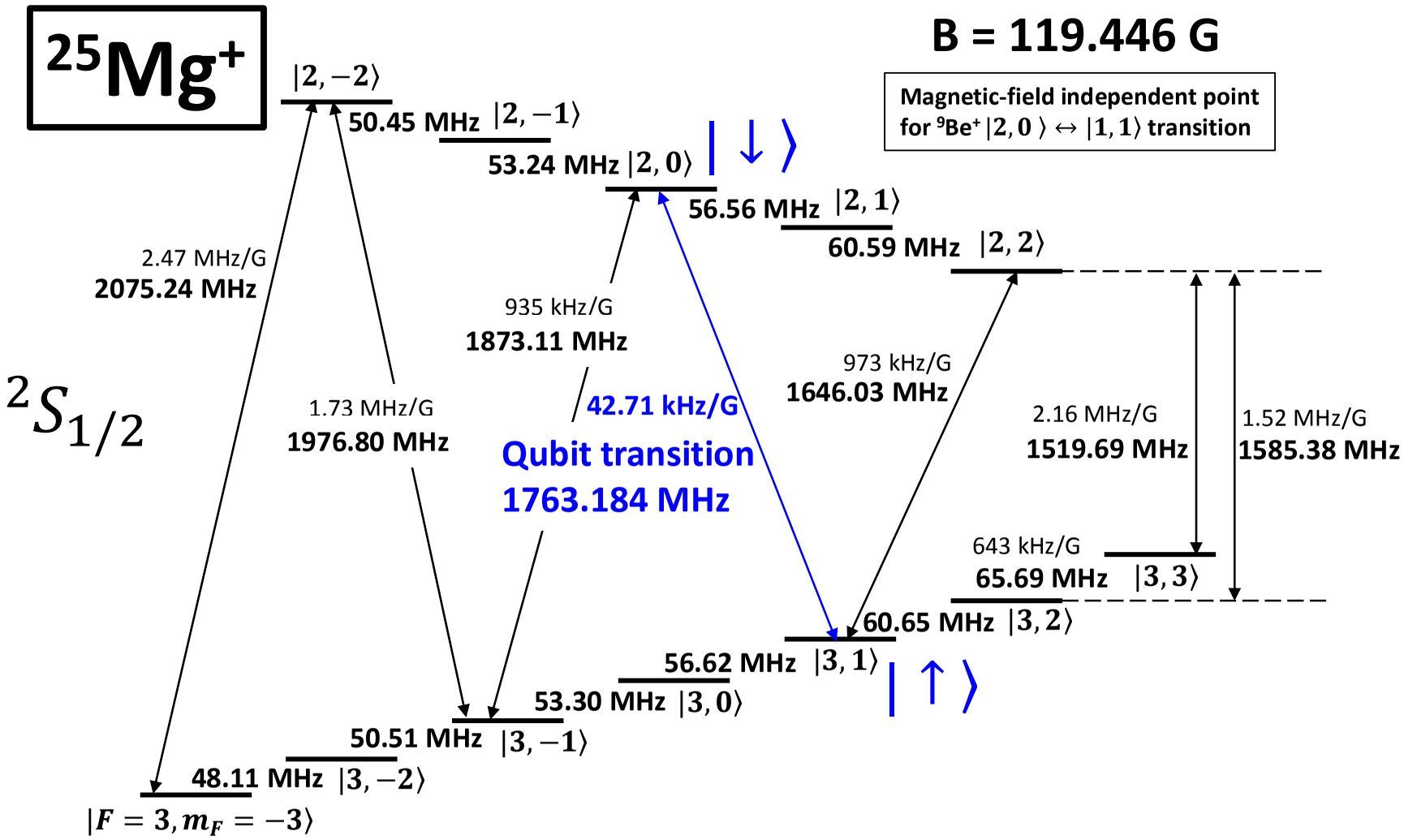

Figure B.1: The electronic ground state of the $^{25}Mg^{+}$ ion at the magnetic-field-insensitive point for the $^{9}Be^{+}$ ion $|F = 2, m_F = 0\rangle \leftrightarrow |1, 1\rangle$ transition. The $^{25}Mg^{+}$ $|F = 3, m_F = 1\rangle \leftrightarrow |2, 0\rangle$ transition is first-order insensitive to magnetic-field fluctuations at B $\simeq$ 109.464 G.

Appendix C

Atom-light Interaction Hamiltonian

In this appendix, we give the Hamiltonians describing an atom's interaction with monochromatic light fields and the Hamiltonians governing the spin-motion transitions driven by stimulated-Raman processes. We will start with the simplest case of a two-level system.

C.1 Two-Level Atoms - Light Interaction

The Hamiltonian of a two-level system interacting with a monochromatic electromagnetic (EM) field (Fig. C.1) can be written as

$$H = H_0 + V(t), \tag{C.1}$$

where $H_0 = \hbar\omega_1|1\rangle\langle 1| + \hbar\omega_2|2\rangle\langle 2|$ is the system's bare Hamiltonian, with $|1\rangle$ and $|2\rangle$ representing the unperturbed states with energies $\hbar\omega_1$ and $\hbar\omega_2$, respectively. Their energy difference is $\omega_0 = \omega_2 - \omega_1$.

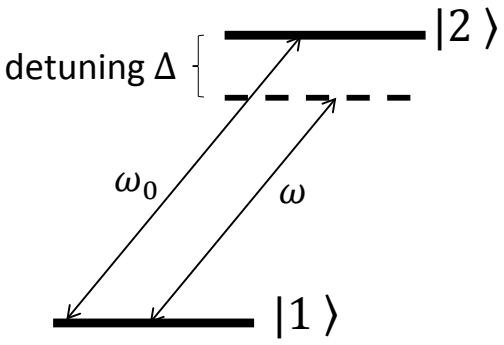

Figure C.1: A two-level system with a detuned interaction.

$V(t)$ describes the interaction between the atom dipole operator, $\boldsymbol{d}$, with an externally applied monochromatic EM field, i.e.

$$V(t) = -\boldsymbol{d} \cdot E\hat{\sigma}_E \cos(\omega t - \phi), \tag{C.2}$$

where E, ω, and ϕ are the amplitude, frequency, and the phase the of applied EM field, respectively. The electric field's polarization vector $\hat{\sigma}_E$ is expressed in terms of linear ($\hat{\pi}$), left ($\hat{\sigma}^-$) and right ($\hat{\sigma}^+$) circular polarizations such that $\hat{\sigma}_E = \epsilon^-\hat{\sigma}^- + \epsilon^0\hat{\pi} + \epsilon^+\hat{\sigma}^+$ with $|\epsilon^-|^2 + |\epsilon^0|^2 + |\epsilon^+|^2 = 1$. Transforming into the interaction picture of the unperturbed system by writing

$$H_I = e^{\frac{iH_0t}{\hbar}} V(t) e^{\frac{-iH_0t}{\hbar}}, \tag{C.3}$$

and after making the rotating-wave approximation, we get

$$H_I = \hbar\Omega|2\rangle\langle 1|e^{-i\Delta t} + h.c., \tag{C.4}$$

where $\Omega = -\frac{\boldsymbol{d}\cdot E\hat{\sigma}_E}{2\hbar}$ and $\Delta = \omega - (\omega_2 - \omega_1)$ are the resonant transition Rabi rate and the detuning of the electromagnetic field from the resonant transition frequency, respectively. For simplicity, we have set $\phi = 0$. In our case, Eq. C.4 is applicable to a transition induced by laser fields between an electronic ground state and an excited state. It can also describe magnetic dipole transitions driven by microwave fields.

C.2 Stimulated-Raman Transition

The simplest case of a stimulated-Raman transition can be seen as a three-level system interacting with two monochromatic light fields (Fig. C.2). For simplicity, we assume that the laser field with frequency ω_a only couples the $|1\rangle$ and $|3\rangle$ states, and does not couple the $|2\rangle$ and $|3\rangle$ states, similarly for the laser field (with frequency ω_b) coupling the $|2\rangle$ and $|3\rangle$ states. Following Eq. C.4, the interaction Hamiltonian in this case is

$$H_I = \hbar\Omega_1|3\rangle\langle 1|e^{-i\Delta_1 t} + \hbar\Omega_2|3\rangle\langle 2|e^{-i\Delta_2 t} + h.c., \tag{C.5}$$

where $|3\rangle$ is the state in which both the $|1\rangle$ and $|2\rangle$ states are coupled to with two light fields that are coherent with each other. The two light fields are detuned by Δ_1 and Δ_2 from each of the

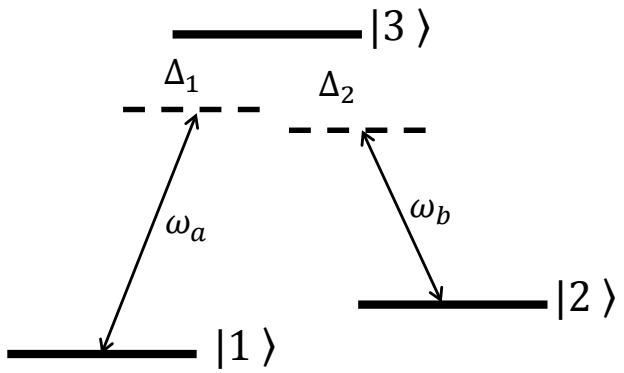

Figure C.2: A three-level system with two detuned interactions. For simplicity, we assume that the light field labeled as ω_a does not couple the $|2\rangle$ and $|3\rangle$ states, and the light field labeled as ω_b does not couple the $|1\rangle$ and $|3\rangle$ states.

transitions, respectively. To relate to our qubit system, we will write $|1\rangle = |\downarrow\rangle$ and $|2\rangle = |\uparrow\rangle$. Thus,

$$H_I = \hbar\Omega_1|3\rangle\langle\downarrow|e^{-i\Delta_1 t} + \hbar\Omega_2|3\rangle\langle\uparrow|e^{-i\Delta_2 t} + h.c.. \tag{C.6}$$

This equation can be transformed into an effective Hamiltonian written as

$$\begin{aligned} H_{eff} = &-\frac{\hbar\Omega_1^2}{\Delta_1}\left(|3\rangle\langle 3| - |\downarrow\rangle\langle\downarrow|\right) - \frac{\hbar\Omega_2^2}{\Delta_2}\left(|3\rangle\langle 3| - |\uparrow\rangle\langle\uparrow|\right) + \\ &\hbar\frac{\Omega_1\Omega_2}{2\bar{\Delta}}\left(|\uparrow\rangle\langle\downarrow|e^{i(\Delta_2-\Delta_1)t} + |\downarrow\rangle\langle\uparrow|e^{-i(\Delta_2-\Delta_1)t}\right), \end{aligned} \tag{C.7}$$

where $\bar{\Delta} = \frac{\Delta_1\Delta_2}{\Delta_1+\Delta_2}$. There are multiple approaches to arrive at Eq. C.7, see for example, Ref. [Wineland 98] with a Schrodinger's equation approach and Ref. [James 07] which give a relatively compact formula for the derivation of the effective Hamiltonian describing the time-averaged dynamics of the system.

The first and second term of Eq. C.7 represent the AC Stark shifts induced by the laser fields, and the third term represents the effective Hamiltonian coupling the qubit $|\uparrow\rangle$ and $|\downarrow\rangle$ states via the stimulated-Raman transition. The latter term can be separated out from the AC Stark shifts terms when we are only interested in the dynamics between the qubit states. A quick inspection and comparison between this term and Eq. C.4 indicates that stimulated-Raman transition can be viewed as an effective coherent Rabi oscillation on the $|\uparrow\rangle \leftrightarrow |\downarrow\rangle$ transition described by

$$H_{Raman} = \hbar\Omega_{Raman}\hat{\sigma}^+ e^{i(\Delta_2-\Delta_1)t} + h.c., \tag{C.8}$$

with an effective Rabi rate of

$$\Omega_{Raman} = \frac{\Omega_1\Omega_2}{2\bar{\Delta}}, \tag{C.9}$$

where $\hat{\sigma}^+ = |\uparrow\rangle\langle\downarrow|$ and its conjugate is $\hat{\sigma}^- = |\downarrow\rangle\langle\uparrow|$. Equation C.8 can be rewriten as

$$H_{Raman} = \hbar\Omega_{Raman}\hat{\sigma}^+ e^{i(\Delta\omega-\omega_0)t} + h.c., \tag{C.10}$$

where $\Delta\omega = \omega_b - \omega_a$, is the frequency difference of the two EM fields depicted in Fig. C.2. A spin-flip oscillation can be driven by setting $\Delta\omega = \omega_0$.

One important effect that has not yet been considered here is the spontaneous emission of photon from the electronic excited state when driving the stimulated-Raman transition. The

spontaneous photon emission rate is approximately proportional to $\frac{\Gamma}{\Delta_R} \times \Omega_{eff}$ where Γ is the excited state's decay rate and $\Delta_R = \Delta_1$ or Δ_2. In most cases, $\Delta_R \gg \Gamma$ such that photon scattering process is suppressed compared to the coherent interaction described by Eq. C.8. Details of spontaneous emissions are described in Sec. 4.4.2.

C.2.1 Rabi Rate of Stimulated-Raman Transitions

The descriptions above provide a simple framework for stimulated-Raman transitions without detailing the coupling strength. The Rabi rate depends on the laser beam electric fields parameter as well as the electronic structure and properties of the addressed atom. If there are j possible excited states that give coupling between the $|\uparrow\rangle$ and $|\downarrow\rangle$ states, the Rabi rate of stimulated-Raman transition driven by two laser fields which are copropagating is [Wineland 98]

$$\Omega_{Raman} = \sum_j \frac{E_1 E_2}{4\hbar^2} \frac{\sum_{p_1} \langle\uparrow|\boldsymbol{d_E} \cdot \hat{\sigma}_{E,1}^{p_1}|j\rangle \sum_{p_2} \langle j|\boldsymbol{d_E} \cdot \hat{\sigma}_{E,2}^{p_2}|\downarrow\rangle}{\Delta_j}, \tag{C.11}$$

where p_1 and p_2 index the polarization components for each of the laser beams, respectively. The atom's electric dipole operator is denoted by $\boldsymbol{d_E}$.

C.3 Spin-Motion Stimulated-Raman Transition

The descriptions above deal only with the interaction between the internal states (spin) of an atom with the electromagnetic fields. Now, adding the motional degree of freedom, the unperturbed system Hamiltonian for a single trapped atom can be written as

$$H_0 = \hbar\frac{\omega_0}{2}\left(|\uparrow\rangle\langle\uparrow| - |\downarrow\rangle\langle\downarrow|\right) + \sum_i^3 \hbar\omega_{\nu,i}\hat{a}_i^\dagger\hat{a}_i, \tag{C.12}$$

where ω_0 is the qubit frequency. For one ion, there are three motional modes, each with a harmonic oscillator frequency of $\omega_{\nu,i}$, and $\hat{a}_i$ represents the harmonic oscillator annihilation operator for the ith mode.

Consider the two-photon stimulated-Raman transition described in Sec. C.2. Taking into account the propagation direction of the two laser beams, the interaction between the dipole operator

and the applied EM waves is

$$V(t) = -\sum_{i}^{2} \boldsymbol{d_E} \cdot E_i \hat{\sigma}_{E,i} \cos\left(\boldsymbol{k_i} \cdot \hat{z} - \omega_i t + \phi_i\right), \tag{C.13}$$

where $\boldsymbol{k_i}$, ω_i and ϕ_i are the wave vector, the laser frequency, and the laser beam phase of the ith beam at the location of the ion. The operator of the ion's motion is given by

$$\hat{z} = z_0 \left(\hat{a} + \hat{a}^\dagger\right) \tag{C.14}$$

where $z_0 = \sqrt{\hbar/(2m\omega_\nu)}$ is the zero-point amplitude of the ion's motional wavefunction, with m as the mass of the ion. The effective Hamiltonian associated with this dipole-light interaction takes the form of Eq. C.10:

$$H_I = \hbar\Omega\hat{\sigma}^+ e^{i[\boldsymbol{\Delta k}\cdot\hat{z} - (\Delta\omega - \omega_0)t + (\phi_2 - \phi_1)]} + h.c., \tag{C.15}$$

where Ω is the Rabi rate which can be computed with Eq. C.11.

In this thesis, we use a pair of laser beams with their wave vector difference $\boldsymbol{\Delta k} = \boldsymbol{k_2} - \boldsymbol{k_1}$ aligned along the axial (z) direction. In this configuration, we only have to consider one motional mode for the interaction. For a $^9Be^+$ ion in a trap with $\omega_z = 2\pi \times 3.6$ MHz, we have $z_0 \simeq 12.5$ nm.

With Eq, C.14, Eq. C.15 can be rewritten as

$$H_I = \hbar\Omega\hat{\sigma}^+ e^{i\left[\eta\left(\hat{a}+\hat{a}^\dagger\right) - (\Delta\omega - \omega_0)t + (\phi_2 - \phi_1)\right]} + h.c., \tag{C.16}$$

where $\eta = |\Delta k| z_0$ is the Lamb-Dicke parameter. In the limit where $\eta \ll 1$, we can expand the first term in the exponent:

$$e^{i\left(\eta(\hat{a}+\hat{a}^\dagger)\right)} = 1 + i\eta(\hat{a} + \hat{a}^\dagger) - \eta^2(\hat{a} + \hat{a}^\dagger)^2 + ... \tag{C.17}$$

such that Eq. C.16 becomes

$$H_I = \hbar\Omega\hat{\sigma}^+ e^{i\omega_0 t}\left[1 + i\eta(\hat{a} + \hat{a}^\dagger) - \eta^2(\hat{a} + \hat{a}^\dagger)^2 + ...\right] e^{i[-\Delta\omega t + (\phi_2 - \phi_1)]} + h.c.. \tag{C.18}$$

Now, we will go into the interaction frame (Eq. C.3) of the harmonic oscillator describing the ion's motion, then

$$H_I = \hbar\Omega\hat{\sigma}^+ e^{i\omega_0 t}\left[1 + i\eta(\hat{a}e^{-i\omega_z t} + \hat{a}^\dagger e^{i\omega_z t}) - \eta^2(\hat{a}e^{-i\omega_z t} + \hat{a}^\dagger e^{-i\omega_z t})^2 + ...\right] \times e^{i[-\Delta\omega t + (\phi_2 - \phi_1)]} + h.c.. \tag{C.19}$$

In most cases, the laser frequency difference $\Delta\omega = \omega_1 - \omega_2$ is set near the qubit frequency ω_0 or $\omega_0 \pm \mathrm{m}\omega_z$, where $\mathrm{m} = 1, 2, ...$ such that most non-resonant terms in Eq. C.19 can be neglected. For example, by setting $\Delta\omega = \omega_0$, and dropping high frequency terms, we have

$$H_{Carrier} = \hbar\Omega\hat{\sigma}^{+}e^{i(\phi_2-\phi_1)} + h.c., \tag{C.20}$$

which is analogous to Eq. C.10 and describes a carrier excitation that drives $|\downarrow, n\rangle \leftrightarrow |\uparrow, n\rangle$ spin-flip oscillations. Likewise, by setting $\Delta\omega = \omega_0 - \omega_z$, the Hamiltonian after dropping fast oscillating terms is

$$H_{RSB} = \hbar\eta\Omega\hat{\sigma}^{+}\hat{a}e^{i(\phi_2-\phi_1)} + h.c., \tag{C.21}$$

which induces a spin-flip $|\downarrow, n\rangle \leftrightarrow |\uparrow, n-1\rangle$ while removing a quanta from the motional harmonic oscillator. This excitation is a red-sideband transition. Analogously, a blue-sideband transition is described by the Hamiltonian

$$H_{BSB} = \hbar\eta\Omega\hat{\sigma}^{+}\hat{a}^{\dagger}e^{i(\phi_2-\phi_1)} + h.c., \tag{C.22}$$

after setting $\Delta\omega = \omega_0 + \omega_z$ and neglecting fast oscillating terms.

It is straightforward to generalize these Hamiltonians to the case where multiple ions are interacting with the laser light fields. For example, for two ions trapped in a harmonic well, there are two normal modes along the axial direction. In this case, we can write the position operator $\hat{z}_j$ of the jth ion in terms of normal mode coordinates

$$\hat{z}_j = \sum_{k=1,2}\left(z_{0,k}\xi_{k,j}(\hat{a}_k + \hat{a}_k^{\dagger}), \right. \tag{C.23}$$

where $z_{0,k} = \sqrt{\hbar/(2m\omega_k)}$ with ω_k, $\xi_{k,j}$ and $\hat{a}_k$ are the normal mode frequency, mode amplitude (of the jth ion) and the annihilation operator for the kth motional mode.

Following Eq. C.16, the interaction Hamiltonian describing two ions interacting with light fields arranged such that their $\boldsymbol{\Delta k}$ aligned along the axial direction is [Wineland 98]

$$H_I = \hbar\sum_{j=1,2}\Omega_j\hat{\sigma}_j^{+}\mathrm{Exp}\left[i\sum_k\left(\eta_k\xi_{k,j}\left(\hat{a}_k + \hat{a}_k^{\dagger}\right) - i(\Delta\omega - \omega_0)t + i(\phi_{2,j} - \phi_{1,j})\right]\right(+ h.c., \tag{C.24}$$

where Ω_j is the resonant Rabi rate of the laser-induced carrier transition for the jth ion, it can be computed with Eq. C.11.

Appendix D

Matrix Representations of State Vectors and Qubit Operations

D.1 Qubit State Vectors

For a two-level atom, the qubit $|\uparrow\rangle$ and $|\downarrow\rangle$ states are defined as the following matrices:

$$|\uparrow\rangle = \begin{pmatrix} 1 \\ 0 \end{pmatrix}, |\downarrow\rangle = \begin{pmatrix} 0 \\ 1 \end{pmatrix}. \tag{D.1}$$

The state vectors for the compound system of two two-level atoms are the results from tensor products of individual atom's state vectors, for example

$$|\uparrow\uparrow\rangle = \begin{pmatrix} 1 \\ 0 \end{pmatrix} \otimes \begin{pmatrix} 1 \\ 0 \end{pmatrix} = \begin{pmatrix} 1 \\ 0 \\ 0 \\ 0 \end{pmatrix}. \tag{D.2}$$

Likewise,

$$|\uparrow\downarrow\rangle = \begin{pmatrix} 0 \\ 1 \\ 0 \\ 0 \end{pmatrix}, |\downarrow\uparrow\rangle = \begin{pmatrix} 0 \\ 0 \\ 1 \\ 0 \end{pmatrix}, |\downarrow\downarrow\rangle = \begin{pmatrix} 0 \\ 0 \\ 0 \\ 1 \end{pmatrix}. \tag{D.3}$$

D.2 Qubit Rotations

Rotation about an axis in the x-y plane of the Bloch sphere of a two-level atom is represented by the following matrix:

$$R(\theta,\phi) = \begin{pmatrix} \cos(\theta/2) & -ie^{-i\phi}\sin(\theta/2) \\ -ie^{i\phi}\sin(\theta/2) & \cos(\theta/2) \end{pmatrix} \tag{D.4}$$

where θ is the rotation angle and ϕ is the azimuthal angle of the rotation axis.

The rotation around z axis of the Bloch sphere with an angle of ξ is defined as

$$R_z(\xi) = \begin{pmatrix} e^{-i\xi/2} & 0 \\ 0 & e^{i\xi/2} \end{pmatrix} \tag{D.5}$$

Similar to the construction of a compound system from smaller systems, the operator representing a global rotation on a two-qubit compound system can be constructed using the tensor product:

$$R_{two}(\theta,\phi) = R(\theta,\phi) \otimes R(\theta,\phi). \tag{D.6}$$

Likewise, the (two-qubit) operator representing a rotation applied on the first qubit without influencing the second qubit is

$$R(\theta,\phi) \otimes \begin{pmatrix} 1 & 0 \\ 0 & 1 \end{pmatrix} \tag{D.7}$$

D.3 Fock State Vectors

Each motional degree of freedom is described by a simple harmonic oscillator. The Fock basis state $|n\rangle$ can be represented by the following matrices:

$$|0\rangle = \begin{pmatrix} 1 \\ 0 \\ 0 \\ \vdots \\ 0 \end{pmatrix}, |1\rangle = \begin{pmatrix} 0 \\ 1 \\ 0 \\ \vdots \\ 0 \end{pmatrix}, |2\rangle = \begin{pmatrix} 0 \\ 0 \\ 1 \\ \vdots \\ 0 \end{pmatrix}, \text{etc.} \tag{D.8}$$

D.4 Creation and Annihilation Operators

The simple harmonic oscillator annihilation operator, $\hat{a}$, and creation operator, $\hat{a}^\dagger$, can be represented by the following matrices

$$\hat{a} = \begin{pmatrix} 0 & 1 & 0 & 0 & \cdots & 0 & \cdots \\ 0 & 0 & \sqrt{2} & 0 & \cdots & 0 & \cdots \\ 0 & 0 & 0 & \sqrt{3} & \cdots & 0 & \cdots \\ 0 & 0 & 0 & 0 & \ddots & \vdots & \cdots \\ \vdots & \vdots & \vdots & \vdots & \ddots & \sqrt{n} & \cdots \\ 0 & 0 & 0 & 0 & \cdots & 0 & \cdots \\ \vdots & \vdots & \vdots & \vdots & \vdots & \vdots & \ddots \end{pmatrix}, \tag{D.9}$$

$$\hat{a}^\dagger = \begin{pmatrix} 0 & 0 & 0 & 0 & \cdots & 0 & \cdots \\ 1 & 0 & 0 & 0 & \cdots & 0 & \cdots \\ 0 & \sqrt{2} & 0 & 0 & \cdots & 0 & \cdots \\ 0 & 0 & \sqrt{3} & 0 & \cdots & 0 & \cdots \\ \vdots & \vdots & \vdots & \ddots & \vdots & \vdots & \cdots \\ 0 & 0 & 0 & 0 & \sqrt{n} & 0 & \cdots \\ \vdots & \vdots & \vdots & \vdots & \vdots & \ddots & \ddots \end{pmatrix}. \tag{D.10}$$

when applying $\hat{a}$ or $\hat{a}^\dagger$ to a Fock state $|n\rangle$, they give

$$\hat{a}|n\rangle = \sqrt{n}|n-1\rangle, \tag{D.11}$$

$$\hat{a^\dagger}|n\rangle = \sqrt{n+1}|n+1\rangle. \tag{D.12}$$

D.5 Atom and Motion Compound System

Similar to that in Eq. D.2, the state vector of the compound system consisting of a two-level atom and one motional mode can be constructed with the tensor product. For example, an atom

in the $|\uparrow\rangle$ state prepared in the ground state of motion is

$$|\uparrow\rangle|n=0\rangle = \begin{pmatrix} 1 \\ 0 \end{pmatrix} \otimes \begin{pmatrix} 1 \\ 0 \\ 0 \\ 0 \\ \vdots \end{pmatrix}. \tag{D.13}$$

Similarly, operators acting on the compound system can be constructed with tensor products. It is straightforward to generalize state vectors and operators to a systems of higher dimension.

D.6 Summary of Qubit Operators

Here we write down some of the common qubit operators which are frequently used in this thesis.

$$\hat{\sigma}_x = \begin{pmatrix} 0 & 1 \\ 1 & 0 \end{pmatrix}, \hat{\sigma}_y = \begin{pmatrix} 0 & -i \\ i & 0 \end{pmatrix}, \hat{\sigma}_z = \begin{pmatrix} 1 & 0 \\ 0 & 1 \end{pmatrix}, \tag{D.14}$$

$$\hat{\sigma}^+ = |\uparrow\rangle\langle\downarrow| = \frac{\hat{\sigma}_x + i\hat{\sigma}_y}{2} = \begin{pmatrix} 0 & 1 \\ 0 & 0 \end{pmatrix}, \tag{D.15}$$

$$\hat{\sigma}^- = |\downarrow\rangle\langle\uparrow| = \frac{\hat{\sigma}_x - i\hat{\sigma}_y}{2} = \begin{pmatrix} 0 & 0 \\ 1 & 0 \end{pmatrix}, \tag{D.16}$$

D.7 Three-Level Atom

For some cases, it is desirable to include an auxiliary atomic state to study the dynamics of the system such as (i) the implementation of the Cirac-Zoller protocol [Cirac 95] (see also Sec. 4.2 and Sec. 5.6), (ii) the effect of out-of-manifold Raman spontaneous scattering processes (see Sec. 4.4.2.1), and (iii) imperfect qubit state preparation and measurement (see for example, Sec. 6.6.2). We label the auxiliary state as $|A\rangle$.

In this case, the state vectors are modified such that

$$|\uparrow\rangle' = \begin{pmatrix} 1 \\ 0 \\ 0 \end{pmatrix}, |\downarrow\rangle' = \begin{pmatrix} 0 \\ 1 \\ 0 \end{pmatrix}, |A\rangle = \begin{pmatrix} 0 \\ 0 \\ 1 \end{pmatrix}. \tag{D.17}$$

Here, we use the superscript $\prime$ to differentiate these state vectors from those of Eq. D.1.

D.8 Qubit Operators in a Three-Level Atom

The $R(\theta\phi)$ rotation (Eq. D.4) between the qubit $|\uparrow\rangle$ and $|\downarrow\rangle$ states becomes

$$R'(\theta,\phi) = \begin{pmatrix} \cos(\theta/2) & -i\phi e^{-i\phi}\sin(\theta/2) & 0 \\ -i\phi e^{i\phi}\sin(\theta/2) & \cos(\theta/2) & 0 \\ 0 & 0 & 1 \end{pmatrix}. \tag{D.18}$$

Similarly for the R_z rotation (Eq. D.5) between the $|\uparrow\rangle$ and $|\downarrow\rangle$ states:

$$R'_z(\xi) = \begin{pmatrix} e^{-i\xi/2} & 0 & 0 \\ 0 & e^{i\xi/2} & 0 \\ 0 & 0 & 1 \end{pmatrix}. \tag{D.19}$$

Other commonly used operators are:

$$\hat{\sigma}^{+\prime} = |\uparrow\rangle'\langle\downarrow|' = \begin{pmatrix} \begin{pmatrix} 0 & 1 & 0 \\ 0 & 0 & 0 \end{pmatrix}, \\ \begin{pmatrix} 0 & 0 & 0 \\ 0 & 0 & 0 \end{pmatrix}, \end{pmatrix} \tag{D.20}$$

$$\hat{\sigma}^{-\prime} = |\downarrow\rangle'\langle\uparrow|' = \begin{pmatrix} \begin{pmatrix} 0 & 0 & 0 \\ 1 & 0 & 0 \end{pmatrix}, \\ \begin{pmatrix} 0 & 0 & 0 \\ 0 & 0 & 0 \end{pmatrix}, \end{pmatrix} \tag{D.21}$$

$$\hat{\sigma}^{+}_{\uparrow A} = |\uparrow\rangle'\langle A| = \begin{pmatrix} \begin{pmatrix} 0 & 0 & 1 \\ 0 & 0 & 0 \end{pmatrix}, \\ \begin{pmatrix} 0 & 0 & 0 \\ 0 & 0 & 0 \end{pmatrix}, \end{pmatrix} \tag{D.22}$$

$$\hat{\sigma}^{-}_{\downarrow A} = |\downarrow\rangle'\langle A| = \begin{pmatrix} \begin{pmatrix} 0 & 0 & 0 \\ 0 & 0 & 1 \end{pmatrix}, \\ \begin{pmatrix} 0 & 0 & 0 \\ 0 & 0 & 0 \end{pmatrix}, \end{pmatrix} \tag{D.23}$$

$$\hat{\sigma}^{+}_{A\uparrow} = |A\rangle\langle\uparrow|' = \begin{pmatrix} \begin{pmatrix} 0 & 0 & 0 \\ 0 & 0 & 0 \end{pmatrix}, \\ \begin{pmatrix} 1 & 0 & 0 \\ 0 & 0 & 0 \end{pmatrix}, \end{pmatrix} \tag{D.24}$$

$$\hat{\sigma}^{-}_{A\downarrow} = |A\rangle\langle\uparrow|' = \begin{pmatrix} \begin{pmatrix} 0 & 0 & 0 \\ 0 & 0 & 0 \end{pmatrix}, \\ \begin{pmatrix} 0 & 1 & 0 \\ 0 & 0 & 0 \end{pmatrix}, \end{pmatrix}. \tag{D.25}$$

With these, it is straightforward to generalize and construct other operators, as needed.